Mechanical Stability of the Electromechanical Properties and Phase Transitions in Lead-Containing and Lead-Free Ferroelectrics

Vom Fachbereich Material- und Geowissenschaften
zur Erlangung des akademischen Grades eines Doktor-Ingenieurs (Dr.-Ing.)
genehmigte Dissertation von Dipl.-Ing. Florian Herbert Schader aus Worms

1. Gutachten: Prof. Dr. Kyle G. Webber
2. Gutachten: Prof. Dr. Bai-Xiang Xu

Tag der Einreichung: 17. Mai 2016, Tag der Prüfung: 04. Juli 2016
August 2016 — Darmstadt — D 17

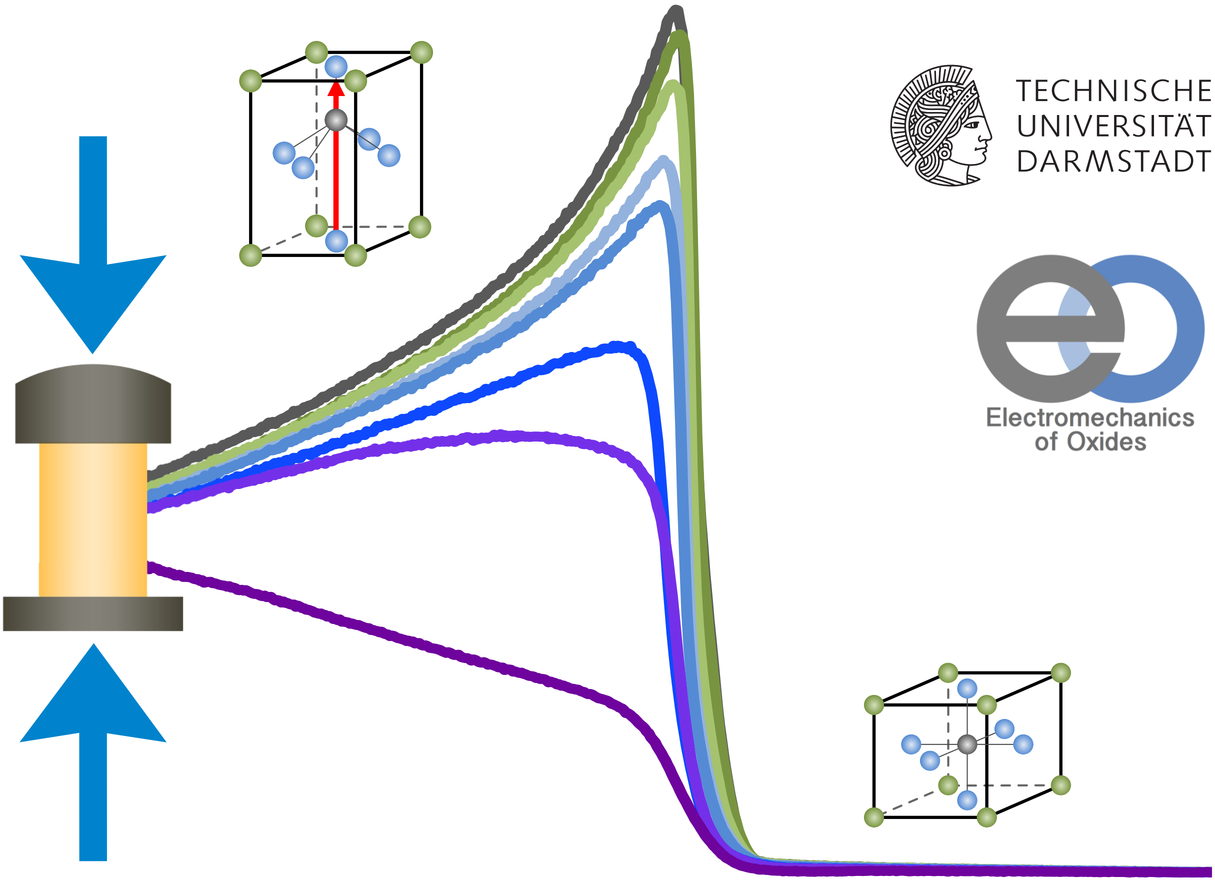

TECHNISCHE
UNIVERSITÄT
DARMSTADT

Electromechanics
of Oxides

Mechanical Stability of the Electromechanical Properties and Phase Transitions in Lead-Containing and Lead-Free Ferroelectrics

Genehmigte Dissertation von Dipl.-Ing. Florian Herbert Schader aus Worms

1. Gutachten: Prof. Dr. Kyle G. Webber
2. Gutachten: Prof. Dr. Bai-Xiang Xu

Tag der Einreichung: 17. Mai 2016
Tag der Prüfung: 04. Juli 2016

Fachbereich Material- und Geowissenschaften
August 2016 — Darmstadt — D 17

Bitte zitieren Sie dieses Dokument als:
URN: urn:nbn:de:tuda-tuprints-55724
URL: http://tuprints.ulb.tu-darmstadt.de/id/eprint/5572

Ever tried. Ever failed. No matter.
Try again. Fail again. Fail better.

– from "Worstward Ho" by Samuel Beckett

Acknowledgements

First and foremost, I would like to thank my supervisor Prof. Dr. Kyle G. Webber for his help and support during the whole time of my PhD. We worked together every day and discussed very intensively. I could not have completed this thesis without him and I learned so much from him. It was also very exciting to witness his development from a postdoc to an Emmy-Noether awardee and Junior Professor, and finally to a Full Professor in Erlangen. Thank you very, very much for all, Kyle, I wish you all the best!

Prof. Dr. Jürgen Rödel gave me the opportunity to do my PhD in his group and supported all the technical and scientifical developments very generously. Thank you very much for the time in NAW!

I would like to thank Prof. Dr. Bai-Xiang Xu, who did not hesitate to agree to review this thesis. In addition, I would like to thank Prof. Dr. Karsten Albe and Prof. Dr. Jens Schneider for being part of the examination commission.

Dipl.-Ing. Emil Aulbach constructed and built the technological foundation of the experiments for this project, for which I would like to express my greatest gratitude. It would not have been possible to develop all the experimental devices during my work without the support of Dipl.-Ing. Daniel Isaia. His creativity and his construction skills were invaluable and are highly acknowledged!

The success of the project was significantly based on the help and support of Michael Weber, the best and most committed electrician on the entire planet. No experiment would have worked without him and the devices he developed were technologically excellent without exception. Michael, thank you so much for all your support and advice, it was a pleasure to work with you!

I would like to thank Michael Heyse, who did a lot of sample preparation for me. Especially when it came to delicate and complicated materials like single crystals or high precision metal and ceramic parts, his expertise and his skillful work were indispensable.

Dipl.-Ing. Gundel Fliß supported me whenever problems with computers, electronics or software arose, and this happened a lot during my PhD. Thank you very, very much, Gundel, for all your kind help and the fast support with all problems. I wish you all the best!

A very special thank-you goes to my student assistants Hans Wardenga, M.Sc., and Valentin Brabänder, B.Sc. I was extremely lucky for having two very skilled, independent, and reliable HiWis, who did nearly all my powder and sample processing. This was not easy, especially not the cylindrical samples and the thin bars for the DMA. Thanks guys, it would have taken me an extra year if you would not have helped me!

I would like to thank Roswita Geier and Gila Völzke for their administrative support and their advice with all organizational problems.

Prof. Dr. George A. Rossetti supported my theoretical work on the phase transitions of barium titante, which is gratefully acknowledged. He also established a contact to Dr. Jun Luo from TRS Technologies Inc., who kindly provided the PIN-PMN-PT single crystals. I am very thankful for the good collaboration with Prof. Dr. John Daniels, Dr. Zhiyang Wang, and Dr. Manuel Hinterstein on the stress-dependent XRD measurements on NBT-xBT. In addition, I would like to thank Prof. Dr. Dragan Damjanovic for giving me the opportunity to stay for two weeks at the EPFL in Lausanne. I will never forget the very interesting and inspiring discussions with him.

Dr. Jurij Koruza and Dr. Nikola Novak read parts of this thesis in its initial stage and gave important and valuable comments for improvement. Thank you so much for you support! In addition, I would like to thank my very dear friend Dipl.-Phys. Kirsten Vincke, who volunteered to proof-read this thesis, which was a very big help for me.

It is my pleasure to thank my wonderful officemates Debbi, Raschid (Colleague No. Uno), Hairui and Sebastian for an extraordinary, great, and exciting time together. I will never forget all our discussions, the earnest, personal and scientific ones as well as the funny and weird ones. Thank you so much, only the very best for all of you! This also counts for my former colleagues and friends Eva, Claudia, Azatuhi, Markus, Philipp, Martin, Robert, and Matias who made my time at NAW really great.

I would like to thank my guest and friend Dr. Espen Wefring, who challenged me a lot with experimental issues during his stay in Darmstadt. It was really great to have you here, Espen, all the best for you!

A special thank-you goes to my colleague and friend Malte for the great collaboration during repairing the RFDA, for discussing weird measurement results, for dealing with very special lab course reports, and for constructing amazing doctor wagons. Thanks for all, Malte, you are a great guy!

At this point, I would like to thank Dr. Eric Patterson for all his support and advise. He read nearly my whole thesis, gave an invaluable amount of scientific input and changed all my strange expressions to correct English language. Eric, thank you so much for everything, I would not have managed to finish this thesis without your support and your fantastic friendship. With good friends you can't lose!

Zu guter Letzt möchte ich mich bei meinen Freunden und meiner Familie bedanken, die mich immer unterstützt haben. Mein besonderer Dank gilt meinen Eltern, die mir diese Ausbildung ermöglichten und die immer bedingungslos an meiner Seite waren.

Preface

It was the aim of this work to investigate the influence of mechanical stress on the properties and the phase transition behavior of ferroelectrics. Similar to the application of electrical fields, mechanical loads are also known to alter the piezoelectric properties of ferroelectric materials and are capable of inducing structural phase transitions. There is a large body of research previously performed on the influence of hydrostatic stress, but investigations on the effects of radial or uniaxial stresses are relatively rare. Notably, uniaxial stress is used in numerous applications, such as prestress in dynamically loaded piezoelectric actuators, underlining the special importance of understanding the influences of such mechanical loads. Most of the experiments presented in the work focus on the characterization of the small signal dielectric and piezoelectric properties of ferroelectrics under various external thermal and mechanical fields. This allowed for combining realistic environmental testing conditions with the possibility of basic research on the physical mechanism responsible for the observed measurement results.

In order to realize the above-described measurements, a significant amount of engineering was necessary to design, built, and incrementally improve new experimental setups and devices. The integration of a piezoelectric actuator in a uniaxial load frame for measuring the small signal piezoelectric coefficient was done by Dipl.-Ing. Emil Aulbach and Prof. Dr. Kyle G. Webber. The remaining experiment was developed as part of this project, which included writing a complex, fully automatic measurement control and data acquisition software as well as the design and integration of additionally required devices and electrical circuits. Together with developing a new method to produce precise cylindrical ceramic samples (±0.2 % geometric tolerance), a substantial amount of time also was spent during this project on the maintaining and extension of the experimental capabilities. In particular, a new load frame and custom-made temperature chamber were purchased, installed, and developed as part of the expansion of measurement capabilities. Here, for example, the programming of the two-channel temperature regulation system, which simultaneously controlled heating and cooling, was a specific challenge. Following numerous complications and error eliminations, the possibility of measuring the piezoelectric and dielectric properties as a function of temperature (20 °C – 450 °C), frequency (50 mHz – 240 Hz), and mechanical bias field (up to 1 GPa) with a comparatively high resolution (±0.1 pC/N) was established. The most important advantage this experimental arrangement is the ability to perform these measurements automatically and simultaneously, which significantly increases the number of possible data points and largely eliminates issues with comparing measurement results from different experimental setups and sample conditions.

The very first measurement results revealed a challenge for data interpretation, as such data has never been previously presented. There is, therefore, a substantial lack in literature, making determination of the physical mechanisms of the observed features difficult. For this reason, this thesis starts with a well-known normal ferroelectric material, $BaTiO_3$, where the influence of a mechanical bias stress on the phase transitions was investigated and theoretically described (Chapter 3). The subsequent measurements of the piezoelectric and dielectric properties of more complex lead-containing ferroelectrics as a function of temperature and uniaxial compression revealed a number of new observations, which lead to improved understanding on the depolarization and phase transition behavior of these materials (Chapter 4). In particular, polar defects, which are necessary to achieve certain special material properties, played an important role in understanding the underlying physical phenomena. Finally, modern lead-free ferroelectrics were investigated, which showed an even more complex and sometimes also surprising behavior under the application of a mechanical load combined with increasing and decreasing temperature (Chapter 5). These materials are of special importance since current regulations restrict the usage of lead-containing materials in electronic devices.

In addition to trying to answer some open questions on ferroelectric materials, this work could also serve to raise new questions and lead to further investigations. A better understanding of ferroelectric materials is not only scientifically interesting, but also highly important for many applications in daily life, in industrial processes, or in medical devices.

Contents

List of Figures

List of Tables

List of Symbols

a_C	Lattice constants of cubic crystals
a_T, c_T	Lattice constants of tetragonal crystals
a_H, c_H	Lattice constants of hexagonal crystals
α, β	Rayleigh parameters
c_{ijkl}	Elastic stiffness tensor
C	Capacitance; Curie constant
χ_{ij}	Dielectric suszeptibility
χ, ξ, ζ	Landau parameters
D_i	Dielectric displacement field
d_{ijkl}	Piezoelectric tensor
d_0	Static piezoelectric coefficient
δ_{ij}	Kronecker delta
E	Elastic Modulus
E_i	Electric field
E_c	Coercive field
$\widehat{E}$	Electric field amplitude
$\widehat{E}_{th}$	Threshold electric field amplitude
ε_{ij}	Dielectric permittivity
ε_0	Permittivity of free space
ε_m	Maximum dielectric permittivity
M_{ijkl}, Q_{ijkl}	Electrostrictive tensors
f	Frequency
F	Mechanical load

G	Gibbs free energy
γ	Critical exponent
p_i	Pyroelectric coefficient
P_i	Polarization
P_r, $P_{r,ideal}$	Remanent polarization; ideal remanent polarization
P_s	Spontaneous polarization
P_{sat}	Saturation polarization
s_{ijkl}	Elastic compliance tensor
S_{ij}	Strain tensor
S_r, $S_{r,ideal}$	Remanent strain; ideal remanent strain
S_{sat}	Saturation strain
t	Goldschmidt tolerance factor
T	Temperature
T_B	Burns temperature
T_C	Curie point
T_d	Depolarization temperature
$T_{F\text{-}R}$	Ferroelectric-to-relaxor transition temperature during heating
$T_{\text{inf}}^{\varepsilon'}$, $T_{\text{inf}}^{d_{33}}$	Inflection point of the permittivity-temperature curve; inflection point of the piezoelectric coefficient-temperature curve
$T_m^{\varepsilon'}$, $T_m^{d_{33}}$	Temperature at maximum permittivity; temperature at maximum piezoelectric coefficient
T_{RE}	Temperature at which the frequency dispersion of the permittivity is vanishing during heating
T_{VF}	Vogel-Fulcher temperature
$\tan(\delta)$	Dissipation factor
θ	Curie-Weiss temperature
U	Potential energy; Voltage
X_{ij}	Stress tensor

$\widehat{X}$	Stress amplitude
$\widehat{X}_{th}$	Threshold stress amplitude
X_c	Coercive stress
X_L	Stress at maximum dielectric loss

BZT-xBCT	$(1–x)\mathrm{Ba}(\mathrm{Ti}_{0.8}\mathrm{Zr}_{0.2})\mathrm{O}_3–x(\mathrm{Ba}_{0.7}\mathrm{Ca}_{0.3})\mathrm{TiO}_3$
KNN	$(\mathrm{K}_{0.5}\mathrm{Na}_{0.5})\mathrm{NbO}_3$
NBT	$(\mathrm{Na}_{1/2}\mathrm{Bi}_{1/2})\mathrm{TiO}_3$
NBT-xBT	$(1–x)(\mathrm{Na}_{1/2}\mathrm{Bi}_{1/2})\mathrm{TiO}_3–x\mathrm{BaTiO}_3$
NBT-xKBT	$(1–x)(\mathrm{Na}_{0.5}\mathrm{Bi}_{0.5})\mathrm{TiO}_3–x(\mathrm{K}_{0.5}\mathrm{Bi}_{0.5})\mathrm{TiO}_3$
PLZT	$\mathrm{Pb}_{1-x}\mathrm{La}_x(\mathrm{Zr}_{1-y}\mathrm{Ti}_y)_{1-x/4}\mathrm{O}_3$
PMN	$\mathrm{Pb}(\mathrm{Mg}_{1/3}\mathrm{Nb}_{2/3})\mathrm{O}_3$
PMN-PT	$(1–x)\mathrm{Pb}(\mathrm{Mg}_{1/3}\mathrm{Nb}_{2/3})\mathrm{O}_3–x\mathrm{PbTiO}_3$
PIN-PMN-PT	$x\mathrm{Pb}(\mathrm{In}_{1/2}\mathrm{Nb}_{1/2})–(1–x–y)\mathrm{Pb}(\mathrm{Mg}_{1/3}\mathrm{Nb}_{2/3})\mathrm{O}_3–y\mathrm{PbTiO}_3$
PZN	$\mathrm{Pb}(\mathrm{Zr}_x\mathrm{Ti}_{1-x})\mathrm{O}_3$
PZN-PT	$(1–x)\mathrm{Pb}(\mathrm{Zn}_{1/3}\mathrm{Nb}_{2/3})\mathrm{O}_3–x\mathrm{PbTiO}_3$
PZT	$\mathrm{Pb}(\mathrm{Zr}_x\mathrm{Ti}_{1-x})\mathrm{O}_3$

LVDT	Linear variable differential transformer
MPB	Morphotropic phase boundary
PC	Pseudo-cubic
PNR	Polar nanoregion
VI	Virtual instrument

$[V_{\mathrm{rms}}]$	Root mean square volatage

Abstract

In this work, novel experimental setups were developed that are capable of automatically and simultaneously measuring the small signal piezoelectric and dielectric properties of ferroelectrics as a function of frequency, temperature, and compressive uniaxial mechanical stress. In addition, ferroelectric and ferroelastic experiments served to characterize the large-signal properties of ferroelectric materials.

The phase transition behavior of single crystal and polycrystalline $BaTiO_3$ was investigated between –150 °C and 250 °C as a function of uniaxial mechanical bias stresses up to –30 MPa (single crystal $BaTiO_3$) and –500 MPa (polycrystalline $BaTiO_3$). An increase of the Curie point and a decrease of the Curie-Weiss temperature with increasing mechanical stress were revealed by the experiments. These observations lead to the conclusion that a mechanical load results in an increase in the first order nature of the ferroelectric-paraelectric phase transition in $BaTiO_3$. By introducing stress-dependent coefficients in the phenomenological LGD theory, a prediction of this change in the nature of the phase transition as well as a qualitative reproduction of the stress-induced shift of the Curie point was achieved. The low-temperature phase transitions could be correlated with anomalies in the temperature-dependent ferroelastic properties of $BaTiO_3$.

Ferroelectrically soft and hard commercial lead-containing PZT compositions were investigated with regards to their stress- and temperature-induced depolarization and phase transition behavior up to a mechanical bias stress of –300 MPa between room temperature and 350 °C (soft PZT) or 450 °C (hard PZT). The hard PZT showed higher resistance against stress-induced and thermal depolarization due to the pinning of domain walls by polar defects, but with the drawback of lower piezoelectric properties if compared to soft PZT. With increasing mechanical stress, the ferroelectric-paraelectric phase transition of both materials was found to increase. Stress-dependent measurements of the piezoelectric coefficient up to –400 MPa performed on slow cooled and air quenched samples indicated that the polar defects in the hard PZT could be realigned by a compressive uniaxial mechanical stress. In addition, temperature- and stress-dependent measurements of the piezoelectric properties of PIN-PMN-PT single crystals revealed a stabilization of the high-temperature tetragonal phase, experimentally observed by a decreasing rhombohedral-tetragonal phase transition temperature.

Lead-free materials based on the NBT-xBT system are of current interest for replacing lead-containing materials in electronic devices. In this work, the piezoelectric and dielectric properties NBT-3BT, NBT-6BT, NBT-9BT, and NBT-12BT were characterized as a function of temperature (up to 400 °C) and uniaxial mechanical compression (up to –300 MPa). In general, the properties of all investigated NBT-xBT materials were found to decrease above a sufficiently large uniaxial mechanical compression. The MPB materials NBT-6BT and NBT-9BT possessed mixed rhombohedral and tetragonal phases after electrical poling and showed the highest stress sensitivity. NBT-6BT was investigated in more detail and a stress-induced phase transition from an initially relaxor to a ferroelectric phase was observed. A stress-temperature diagram could be constructed based on stress-dependent permittivity measurements up to –600 MPa at various temperatures between –50 °C and 160 °C. NBT-xBT compositions doped with 1 mol% Fe showed an apparent inhomogeneous coloring after high-temperature electrical poling, most likely due to the migration of oxygen vacancies. The piezoelectric properties of these materials were found to be significantly lower than the properties of the undoped compositions, which was due to polar defects induced by the Fe-doping. In addition, high ionic conductivity dominated the piezoelectric and dielectric response at higher temperatures. The application of a uniaxial mechanical stress decreased the properties of NBT-xBT:Fe even more and resulted in a shift of the depolarization temperatures, similar to the findings in the undoped material.

1 Introduction

The understanding of ferroelectric materials has a long history, during which the discovery or the development of new materials and compounds and the investigation of physical phenomena both led to a deeper understanding. It is the aim of this chapter to introduce the most important physical concepts necessary to describe and to understand the results presented in this thesis. After a brief description of the elastic, dielectric, and piezoelectric properties of materials, the physical principles and mechanisms in ferroelectric and ferroelastic materials will be presented. Special focus is put on structural phase transitions, including the basics of a thermodynamic theory suitable to phenomenologically describe the electromechanical properties and the phase transition behavior of ferroelectrics. An introduction to the materials relevant for this work, namely barium titanate, lead-zirconate-titanate, and sodium-bismuth-titanate-barium-titanate, will be given as well. Finally, an overview on the influence of different types of mechanical stress on ferroelectric materials is presented in combination with a collection of relevant publications. In the following sections, numerous information was taken from an introductory paper by Damjanovic [1] and from the textbooks by Jona & Shirane [2], Jaffe, Cook, & Jaffe [3], Lines & Glass [4], Moulson & Herbert [5], and Newnham [6].

1.1 Elasticity

If a body is subjected to mechanical stresses, a corresponding strain occurs. The stress and strain fields both consist of six independent normal and shear components, leading to the stress tensor X_{ij} and the strain tensor S_{kl}. Stress and strain are connected via the elastic stiffness tensor c_{ijkl}, which is given for a pure linear-elastic behavior by Hooke's law:

$$X_{ij} = c_{ijkl}\, S_{kl}. \tag{1.1}$$

Please note that Einstein notation is used throughout the text, which implies a summation of all terms with equal indices. For isotropic materials and if only principal stresses are applied, Equation 1.1 is reduced to $X_i = E\, S_i$, where E is the elastic modulus (or Young's Modulus).

1.2 Dielectricity

In any insulating material, the application of an electric field E_i causes a dielectric displacement field D_i, which is the sum of the electric displacement field of vacuum and the induced polarization P_i:

$$D_i = \varepsilon_0 \, E_i + P_i, \tag{1.2}$$

where ε_0 is the dielectric permittivity of free space ($\varepsilon_0 = 8.854187817 \times 10^{-12}\,\mathrm{F/m}$) [7]. The polarization is proportional to the applied electric field and can be expressed as

$$P_i = \chi_{ij} \, \varepsilon_0 \, E_j, \tag{1.3}$$

where χ_{ij} is the dielectric susceptibility. Combining Equations 1.2 and 1.3 gives

$$D_i = \left(\delta_{ij} + \chi_{ij}\right) \, \varepsilon_0 \, E_j = \varepsilon_{ij} \, E_j, \tag{1.4}$$

where δ_{ij} is the Kronecker delta. Equation 1.4 also defines the tensor of the dielectric permittivity ε_{ij}, which is a measure of the ability of a material to store charge. Contributions to the permittivity of a material in an electric field are, e.g., the shift of the electron shell relative to the nucleus, the opposite displacement of anions and cations in an ionic compound, the rotation of dipoles and polar molecules, or the migration of space charges.

1.3 Electrostriction

An electric field applied to a dielectric material does not only induce a polarization, it also results in a strain by coupling dielectric and mechanical properties. This strain is always positive and originates from the opposite shift of positively or negatively charged ions in the lattice of the material. This effect is called "electrostriction" and relates the strain to the square of the electric field or the polarization:

$$S_{ij} = M_{ijkl} \, E_k \, E_l, \tag{1.5}$$

$$S_{ij} = Q_{ijkl} \, P_k \, P_l, \tag{1.6}$$

where M_{ijkl} and Q_{ijkl} are the electrostrictive tensors.

In addition to this direct electrostrictive effect also a converse effect exists, which shows a linear dependency of the permittivity on an applied mechanical stress [8]:

$$\varepsilon_{ij} \propto X_{ij}. \tag{1.7}$$

The number of nonzero and independent elements in the electrostrictive tensor depends on the symmetry of crystal. In the case of a cubic crystals only the coefficients Q_{1111}, Q_{1122}, and Q_{2323} coefficients are nonzero. For isotropic materials, such as polycrystalline ceramics, the latter coefficient is not independent and given by $Q_{2323} = 1/2\ (Q_{1111} - Q_{1122})$. In addition, the absolute value of the coefficient Q_{1111} is usually larger than the one of the negative Q_{1122}.

1.4 Piezoelectricity

In 1880, Pierre and Jaques Curie discovered that a quartz crystal produces an electrical voltage if a mechanical stress is applied [9]. This so-called direct "piezoelectric" effect originates from a stress-induced change in the dimensions of the unit cell of an ionic crystal, which results in a separation of the positive and the negative center of charge, *i.e.* the formation of a dipole moment. Not all crystals can exhibit the piezoelectric effect, since a polar axis is required. It is shown in the diagram in Figure 1.1 that 20 out of the 32 point groups possess such a polar axis due to the lack of centrosymmetry. As a first approximation, the direct piezoelectric effect is described with a linear relationship between the dielectric displacement field and the applied mechanical stress:

$$D_i = d_{ijk}\, X_{jk}, \tag{1.8}$$

where d_{ijk} is the piezoelectric tensor. In the case of the indirect piezoelectric effect, an electric field is applied, which generates a strain of the unit cell due to the field-induced shift of the ions of the crystal lattice:

$$S_{ij} = d_{kij}\, E_k. \tag{1.9}$$

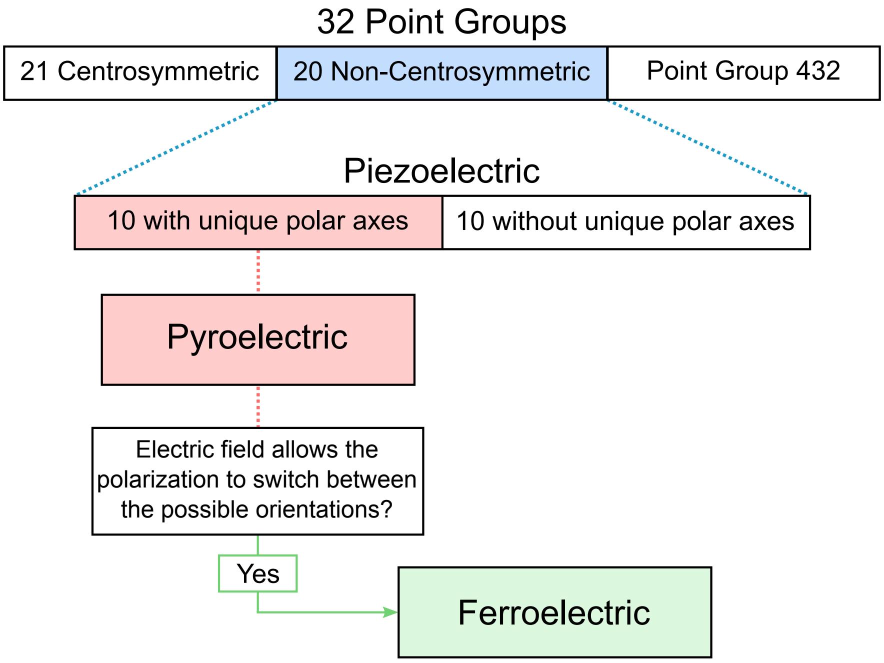

Figure 1.1: Relationship between the symmetry and the properties of dielectric crystals. The 20 non-centrosymmetry point groups possess a polar axis and therefore show the piezoelectric effect. If this polar axis is unique, a temperature change results in an electrical voltage due to the pyroelectric effect. A crystal is called "ferroelectric" if an electric field can switch this spontaneous polarization of pyroelectrics to another orientation.

1.5 Pyroelectricity

Some piezoelectric crystals show a charge creation on opposite faces during heating or cooling. This phenomenon is called "pyroelectricity" and was actually discovered far before the piezoelectric effect. As depicted in Figure 1.1, 10 out of the 20 piezoelectric point groups possess a unique polar axis, *i.e.*, a polar axis that is not (like in quartz crystals) compensated by other polar axes. This results in a permanent electrical dipole moment and therefore macroscopically in a so-called spontaneous polarization, which is accompanied by a corresponding spontaneous strain due to electrostriction (see Equation 1.6). If such a crystal is subjected to a uniform temperature change ΔT, the lattice constants increase or decrease because of the thermal expansion or contraction. As a result, the spontaneous polarization of a pyroelectric crystal changes by ΔP_i and an electric voltage between two opposite faces can be observed. The pyroelectric constant p_i relates ΔP_i linearly to ΔT:

$$\Delta P_i = p_i \, \Delta T. \tag{1.10}$$

1.6 Ferroelectricity

The dipole moment occurring in a unit cell of a pyroelectric crystal is affected by the application of an electric field. If the electric field is able to switch the spontaneous polarization of a pyroelectric crystal between at least two different energetically equivalent orientations, the crystal is called "ferroelectric". Unlike pyroelectric and piezoelectric crystals, which possess specific properties due their symmetry, it must be experimentally determined if a crystal is ferroelectric or not. In practice this means that the dielectric strength of a material needs to be larger than the electric field necessary to switch the spontaneous polarization.

Usually, not all dipole moments of a ferroelectric crystal point in the same direction because this configuration would be energetically unfavorable due to depolarization fields. The crystal is therefore divided into smaller regions of equal polarization direction ("domains"), which are differently oriented relative to each other. As a result, the macroscopic electric field originating from the dipoles is minimized and the crystal does not show a macroscopic polarization. Domains are separated by domain walls with a typical width of a few unit cells, in which the polarization is successively changed to the other orientation. Therefore, domain walls possess internal strains and increase the overall energy of the crystal, which is why the density of domain walls is in energetic balance with the number of domains. The angle between the polarization directions of two domains is defined by the crystal's symmetry and could be, for example, 90° or 180° in a tetragonal crystal. Hence, the corresponding domain walls are called "90° domain wall" or "180° domain wall". Domain walls and their interplay with internal and external influences are crucial for the properties of ferroelectric materials and will be discussed in detail in this work.

1.6.1 Ferroelectric Hysteresis

A typical observation made for ferroelectric crystals is the hysteretic behavior of polarization P and strain S during the application of a sufficiently large electric field, which originates from the switching behavior of domains associated with the nucleation of domains and the translation of domain walls. Figure 1.2 schematically depicts such hysteresis loops together with the idealized domain configuration of a tetragonal crystal at selected points A-J.

In the virgin state at point A, the crystal possesses no macroscopic polarization and domain walls are formed in order to minimize the electrical and mechanical energy of the crystal.

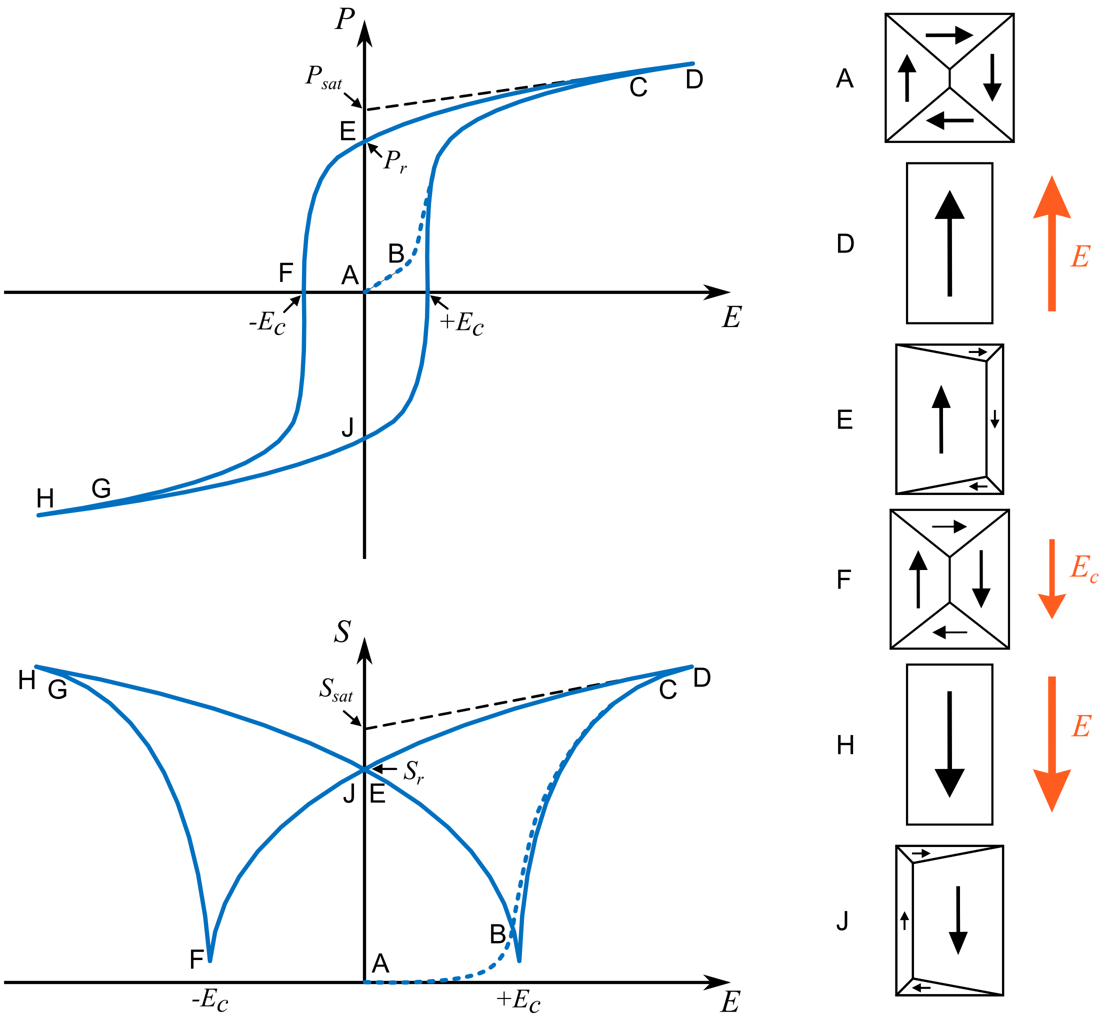

Figure 1.2: Schematic of the hysteretic ferroelectric behavior of the polarization P and the strain S during the application of a bipolar electric field E. An idealized domain configuration of a tetragonal crystal is given for selected points A-J of the loops, where the black arrows represent the direction of the spontaneous polarization within a single domain. A detailed description is given in the text. (modified from [10])

With increasing electric field between A and B, the polarization increases linearly according to Equation 1.3 and the strain increases quadratically due to electrostriction (Equation 1.5). Until now, the electric field was not large enough to initiate irreversible domain wall motion. This changes with further increasing field and a nonlinear behavior is observed for P, corresponding to a non-quadratic increase in S. At point C, all domains are oriented parallel to the electric field and the further behavior of both polarization and strain up to the maximum applied electric field at D is linear according to Equations 1.3 and 1.9. With decreasing electric field, P and S show a deviation from the linear field dependence, which originates from the backswitching of domains to their initial orientation due to internal electrical and mechanical fields. At zero electric field (point E), a remanent polarization P_r and a remanent strain S_r occur since a certain amount of domains stay in their new orientation aligned by the applied electric field. An extrapolation of the linear part of the curve during the decrease of the electric field to zero (black dashed lines in Figure 1.2) gives the saturation values P_{sat} and S_{sat}, which represent the ideal remanent polarization and strain without the contribution of domain backswitching processes.

A subsequent increase of the electric field in the opposite direction results in a further decrease of the polarization and the strain (E-F in Figure 1.2), finally reaching a specific electric field value ("coercive field", $-E_c$) at which P is vanishing. At the coercive field, the rate of domain switching is maximized and the net macroscopic polarization is zero, but the same is not necessarily true for the strain. The reason for that is that the domain configuration could lead to a nonzero strain at E_c even if $P = 0$ as depicted schematically in Figure 1.2. With further increase of the (negative) electric field along the path F-G-H, a switching and saturation behavior similar to the positive electric field branch can be observed. After removing the electric field (point J), the crystal shows again remanent polarization and remanent strain, but the former points now in opposite direction than before. Renewed application of a positive electric field would yield again another reversal of the macroscopic polarization at the coercive field $-E_c$ and finally to a closing of both hysteresis loops.

The occurrence of a remanent polarization is of special importance for the fabrication of ferroelectric devices, since polycrystalline materials do not show an initial macroscopic polarization due to their randomly oriented grains. In order to create a persisting macroscopic polarization, samples are subjected to an electric field similar to the A-E branch of Figure 1.2. This process is called "poling" and is crucial for the final piezoelectric properties of a device. Poling is usually done at elevated temperatures to enhance ferroelectric switching and to achieve the highest possible poling efficiency. Commonly used poling procedures for commercial materials could include several heating, cooling and electric field steps, specifically optimized for different materials. In general, changes in temperature affect the overall shape of hysteresis loops and result in an increase or decrease of P_r, S_r, and E_c with increasing or decreasing temperature, respectively [11–13].

A shifting of ions within a crystal's unit cell is not a diffusion process and hence, the piezoelectric response is nearly instantaneous. In contrast, the domain switching process is not instantaneous and time resolved X-ray diffraction (XRD) measurements revealed the details of the polarization reversal. The switching was found to be a two-step process with an intermediate domain orientation state and with two different time constants in the range of milliseconds [14]. Ferroelectric switching of polycrystalline materials is additionally complicated due to the presence of grain boundaries, but physical models [15, 16] and finite-element simulations [17] are available to understand and describe the formation and motion of domain walls also in polycrystals.

1.6.2 Contributions to the Piezoelectric Effect in Ferroelectric Materials

The piezoelectric effect in an ideal, mono-domain single crystal is only due to the stress- or electric field-induced shift of ions. However, in most cases domain walls are present that highly influence the piezoelectric behavior. Besides the "intrinsic" piezoelectric effect, the oscillation or the motion of domain walls and interphase boundaries contribute to the piezoelectric response as well ("extrinsic" contributions) [18, 19]. Whereas the motion of 180° domain walls account only for the polarization response, the motion of non-180° domain walls also contribute to the strain if an electric field or a mechanical stress is applied. Due to the interaction of domain walls with, e.g., (polar) defects, internal strains, grain boundaries, or other domain walls, the behavior of domain walls is governed by a complex potential energy landscape as depicted in Figure 1.3. This landscape is also dependent on external boundary conditions such as temperature or external electrical and mechanical fields. Small domain wall oscillations originating from the application of weak electrical or mechanical fields are an important contribution to the piezoelectric properties [20] and are always reversible due to restoring forces in the crystal. The shift of the domain wall to another minimum requires a larger external field and is irreversible, because the domain wall cannot move back to its initial position after field removal. Intrinsic contributions to the piezoelectric properties are always reversible [18].

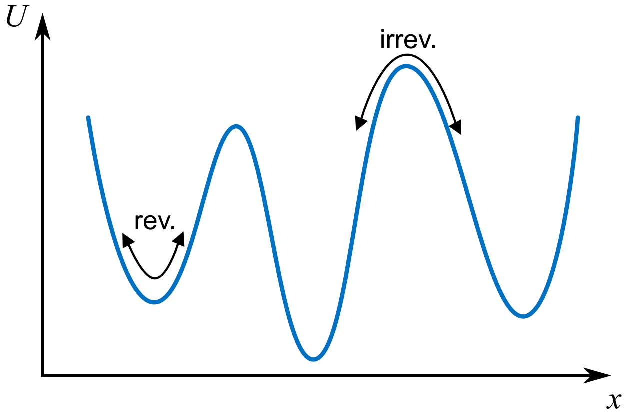

Figure 1.3: Potential energy U of a domain wall as a function of position x. The shape of $U(x)$ is determined by e.g. (polar) defects, internal strains, grain boundaries, other domain walls, and external boundary conditions. The motion of a domain wall within a minimum of $U(x)$ is always reversible, while field-induced switching between different minima is irreversible and requires an opposite field to switch back. (modified from [10])

It is an experimental task to separate reversible and irreversible contributions from each other, which is normally done by varying the amplitude and frequency of an applied electrical or mechanical oscillating field [18, 21–25]. In 1887, Rayleigh developed a law initially meant for ferromagnetic materials [26], which can serve to describe reversible and irreversible contributions to the dielectric permittivity ε as a function of the amplitude $\widehat{E}_0$ of the electric field. For simplicity, the resulting Equation 1.11 is given here in scalar from [27]:

$$\varepsilon\left(\widehat{E}_0\right)=\varepsilon(0)+\alpha\left(\widehat{E}_0-\widehat{E}_{th}\right), \tag{1.11}$$

where $\varepsilon(0)$ is the intrinsic permittivity at zero electric field amplitude, α is the Rayleigh parameter describing the irreversible contributions, and $\widehat{E}_{th}$ is the threshold field below which no irreversible contributions can occur. Equation 1.11 can be rewritten in order to describe the influence of reversible and irreversible contributions to the direct piezoelectric effect as well. This results in the following equation for the piezoelectric coefficient $d\left(\widehat{X}_0\right)$ as a function of stress amplitude $\widehat{X}_0$, again in scalar notation [21, 24, 28]:

$$d\left(\widehat{X}_0\right)=d(0)+\beta\left(\widehat{X}_0-\widehat{X}_{th}\right), \tag{1.12}$$

where $d(0)$ is the static piezoelectric coefficient at zero stress, β is a Rayleigh-type parameter describing the irreversible domain wall motion, and $\widehat{X}_{th}$ the threshold stress similar to $\widehat{E}_{th}$ in Equation 1.11.

Higher stress amplitudes applied to a ferroelectric material cause increased irreversible domain wall translations, resulting in a larger observed piezoelectric response [21, 29]. On the other hand, the piezoelectric response usually decreases with increasing frequency since the domain walls cannot follow the oscillating stress at high frequencies [22, 30]. In addition, it was also found that internal stresses in polycrystalline materials could decrease the piezoelectric properties due to hindered domain wall motion [31]. Such a reduction of the domain wall dynamics can also originate from polar defects, which will be discussed in detail in Section 1.10.2.

Unlike the intrinsic contributions to the piezoelectric effect, domain wall oscillation and translation cause energy dissipation, which leads to a phase shift δ between the applied electrical or mechanical field and the resulting strain or polarization. The main contribution to this loss is the damping of the domain wall motion [32], but also effects like conductivity need to be taken into account especially at elevated temperatures. It is common to use $\tan(\delta)$, the so-called dissipation factor, as a measure for the loss. If the dielectric and piezoelectric properties are considered as complex quantities, $\tan(\delta)$ is the ratio of imaginary and real part.

1.7 Ferroelasticity

Similar to the electric field-induced ferroelectric switching of the spontaneous polarization discussed in Section 1.6, a mechanical stress is capable of changing the orientation of the spontaneous strain in a non-centrosymmetric crystal. In the first instance, this does not necessarily require a spontaneous polarization, because a spontaneous strain can also appear in nonpolar materials and forms an "elastic dipole" [33]. Since the resulting stress-induced switching process is associated with a hysteresis, the effect is called "ferroelastic" in analogy to ferroelectric materials. Nonpolar ferroelastic materials are, for instance, $Pb_3(PO_4)_2$–$Pb_3(VO_4)_2$ [34, 35] or Ce-doped tetragonal ZrO_2 [36], which both show a hysteretic behavior in the stress-strain curve. Ferroelectric materials are usually also ferroelastic, but strictly speaking, the spontaneous strain is the property that is directly influenced by a mechanical stress. However, spontaneous strain and spontaneous polarization are inseparably connected in ferroelectrics and therefore it is common to call the influence of a mechanical stress as the switching of the polarization of the domains.

Since ceramic materials tend to crack easily during tensile loading, ferroelastic measurements are usually performed under compression only. Nevertheless, some publications reported shear [34] or tensile [37] ferroelastic measurements and investigated the switching behavior of ferroelastic materials also in this loading regime. Figure 1.4 schematically depicts a uniaxial stress-strain and a uniaxial stress-polarization curve typically observed for polarized ferroelectric materials under compression. It is important to note that an experiment like the one presented in Figure 1.4 can only determine changes of the strain and polarization, since the actual remanent strain and remanent polarization values after the poling process are usually not known. In general, the application of a uniaxial stress decreases the macroscopic polarization and the strain induced by the electrical poling.

In the initial section A-B in Figure 1.4, the applied stress is not large enough to cause domain switching. Therefore, polarization and strain are linear functions of stress due to the direct piezoelectric effect (Equation 1.9) and elasticity (Equation 1.1). With further increasing stress along B-C-D, both curves become nonlinear due to the onset of domain switching processes [38–40]. This direct relation between nonlinearity and domain switching was confirmed by *in-situ* neutron diffraction and XRD measurements [41]. The highest switching rate occurs at the inflection point D of the stress-strain and stress-polarization curve, which is called "coercive stress" X_c in analogy to the ferroelectric hysteresis curves. In the nonlinear regime C-D, the material behavior consists of both linear and nonlinear contributions. These contributions can be effectively sepa-

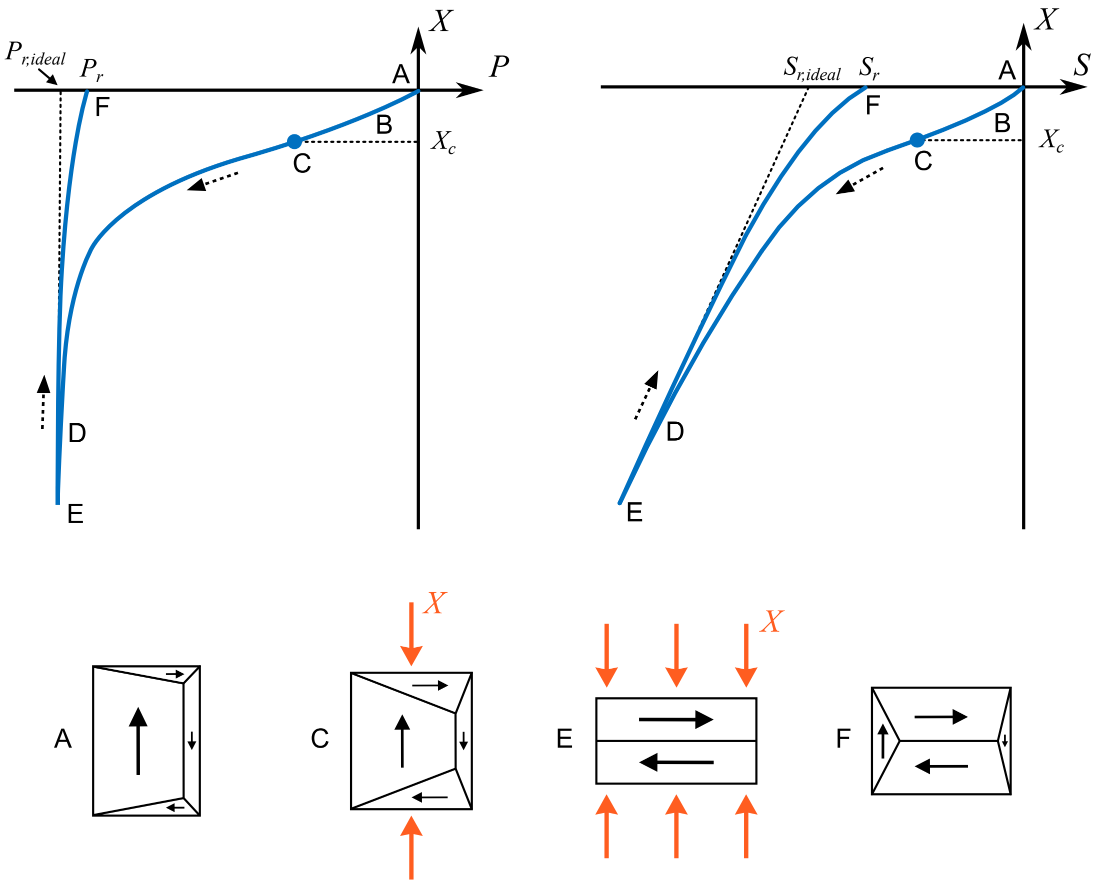

Figure 1.4: Schematic of the hysteretic ferroelastic behavior of the polarization P and the strain S of a poled ferroelectric material during the application of a uniaxial compressive stress X. The dashed arrows indicate the loading direction. An idealized domain configuration of a tetragonal crystal is given for selected points A-F of the loops, where the black arrows represent the direction of the spontaneous polarization and the spontaneous strain within a single domain. A detailed description is given in the text. (modified from [10])

rated by repeated small partial unloading of the sample during the measurement [42, 43]. These small unloading parts reveal the linear contribution to the overall measurement curves. At high stresses above the point D in Figure 1.4, all domains switched ferroelastically and the material response is linear-elastic again. In the case of the polarization, the ferroelastic reorientation of domains has been exhausted, resulting in a vertical line in the stress-polarization diagram.

During unloading, the material behaves initially linear-elastic, but at a certain stress the stress-strain and stress-polarization curves start to deviate from the linear course. This behavior originates from the backswitching of domains into their initial orientation, similar to the observations made for the ferroelectric hysteresis in Figure 1.2. Since a certain fraction of the domains was irreversibly switched by the mechanical stress, a remanent polarization P_r and a remanent strain S_r remain after complete unloading at point F. An extrapolation of the linear part of the unloading branch of the curves in Figure 1.4 beginning at point D reveals the ideal remanent polarization $P_{r,ideal}$ and ideal remanent strain $S_{r,ideal}$, which do not include the domain backswitching processes.

Ferroelectric switching due to an electric field causes domains to switch in a manner that the polarization of all domains align closely in one direction, namely in the direction of the applied electric field. This is a crucial difference to the effect of a uniaxial mechanical load, since such a stress causes the domains to switch to positions perpendicular to the loading direction. This process does not create a macroscopic polarization since the domains are likely to point antiparallel to each other to minimize the internal depolarization field. A comparison of the idealized domain configuration of a tetragonal crystal during a ferroelectric (Figure 1.2) and a ferroelastic (Figure 1.4) experiment visualizes the different behavior. This also implies that an electric field is capable to cause 180° and non-180° domain wall motion, whereas 180° domain walls cannot be directly influenced by a uniaxial mechanical stress.

Similar to the behavior of the ferroelectric hysteresis, the ferroelastic properties were found to be temperature-dependent. In practice, this results in a decrease of X_c, P_r, and S_r with increasing temperature [43–45]. Electric fields applied in combination with mechanical stresses can have significant influence on the ferroelastic behavior and increase or decrease the ferroelastic properties, because an electric field can act either against or in favor of the mechanical stress [44, 46]. Ferroelastic measurement can also serve to separate the reversible and irreversible contributions to the material's response (see Section 1.6.2). In order to accomplish this, the sample is partially unloaded to different stress values throughout the actual ferroelastic measurement [47]. Hence, small unloading amplitudes cover the reversible contributions, while larger amplitudes account for the irreversible domain wall motion.

1.8 Phase Transitions in Ferroelectrics

Ferroelectric materials show unique properties usually only in a limited temperature range and possess a transition between the ferroelectric and non-ferroelectric ("paraelectric") phase at a specific temperature ("Curie point"). This transition can be rationalized by the occurrence of a soft optical mode in the crystal lattice vibrations, which freezes at the Curie point and usually results in the formation of ferroelectric domains because of energy minimization. However, the presence of a soft optical mode is necessary but not sufficient for a paraelectric-ferroelectric phase transition since there are indeed materials like $SrTiO_3$ [48], which possess a soft optical mode but never show a ferroelectric phase down to lowest temperatures. Quantum fluctuations prevent the freezing of the soft mode even at 0 K and consequently, these materials are called "incipient" ferroelectrics [48].

Structural phase transitions are usually governed by changes in temperature, but also other external influences can induce a phase transition in a ferroelectric material. For example, an electric field applied to a single crystal or polycrystalline $BaTiO_3$ was found to induce a ferroelectric, tetragonal phase above the Curie point [49–52], a tetragonal-to-orthorhombic phase transition between 20 °C and 50 °C [53], and a cubic-to-orthorhombic phase transition above T_C [54]. In contrast to the temperature, which is a nondirectional, scalar quantity, an electric field or a uniaxial mechanical stress is a vectorial quantity. Therefore, an electric field can have different effects on the phases transitions in ferroelectrics depending on the crystallographic direction of the applied field (compare for instance [49] and [54]). Those effects are also known from the application of a mechanical stress, which will be presented and discussed in Section 1.13.

Before analyzing phase transitions in ferroelectrics in more detail, it appears to be convenient to first introduce the ferroelectric material $BaTiO_3$. This material serves as a prototype ferroelectric material and helps to better understand many of the effects described later on.

1.8.1 The Prototype Ferroelectric Material $BaTiO_3$

$BaTiO_3$ shows a relative large room-temperature dielectric permittivity in the order of 10^3 [55], making it interesting for multilayer capacitors, since $C = \varepsilon_{ij}\ A/d$, where C is the capacitance, A the area, and d the distance between the electrodes of a capacitor. Megaw [56–58] and Kay & Vousden [59] determined the crystal structure of $BaTiO_3$ to be rhombohedral ($R3m$) below –90 °C, orthorhombic ($Amm2$) between –90 °C and 0 °C, tetragonal ($P4mm$) between 0 °C and 130 °C, and cubic ($Pm\bar{3}m$) above 130 °C (= T_C, Curie point). The cubic phase is paraelectric, whereas all other phases are found to be ferroelectric. Figure 1.5 depicts the crystal structures and the atom positions in the lattice for the different phases of $BaTiO_3$.

The structure of $BaTiO_3$ is of the perovskite type, which has the general chemical formula ABO_3. Ba^{2+} ions occupy the A-sites of the structure and form a cubic lattice above T_C, whereas the O^{2-} ions are centered at the faces of the cube. The Ti^{4+} ion is located in the center of the cubic unit cell on the B-site of the perovskite structure. With decreasing temperature there is a relative shift of the A-, B-, and O-sites, resulting in a distortion of the unit cell [60, 61]. This breaks the cubic symmetry and separates the positive and the negative centers of charge, resulting in an electrical dipole moment. Macroscopically, the crystal shows a spontaneous polarization, which is depicted by red arrows in Figure 1.5. The mechanical distortion, *i.e.*, the spontaneous strain, of the

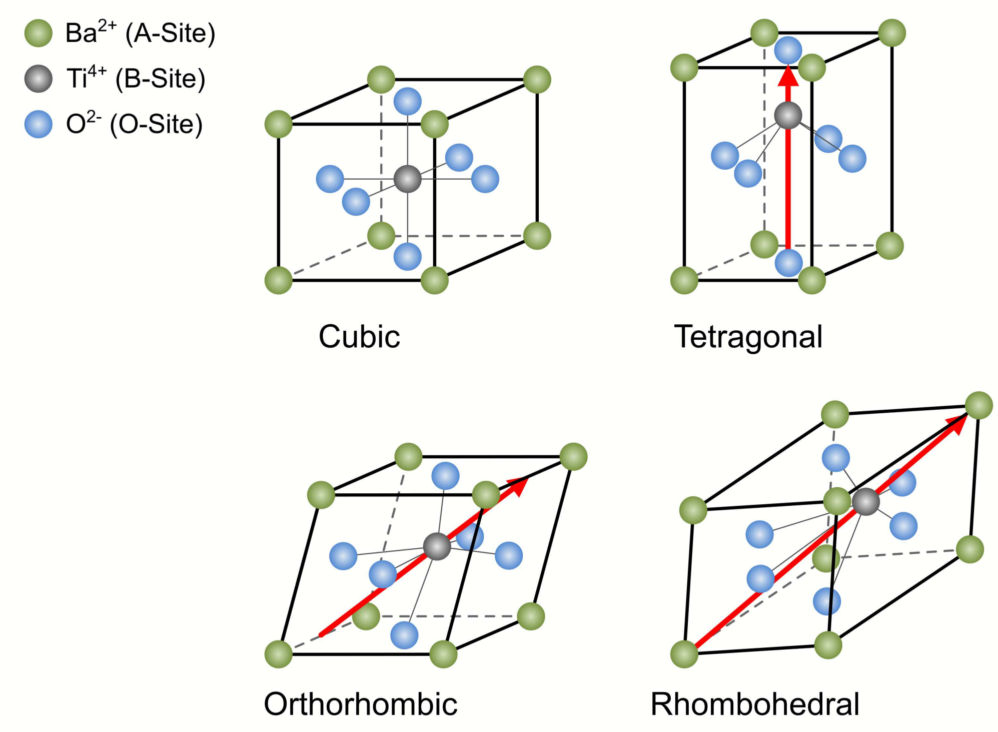

Figure 1.5: Crystal structures of $BaTiO_3$. The cubic structure is stable above 130 °C, the tetragonal phase between 130 °C and 0 °C, the orthorhombic phase between 0 °C and −90 °C, and the rhombohedral phase below −90 °C. The spontaneous polarization is represented by red arrows. (modified from [10])

initially cubic unit cell is actually quite small (about 1 % [58]), which is why the lower-temperature phases are often referred to as pseudo-cubic. However, the lattice constants change abruptly and measureable at the phase transition temperatures and the dielectric permittivity, which was found to be dependent on the crystallographic direction, shows sharp peaks [62]. The ferroelectricity of $BaTiO_3$ was discovered in 1946 by von Hippel *et al.* [11] and Wul [63], which means that the spontaneous polarization can be switched to different orientations by an electric field in the prototype ferroelectric material.

Several factors were found to influence the properties and the phase transition temperatures of $BaTiO_3$. For example, a decreasing grain size in polycrystalline $BaTiO_3$ results into a decreasing Curie point and in an increase of the other phase transition temperatures [64–66]. The dielectric and the piezoelectric properties are found to be grain size-dependent as well and show a maximum around a grain size between 1 μm and 2 μm [67–69]. Another way to alter the phase transition behavior of $BaTiO_3$ is the chemical modification with other elements, which was investigated by, amongst others, Jonker *et al.*, who found a decrease in the Curie point with increasing Sr content [61]. Furthermore, the phase transition temperatures depend on the quality and the form (single crystalline or polycrystalline) of the material [62, 70, 71]. Also external factors can influence the phase transition behavior of $BaTiO_3$ like, for example, the shift of the phase transitions temperatures due to the application of an electric bias field [54, 72]. Similar observations were made for the applications of a mechanical stress, which will be discussed in more detail in Section 1.13.

The application of $BaTiO_3$ as a ferroelectric is limited by its relatively low Curie point of 130 °C and by its rather small electromechanical response. For example, a longitudinal piezoelectric coefficient of 191 pC/N was observed for polycrystalline $BaTiO_3$ [73], whereas widely used commercial polycrystalline lead-based ferroelectric materials typically reach values above 500 pC/N [74]. Therefore, $BaTiO_3$ has its main application field in electronic devices like multilayer capacitors in integrated circuits [75], but renewed interest arose in the last years due to the development of environmental friendly, lead-free ferroelectric materials with $BaTiO_3$ as an end member. These materials will be discussed in Section 1.12.

1.8.2 Material Properties in the Vicinity of a Phase Transition Temperature

In ferroelectric materials like $BaTiO_3$ or $PbTiO_3$, the transition between two ferroelectric phases or between a ferroelectric and a paraelectric phase is a structural phase transition (see also Section 1.8.1). Figure 1.6 exemplarily shows the lattice constants a_T and c_T of an initially tetragonal, ferroelectric material as function of temperature, which undergoes a ferroelectric-to-paraelectric phase transition into the cubic symmetry (lattice constant a_C) at the Curie point. The tetragonality of the crystal lattice decreases with increasing temperature and vanishes at T_C, above which a_C increases linearly with temperature due to thermal expansion. At the same time, the spontaneous polarization decreases with temperature as well due to the reduced tetragonality (ratio c_T:a_T) and reaches finally zero at T_C.

Ferroelectric materials show a significant change in the material properties in the vicinity of phase transitions, as it depicted for the dielectric permittivity and the elastic modulus in Figure 1.6. Depending on the form of the material (single crystal or polycrystal), the shape of the anomalies in both parameters can vary, which will be shown in detail in Chapter 3. The peak in the dielectric permittivity is of special interest, since it is a common way to determine the phase transition temperature of classical ferroelectrics. Above T_C, the permittivity follows the Curie-Weiss law

$$\varepsilon_{ij} = \frac{C}{T-\theta}, \tag{1.13}$$

where C is the Curie constant, T the temperature and θ the Curie-Weiss temperature.

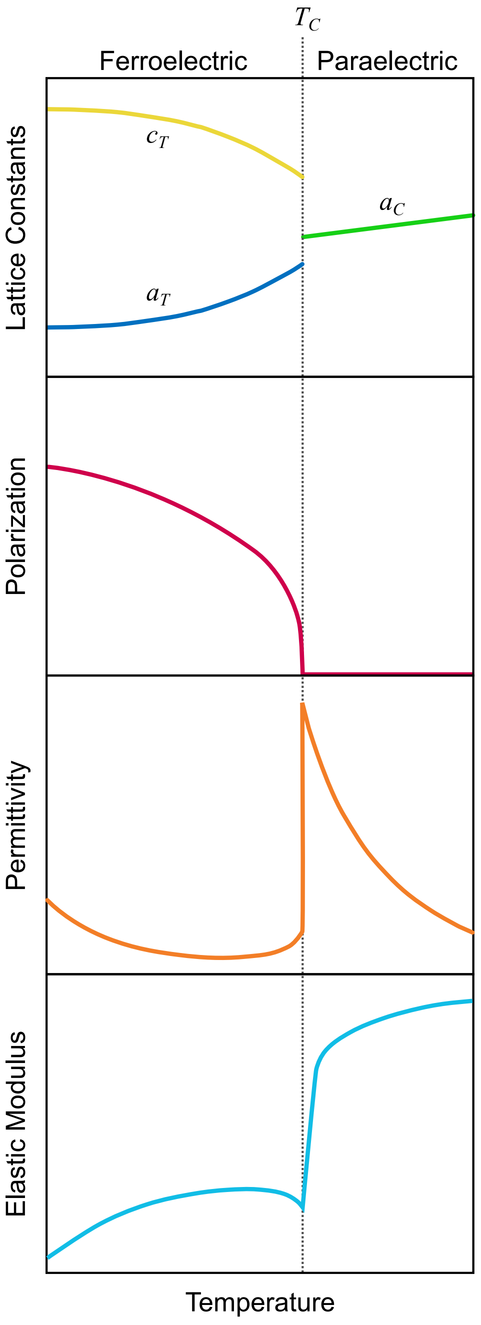

Figure 1.6: Temperature-dependent lattice constants (modified from [58, 59]), polarization, permittivity, and elastic modulus of an exemplary tetragonal ferroelectric material, undergoing a ferroelectric-to-tetragonal phase transition into cubic phase at the Curie point T_C.

1.8.3 Thermodynamic Theory of Phase Transitions

A general theory describing second-order phase transitions was developed by Landau in 1937 [76–80], who introduced an expansion of a thermodynamic potential function to powers of an order parameter. This order parameter is zero in the high symmetry phase and nonzero in the low symmetry phases. Ginzburg [81, 82] and Devonshire [83–85] expanded this theory for phase transitions in ferroelectric materials and chose the polarization as order parameter (others are also possible, see [86]). It was Devonshire, who presented a fundamental phenomenological theory of $BaTiO_3$ by using Landau's ansatz and by including also elastic contributions in the potential function as proposed by Müller [87, 88]. Strictly speaking, the so-called Landau-Ginzburg-Devonshire (LGD) theory is only valid in the vicinity of a phase transition, since the potential function is expanded only around the phase transition. The state of equilibrium is given by the minimum of the potential function and measures like, e.g., the polarization at a given temperature can be derived from this condition.

In the following, a brief introduction to the LGD theory will be given under the assumption of a ferroelectric, tetragonal crystal with only one possible polarization direction in the absence of any external electrical or mechanical fields. Like it is shown in various derivations of the LGD theory [1, 4, 89, 90], the Gibbs free energy G is used as thermodynamic potential and expanded to powers of the polarization P up to the sixth order.

$$G = \frac{1}{2}\,\chi\,P^2 + \frac{1}{4}\,\xi\,P^4 + \frac{1}{6}\,\zeta\,P^6, \tag{1.14}$$

where χ, ξ, and ζ are the Landau parameters, which are functions of temperature and stress in general. For simplicity, only χ is assumed to be a function of temperature in the following discussion:

$$\chi = \chi_0(T - \theta), \tag{1.15}$$

where χ_0 is a constant and θ is the Curie-Weiss temperature. Whereas ξ could be either positive or negative, ζ is always positive to ensure finite minima in G. The spontaneous polarization results from the equilibrium condition $\partial G/\partial P = 0$, which has a trivial solution $P_s^2 = 0$ and a nontrivial solution

$$P_s^2 = \frac{-\xi \pm \sqrt{\xi^2 - 2\,\chi_0(T-\theta)\zeta}}{2\zeta}. \tag{1.16}$$

Figure 1.7 schematically shows the Gibbs free energy as a function of P at different temperatures (Equation 1.14) and the spontaneous polarization (Equation 1.16) as a function of temperature. A first order ferroelectric-to-paraelectric phase transition occurs if $\xi < 0$, which is characterized by a discontinuous drop of the spontaneous polarization to zero at the phase transition temperature T_C (Figure 1.7b). In this case, the Curie-Weiss temperature θ in Equation 1.15 is not equal to T_C. At temperatures below T_C, the free energy function in Figure 1.7b reveals two minima at $-P_s$ and $+P_s$, which correspond to the two possible orientations (0° and 180° rotated) of the dipole in a tetragonal crystal (see Figure 1.5 for $BaTiO_3$). By increasing the temperature to $T = T_C$, three minima occur in G, which represent the trivial solution of $\partial G/\partial P = 0$ and the solution in Equation 1.16 at T_C. This results in a discontinuity of the spontaneous polarization at T_C (Figure 1.7b). With further increasing temperature, only one minimum in G remains at $P = 0$ in the cubic, paraelectric state.

In the case of a second order phase transition, $\xi > 0$ and P_s continuously decreases to zero as shown in Figure 1.7d. The free energy function G in Figure 1.7c shows again two minima for the

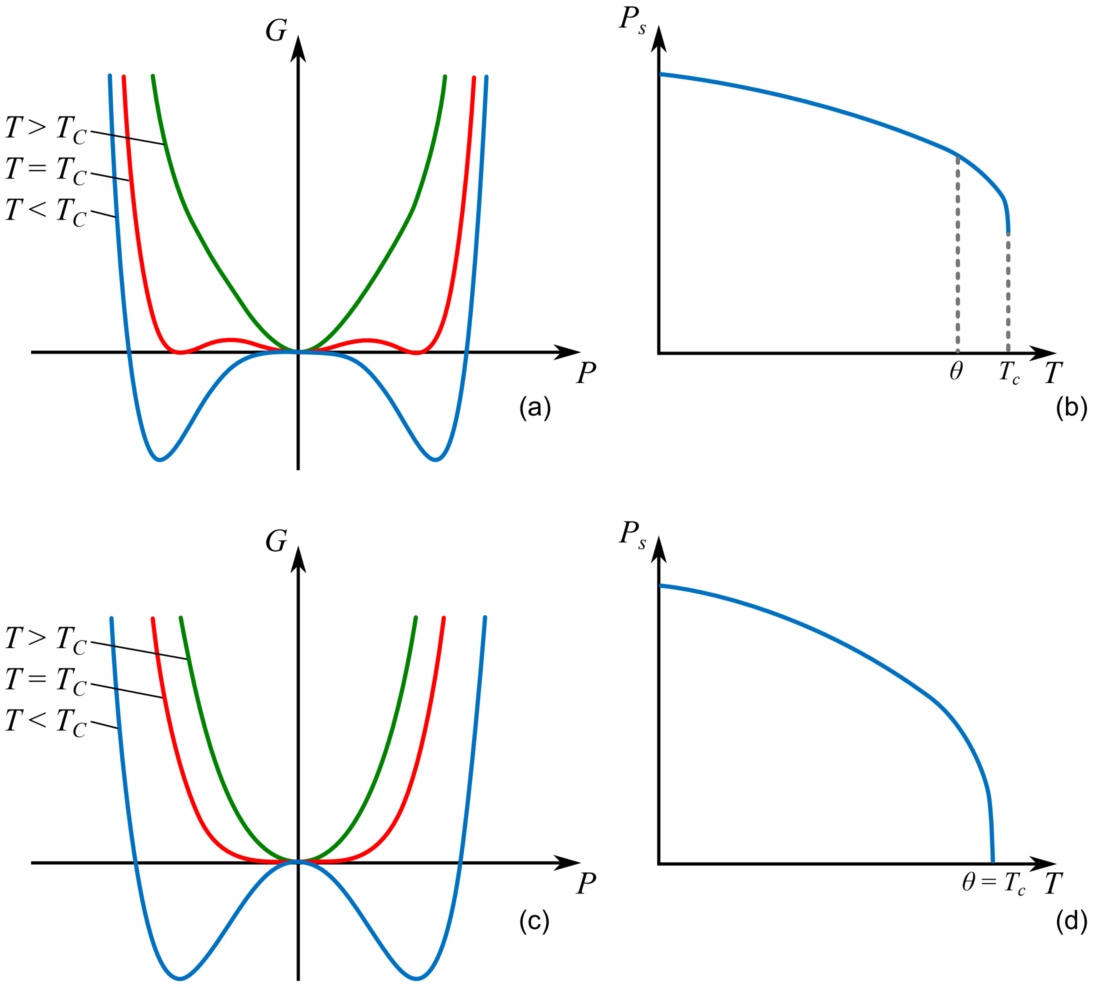

Figure 1.7: Gibbs free energy G as a function of polarization P at different temperatures and spontaneous polarization P_s as a function of temperature for a first order (a+b) and a second order (c+d) phase transition.

two polarization directions, but at $T = T_C$ only one minimum at $P = 0$ remains. No discontinuity in P_s appears in that case and θ equals the phase transition temperature.

For both first and second order phase transitions, the free energy function was found to be relatively flat at T_C. As already described in Section 1.8.2, the properties of ferroelectrics are enhanced in the vicinity of a phase transition. This follows also from the LGD theory, which gives $\partial^2 G/\partial P^2 \propto 1/\varepsilon_{ij}$ for the permittivity. Since G is flat around the phase transition, $\partial^2 G/\partial P^2$ becomes small, which results in a large permittivity if the temperature approaches T_C [91, 92]. In addition, Zhang *et al.* showed theoretically that especially materials with a first order ferroelectric-to-paraelectric phase transition show exceptionally large piezoelectric properties [93].

A drawback of the LGD theory is that the Landau parameters in Equation 1.14 need to be determined either experimentally or by, e.g., first-principle calculations. It is also important to note that this phenomenological theory is only valid for single-domain single crystals and the description of polycrystalline or inhomogeneous materials is limited.

LGD theory has been extensively used to describe the properties and the phase transition behavior of ferroelectric materials under the thermal, electrical, and mechanical fields. For example, this theory has been used to describe the stress-induced shift of the Curie point in epitaxial $PbTiO_3$ [94] and $BaTiO_3$ [95] thin films and in $PbTiO_3$ [96] and $BaTiO_3$ [97] single crystals. Bell & Cross determined a full set of Landau parameters of $BaTiO_3$ [98] and described the shift of T_C due to an applied electric field [99]. Haeni *et al.* [100] theoretically described an observed stress-induced room-temperature ferroelectricity in $SrTiO_3$ thin films, whereas Zhu *et al.* [101] analyzed the phase stability of $BaTiO_3$ and $PbTiO_3$ during the application of mechanical stresses. The effect of radial pressure on $BaTiO_3$ [102] as well as the influence of internal stresses on the dielectric properties and phase transitions of polycrystalline $BaTiO_3$ [103–105] could be also described. Even the properties of ferroelectric domain walls in $BaTiO_3$ [106], the influence of particle size on the phase transitions in ferroelectrics [107] and the effect of strain in $BaTiO_3$ nanowires [108] were subjected to theoretical investigation using the LGD theory. Franzbach *et al.* used the LGD theory to analyze the electric field-induced tetragonal-orthorhombic phase transition in $BaTiO_3$ single crystals [53] and the electric field-induced tetragonal-rhombohedral phase transition in $Pb(Zr_xTi_{1-x})O_3$ (PZT) [109]. The PZT system was also theoretically described by Haun *et al.* [110] and a full set of Landau coefficients of PZT was derived by Amin *et al.* [111]. Finally, Seo *et al.* explained stress-induced phase transitions in PZT with the LGD theory [112].

Usually, an expansion of the thermodynamic potential in Equation 1.14 up to the sixth order is used to describe the properties and the phase transition behavior of ferroelectric materials. However, several authors report the necessity of an expansion of G up to the 12$^{\text{th}}$ order for describing, e.g., the effect of an electric field and large mechanical stresses [113], lower symmetry phases like triclinic and monoclinic [114], or materials with exceptionally large piezoelectric properties [115]. It is still under debate if these higher-order terms are essential or if they just provide a better approximation of the theory to the measurement data. Alternatively, the Landau parameters could be directly modified in order to account for the observed effects. An attempt to do so will be presented in Chapter 3.

1.9 Relaxor Ferroelectrics

Ferroelectric materials usually show minor changes in the dielectric permittivity with frequency due to domain wall oscillations in weak a.c. electric fields. However, some dielectric materials without any ferroelectric long-range order possess significant frequency dispersion in the permittivity, which originates from relaxational processes. Because of that, these materials are called "relaxors" or "relaxor ferroelectrics" and well-known examples are $Pb(Mg_{1/3}Nb_{2/3})O_3$ (PMN), $(1-x)Pb(Mg_{1/3}Nb_{2/3})O_3-xPbTiO_3$ (PMN-PT), and $Pb_{1-x}La_x(Zr_{1-y}Ti_y)_{1-x/4}O_3$ (PLZT). The high dielectric and piezoelectric properties of relaxor ferroelectrics make this material class highly interesting for industrial applications. Based on several selected review articles [116–122], the fundamental concepts and properties of relaxor ferroelectrics will be presented.

The apparent frequency dispersion of relaxors is usually attributed to the presence of chemically disordered regions, which can appear due to, e.g., thermal fluctuations or defects. These nanometer-scale regions are embedded in a highly polarizable, cubic matrix and can contain dipole moments due to the lattice distortion induced by the chemical disorder. If these dipole moments are coupled, they form a region with a local polarization ("polar nanoregion", PNR). A typical temperature-dependent permittivity curve of a relaxor material is shown in Figure 1.8, which will be used to discuss the thermal evolution of this material class.

At high temperatures, the dipoles in the chemical disordered regions are highly mobile and uncorrelated [123]. Therefore, thermal fluctuations prevent these regions from developing a local polarization and the Curie-Weiss law (Equation 1.13) is valid in this paraelectric temperature range without showing any frequency dispersion in the permittivity.

With decreasing temperature, the permittivity curve starts to deviate from the Curie-Weiss law at the Burns temperature T_B [124]. At this temperature, the dipoles in the disordered region

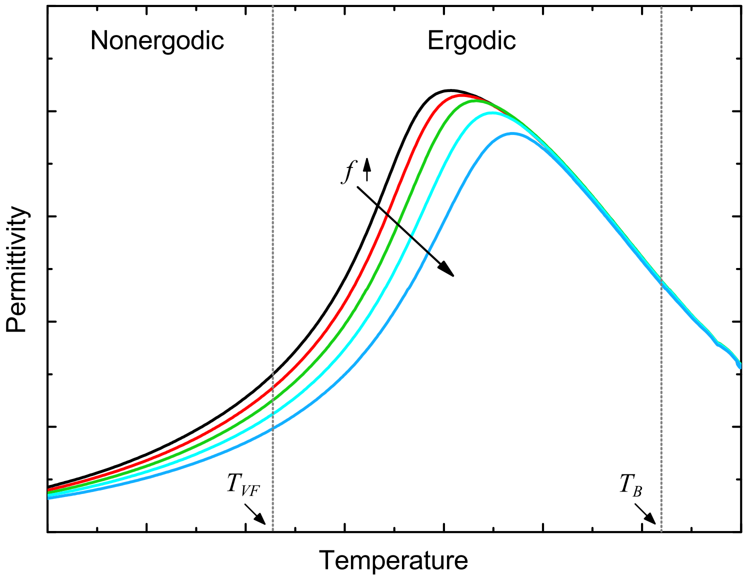

Figure 1.8: Exemplary permittivity-temperature curve of a relaxor ferroelectric measured at various frequencies. At the Burns temperature T_B, polar nanoregions are forming during cooling, whereas the motion of these regions freezes at the Vogel-Fulcher temperature T_{VF}.

become increasingly correlated and PNRs are formed [125–128], which change the symmetry of the material on a local, nanometer sized scale. The PNRs are mobile and not yet correlated to each other, which is why still no frequency dispersion is occurring at temperatures close to T_B [125, 126]. Below T_B and above the Vogel-Fulcher temperature T_{VF} in Figure 1.8, the relaxor is in the ergodic state, in which the spatial and the time average of the polarization directions of the PNRs are equal. The PNRs increase in number and size with further cooling between T_B and the maximum of the permittivity curve T_m [129]. In connection with that, the local polarization increases and dielectric response is enhanced.

The position of the permittivity maximum in Figure 1.8 is frequency-dependent, which is a typical feature of a relaxor material. At T_m, the correlation length of the PNRs is large enough to overlap with other PNRs. This leads to a reduced mobility in an applied electric field and therefore to a decrease of the dielectric response of the material. With further decrease in temperature, this correlation continues for PNRs with smaller correlation length and T_m occurs at lower temperatures when measured at lower frequencies. It is important to note that no structural phase transition occurs at T_m in a relaxor, which in contrast to a classical ferroelectric material.

At temperatures below T_m, the correlation of the PNRs increases and the thermally activated reorientation of PNRs decreases. Both effects result in a lower permittivity with decreasing temperature (Figure 1.8). The frequency dispersion is a consequence of the dielectric relaxation of the differently sized and correlated PNRs in a weak oscillating electric field. Larger PNRs react slower to the electrical field and show therefore reduced dielectric properties at higher frequencies, where smaller PNRs still can follow the electric field at higher frequencies. This kind of relaxation process does not possess a single characteristic relaxation time, but a distribution of relaxation times due to the differently sized and correlated PNRs. Like in the case of polymers, this relaxation can be described by a Vogel-Fulcher type relationship, which results in the observed frequency-dependency of the permittivity.

By approaching the Vogel-Fulcher temperature T_{VF}, the motion of the PNRs freezes, *i.e.*, the relaxations times diverge towards infinity and the spatial and the time average of the PNRs are not equal anymore. Therefore, the relaxor changes to the nonergodic state at T_{VF}, but this state change is not accompanied by a structural phase transition and only connected to the frozen dynamics of the PNRs. In addition, no signature of the state change can be observed in the permittivity-temperature curve in Figure 1.8 unless the frequency-dependency of the permittivity is evaluated. The freezing temperature T_{VF} is influenced by the application of an electric field [13, 130]. Finally, the permittivity decreases with further cooling below T_{VF} due to reduced motion of the dipoles and the PNR walls.

In some materials like PMN-PT, a sharp or diffuse phase transition from a relaxor to a ferroelectric phase can occur during cooling, which is usually marked by an anomaly in the permittivity at the phase transition temperature [121, 131, 132]. In addition, it is also possible to induce a ferroelectric phase by applying an electric field to a relaxor. Various authors reported such induced phase transition in e.g. PMN [133–135], PLZT [136–138], PMN-PT [139, 140], $(1-x)\mathrm{Pb(Zn_{1/3}Nb_{2/3})O_3}$–$x\mathrm{PbTiO_3}$ (PZN-PT) [140], $(1-x)\mathrm{(Na_{1/2}Bi_{1/2})TiO_3}$–$x\mathrm{BaTiO_3}$ (NBT-xBT) [13, 141], or Mn-doped $\mathrm{Bi_{0.5}(Na_{0.9}K_{0.1})_{0.5}TiO_3}$ [142]. Figure 1.9 shows the temperature-dependent permittivity of a PMN-PT single crystal [139] and of PLZT [143] during heating. Prior to the measurements, the samples were poled with a d.c. electric field. It can be clearly seen that the permittivity shows an anomaly (PMN-PT) or a peak (PLZT) at the ferroelectric-to-relaxor transition temperature $T_{F\text{-}R}$.

The mechanism behind the electric field-induced phase transition is not completely understood. It is known that the PNRs initially align and grow with the application of an electric field [134], but the step following a further increase of the field is proposed to be either complete coalescence [144] or percolation [145] of PNRs, which could probably also depend on the material under investigation. In any case, a remanent ferroelectric phase can only be induced if the relaxor is in the nonergodic state below T_{VF}, because thermally enhanced motion of the PNRs would destroy the ferroelectric order on the ergodic state. It is important to note that $T_{F\text{-}R}$ (occurs during heating) and T_{VF} (occurs during cooling) does not necessarily need to coincide, since the induced long-range ferroelectric order might be already thermally destroyed

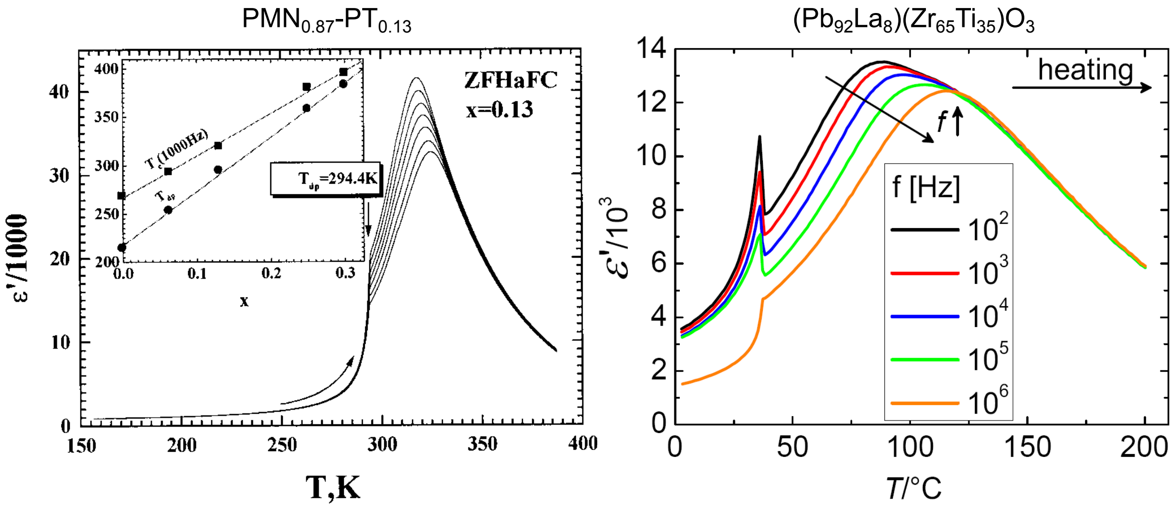

Figure 1.9: Temperature-dependent permittivity of a PMN-PT single crystal [reprinted from Colla, E. V., Yushin, N. K. & Viehland, D., *Journal of Applied Physics*, Vol. 83, Pages 3298-3304, (1998), with the permission of AIP Publishing] and of PLZT (reprinted from Ref. [143]) during heating. The samples were electrically poled prior to each measurement, which induced a ferroelectric phase. The anomalies in both curves mark the ferroelectric-to-relaxor phase transition temperature $T_{F\text{-}R}$.

below T_{VF} [146, 147]. However, a large unipolar strain could be achieved in the ergodic phase due to the now reversible electric field-induced phase transition. Such a behavior was found in polycrystalline $(94–x)(Na_{1/2}Bi_{1/2})TiO_3–6BaTiO_3–x(K_{1/2}Na_{1/2})NbO_3$ for $x = 2\,\text{mol\%}$ and $6\,\text{mol\%}$, which is in the ergodic state at room temperature [148–151].

Several theories exist that attempt to describe the observed electromechanical behavior of relaxor ferroelectrics. For example, the random-field theory attributes the proposed interactions between the PNRs to random electric fields, which originate from fluctuating disorder in the material [152–154]. Such regions would then interact with each other via the polarizable matrix material. The dipolar glass model proposed by Viehland *et al.* [124, 155, 156] expands the superparaelectric model of Cross [116] and considers the randomized dipoles in a relaxor as a glassy state. As a result, PNRs form and the freezing of their motion could be rationalized by the increased interaction of the PNRs with decreasing temperature. Another approach to explain the dielectric response of relaxors is the "breathing model", which accounts the vibration of PNR-boundaries in an oscillating electric field [157–159]. This is similar to the behavior of ferroelectric domains and domain walls. In addition, there are also phenomenological approaches [160, 161]. However, the theory of relaxor ferroelectrics and even the concept of PNRs are still under debate [162].

1.10 Lead-Containing Ferroelectrics

The most important materials for the application of ferroelectrics are lead-based compositions, since these materials show excellent electromechanical properties combined with good thermal stability and cost-effective mass production [3, 5, 163]. In the following sub-sections, the classical ferroelectric material system Pb(Zr_xTi_{1-x})O_3 (PZT) and two commercial PZT compositions will be presented and discussed together with an overview of the influence of dopants in ferroelectric materials. Lead-containing ferroelectric single crystals, which are of special interest for high-power and high-performance applications, will be a part of this introduction as well.

1.10.1 Lead-Zirconate-Titanate (PZT)

PZT is a solid solution of $PbTiO_3$ and $PbZrO_3$. The former material is ferroelectric and structurally equal to $BaTiO_3$, but with a Curie point at 500 °C [164]. In contrast, $PbZrO_3$ is antiferroelectric, orthorhombic and possesses a T_C of 230 °C [3]. Together, these two materials form one of the most investigated ferroelectric material systems, which is described by the phase diagram shown in Figure 1.10.

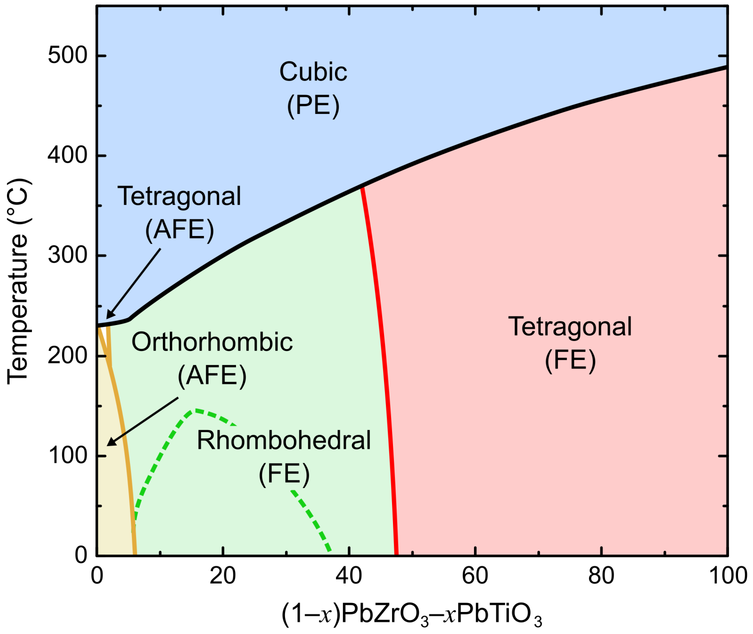

Figure 1.10: Phase diagram of PZT, showing paraelectric (PE), ferroelectric (FE), and antiferroelectric (AFE) regions. (modified from [3, 165])

Depending on temperature and composition, PZT could be paraelectric, ferroelectric or antiferroelectric and possesses cubic ($Pm\bar{3}m$), tetragonal ($P4mm$), orthorhombic ($Pbam$), or rhombohedral symmetry [166]. The rhombohedral phase is divided into a low-temperature ($R3c$) and a high-temperature ($R3m$) phase as depicted in Figure 1.10 by the dashed green phase boundary [167, 168]. It was reported in many publications that the properties of PZT vary with composition and temperature [169–172]. Similar to findings in $BaTiO_3$, these properties depend also on grain size [173, 174]. Additional effects resulting from the application of a mechanical stresses will be discussed in Section 1.13.

One of the most important and most investigated features in the phase diagram of PZT is the nearly vertical phase boundary between the tetragonal and the rhombohedral phase. In the vicinity of this so-called "morphotropic phase boundary" (MPB), the structure of the material changes nearly only with composition. The MPB appears as sharp line in Figure 1.10, but more recent investigations revealed that it is rather a region of coexisting tetragonal and monoclinic symmetry [175]. It was found that especially compositions on the more tetragonal side of the MPB possess superior piezoelectric properties [169]. A reason for that is that the polarization can rotate quite easily due to the coexistence of two phases at the MPB [176] or due to the additional monoclinic phase [177, 178], leading to significantly enhanced electromechanical properties. Phenomenological investigations based on the LGD theory have shown an apparent flattening of the free energy at the MPB [179], which lead also theoretically to an enhanced polarization rotation and extension. Furthermore, a coupling of the piezoelectric and dielectric properties [180] or the existence of polar nanodomains [181, 182] could also help to explain this enhancement of the electromechanical properties of PZT.

1.10.2 Influence of Dopants in Ferroelectrics

Additional chemical elements in the crystal structure of ferroelectric materials can highly alter the properties and the phase transition behavior (see e.g. [3, 183]). In literature, this process is usually called "doping", even if the amount of additional elements in the compositions is substantial and could easily reach several percent. This should not be confused with doping in semiconductor materials, where the term "doping" refers to the addition of a small amount of atoms in the range of ppm. Doping in ferroelectric materials is an important way to achieve desired material properties such as, for instance, the enhancement of the thermal stability, the increase of the piezoelectric properties, or the resistance of the electromechanical properties against mechanical stress. For example, the addition of Sr in $BaTiO_3$ results in a lower Curie point and lower tetragonal-orthorhombic transition, but the orthorhombic-rhombohedral phase transition remains unchanged [61, 184, 185]. In contrast, the doping of $BaTiO_3$ with Pb decreases both lower-temperature phase transitions and increases the Curie point [3, 186].

Not all chemical elements are suitable as dopants in ferroelectrics, since the ionic radii need to roughly match the radii of the ions of the original structure. The stability of a perovskite structure with respect to the radii of the A-site ion (r_A), the B-site ion (r_B), and the oxygen ion (r_O) is given by the Goldschmidt tolerance factor t [187]

$$t = \frac{r_A + r_O}{\sqrt{2}(r_B + r_O)}. \tag{1.17}$$

The perovskite structure is stable for values of t between approximately 0.80 and 1.06. At $t = 1$, the symmetry would be perfectly cubic, whereas slightly higher or lower values lead to a tetragonal or rhombohedral distortion, respectively [188]. Besides the size restrictions of the ions a doped crystal still needs to obey electroneutrality. If a dopant has a different charge than the substituted ion, defects will be created in order to keep the net charge zero.

In general, dopants can be isovalent or aliovalent. It was found in PZT that isovalent dopants have rather minor impact on the electromechanical properties and influence mainly the Curie point and the permittivity [38, 183]. Thus, aliovalent dopants are more important to tune (*i.e.* to enhance) the properties of ferroelectric materials. Such dopant ions can carry either a higher positive charge ("donor" dopant) or a lower positive charge ("acceptor" dopant) than the ions they are replacing. These two cases are schematically shown for a cubic perovskite structure in Figure 1.11, which reveals that aliovalent doping usually requires the formation of vacancies in the lattice in order to ensure the charge neutrality of the crystal.

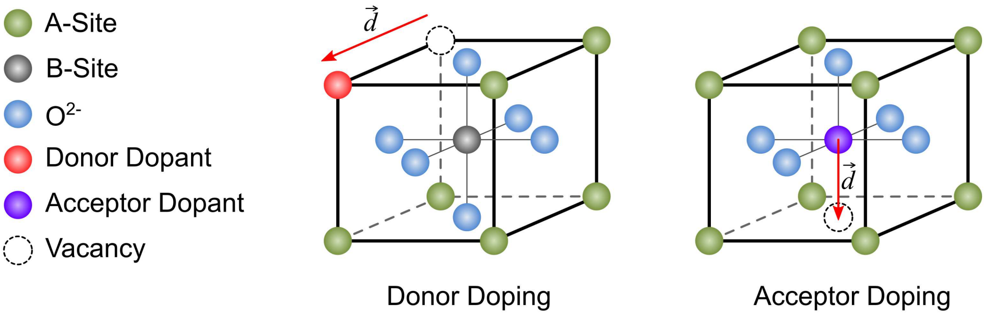

Figure 1.11: Influence of aliovalent dopants on a perovskite crystal. Donor dopants create A- or B-site vacancies, whereas acceptor dopants result in oxygen vacancies in order to keep the charge neutrality of the crystal. The resulting electrical dipoles are represented by red arrows.

Donor doping of e.g. PZT with La^{3+}, Sb^{5+}, or Nb^{5+} result in negatively charged A- or B-site vacancies, which could form a defect dipole within the crystal lattice. A- or B-site vacancies are known to be difficult to move, which is why the resulting defect dipoles stay usually randomly oriented ("frustrated") even during the application of an electric field [5]. Donor doped materials show higher dielectric and electromechanical properties [183] and are referred to as "soft" ferroelectrics, since external electrical or mechanical fields can alter the properties quite easily [1].

Acceptor dopants (for instance K^{1+} or Fe^{3+} in PZT) have a more severe influence on the behavior and the electromechanical properties of ferroelectrics. They enhance the thermal and mechanical stability of ferroelectrics accompanied by an increase in coercive field, but with the drawback of lower piezoelectric and dielectric properties [1, 38, 171, 183]. Due to these properties, acceptor doped ferroelectrics are called "hard" ferroelectrics.

It can be revealed from Figure 1.11 that acceptor doping results in positively charged oxygen vacancies in order to keep charge neutrality. The oxygen vacancies form polar defect complexes with the dopants [189–191], which are reorientable due to the mobility of oxygen vacancies [5]. As a consequence, polar defects effectively hinder domain wall motion ("pinning") if they are allowed to align with the domains ("ageing") [192–194]. This results in pinched polarization-electric field hysteresis loops, since the electric field has to reach a certain value to move domain walls pinned by polar defects [192, 195]. Polar defects can be reoriented and aligned by an electric field due to oxygen vacancy motion, particularly at elevated temperatures [196, 197]. This reorientation process and also the actual formation of polar defects was found to be time-dependent because of the motion of the oxygen vacancies in the crystal lattice [198, 199]. Due to the alignment of the polar defects, an internal bias field is established [192, 198], which could be experimentally determined by the shift of the polarization-electric field hysteresis loop along the electric field-axis [193]. Although point defects in a crystal lattice can also act to hinder domain wall motion [200], but the influence of defect complexes was found to be more severe [194]. Besides that, defect dipoles can increase the amount of nanodomains and rhombohedral phase in Fe^{3+}-doped PZT [201] and are accompanied by an elastic dipole [198, 202].

1.10.3 Commercial PZT Materials

A large number of commercial ferroelectric materials based on PZT are available, which are especially designed for all different kinds of possible applications. Two different materials from PI Ceramic GmbH (Lederhose, Germany) will be investigated in this work, namely a soft (PIC151) and a hard (PIC181) PZT composition. In order to achieve the optimum properties, both materials are located close to the MPB at the tetragonal side of the phase diagram in Figure 1.10 and are highly modified by substitutional chemical elements.

PIC151 possesses high dielectric and piezoelectric properties [74] and has the composition $Pb_{0.99}[Zr_{0.45}Ti_{0.47}(Ni_{0.33}Sb_{0.67})_{0.08}]_{1.00}O_3$ [44]. Ni^{2+} is believed to act as acceptor dopant on the B-site of the perovskite structure, since it has an ionic radius similar to Ti^{4+} or Zr^{4+} [203]. The role of Sb in PIC151 is not clear, because it could either substitute Pb^{2+} on the A-site or Ti^{4+} and Zr^{4+} on the B-site. It was argued that Sb would occupy the B-site in PZT as Sb^{3+} due to its ionic radius [204]. However, PIC151 clearly shows soft ferroelectric behavior due to its low coercive field and large piezoelectric coefficient [40]. This leads to the conclusion that Sb acts as donor dopant either on the A-site as Sb^{3+} or on the B-site as Sb^{5+}.

The hard PZT composition $Pb_{1.00}[Zr_{0.47}Ti_{0.48}(Mn_{0.33}Sb_{0.32}Nb_{0.33})_{0.05}]_{1.00}O_3$ (PIC181) shows a low dielectric loss and an relatively high coercive field due to the high concentration of polar defects, but lower piezoelectric properties than PIC151 [44]. An advantage of PIC181 is the high thermal stability of the ferroelectric properties, which is reflected by a high Curie point of 330 °C (PIC151: 250 °C) [74]. In this composition, Mn^{2+} is acting as acceptor dopant on the B-site and is therefore the origin of the hard ferroelectric properties of PIC181. Nb^{5+} acts as donor dopant.

1.10.4 Application of Piezoelectric and Ferroelectric Materials

Piezoelectric and ferroelectric materials are used in numerous applications ranging from everyday products like piezoelectric lighters to large array undersea sonar in submarines, which could contain several tons of piezoelectric material [4, 5, 205]. Most applications use the unique property of these materials to convert electrical voltage nearly instantaneously into displacement and vice versa. Transducers and sensors [165, 206] made out of piezoelectric materials are used in numerous automotive or medical (ultrasound) applications and can also be found in microphones, guitar pickups, or in sensors of electrical drum pads. Actuating applications are of special importance for industry in e.g. positioning systems [207] or in diesel fuel injection devices [208, 209]. In these cases, ferroelectric multilayer actuators are used, which show high strain and high force in both quasi-static and dynamic applications. Making use of the direct piezoelectric effect, energy harvesters [210, 211] transform deformation into electrical energy, which could probably be used in the future to power pacemakers directly in the body without the need of changing a battery anymore [212]. Even more exotic applications like ultrasonic micro-motors for industrial and medical applications could be realized by using ferroelectric materials and adequate processing techniques [213]. Ferroelectric thin films play an important role in micro-electromechanical systems (MEMS), which could help reduce material and volume due to the miniaturization of sensors and actuators [214]. Finally, nonvolatile random access memory devices use the possibility of polarization switching in ferroelectric materials in order to read and write data.

1.11 Lead-Containing Ferroelectric Single Crystals

Ferroelectric single crystals possess superior electromechanical properties such as, e.g., an up to an order of magnitude larger piezoelectric coefficient than conventional polycrystalline PZT, making them especially interesting for high-power applications [215–217]. Examples for such high-performance single crystals are PMN-PT [218–220], PZN-PT [221], PMN-PZT [222], or $x\mathrm{Pb}(\mathrm{In}_{1/2}\mathrm{Nb}_{1/2})–(1–x–y)\mathrm{Pb}(\mathrm{Mg}_{1/3}\mathrm{Nb}_{2/3})\mathrm{O}_3–y\mathrm{PbTiO}_3$ (PIN-PMN-PT) [220, 223–226]. Similar to PZT close to the MPB, the essential mechanism behind the high properties is enhanced polarization rotation [227]. In order to achieve the largest properties, domain engineering is of additional importance. This technique tries to maximize the material's response by applying the electrical poling field in special crystallographic directions, which results in an optimized domain state [228–230]. Similar to observations made for other ferroelectric materials like $\mathrm{BaTiO_3}$ or PZT, an electric field is able to induce phase transitions in lead-containing single crystals [140, 231].

A major drawback of single crystals is the complicated, time-intensive, and expensive crystal growth process. In addition, the comparatively low coercive field of less than 0.25 kV/mm [220] and low depolarization temperature between 70 °C and 95 °C [232] of, e.g., PMN-PT limit these materials to low-power and low-temperature applications. PIM-PMN-PT was developed to overcome these drawbacks and will be investigated in more detail in Section 4.5. PIN-PMN-PT single crystals possess a coercive field of up to 1 kV/mm, a depolarization temperature of up to 120 °C and can be grown relatively easily into large single crystals [233–237]. It depends on the composition if this material is in the rhombohedral or the tetragonal phase at room temperature [220, 238], but again the best electromechanical properties were observed for compositions near the MPB also present the PIN-PMN-PT system [238, 239]. During heating, the material transforms subsequently from the ferroelectric, rhombohedral phase to a ferroelectric, tetragonal phase and finally to a paraelectric, cubic phase [231, 233, 238]. Doping of PIN-PMN-PT with Mn was found to be a successful way to enhance the electromechanical and high-power properties and their thermal stability even more [225, 239–242].

Important applications for lead-containing ferroelectric single crystals are for example undersea sonar transducers [243, 244] or medical ultrasonic imaging and related biomedical applications [245, 246]. Due to the superior properties of single crystals, also advanced applications like piezoelectric motors [247], imaging [224], energy harvesting [248] or even electric scalpels [249] are of growing interest.

1.12 Lead-Free Ferroelectrics

The most crucial drawback of lead-containing materials is the chemical element lead, which is toxic in both the metallic and oxide form. Especially PbO, which is used during the manufacturing process of PZT, is a problem for workers and environment. It was also found that leads-containing ceramics like PZT seem to be unstable in water [250], which raises a serious problem in non-recycled electronic waste and contact with acid rain. Based on these concerns, governments in numerous countries have issued regulations on the usage of lead and lead-containing substances in electronic devices [251–254]. One of the first and most important legislative actions was taken by the European Union, which passed a directive on the "restriction of the use of certain hazardous substances in electrical and electronic equipment" (RoHS) in its initial version in 2003 and in a renewed version in 2011 [255]. Based on this directive, lead-containing materials are supposed to be replaced as soon as adequate lead-free alternatives are available. The industry is allowed to apply for several exemptions, which still permit the use of lead-containing substances, but this needs to be re-assessed every five years. In connection with RoHS, additional directives such as WEEE (directive on the "waste electrical and electronic equipment", [256]) and ELV (directive on the "on the end-of life vehicles", [257, 258]) were passed to cover waste recycling and automotive applications as well.

Due to this, a lively research field on lead-free electronic materials developed in the last ten years in both industry and academia, which was clearly stimulated by the legislative restrictions on lead-containing ferroelectrics. Numerous detailed review articles [259–267] have been published in order to cover all aspects of lead-free ferroelectrics, ranging from the fundamental physical and chemical mechanisms to the possible implementation of the novel materials in applications.

1.12.1 Candidates for Replacing Lead-Containing Ferroelectrics

Compositions based on lead-free, nontoxic $(K_{0.5}Na_{0.5})NbO_3$ (KNN) were among the first materials proposed for replacing lead-containing ferroelectrics and possess electromechanical properties comparable to PZT materials in combination with a high Curie point and bio-compatibility [268–271]. Another promising material system, based on the solid solution $(1\text{–}x)Ba(Ti_{0.8}Zr_{0.2})O_3\text{–}x(Ba_{0.7}Ca_{0.3})TiO_3$ (BZT-xBCT), has been discovered [272–274], which possess piezoelectric properties superior to soft PZT, but with the drawback of a lower temperature-dependent fracture toughness [275]. Especially the latter is problematic in multilayer actuator applications.

One the most intensively investigated concepts for novel ferroelectrics is the replacement of lead with bismuth and therefore, promising material systems are often based on $(Na_{1/2}Bi_{1/2})TiO_3$ (NBT). For example, the $(1\text{–}x)(Na_{0.5}Bi_{0.5})TiO_3\text{–}x(K_{0.5}Bi_{0.5})TiO_3$ (NBT-xKBT) system possesses an MPB at which electromechanical properties are increased similar to the PZT system [276, 277]. Furthermore, the addition of 6 mol% $BaTiO_3$ and 2 mol% KNN to NBT results in the composition NBT-6BT-2KNN, which shows a unipolar strain larger than soft PZT [148–151, 278].

In contrast to PZT, lead-free materials possess usually either large electromechanical properties and low thermal stability or vice versa [265]. For example, BZT-BCT materials possess high piezoelectric properties in a relatively small temperature range, whereas KNN-based materials are thermally stable but a show minor piezoelectric response [279, 280]. Therefore, different application environments still require significantly different lead-free materials, which is in contrast to the nearly universal applicability of PZT and its modifications.

1.12.2 NBT-xBT

The high unipolar strain of lead-free NBT-xBT makes it an interesting candidate for replacing PZT in actuator applications [122, 261, 262, 281–283]. Due to its promising properties and its utilization as an end member in high-performance compositions like NBT-xBT-yKNN or others [151, 284], this material will be investigated in the present work. Besides the application-oriented polycrystalline form of NBT-xBT, single crystals are of scientific interest in order to clarify, for example, the direction-dependency of the electromechanical properties [285–287].

NBT-xBT is a solid solution of NBT and $BaTiO_3$. NBT and other related (relaxor) ferroelectric materials were already described in 1961 by Smolenskii *et al.* [288–290] and possess a rhombohedral symmetry at room temperature [291]. The phase diagram of NBT-xBT is still subjected to constant debate, since structure and properties of NBT-xBT change with composition, temperature and applied electric field. Figure 1.12 shows a temperature-dependent and Figure 1.13 an electric field-dependent phase diagram of NBT-xBT, mainly based on in-situ transmission electron microscopy (TEM) studies and dielectric measurements [292, 293]. Like in PZT and many other ferroelectric solid solutions, an MPB region occurs in NBT-xBT between approximately 6 mol% and 7 mol% $BaTiO_3$ content. However, these values differ from publication to publication [144, 293–295].

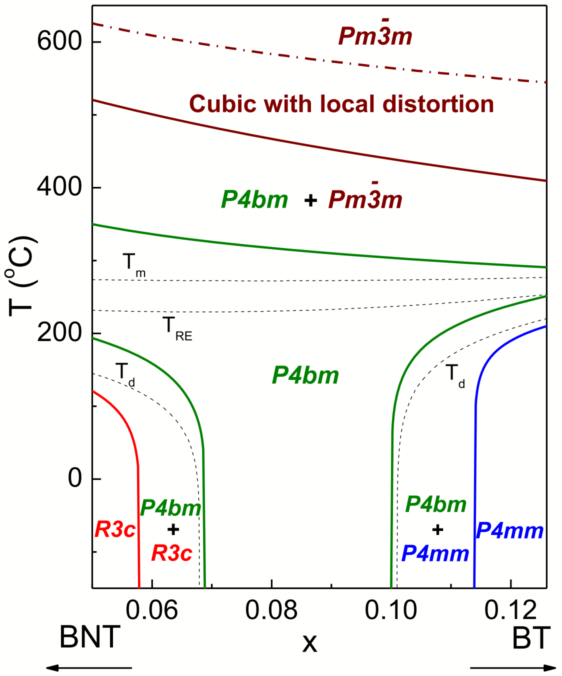

Figure 1.12: Temperature-dependent phase diagram of NBT-xBT. T_m represents the temperature at maximum dielectric permittivity, T_{RE} the temperature at which the frequency dispersion of the dielectric permittivity vanishes, and T_d the transition temperature between the ferroelectric and the proposed "relaxor antiferroelectric" phase. [Copyright (2011) Wiley. Used with permission from Ma, C. & Tan, X., *In situ* Transmission Electron Microscopy Study on the Phase Transitions in Lead-Free (1–x)($Bi_{1/2}Na_{1/2}$)TiO_3–$x$$BaTiO_3$ Ceramics, *Journal of the American Ceramic Society* 94, The American Ceramic Society.]

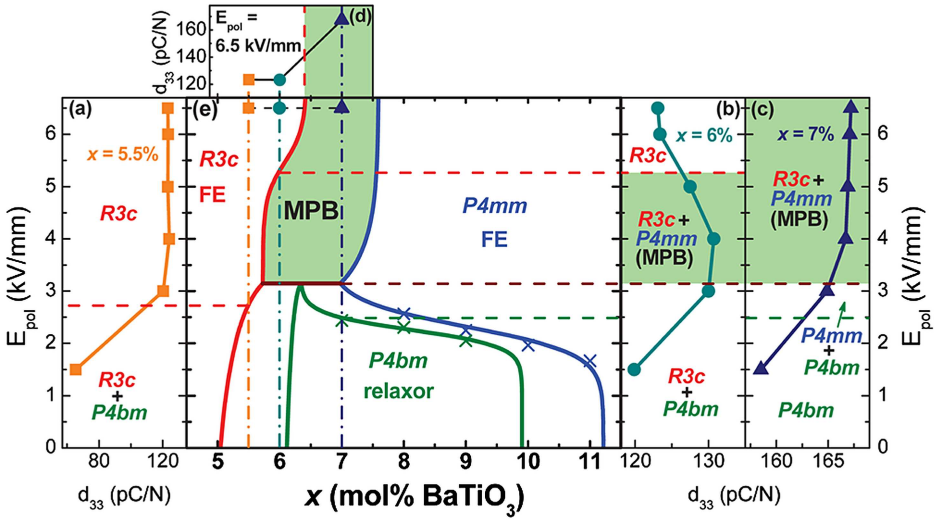

Figure 1.13: Electric field-dependent phase diagram of NBT-xBT. In addition to the different composition-dependent phases, the piezoelectric coefficient d_{33} is given as function of electric poling field E_{pol} for selected NBT-xBT compositions. [Reproduced from Ma, C., Guo, H., Beckman, S. P. & Tan, X., *Physical Review Letters*, Vol. 109, Page 107602, (2012), with the permission of AIP Publishing.]

It is usually argued that NBT-xBT compositions at the NBT side of the MPB possess a ferroelectric, rhombohedral structure in the unpoled state, whereas compositions located at the $BaTiO_3$ side show a ferroelectric long-range order and tetragonal symmetry [293, 296–298]. However, Ma *et al.* found a monoclinic structure for pure NBT and an additional monoclinic-rhombohedral phase boundary with increasing $BaTiO_3$ content between 3 mol% and 4 mol% [299]. Reports on the less investigated $BaTiO_3$-rich side of the phase diagram revealed that the introduction of NBT into $BaTiO_3$ suppresses immediately the tetragonal-orthorhombic and the orthorhombic-rhombohedral phase transition of pure $BaTiO_3$ (see Figure 1.5) [300, 301]. The $BaTiO_3$-rich compositions were also found to be interesting for positive temperature coefficient ceramics, which show a decrease in electrical resistance with increasing temperature [302].

The thermal evolution of the phases in the NBT-xBT system are quite complex, which could be seen in the temperature-dependent phase diagram in Figure 1.12. Measurements of the temperature-dependent permittivity and the elastic behavior as well as *in-situ* XRD and TEM experiments revealed several transition temperatures, which are not all well understood [293, 296–298, 303, 304]. At high temperatures, NBT-xBT transforms into a relaxor state. However, the permittivity-temperature curve differs from the one typically observed for relaxor materials (Figure 1.8) in the way that a second, frequency-independent maximum appears at higher temperatures (see Figure 1.14). In addition, the frequency dispersion of the permittivity vanishes already at temperatures below T_m, which are marked as T_{RE} in Figure 1.12. It is important to note that a structural phase transition takes place neither at T_{RE} nor at T_m in NBT-xBT.

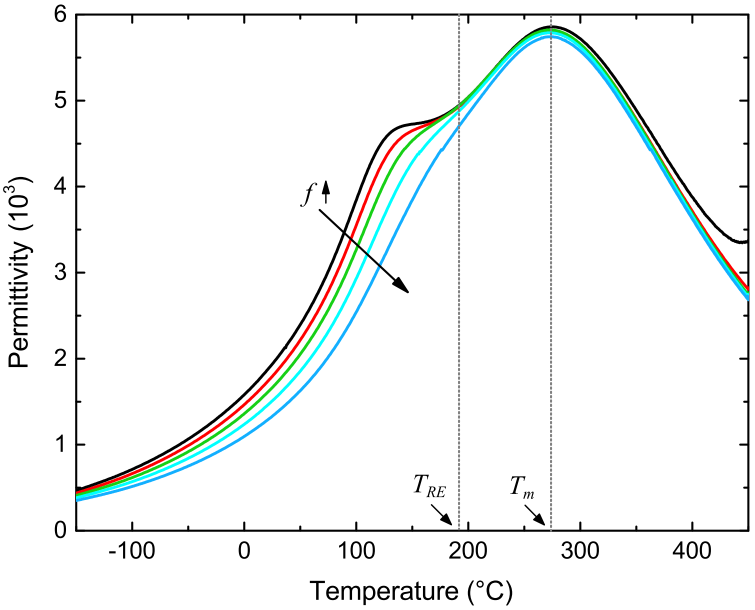

Figure 1.14: Temperature-dependent dielectric permittivity of NBT-6BT measured at different frequencies. In contrast to a canonical relaxor, the frequency dispersion vanishes at T_{RE}, significantly below the temperature at maximum permittivity T_m.

Similar to other material systems discussed in this chapter, the electromechanical properties of NBT-xBT are maximized in the vicinity of the MPB. In this region, unpoled NBT-xBT exhibits a pseudo-cubic relaxor phase, which possesses typical PNRs [305–307]. However, the strict separation between ferroelectric and relaxor (MPB) phases in unpoled NBT-xBT is controversially discussed in literature, since several authors found (at least partial) relaxor behavior and/or mixed phases also in compositions on the NBT side of the MPB [308–310].

By applying an electric field, a long-range ferroelectric order with mixed rhombohedral and tetragonal symmetry can be induced either globally in the whole sample or, at weak field, locally in the PNRs [141, 144, 293, 295, 304, 306, 307, 311, 312]. It was shown that the large strain response observed in NBT-xBT in the MPB region and also in NBT-6BT-yKNN is due to this electric field-induced phase transition and not due to polarization rotation like in PZT [282, 313–315]. As already described in Section 1.9 for electric field-induced ferroelectric phases in lead-containing relaxor materials, the long-range ferroelectric order breaks at T_{F-R} and the piezoelectric properties decrease significantly [316, 317]. In the poled state, NBT-xBT shows typical ferroelectric polarization- and strain-electric field hysteresis loops similar to those presented in Figure 1.2 [316, 318, 319], but the piezoelectric properties were found to be dependent on the electrical poling field (see Figure 1.13).

The compositions investigated in this work contained 3 mol%, 6 mol%, 9 mol%, and 12 mol% $BaTiO_3$ and will be denoted as NBT-3BT, NBT-6BT, NBT-9BT, and NBT-12BT, respectively. Unpoled

NBT-3BT is located in the rhombohedral, ferroelectric region of the phase diagram, whereas NBT-12BT in the solely tetragonal, ferroelectric side. NBT-6BT was chosen due to its position in the MPB region and it exhibits mixed rhombohedral and tetragonal symmetry after poling with an electric field [144]. Finally, NBT-9BT is also considered to be located at the border of the MPB region, but in the poled state it possesses mainly tetragonal symmetry with a minor amount of rhombohedral phase [144]. Although the phase diagram shown in Figure 1.13 excludes this composition from the MPB, it will be shown in this work that the behavior of NBT-9BT is quite comparable to the MPB composition NBT-6BT.

1.13 Influence of Mechanical Stress on Ferroelectric Materials

It was discussed in the previous sections that an electric field has significant influence on the properties and the phase transitions in ferroelectric materials. Based on ferroelasticity, mechanical loads also alter the material behavior due to ferroelastic switching of domains (see Section 1.7). Crucial differences between an electrical and mechanical load are that stresses act only indirectly on the polarization via switching of the spontaneous strain and that mechanical stresses could possess more than one direction in contrast to a (unipolar) electric field.

There are many applications that require applying mechanical stresses on piezoelectric and ferroelectric devices. For example, the actuator in a piezoelectric fuel injection system has to act against the pressure in the cylinder of a car's engine and multilayer actuators are usually substantially prestressed in order to prevent cracking due to tensile stresses at the partial electrode edges or during operation in dynamic range [320]. In this context, the blocking force, defined as the force produced by an actuator in the fully clamped state, is an important temperature-dependent parameter for applications [321]. Modern lead-free materials like NBT-5BT-KNN or BZT-BCT were found to possess an exceptional large blocking force, which could even exceed the values usually achieved with soft PZT compositions [322, 323]. It is possible to find a specific combination of electrical and mechanical loading to gain optimum performance and durability of actuator materials [324–326]. Furthermore, the operational range of an actuator can be determined by measuring the dynamic electromechanical performance as a function of mechanical preload [320, 327].

Mechanical stresses could have a significant impact on the phase transition behavior of ferroelectric materials depending on whether hydrostatic, radial or uniaxial stress is applied. Bancroft in 1938 [328] and later by Samara in 1965 [329] showed that hydrostatic compression increased the phase transition temperatures of $KNaC_4H_4O_6 \cdot 4\,H_2O$ ("Rochell salt"). In the case of $BaTiO_3$, numerous publications reported the decrease of the Curie point with increasing hydrostatic compression [330–334]. Similar observations regarding the phase transition behavior under hydrostatic stress were made for $Ba_{0.75}Sr_{0.25}TiO_3$ [335] and $PbTiO_3$ [336]. The shift of the Curie point of $BaTiO_3$ and $PbTiO_3$ with increasing hydrostatic pressure could also be predicted theoretically by utilizing the LGD theory [96, 97, 337]. Interestingly, it was found that the application of a hydrostatic pressure also changed the order of the phase transition at T_C in $BaTiO_3$ from first to second order if a critical hydrostatic stress was exceeded [334, 336, 338–340]. Consequently, the discontinuous drop in P_S at T_C, which is typical for first order phase transitions, was found to decrease with increasing hydrostatic compression [334] and the observed change in the order of the phase transition could be successfully predicted by using the LGD theory [339]. Finally, Ishidate *et al.* reported decreasing transition temperatures with increasing hydrostatic compression for all phase transitions in $BaTiO_3$ [341].

The influence of radial stresses on the phase transitions in ferroelectrics was less investigated in literature than the effect of hydrostatic stress. Compressive radial loads were found to increase the Curie point of $Ba_{0.75}Sr_{0.25}TiO_3$ [335] and $BaTiO_3$ [342, 343] due to the stabilization of the tetragonal phase by the mechanical stresses. A significant increase in the Curie point of the incipient ferroelectric material $SrTiO_3$ by several hundred degrees centigrade was observed by Haeni *et al.* due to radial stresses in thin films [100]. Similar effects of radial mechanical loads were observed in thin film $PbTiO_3$, which could be also described with the LGD theory [94]. In addition, the increase in Curie point of thin film $BaTiO_3$ due to radial stresses has been reported [344].

Investigations on the effect of uniaxial stress revealed a decrease in the Curie point of $BaTiO_3$ [51, 345, 346], and 99.34BT-0.66ZnO [346] with increasing uniaxial compression. Furthermore, a decrease of the Curie-Weiss temperature with increasing uniaxial stress was found in $BaTiO_3$ [347] and an increase of the rhombohedral-tetragonal phase transition temperature in single crystal NBT [348]. In the latter case, a stress-induced change from a first order to a second order phase transition was reported as well.

Stress-induced phase transitions in ferroelectric materials are comparable to phase transitions caused by the application of an electric field and were subjected to intensive research. For example, a uniaxial compressive stress was found to induce a ferroelectric phase in $BaTiO_3$ above T_C, which was experimentally shown as a ferroelastic double hysteresis loop [349, 350]. Similar observations were made during the application of uniaxial compressive stresses on NBT-6BT at elevated temperatures [351], whereas a stress-induced rhombohedral-to-orthorhombic phase transition was reported for PMN-PT and PZN-PT [25, 352]. Uniaxial compression was also found to cause a ferroelectric-to-antiferroelectric phase transition in Nb-doped PZT [353] and even a hydrostatic stress-induced formation of an MPB in pure $PbTiO_3$ was observed [354]. The occurrence of a structural phase transition induced by hydrostatic compression in NBT could be successfully modeled with the help of ab-initio calculations [355] and LGD theory gave evidence to a stress-induced tetragonal-to-rhombohedral phase transition in soft PZT [112].

Not only are the phase transitions of ferroelectrics affected by the application of mechanical stress, but also the dielectric and piezoelectric properties. The dielectric permittivity was found to increase or decrease with mechanical stress, but the actual behavior differs among different materials and is also dependent on factors like grain size, loading history, and the type of the mechanical stress [102, 356–360]. The electromechanical properties of soft PZT were found to decrease with the application of uniaxial mechanical compression, since it is relatively easy to mechanically switch domains in this material [361–364]. However, hard PZT is more mechanical stress-resistant and shows an initial increase in the piezoelectric properties by applying uniaxial compressive stress [46, 361–363, 365]. This is usually rationalized by the stress-induced release of domain walls from the pinning by polar defects ("de-ageing"), which increases the extrinsic contribution to the piezoelectric properties of the material. A decrease of the piezoelectric properties with increasing uniaxial mechanical stress was also observed for BZT-BCT, which originated from mechanical depolarization and increased domain wall density [366]. Mechanical stresses can also affect the elastic properties of ferroelectrics due to the anisotropy of the elastic constants in a single unit cell. This was e.g. observed in soft PZT during uniaxial load and unloading, which revealed a nonlinear increase and decrease of the elastic modulus, similar to the course of the ferroelastic stress-strain curve [42, 43]. Interestingly, hydrostatic compression was found to decrease the piezoelectric properties of single crystalline PIN-PMN-PT, but also an increase of the piezoelectric response of single crystalline $BaTiO_3$ and $PbTiO_3$ with increasing hydrostatic stress along certain crystallographic directions could be predicted by utilizing the LGD theory [367, 368].

A uniaxial stress can also have significant influence on the electromechanical behavior of ferroelectrics, since stress and electric field work antagonistically if applied along the same axis. This results in a temperature-dependent decrease of the remanent polarization and strain with increasing uniaxial compression in for instance soft PZT [369], PLZT [370], $BaTiO_3$ [371], NBT-6BT [372], or BZT-BCT [373]. However, radial stresses in combination with an electric field applied perpendicular to the mechanical load can enhance the electromechanical properties of ferroelectrics. For instance, the application of mechanical radial compression increases P_r and decreases E_c of PZT [374], whereas in-plane strained NBT-xBT thin films show enhanced piezoelectric properties [375].

Relaxor ferroelectrics subjected to stress usually reveal changes in their relaxational and piezoelectric properties. An increasing hydrostatic pressure was found to decrease T_m in Zr-modified $Pb(Mg_{1/3}Ta_{2/3})O_3$ [376], which was attributed to the decrease of the correlation length of the PNRs [377–379]. This decrease in correlation length can also lead to a suppression of the spontaneous relaxor-ferroelectric transition observed in PLZT and to a stress-induced relaxor state in Ca-doped $KTa_{1-x}Nb_xO_3$ [378, 380–382]. Such stress-induced relaxor-ferroelectric transitions were also theoretically analyzed [383].

1.14 Definitions and Conventions used in this Thesis

For clarity, some expressions and phrases used in the following text are defined. All dielectric experiments presented in this work revealed the real part of relative permittivity $\varepsilon^r_{ij} = \varepsilon_{ij}/\varepsilon_0$, which was always measured in parallel to the application of a small oscillating electric field. Therefore, ε^r_{ij} will be simply referred to as "permittivity" and will be denoted by ε'. It should be also noted that the permittivity equals the dielectric susceptibility here, because χ_{ij} is usually in the order of 10^3 in ferroelectric materials.

The polarization is identified with the dielectric displacement field. In Equation 1.2, the electric field is usually in the order of $10^6\,\mathrm{V/m}$, whereas polarizations in ferroelectrics are in the order of $10^{-1}\,\mathrm{C/m^2}$. This results in $\varepsilon_0\ E_i \ll P_i$ and, therefore $D_i \approx P_i$. Since the polarization will be always measured parallel to the electric field in this work, it will be denoted as P throughout the text.

Mechanical stresses will be always uniaxial in the following discussion. Following the Voigt notation, X_{11}, X_{22}, and X_{33} can be abbreviated as X_1, X_2, and X_3, respectively. The longitudinal piezoelectric coefficient d_{333}, which is the only coefficient measured in this work, therefore reduces to d_{33} and the electrostrictive coefficients Q_{1111}, Q_{1122}, and Q_{2323} to Q_{11}, Q_{12}, and Q_{44}. In the same way, the elastic compliances s_{1111}, s_{1122}, and s_{2323} are abbreviated with s_{11}, s_{12}, and s_{44}. Compressive stresses carry a negative sign. Due to this sign convention, a stress of –50 MPa would be (from a mathematical point of view) smaller then a stress of –20 MPa. Since this phrasing is highly unintuitive and in order to prevent confusion, –50 MPa will be always called *larger* than –20 MPa.

2 Experimental Methodology

2.1 Powder Processing

The investigation on the electromechanical properties of the ferroelectric lead-free material NBT-xBT required the synthesis of powders with the final compositions x = 3 mol%, 6 mol%, 9 mol%, 12 mol%. The powders were produced via the conventional mixed solid oxide route (see Figure 2.1), high purity starting powders of Bi_2O_3 (99.975 %), $NaCO_3$ (99.5 %), $BaCO_3$ (99.8 %), and TiO_2 (99.6 %) were purchased from Alfa Aesar (Heysham, Lancashire, UK). After weighing out the stoichiometric amount of powder, batches of 30 g each were filled into nylon milling containers together with zirconia milling balls and ethanol. A planetary mill (pulverisette 5, Fritsch GmbH, Idar-Oberstein, Germany) was used to mix and grind the powders for 24 h at 250 rpm.

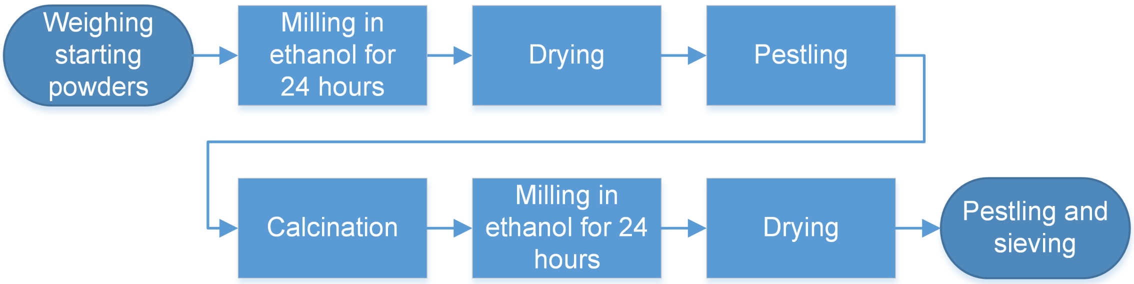

Figure 2.1: Flow chart of the mixed oxide powder processing route for producing NBT-xBT powders with x = 3 mol%, 6 mol%, 9 mol%, 12 mol%.

After drying for at least 48 h in a specially ventilated oven, the milled powders were pestled in an agate stone mortar and deposited into alumina crucibles for calcination. The crucibles were covered with a corresponding alumina lid, but filled only halfway to ensure a sufficient flow of the gaseous products from the powder during the solid state reaction. A two-step process was used for calcination, *i.e.*, heating the powders to 700 °C with a rate of 5 °C/min and dwelling for 2 h followed by a final step at 800 °C with a dwell time of 3 h. Afterwards, the furnace was switched off and cooled down to room temperature without a defined cooling rate. The calcined powders were then again milled in ethanol for 24 h. After drying and pestling, a 160 μm sieve was used to break up larger agglomerates in the final powder and to sort out possible unwanted particles, e.g. parts of broken milling balls.

2.2 Sample Preparation

In order to prepare polycrystalline $BaTiO_3$ samples, a commercial powder (KBT-03, Ferro Corp., Mayfield Heights, OH, USA) was uniaxially pressed into pellets with approximately 25 mm diameter and a weight of 10 g each. Afterwards, the samples were vacuum sealed in latex tubes for the subsequent cold isostatic pressing in oil (press: KIP 100 E, oil: HLPD 10, P/O/Weber GmbH, Remshalden, Germany) at –356.5 MPa for 1.5 min. The green bodies were then placed on a $BaTiO_3$ powder bed on an alumina plate and covered with a small amount of $BaTiO_3$ powder. The samples were then capped with an alumina crucible and were sintered in an oven at 1280 °C for 5 h using a heating rate of 5 °C/min and furnace cooling to room temperature.

After sintering, the samples were glued onto a glass plate, where cylindrical samples with a diameter of approximately 5.8 mm were core drilled out from the dense plate with a water-cooled diamond hollow drill. In order to prevent the upper edges of the samples from being damaged during drilling, a thin glass plate was glued on top of the $BaTiO_3$ pellets. Subsequently, the samples were ground with a surface grinder to a final height of 6 mm. The surface grinder also ensured that the circular faces were plane and parallel, which was of special importance for all mechanical experiments. In order to remove residual stresses and potentially reoriented domains induced by the machining processes, the samples were annealed in an oven at 150 °C for 30 min, which is above the ferroelectric-paraelectric transition temperature. Finally, silver was sputtered (Emitech K950X, Quorum Technologies Ltd., Laughton, East Sussex, UK) on both sides of the samples to serve as electrodes.

In the case of the PZT ceramics, the commercial available materials PIC151 ($Pb_{0.99}[Zr_{0.45}Ti_{0.47}(Ni_{0.33}Sb_{0.67})_{0.08}]_{1.00}O_3$) and PIC181 ($Pb_{1.00}[Zr_{0.47}Ti_{0.48}(Mn_{0.33}Sb_{0.32}Nb_{0.33})_{0.05}]_{1.00}O_3$) were received from PI Ceramic GmbH (Lederhose, Germany) as sintered plates. The samples were core drilled from of these disks using the same previously described procedure. Following this, the samples were sputtered with platinum or gold-palladium electrodes. The poling procedures and annealing temperatures differed for the different compositions and also from one experiment to another and are therefore not given here but rather directly in the corresponding sections.

The preparation of polycrystalline samples of NBT-xBT required a different procedure than described above, because the material was more difficult to machine. At first, the powder was uniaxially and cold isostatically pressed into green bodies with dimensions close to the final height and diameter. Except for using a different sintering temperature of 1150 °C and a shorter dwelling time of 3 h, the sintering procedure was otherwise the same as in the case of $BaTiO_3$. Next, the as-sintered samples were glued with one of their parallel faces onto a special aluminum holder, mounted into a lathe and ground down to a diameter of 5.8 mm with a special grinding attachment mounted to the lathe. During this process the sample was water-cooled to prevent cracking or chipping. Prior to further grinding of the circular surfaces, the samples were annealed at 400 °C for 30 min with a maximum heating/cooling rate of 1 °C/min in order to relieve all induced stresses. This intermediate annealing step was found to be necessary to prevent the samples from being damaged on the surfaces and edges by the necessary subsequent machining. Finally, the samples were ground with a surface grinder down to the required height of 6 mm, followed by another annealing step (identical to the first) and the final sputtering of platinum electrodes. The poling procedures differed between experiments and will be discussed in the pertinent sections.

For measuring the elastic modulus as a function of temperature, bar shaped samples of PIC151, PIC181, and $BaTiO_3$ were prepared. The sample dimensions were approximately 25-28 x 3-4 x 1-3 mm^3. Gold electrodes were sputtered on the 25-28 x 3-4 mm^2 faces. In order to realize short circuit conditions during characterization of poled samples, one of the 25-28 x 1-3 mm^2 faces was additionally sputtered with gold after poling between the two 25-28 x 3-4 mm^2 faces.

2.3 Large Signal Electrical Measurements

The large signal electrical behavior of a ferroelectric material, *i.e.*, the measurements of the electric field-polarization hysteresis loops, was characterized with a modified Sawyer-Tower electrical circuit [384]. A schematic wiring diagram is depicted in Figure 2.2, which shows a sample, a reference capacitor and a high voltage source connected in series. The voltage source consisted of a high voltage amplifier (20/20C, TREK Inc., Lockport, NY, USA) controlled by either a function generator (HP 33120A, Agilent Technologies Inc., Santa Clara, CA, USA) or a LabVIEW program via an analog output device (NI PCI-6221 or NI USB-6356, National Instruments Corp. (NI), Austin, TX, USA).

An impedance converter, *i.e.*, a 1:1 operational amplifier, served to increase the input resistance from the typical MΩ range to the TΩ range. This allowed the connected data acquisition (DAQ) device (NI PCI-6133 or NI USB-6356) to measure the voltage at the reference capacitor without reducing this voltage significantly. If the capacitance C_{ref} of the reference capacitor is several orders of magnitude larger than the capacitance of the sample, the polarization P of the sample could be calculated by using Equation 2.1.

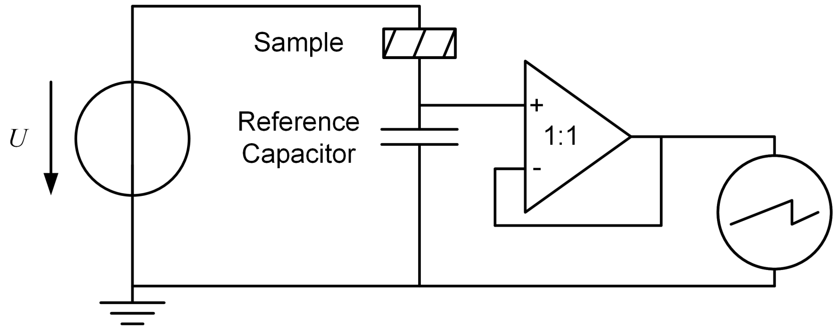

Figure 2.2: Experimental setup for measuring electric field-polarization hysteresis loops. The electrical circuit was a modified version of the setup initially developed by Sawyer and Tower [384]. In this circuit, the sample is connected in series to a reference capacitor with a known capacitance. The voltage measured at the reference capacitor is proportional to the change in polarization of the sample.

$$P = \frac{C_{ref} \cdot U_{ref}}{A}, \tag{2.1}$$

where U_{ref} is the measured voltage at the reference capacitor and A the cross-sectional area of the sample. Equation 2.1 follows from the charge equality of both sample and reference capacitor.

The capacitance of the samples used in this investigation typically ranged from pF to a few nF, while the reference capacitors were in the range of μF. In order to prevent short circuiting through air, the sample was mounted into a sample holder and placed in a silicone oil bath. All data was acquired and processed by a custom-built LabVIEW program (Figure 2.3), which also had the possibility of recording a strain signal (see also Section 2.4).

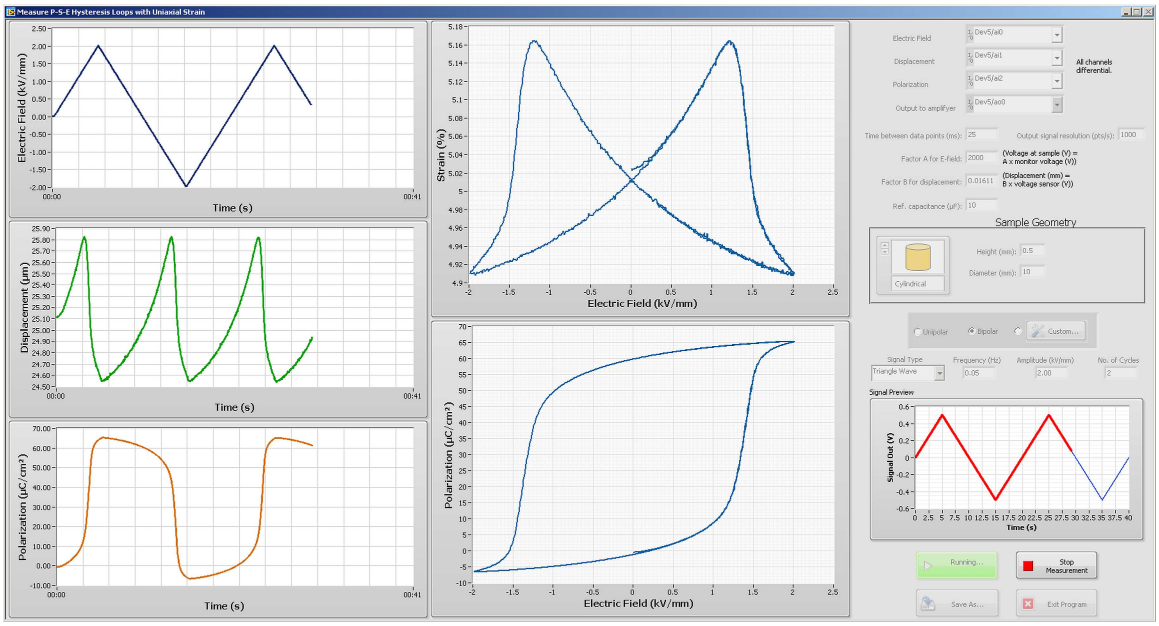

Electric Field: Dev5/ai0
Displacement: Dev5/ai1
Polarization: Dev5/ai2
Output to amplifyer: Dev5/ao0
All channels differential.
Time between data points (ms): 25
Output signal resolution (pts/s): 1000
Factor A for E-field: 2000 (Voltage at sample (V) = A x monitor voltage (V))
Factor B for displacement: 0.01611 (Displacement (mm) = B x voltage sensor (V))
Ref. capacitance (µF): 10
Sample Geometry: Cylindrical
Height (mm): 0.5
Diameter (mm): 10
○ Unipolar ● Bipolar ○ Custom...
Signal Type: Triangle Wave
Frequency (Hz): 0.05
Amplitude (kV/mm): 2.00
No. of Cycles: 2

Figure 2.3: Custom-built LabVIEW program for measureing electric field-polarization and electric field-strain hysteresis loops. The left column of the frontpanel shows the measurement signals of all three parameters as a function of time, while the center column provides directly the measured hysteresis loops. All parameters (e.g. I/O settings, measurement speed, conversion factors or sample geometry) are accessible for modification in the third column. An integrated function generator (bottom right corner) provides different forms of input signals for the high voltage amplifier.

The built-in linear variable differential transformer (LVDT) system allowed recording the electric field-strain hysteresis loops as well, using an external data acquisition system (MGCplus with AB22A and ML55B, HBM GmbH, Darmstadt, Germany). This device drove the LVDT and provided an analog signal proportional to the current displacement value, which could be read with the DAQ devices and the LabVIEW program described above. In order to measure stress and temperature-dependent hysteresis loops, the sample was placed in a uniaxial load frame described in Section 2.4, which ensured a nearly constant load during the application of the electric field.

2.4 Measurement of the Ferroelastic and Dielectric Properties as a Function of Uniaxial Compressive Stress and Temperature

A commercial screw-driven uniaxial load frame (Zwick/Roell Z030, Zwick GmbH & Co.KG, Ulm, Germany) was used as the basis for all measurements described in this section. Several modifications and extensions were designed and built in order to make a wide variety of electromechanical measurements possible. Figure 2.4 shows a schematic drawing of the experimental setup. The sample was located in the center of the machine between well polished bearings made out of tungsten carbide (WC), which is not only a highly stiff material ($E = 420\,\text{GPa} - 710\,\text{GPa}$ [385]) but also electrically conductive. The WC bearings also served as electrical contacts to the samples, whereas the load transferring alumina tubes insulated the sample from the rest of the machine. An integrated oven (SV800, Thermal Technology GmbH, Bayreuth, Germany) was capable of heating the samples up to 800 °C. Displacement measurements were done with a custom-built LVDT system (W1ELA/0, HBM GmbH, Darmstadt, Germany), which measured the change in length between the bottom surfaces of the upper and the lower WC bearings. This included not only the sample dimension change but also the contribution of the lower bearing, so a temperature-dependent calibration of the strain measurement with alumina was needed to correct for this systematic measurement error. Further information about the strain measurement and the sample holder design can be found elsewhere [43] and will not be described here in further detail.

Considerable effort was put into centering and aligning all of the parts inside the machine, which was essential for accurate measurement and ensuring a homogeneous uniaxial stress state inside the sample. The relevant mechanical issues dealt with ranged from machining and aligning the alumina rods and the sample holder, to designing and producing centering tools for various sample geometries to be tested. A detailed description of all technical and mechanical aspects of the experimental setup would be far beyond the scope of this thesis and therefore only the most important information is given, as appropriate.

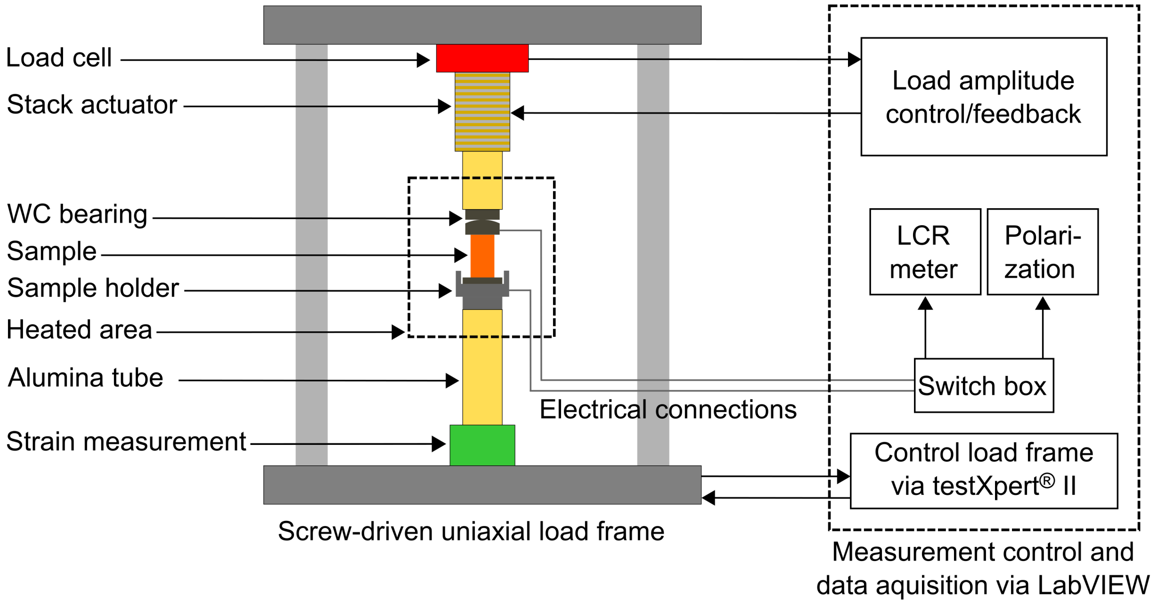

Figure 2.4: Schematic drawing of the experimental setup used for temperature-, stress-, frequency-, and electric field-dependent electromechanical characterization of ferroelectric materials. The configuration shown here was used for stress and temperature-dependent measurements of the piezoelectric coefficient and the permittivity.

During ferroelastic testing and in the case of poled samples, the strain and load data was acquired simultaneously with the polarization signal by the load frame. Both the control and recording of this data was performed by the software testXpert II (Zwick). The polarization measurement was carried out using a modified Sawyer-Tower setup, shown in Figure 2.5, where an analog input of the load frame's electronics was connected to the output of the measurement box.

It was also possible to choose within a set of different reference capacitors, ranging from 1 μF to 22 μF, which was approximately 1000 times larger than the typical capacitance of the samples. This difference ensured that the reference capacitor did not distort the signal of the sample. All

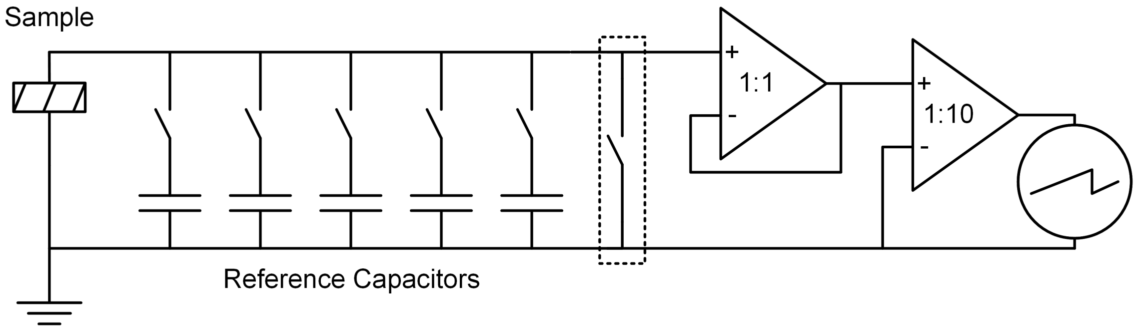

Figure 2.5: Modified Sawyer-Tower like setup for measuring the stress-induced polarization change of a sample. The different sized reference capacitors could be combined freely and discharged with a switch (dotted box), which could be also operated remotely with a digital control signal.

parts were contained with a metal box to shield the electronics from external parasitic signals. The switch marked with a dotted box in Figure 2.5 discharged the reference capacitors and can be operated via a digital control signal (low level (logical 0): 0.0 V – 0.8 V, high level (logical 1): 2.2 V – 5.0 V) provided by LabVIEW in conjunction with an I/O module. It was essential for these measurements to transfer all charge created by the sample to the reference capacitors, which required all connected devices to be highly resistive. For that reason, the connection between the discharge switch and DAQ device was made with an optocoupler, which physically and electrically separated the measurement circuit from the I/O module. The entire electrical circuit was developed and built by Michael Weber (Electrician, Materials Science Department, TU Darmstadt).

For measuring the capacitance C of a sample as a function of stress and temperature, an LCR meter (HP 4284A, Agilent Technologies Inc., Santa Clara, CA, USA) was connected to the sample instead of the polarization measurement box. During heating, the load frame was typically used to ensure a constant bias load, which was held while measuring the capacitance at several frequencies. It could alternatively be used for applying different stress steps or a loading rate at constant temperature for stress-dependent measurements of the capacitance. The temperature, capacitance, and loss data were acquired by a LabVIEW program that was connected via GPIB (General Purpose Interface Bus, IEC-625-Bus) and serial connection (RS-232) to the LCR meter and the Eurotherm temperature controller (3204, Invensys Systems GmbH, Limburg a. d. Lahn, Germany), respectively. The real part of the permittivity ε' could then be calculated using:

$$\varepsilon' = \frac{C\,A}{\varepsilon_0\,d}, \tag{2.2}$$

where d is the height of the sample.

In addition to the setup described above, an additional new measurement system was constructed as part of this work. Again, the basic device was a screw-driven uniaxial load frame (5967, Instron GmbH, Darmstadt, Germany) together with a custom-installed and calibrated temperature chamber (TK 26.600.LN2, Fresenberger GmbH, Wipperfürth, Germany). The advantage of this system was the extension of the low end of the temperature range (between –150 °C and 600 °C) achieved by liquid nitrogen cooling. For that reason, a complex Eurotherm temperature controller (2604, Invensys) was installed and optimized to stabilize the temperature within ±0.1 °C to ±0.5 °C during heating, cooling, and dwelling over the entire range of temperatures. Both experimental setups could also be used for stress and temperature-dependent impedance spectroscopy.

2.5 Measurement of the Piezoelectric Coefficient as a Function of Temperature, Frequency, and Uniaxial Compressive Stress

2.5.1 General Description of the Measurement Setup and the Hardware

The experimental setup presented in Figure 2.4 was also built for measuring the piezoelectric coefficient d_{33} of a sample at different uniaxial compressive stresses and/or different temperatures. For that purpose, a piezoelectric stack actuator (P-025.80, PI Ceramic) was built into the load frame and unloaded the sample sinusoidally so that the stress never exceeded the bias load during the measurement. This measurement mode was chosen for all experiments in order to prevent further change of the sample state because of additional loading above the bias stress maintained by the load frame.

Due to the direct piezoelectric effect, the sample produced a voltage signal proportional to the applied mechanical (unloading) stress change. These changes in polarization could be measured by using the electrical circuit shown in Figure 2.5. A load amplitude of ±0.5 MPa was used as the default value, but smaller and larger amplitudes between ±0.1 MPa and ±20 MPa were possible as well. The choice of signal amplitude depended on the elastic and piezoelectric properties of the material, the sample dimensions, and the magnitude of the resulting polarization signal. The frequencies used in this work ranged from 0.1 mHz to 240 Hz. From the resulting stress and polarization amplitudes, ΔX and ΔP, the piezoelectric coefficient d_{33} could be calculated by using:

$$d_{33} = \frac{\Delta P}{\Delta X}. \tag{2.3}$$

A specially designed and custom-built LabVIEW program, which will be presented in further detail in Section 2.5.2, was used for controlling the overall measurement and together with testXpert II for acquiring, processing, evaluating, and saving all incoming data. This required to read in all measurement signals with a DAQ device (NI PCI-6133) connected to LabVIEW, which was possible for all signals except the stress signal measured by the built-in load cell of the uniaxial load frame. The electronics of the load frame did not allow diverting the load signal without processing and filtering. Therefore, a special electronic circuit designed and built by Michael Weber (Electrician, Materials Science Department, TU Darmstadt) was connected directly to the output of the load cell in addition to the load frame electronics. This device amplified the resulting signal by the factor of 1000, which was then suitable for use as an input signal for the DAQ device from NI.

The uniaxial load frame was able to work in two standard control modes: (i) load controlled mode, where the machine maintains a constant load or load rate, and (ii) position controlled mode, where the load frame's crosshead position is held constant. The load controlled mode was essential to compensate for the thermal expansion of the sample and all other parts of the machine inside the oven during heating. This prevented the sample and, even more importantly, the machine itself from being damaged. While applying the aforementioned sinusoidal mechanically unloading waveform for measuring the piezoelectric coefficient, the machine needed to be switched to the position controlled mode. Otherwise, the load frame would try to compensate for the in this case intended load change as well. This control mode switching was done by the LabVIEW program automatically via a digital connection to the I/O board of the load frame's electronics. Another electrical circuit developed by Michael Weber (Electrician, Materials Science Department, TU Darmstadt) transformed the digital control signal of the NI I/O device (part of NI PCI-6221) to the digital control signal (low level (logical 0): 0 V – 7 V, high level (logical 1): 12 V – 30 V) required by the electronics of the load frame.

Some of the temperature-dependent d_{33} measurements presented in this work took up to 14 h to complete. This could be problematic, especially for overnight measurements, as it was not possible to maintain a constant manual monitoring of the status of the measurement and the devices involved in all instances. The time consuming heating process was particularly important to monitor, because a crash of the software testXpert II during this time would stop the machine's load control system. This would then lead to a critical increase in stress at the sample due to the heating, resulting in damaging and/or destroying the sample or parts of the load frame. Therefore, LabVIEW constantly monitored the mechanical stress at the sample and turned off the oven if a critical predefined stress was exceeded. In the case of a crash of the LabVIEW program or of the computer on which LabVIEW was running, testXpert II automatically switched to load controlled mode to prevent overloading of the sample.

Two main measurement scenarios were used in this work: (i) load-dependent measurement of the piezoelectric coefficient at constant temperature (Figure 2.6a) and (ii) temperature-dependent measurement of d_{33} at constant uniaxial compressive stress (Figure 2.6b). Both measurements were also done over a range of frequencies in order to analyze the frequency dependence of the piezoelectric coefficient. In the case of a temperature-dependent measurement, during which the sample was heated up with a constant heating rate, a compromise needed to be found between reasonable measurement time and lowest frequency investigated in order to keep the temperature change as low as possible within a measurement at one single frequency. In general, both

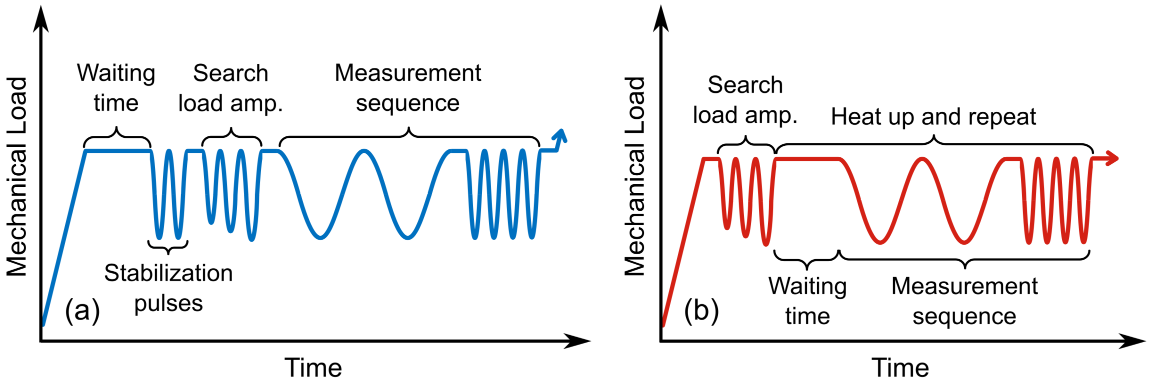

Figure 2.6: Schematic of the two main measurement modes used in this work for measuring the piezoelectric coefficient as a function of frequency and (a) uniaxial compressive stress at constant temperature or (b) temperature at constant mechanical load. It was also possible to measure the capacitance of a sample after the waiting time in addition to the d_{33} measurement.

measurement modes required the load frame to switch to the position controlled mode following the waiting time and then switch back to the load controlled mode at the end of the measurement sequence.

For load-dependent measurements depicted in Figure 2.6a, an initial waiting time of 4 min after each increase or decrease in mechanical stress was used to ensure that the sample was close to a state of equilibrium. It was found to be useful that an initial vibration of 10 Hz for 5 s applied to the sample prior to each measurement helped to settle the mechanical components of the system at the new stress state. Since the amplifier (E-481.00, PI Ceramic) for the stack actuator required an analog input signal proportional to the output voltage to the actuator, the voltage amplitude needed to be set manually or automatically to match the desired sinusoidal load signal. The required voltage amplitude was found to be both frequency and stress-dependent, since the stack actuator is itself also a piezoelectric material. For this purpose, an additional LabVIEW program provided a feedback loop in order to set the voltage amplitude to the correct value, resulting in the predefined stress amplitude at the sample. An empirical calibration function corrected the voltage amplitude applied on the stack for the mentioned frequency dependence of the stack. Finally, the actual measurement sequence started, data was acquired, and the whole cycle was repeated at each new load step.

In contrast to the load-dependent measurements, the initial search for the required voltage amplitude at the actuator was done only once in the beginning of a temperature-dependent measurement shown schematically in Figure 2.6b. The load frame needed to switch to the position controlled mode during the measurement process which would result in a significant increase in stress due to thermal expansion if this state was held for too long. Because of that, the measurement time needed to be as short as possible and only the actual measurement sequence was permanently repeated, using the initially set parameters. The drawback of this procedure was that the load amplitude typically deviated by 5 % to 6 % (depending on the material under test) from the initial set value during heating due to thermal changes in the elastic properties.

It was also possible to determine the capacitance of a sample using the above mentioned LCR meter. The capacitance measurement was then included in the measurement cycle right after the waiting time (see Figure 2.6). In order to switch the measurement between the four terminal capacitance measurement and the two terminal polarization measurement, a switching box specially designed for this purpose by Michael Weber (Electrician, Materials Science Department, TU Darmstadt) was inserted into the electrical connections between the sample and the measurement devices. This box allowed for changing the measurement mode not only manually but also remotely with a digital control signal.

2.5.2 Custom-Built LabVIEW Program for Stress, Temperature- and Frequency-Dependent d_{33} Measurements

In general, the structure of the LabVIEW program (or VI, Virtual Instrument) built for the above-described measurements was based on the producer/consumer design pattern. This structure allowed LabVIEW to run different parts of the code independently and in parallel on different cores of the CPU, which made the program significantly faster and prevented buffer overflows during data acquisition. The analog output to the stack amplifier and the data acquisition represented the producer loops, whereas the routines for saving, processing, and analyzing the data were included as the consumer loops. An event structure served as core element of the software, controlling the overall measurement and processing all of the user interaction while minimizing the CPU utilization. The optional load monitoring function during heating (see Section 2.5) was included in a second event structure, guaranteeing the independence of this safety-relevant process from the primary data acquisition structure. Since this programming project became relatively large, it was necessary to write the code in a modular way, *i.e.*, dividing the program into sub-VIs in order to make the code more readable and clear. Internal LabVIEW functions like "queues", "notifiers", and "occurrences" ensured the synchronization between all structures of the program, whereas trigger signals synchronized the input and output times of the various devices. For fully automatic measurements, LabVIEW communicated with the load frame control software testXpert II through digital control signals. Another such signal coming this time from testXpert II triggered the start of a single measurement sequence done by LabVIEW. For this purpose, a built-in function named "change detection" of the DAQ device was used, which constantly monitored a specific digital input channel for a state change, *i.e.*, an incoming trigger signal from the load frame.

Before starting the program, the user needed to define the desired type of experiment, *i.e.*, to choose the signals to be measured, for example polarization, temperature, or permittivity. With the exception of specifying the file path for saving, all other relevant fields such as sample dimensions, analog input signal conversion factors (gains), frequencies for permittivity, and frequencies and amplitudes for the d_{33} measurement could be also set or changed during run-time. After the main VI was manually executed, a pop-up window appeared (see Figure 2.7), showing all hardware connections, e.g. trigger lines, analog inputs/outputs, or the serial connection to the temperature controller. These connection settings could be changed if necessary, especially after adding or removing hardware.

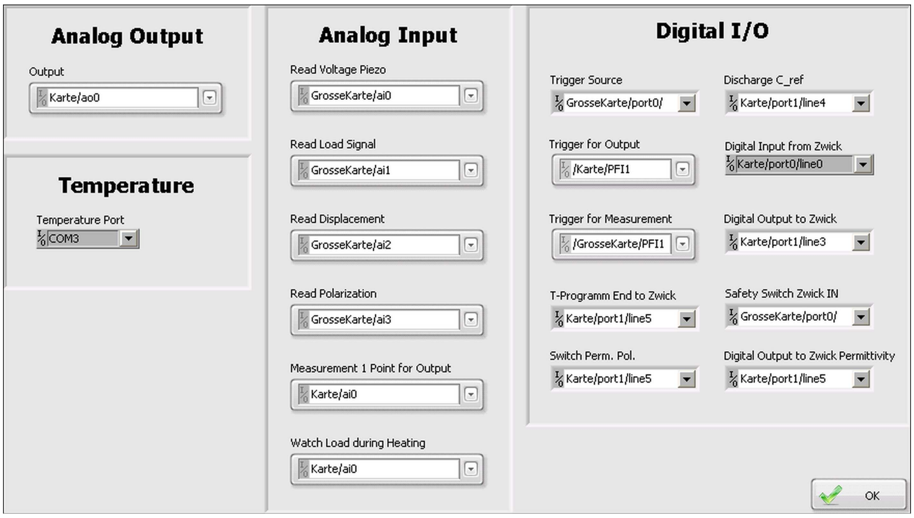

Analog Output

Output
Karte/ao0

Temperature

Temperature Port
COM3

Analog Input

Read Voltage Piezo
GrosseKarte/ai0

Read Load Signal
GrosseKarte/ai1

Read Displacement
GrosseKarte/ai2

Read Polarization
GrosseKarte/ai3

Measurement 1 Point for Output
Karte/ai0

Watch Load during Heating
Karte/ai0

Digital I/O

Trigger Source
GrosseKarte/port0/

Discharge C_ref
Karte/port1/line4

Trigger for Output
/Karte/PFI1

Digital Input from Zwick
Karte/port0/line0

Trigger for Measurement
/GrosseKarte/PFI1

Digital Output to Zwick
Karte/port1/line3

T-Programm End to Zwick
Karte/port1/line5

Safety Switch Zwick IN
GrosseKarte/port0/

Switch Perm. Pol.
Karte/port1/line5

Digital Output to Zwick Permittivity
Karte/port1/line5

Figure 2.7: Pop-up window appeared prior to the start of the main program for measuring d_{33}. In this panel, all hardware connections could be checked and changed if necessary.

Following approval of the connections settings, the main window became active, which is shown and described in further detail in Figure 2.8. Internally, all needed controls, indicators, variables, diagrams, and most of the I/O tasks were initialized before any user input was possible. No stress on the sample was allowed at this time, because the voltage at the stack actuator needed be ramped to a predefined value first. The reason for this was that the stack worked only in unipolar mode, *i.e.*, the stack needed to shorten to unload the sample periodically during the measurement. This was only possible if a constant bias voltage was applied to the stack beforehand. Furthermore, the load value needed to be zeroed after this step because the load cell delivers the absolute load value including the weight of the stack and the other mechanical parts. After this procedure, a preload could be applied to the sample by using the control software of the load frame.

File Settings

Folder Path: E:\Florian\Data\Test

Name of Experiment: PIC Bilder

Watch Load while heating?

Max. Load allowed (N): 10000

Measure Noise?

Brutto Load (N): 492,111

Current Temperature (°C): 169,198

Load Monitoring done? ●

Experiment Settings

Gain Load: 1000

Gain Strain (µm/V): 50

Gain Polarization: 10

Sample Height (mm): 5,93

Sample Diameter (mm): 5,82

Ref. Capacitance (µF): 4,514

Sampling Rate Output: 400k

Meas. Samples per Wave: 9k

Max. Measurement Rate: 18k

Frequencies for Permittivity (Hz): 100, 1000, 10000, 100000, 1000000

Current Status: Measurement Running

Current Frequency (Hz): 10

Dataset No.: 223

Target Amp. (MPa): 0,5

Current Meas. Rate (Hz): 18k

Wave Settings

Wave OK? ●

Course of Experiment

Frequency	# Waves	Amplitude
1	5	0,0967188
5	10	0,0967188
10	20	0,0967188
40	20	0,0967188
120	20	0,0967188
200	20	0,0967188
240	20	0,0967188

Initial Amp. (V): 0,05

Control Mode: ● Voltage (V) ○ Load (MPa)

Cal. Frequency (Hz): 10

Corr. Amp. (V): 0,0967

Baseline (V): 5

Ramp Rate (V/s): 1

Current Amp. (V): 0,0967

Estimated Duration of Experiment (s): 11,05

Figure 2.8: Front panel of the main VI for measuring the piezoelectric coefficient and the permittivity as a function of uniaxial compressive stress, temperature, and frequency. The controls allowed specifying the type of properties to be measured as well as setting all of the details about the course of the experiment, the sample dimensions, and some specific instrumental parameters like the size of the reference capacitor. The diagram in the bottom left corner gave a rough preview over the measurement sequence, whereas the plots on the right hand side depicted the raw data, updated every second over the course of the experiment. In the top right corner, all central experiment controls were located and the current status of the measurement was given.

If the temperature-dependent measurement mode was selected, the required voltage amplitude to be applied to the actuator needed to be found and set once in advance as already explained in Section 2.5 and depicted in Figure 2.6b. In order to accomplish that, a corresponding subVI was written that adjusted the voltage amplitude automatically to the right value with a basic feedback loop (see Figure 2.9). By default, five load oscillations at 10 Hz were applied to the sample and the stress amplitude was determined and compared to the target amplitude. Based on the result of the comparison, the voltage amplitude was then increased or decreased stepwise until the amplitude was within a range of ±0.5 % of the target value. In this case, a counter was increased by 1. If the value of the counter was equal to 8, the voltage amplitude was assumed to be sufficiently determined and the search stopped. During the automatic search, the step width for increasing/decreasing the amplitude was halved if the program was not able to match the ±0.5 %-criteria. The value of the amplitude must then be copied manually into the table defining the parameters of the experiment in the main front panel. By clicking on the "Build Wave" button, the program finally checked all values for self-consistency and would alert the user if an erroneous input (e.g. blank field, too high amplitude, etc.) has been made.

After this step, it was possible to start the actual measurement either manually or automatically. For a manual measurement, the user needed to apply the desired mechanical stress with the load frame, then start the measurement sequence defined in the "Course of Experiment" table.

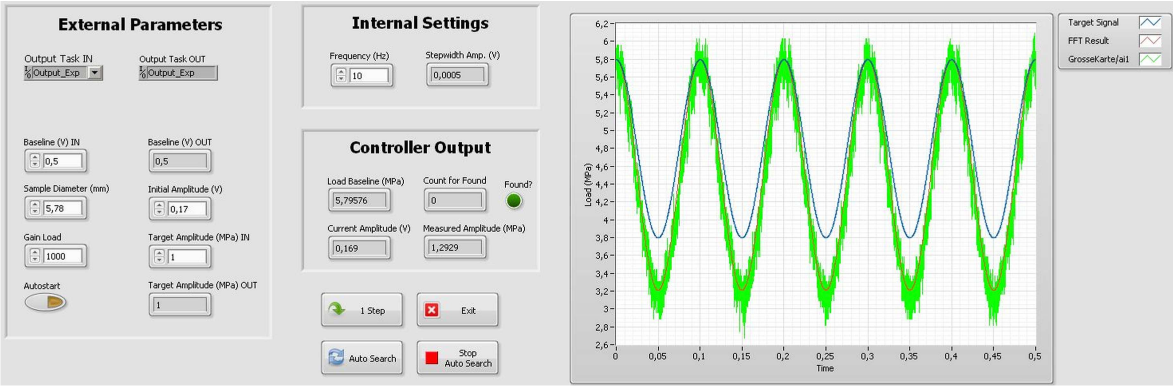

External Parameters

Output Task IN: Output_Exp
Output Task OUT: Output_Exp
Baseline (V) IN: 0,5
Baseline (V) OUT: 0,5
Sample Diameter (mm): 5,78
Initial Amplitude (V): 0,17
Gain Load: 1000
Target Amplitude (MPa) IN: 1
Autostart
Target Amplitude (MPa) OUT: 1

Internal Settings

Frequency (Hz): 10
Stepwidth Amp. (V): 0,0005

Controller Output

Load Baseline (MPa): 5,79576
Count for Found: 0
Found? ●
Current Amplitude (V): 0,169
Measured Amplitude (MPa): 1,2929

Figure 2.9: SubVI for searching the voltage amplitude at the stack actuator corresponding to the desired load amplitude. The program worked automatically, but could be started either manually or programmatically. On the right hand side a diagram depicted the measured load data and the (simulated) target signal. All input fields were automatically filled by the main VI.

In the case of a fully automatic measurement, the software testXpert II needed to be started first with a specially designed program sequence, then the whole experiment including the measurement with the LabVIEW program would be performed without further user action. At first, the system waited for a pre-set period of time, then executed a permittivity measurement if requested. If this was the case, LabVIEW switched the electrical connections to the LCR meter with a digital control signal sent the switch box. During load-dependent measurements, the aforementioned initial load oscillations were now applied to the sample and the subVI for setting the correct voltage amplitude was executed. Both of these steps were skipped during a temperature-dependent measurement. Next, the DAQ devices were initialized, the sinusoidal output signal to the amplifier of the stack was prepared and the triggers were armed. The frequency-dependent measurement of the piezoelectric coefficient started with the firing of these trigger signals, initiating the amplifier output signal, and activating the data acquisition. In general, the measurement could be interrupted by the user after each completed frequency block.

Since typical reading rates for the DAQs ranged between 0.9 kHz and 18 kHz in this work, the reading process, as well as the writing process, were divided in segments of 1 s in order to prevent buffer overflow and to optimize CPU utilization. All raw data was plotted in the main window and saved to a TDMS (Technical Data Management Streaming) file, a binary file format provided by NI. This format allowed fast streaming of a large amount data (the final file size could reach several gigabytes for each of these measurements) and the LabVIEW program sorted the data into specifically named containers inside the TDMS file for easy access later on. The experiment automatically stopped after the load or temperature-dependent program was finished.

After each measurement sequence at a single frequency, the data was analyzed in the subVI shown on Figure 2.10, which also displayed the results of the data evaluation, *i.e.*, the piezoelectric

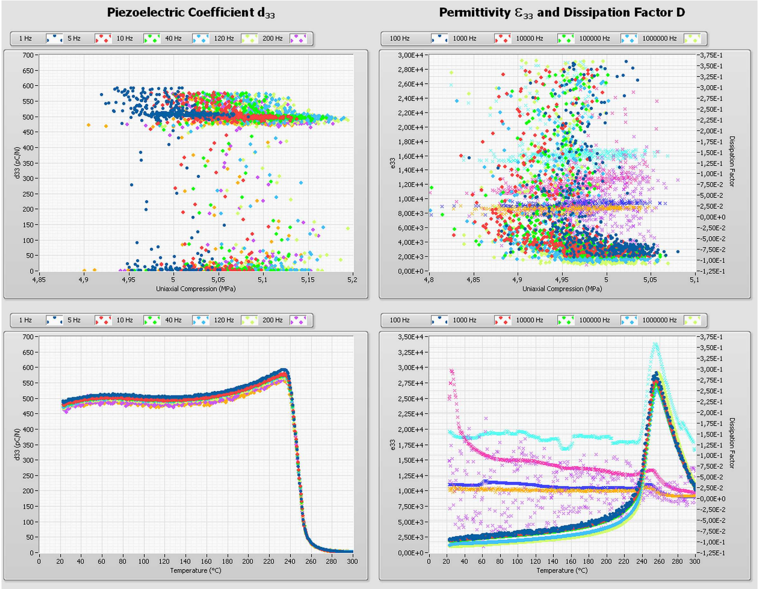

Figure 2.10: Front panel of the subVI for data processing, data evaluation, and for displaying the results of the measurement of the piezoelectric coefficient (left column) and the permittivity and loss (right column) as a function of frequency and uniaxial mechanical stress or temperature.

coefficient, the permittivity, and the dielectric loss as a function of frequency and uniaxial mechanical compression or temperature. Initially, the raw data of the d_{33} measurement was read from the TDMS file and required a baseline correction. The reason for this was that the polarization signal could drift even after the 4 min waiting time prior to each measurement. This was either due to an applied load step or due to heating. Since this drift was mostly linear, a linear regression was performed and the resulting baseline shift was subtracted from the original signal. In the next step, the signal was transformed to the frequency space by a Fourier transform and a small interval around the measurement frequency was cut out. A Fourier synthesis transformed this part of the signal back into the time domain. This process was equal to a sharp band-pass filter and is depicted exemplarily by means of sample data in Figure 2.11. After filtering, the signal was ready for extracting the amplitude, the frequency, and the phase by a built-in LabVIEW function. Finally, the piezoelectric coefficient was calculated by using Equation 2.3 and the results were plotted in a diagram in the same subVI (see Figure 2.10). In the case of the permittivity, the measured capacitance was converted using Equation 2.2.

In addition to the LabVIEW program, the control software of the load frame needed to be configured in a special way in order to apply and/or maintain mechanical bias stress to the sample while communicating with LabVIEW. For that purpose, a highly flexible, graphical programming interface of testXpert II was used to build a completely flexible and user defined loading sequence. In some cases it was even necessary to go back to the proprietary high level programming language ZIMT (Zwick Interpreter for Materials Testing) to enable such flexibility in the parameter input as desired. The test specifications in testXpert II included also digital I/O connections to synchronize the experiment with LabVIEW and ensure that the previously mentioned essential switching of the load frame electronics between load and position control mode was possible.

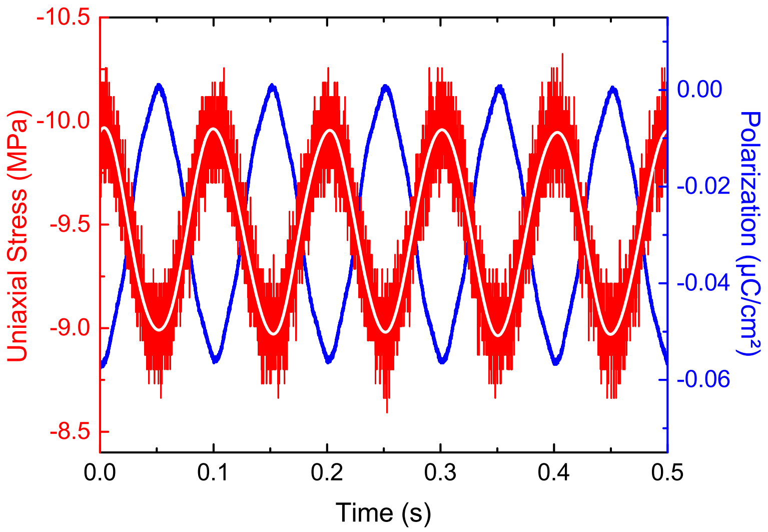

Figure 2.11: Exemplary load and polarization signals taken from a d_{33} measurement. The white line indicates the filtered and reconstructed load signal. After determining the amplitudes of both signals, the piezoelectric coefficient could be calculated.

2.6 Measurement of the Elastic Modulus as a Function of Temperature

A commercial system was used for characterize the elastic properties of a sample as a function of temperature (RFDA-HT1750, IMCE n.v., Genk, Belgium). The basic principle of the RFDA (Resonant Frequency and Damping Analyzer) is to record the acoustic spectrum emitted by a bar shaped sample that is hit by a cylindrical shaped rod or "hammer" with a low level of force to the bottom-center of the sample (see Figure 2.12). Therefore, the sample was clamped into an alumina sample holder and placed in an oven. In order to minimize the influence of the sample holder, the cuboid sample was supported only at the vibration nodes.

The software package provided by the manufacturer of the device was used to run the overall measurement and to evaluate the received spectra. During the evaluation process, a built-in fast Fourier transform was performed on the signal and the resonance frequency was determined from which the elastic modulus can be calculated. Manual post-processing had to be done to the resulting data, because the software was not able to correctly identify the resonance frequency for every measurement. Also, the original temperature measurement (type S thermocouple) was completely refurbished and tested during this work, resulting in accurate and repeatable measurements.

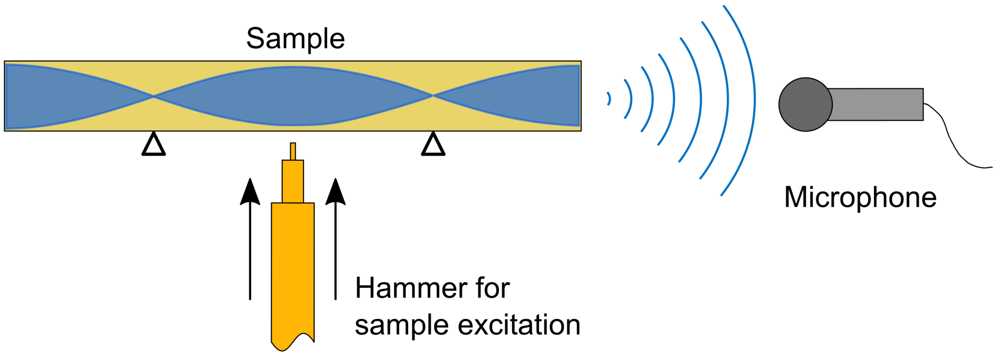

Figure 2.12: Schematic of the commercial experimental setup for measuring the elastic modus of a sample as a function of temperature. An alumina hammer hit the sample from below, causing an excitation of acoustic waves (schematically indicated as the blue colored areas) that were emitted by the sample. The spectrum was recorded by a microphone and analyzed by a proprietary software package.

2.7 Measurement Errors

Physics is a science that tells you precisely how imprecise it is. However, it is a challenging task to determine the uncertainty of a single measurement in complex experimental systems like those presented above. Many discussions in the following chapters will deal with the general evolution of the properties of ferroelectrics with temperature or stress, for example. Since modern electronic measurement devices allows for the collection of a large number of data points, the scattering of the data and the unavoidable differences between different samples are actually more meaningful than the error of a single measurement. Nevertheless, a conservative estimation of the measurement uncertainties will be given in the following.

Sample Geometry

The dimensions of the samples were determined with a digital caliper, which has a typical precision of ±30 μm according to the manufacturer. In addition, due to a possible slight conicality caused by the sample preparation, the total measurement error is therefore estimated to be ±50 μm. This was the most influential error of all of the experiment parameters and it is assumed to overbalance all other error sources. In a subsequent series of measurements performed on a single sample, e.g., a single run of a temperature-dependent permittivity measurement, the error of the sample dimension is not a statistical but rather a systematical error since it is constant within the measurement series.

Permittivity

According to Equation 2.2, the permittivity was calculated from the sample dimensions and from the capacitance of the sample measured by the LCR meter (the value of ε_0 is exact). The accuracy of the HP 4284A precision LCR meter could be assumed to be negligible compared to the error induced by the sample geometry measurement. For a typical sample, the maximum error was approximately ±2.5 % based on the ±50 μm error in dimensional measurement, but it was a systematic error.

Mechanical Stress

Both uniaxial load frames were equipped with precision load cells, which measured the mechanical force applied to the sample. Based on the specifications given by the manufacturer, the load cells have an accuracy class 0.5, but the actual precision of the measurement revealed during calibration is significantly better. Since the relative error of the load cells is not known, but understood to be significantly better than the absolute error of 0.5 %, the error of the sample geometry measurement (±50 μm) becomes the dominating factor again and results in a systematic uncertainty in the mechanical stress of approximately ±2 %.

Strain

The sample's displacement was determined by an LVDT via a high-precision measurement amplifier. Previous investigations have shown that stress-strain measurements in this experimental arrangement have a maximum uncertainty of approximately ±5 % [386], originating from a combination of potential misalignments in the setup and the systematic error of the sample geometry.

Polarization

A data acquisition device measured the amplified voltage at the reference capacitor according to Figures 2.2 and 2.5, from which the polarization was calculated according to Equation 2.1. The uncertainty depends on the measurement range as well as on the actual device, e.g., an NI PCI data acquisition board or an analog input of one of the load frame's electronics, and is in any case negligible compared to the error caused by the measurement of the sample geometry. It is assumed that the error of the (measured) value of the capacitance of the reference capacitors is negligible and therefore, a systematic error of ±2 % could be expected.

Piezoelectric Coefficient d_{33}

According to Equation 2.3, the piezoelectric coefficient was calculated from the polarization and stress amplitudes detected by a built-in function of LabVIEW. It is not possible to give a reliable precision of this analysis and therefore, the range of the data point scattering was considered to be an appropriate measure of the uncertainty in d_{33} instead.

Elastic Modulus

The elastic modulus was measured by a commercial system and was calculated following a number of analyzing and filtering steps, which were built into the commercial system and not accessible to the user. In addition, there was no information about measurement accuracy provided by the manufacturer and therefore, is not possible to give an uncertainty of the measurement results. However, data point scattering gave a measure of the precision of the experiment. As such, these data are used only to discuss the temperature-dependent trend and not absolute values.

Temperature

An accurate measurement of the temperature is a very difficult task and needs to be treated very carefully. For example, a possible source of error could be that the thermocouple was located some millimeters away from the sample. Another issue was that thermocouples are known to age with time and temperature, however repeated experiments under the same conditions revealed sufficiently stable measurement results over the entire course of these studies. In this work, mostly type K thermocouples were used, which have a specified absolute accuracy of ±2.5 °C, which is believed to be systematic. However, comparative measurement revealed a significantly better precision, but it is unrealistic to give a definite number. Since this work will deal mainly with relative shifts of characteristic temperatures, the absolute accuracy is assumed to be a minor experimental problem.

3 Influence of Uniaxial Mechanical Stress on the Phase Transitions in Barium Titanate

3.1 Introduction

Barium titanate ($BaTiO_3$) is one of the most extensively investigated ferroelectric materials with a history of more than 70 years of research [55]. This has resulted in an enormous amount of publications directly about or related to $BaTiO_3$. Single crystalline as well as polycrystalline $BaTiO_3$ have been intensively studied and serve as a prototype ferroelectric perovskite material. The comparatively high permittivity of $BaTiO_3$ makes it important for applications like multilayer ceramic capacitors [75]. The implementation of the material is, however, limited by its relatively low Curie point at approximately 130 °C. Recent governmental restrictions on the usage of lead-containing materials [255] renewed interest in basic research of $BaTiO_3$, because of promising lead-free piezoelectric materials like NBT-xBT-yKNN and BZT-xBCT [148, 265, 272]. As previously shown in Section 1.8.1, $BaTiO_3$ shows three structural phase transitions between rhombohedral ($R3m$) and orthorhombic ($Amm2$), orthorhombic and tetragonal ($P4mm$), and tetragonal and cubic ($Pm\bar{3}m$) crystal symmetries at –90 °C, 0 °C, and 130 °C, respectively. The transition temperatures and the order of the phase transitions were found to depend on an external electric field as well as on an applied mechanical stress (see Sections 1.8.1 and 1.13).

A first theoretical analysis of the phase transition behavior and the corresponding changes in the dielectric and electromechanical properties of ferroelectrics was done by Devonshire, who used the phenomenological Landau-Ginzburg theory to describe the behavior of the ferroelectric material $BaTiO_3$ [83–85]. This so-called Landau-Ginzburg-Devonshire (LGD) theory, which has already been introduced in Section 1.8.3, is strictly only valid for monodomain single crystals and but has been used for analyzing the influence of electric fields and mechanical stresses on the phase transition behavior of ferroelectrics [97–99]. In addition to the theoretical description of phase transitions, the LGD theory is also capable of explaining changes in the order of the phase transitions that are induced by hydrostatic stress [339]. In this chapter, the LGD theory will be expanded in order to also account for the effect of a uniaxial stress on the phase transition behavior of $BaTiO_3$.

Section 3.2 combines temperature-dependent permittivity data of single crystal and polycrystalline $BaTiO_3$ under uniaxial mechanical compression with a phenomenological description of the observed change in the tetragonal-to-cubic phase transition of $BaTiO_3$ at the Curie point. To do so, stress-dependent Landau coefficients will be introduced in the Gibbs free energy function. The results of this analysis have been published in Schader *et al.*, Journal of Applied Physics 113, 174103 (2013) [387] and could be important for modeling the behavior of strained thins films [100, 388] or sensors [206, 214], which can be described as inherently operating under elevated mechanical preloads during application. In Section 3.3, an overview about recent temperature-dependent permittivity measurements will be given, which were intended to extend the discussion of the influence of a uniaxial mechanical load on the Curie point to the two other phase transition of polycrystalline $BaTiO_3$ occurring at lower temperatures. Finally, the temperature-dependent phase transition behavior of $BaTiO_3$ will be correlated to its ferroelastic behavior.

3.2 Influence of Uniaxial Mechanical Stress on the Curie Point of Single Crystal and Polycrystalline $BaTiO_3$

Commercial $BaTiO_3$ powder was used to produce cylindrical polycrystalline samples with a height of 6 mm and a diameter of 5.8 mm (see Section 2.1 and 2.2 for further details). The $BaTiO_3$ single crystals investigated in the study (SurfaceNet GmbH, Rheine, Germany) had dimensions of approximately 4.7 x 4.9 x 1 mm^3 and were oriented along the $<001>_{PC}$ crystallographic direction perpendicular to the 4.7 x 4.9 mm^2 surface. A uniaxial screw-driven load frame (see Section 2.4) applied compressive mechanical bias stresses between –0.8 MPa and –300 MPa to the polycrystalline material while heating the samples up to 200 °C with a rate of 3 °C/min. During the heating processes, the permittivity was measured at a frequency of 1 kHz by applying an oscillating voltage with a maximum amplitude of 1 V_{rms}. In the case of the $BaTiO_3$ single crystals, the heating rate was reduced to 0.5 °C/min in order to prevent cracking during the measurement and the applied mechanical bias stresses ranged from –0.9 MPa to –30 MPa.

3.2.1 Permittivity under Uniaxial Mechanical Compression

Figure 3.1 shows the temperature-dependent permittivity ε' of single crystal and polycrystalline $BaTiO_3$ at various compressive mechanical bias stresses. For the evaluation and analysis of the data, five measurements were done on polycrystalline $BaTiO_3$ at each stress to ensure repeatability. Only one measurement was done at mechanical load between –0.9 MPa and –30 MPa on $BaTiO_3$ single crystals because of the risk of cracking.

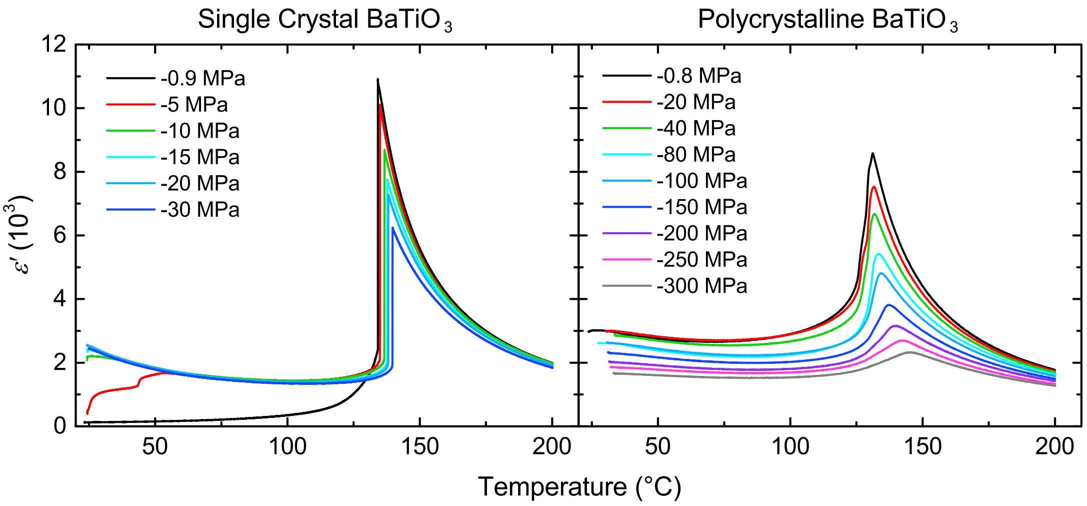

Figure 3.1: Permittivity ε' of single crystal and polycrystalline $BaTiO_3$ as a function temperature at various mechanical loads. A constant uniaxial compressive stress between –0.9 MPa and –30 MPa (single crystal $BaTiO_3$) and –0.8 MPa and –300 MPa (polycrystalline $BaTiO_3$) was applied. Small signal dielectric measurements were performed at 1 kHz during heating. (after Ref. [387])

The temperature-dependent permittivity of the polycrystalline $BaTiO_3$ at the lowest mechanical preload was found to be in good agreement with previously reported data [2, 60, 70]. With increasing temperature, an initial decrease in permittivity was observed for polycrystalline $BaTiO_3$ for all bias stresses. The reason for this behavior is the proximity of the orthorhombic-to-tetragonal phase transition occurring at approximately 0 °C, which is marked by a maximum in $\varepsilon'(T)$ as well [62]. With further increasing temperature, a peak in permittivity occurred at the Curie point (T_C), followed by a decrease in $\varepsilon'(T)$ with further heating in the paraelectric phase. The shoulder in the permittivity-temperature curve of the polycrystalline $BaTiO_3$ several degrees below T_C was due to differently sized grains in the sample. Abnormal grain growth during sintering resulted in grains with diameters up to 250 μm embedded in a matrix of grains with an average size of approximately 1.4 μm. Since there is a dependence of the Curie point of $BaTiO_3$ on the grain size, the shoulder in $\varepsilon'(T)$ below the peak could probably be attributed to the Curie point of the smaller grains of the matrix, whereas the main peak represented the phase transition temperature of the larger grains [64, 66, 389].

In the case of the $BaTiO_3$ single crystals, the observed permittivity-temperature curves were similar to those measured in pervious investigations on differently oriented crystals, especially regarding the sharp peak in $\varepsilon'(T)$ at the Curie point [54, 185, 390, 391]. A comparison of $\varepsilon'(T)$ for the $BaTiO_3$ single crystal in Figure 3.1 with experiments done by Meyerhofer [54] and Merz [392] indicates that the domains of the crystal were initially aligned parallel to the measurement and loading direction at –0.9 MPa preload. This configuration is schematically shown in Figure 3.2. With the application of a compressive uniaxial mechanical bias stress, severe changes of the temperature-dependent behavior of $BaTiO_3$ could be observed. A sufficiently large uniaxial stress causes ferroelastic switching of the domains to orientations perpendicular to the loading direction. As a result, the permittivity increases with the application of stress due to the anisotropy of ε' between the a- and the c-axes in tetragonal $BaTiO_3$ [54, 392], which can be seen in Figure 3.2 for the single crystal.

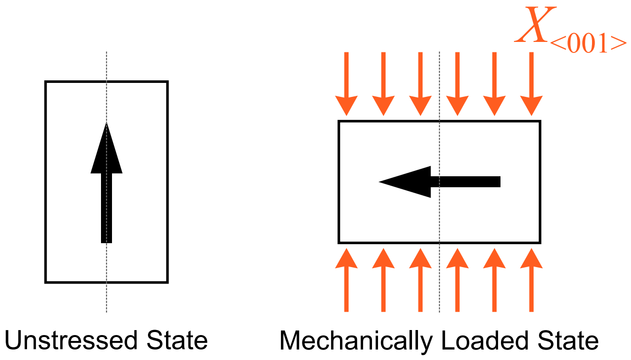

Figure 3.2: Schematic showing the polarization direction in stressed and unstressed $<001>_{PC}$ single crystal $BaTiO_3$. The permittivity was measured parallel to the dashed line, which is also parallel to the direction of applied compressive bias stress, $X_{<001>}$. (after Ref. [387])

It can be seen from the permittivity measurement on the $BaTiO_3$ single crystal at –5 MPa mechanical bias stress in Figure 3.1 that the stress necessary for domain switching, *i.e.* the coercive stress, was temperature-dependent. Below T_C, the permittivity showed a two-step increase before finally coinciding with the measurement curves at higher bias stresses. This was because the applied mechanical bias load (–5 MPa) was not large enough to completely switch all domains of the $BaTiO_3$ single crystal at room temperature. With increasing temperature, the coercive stress was sufficiently lowered allowing all domains to switch to orientations perpendicular to the loading direction. The stepwise increase in $\varepsilon'(T)$ due to the higher value of ε' in a-direction was finally completed at approximately 50 °C. A behavior similar to these findings could not be observed for experiments done at mechanical bias stresses above –5 MPa, which indicates that most of the domains were already aligned perpendicular to the measurement and loading direction at room temperature. Therefore, the temperature dependence of the permittivity in a-direction dominated the overall measured $\varepsilon'(T)$ of the $BaTiO_3$ single crystal in Figure 3.1. This finding is also supported by the initially decreasing ε' with increasing temperature in the vicinity of the orthorhombic-to-tetragonal phase transition at approximately 0 °C. It is known from previous experiments that this increase in $\varepsilon'(T)$ is pronounced along in the crystallographic a-direction [54, 392].

The application of a uniaxial mechanical bias stress did not change the overall shape of the permittivity-temperature curve of the $BaTiO_3$ single crystals (Figure 3.1). In particular, the sharpness of the peak at T_C remained unchanged even at a bias stress of –30 MPa and the discontinuity in $\varepsilon'(T)$ at T_C occurred within a temperature window of approximately 0.1 °C. However, the height of the permittivity peak was found to decrease with increasing mechanical bias load by 43 % between –0.9 MPa and –30 MPa bias stress levels. In addition, the peak was shifted to higher temperatures with increasing stress, which will be discussed in detail in the next subsection. The permittivity was found to decrease with increasing stress in the paraelectric region due to the converse electrostrictive effect [359, 393].

In contrast to the findings for the single crystals, polycrystalline $BaTiO_3$ showed a decrease in permittivity with increasing bias stress already in the ferroelectric phase below T_C, which is consistent with previous investigations [345, 359]. The value of ε' was found to decrease by 48 % between –0.8 MPa and –300 MPa at room temperature and the maximum in $\varepsilon'(T)$ at T_C was lowered by 73 % in the same stress region. Initially it would be expected that the permittivity increases with increasing stress due to the volume fraction of domains perpendicular to the loading direction increases with increasing uniaxial mechanical compression, similar to results for $BaTiO_3$ single crystal. In a polycrystalline material, however, the extrinsic contributions, *i.e.* domain wall oscillations, to the permittivity are comparatively large. With increasing mechanical load, single crystals can accommodate the arising internal stresses by domain switching. This mechanism is hindered in polycrystalline materials, which is why the domain walls are substantially clamped by the increasing mechanical compression. As a result, the permittivity is reduced [21, 394] and this effect outweighs the ferroelastic reorientation of domains. In addition, it can be shown with LGD theory that the a- and the c-direction of tetragonal $BaTiO_3$ possess a different stress dependence of the intrinsic permittivity. The permittivity in c-direction increases with increasing stress, whereas the value in a-direction is lowered [359]. Since the latter effect is stronger than the former, this results in a net decrease of the intrinsic contribution to ε' with increasing mechanical compression. Like in single crystal BaTiO3, the decrease of ε' with increasing uniaxial mechanical compression in the paraelectric region above T_C can be explained with the converse electrostrictive effect [359, 393].

The Curie point of polycrystalline $BaTiO_3$ was found to shift to higher temperatures with increasing mechanical stress similar to the observations in single crystal $BaTiO_3$ and consistent with previous reports [346]. It is apparent from Figure 3.1 that the permittivity peak at T_C of polycrystalline $BaTiO_3$ was broader than the sharp peak of the single crystalline material. The randomly oriented grains in the polycrystalline material possessed different stress states due to variations in grain-to-grain crystallographic orientations that lead to internal stresses. Hence, the Curie point is locally increased or decreased, depending on the stress state of the individual grains. This can be thought of as a distribution of transition temperatures in the sample, which results in the observed broader permittivity peak since not all grains undergo the ferroelectric-paraelectric phase transition at the same temperature. Externally applied uniaxial mechanical stresses act to alter this distribution of transition temperatures, because it changes the stress states of the grains, which are all differently oriented relative to the loading direction. As a consequence, the permittivity peak broadens even more for polycrystalline samples with increasing uniaxial mechanical compression in addition to shifting its location to higher temperatures.

Above the Curie point in the paraelectric region, the temperature-dependent permittivity of both single crystalline and polycrystalline $BaTiO_3$ obeyed the Curie-Weiss law (Equation 1.13). The definition of the parameters C and θ is shown in Figure 3.3 on a representative permittivity-temperature curve. In order to determine C and θ, the inverse permittivity was plotted as a function of temperature and a linear regression was performed in the paraelectric region between 170 °C and 200 °C. The inverse permittivity was found to be sufficiently linear in this temperature interval for all mechanical bias stresses.

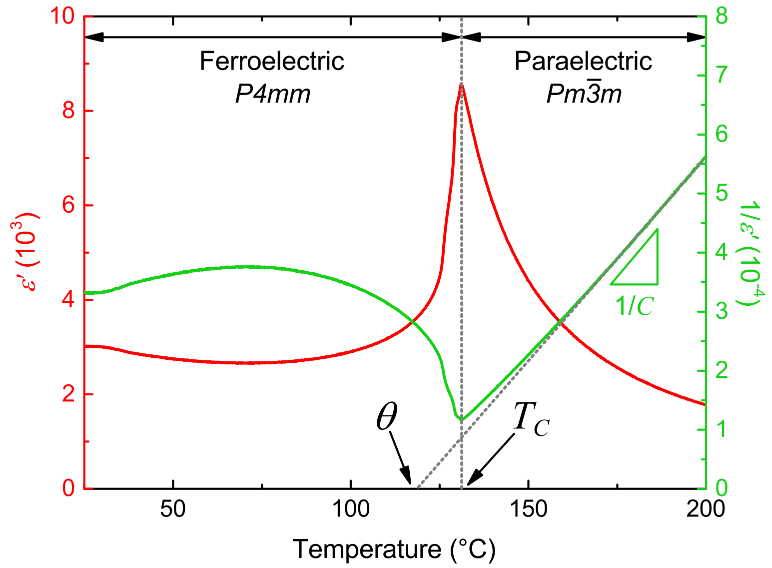

Figure 3.3: Permittivity ε' of polycrystalline $BaTiO_3$ as a function of temperature at −0.8 MPa mechanical prestress. The Curie point T_C was determined from the maximum of the permittivity curve. The Curie-Weiss temperature θ and the Curie constant C were obtained from linear regression fits to plots of the inverse permittivity versus temperature at 170 °C < T < 200 °C. (after Ref. [387])

Previous investigations on $BaTiO_3$ single crystals suggested that a uniaxial mechanical stress could lead to a diffuse phase transition at the Curie point [347]. In that case, the Curie-Weiss law in Equation 1.13 would not be valid at higher stresses and both C and θ could not be determined with the procedure shown in Figure 3.3. In order to elucidate this in more detail, the high-temperature dielectric properties of $BaTiO_3$ in the paraelectric phase were characterized with a modified Curie-Weiss law, which was proposed by Uchino and Nomura [395] for describing the $\varepsilon'(T)$ behavior of materials with a diffuse phase transition as well as normal ferroelectrics without a diffuse transition, such as pure, unstressed $BaTiO_3$:

$$\frac{1}{\varepsilon'} - \frac{1}{\varepsilon'_m} = \frac{K}{(T - T_m)^{\gamma}}, \tag{3.1}$$

where ε'_m is the maximum permittivity at T_m, K is a constant, and γ is the critical exponent, which can have values between $\gamma = 1$ (no diffuse transition) and $\gamma = 2$ (complete diffuse transition). Both parameters γ and K were determined by a linear regression of $\ln\left(1/\varepsilon' - 1/\varepsilon'_m\right)$ as a function of $\ln(T - T_m)$ in the paraelectric region for all tested compressive mechanical bias stresses. The resultant stress dependence of the exponent γ for both single crystal and polycrystalline $BaTiO_3$ is shown in Figure 3.4.

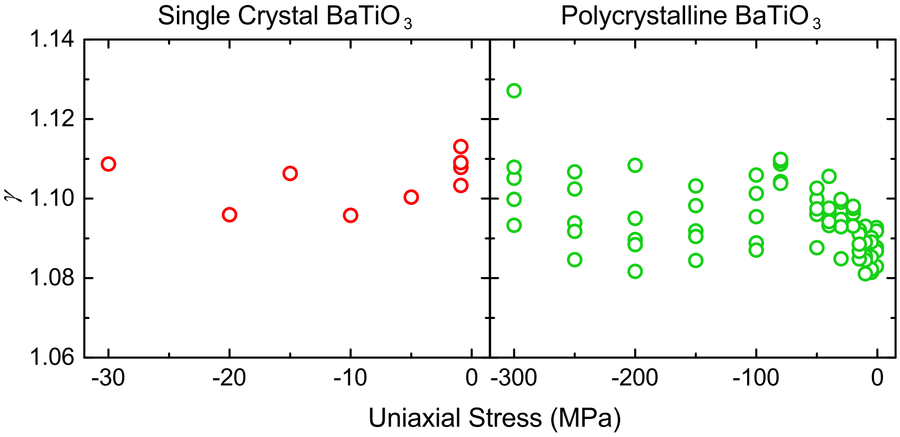

Figure 3.4: Exponent γ in Equation 3.1 of single crystal and polycrystalline $BaTiO_3$ as a function of compressive mechanical bias stress. In the case of the polycrystalline samples five measurements were carried out at each load step, whereas this was done only for the measurement at –0.9 MPa in the case of single crystal $BaTiO_3$. (after Ref. [387])

The stress-free value of γ was determined to approximately 1.11 and 1.09 for single crystal and polycrystalline $BaTiO_3$, respectively, which was in good agreement with the results of Uchino and Nomura [395]. Nearly no change in γ with increasing mechanical bias stress could be found for the single crystal material, whereas the polycrystalline $BaTiO_3$ showed a weak increase in γ with increasing stress up to –50 MPa. These results indicate that although the tetragonal-to-cubic phase transition in $BaTiO_3$ revealed to be diffuse, the Curie-Weiss law in Equation 1.13 was sufficiently obeyed in the paraelectric phase at all stress levels. Therefore, the Curie-Weiss temperature and the Curie constant could be correctly determined from Equation 1.13.

In addition to the strong discontinuity in $\varepsilon'(T)$ at the Curie point, the elastic properties of $BaTiO_3$ also changed significantly in the vicinity of the phase transition temperature. Figure 3.5 shows a comparison of the temperature-dependent permittivity and the elastic modulus E of polycrystalline $BaTiO_3$. The latter measurement was performed on a bar-shaped sample by using acoustic emission spectroscopy (see Section 2.2 and Section 2.6 for further details) during heating the sample up to 800 °C with a heating rate of 2 °C/min.

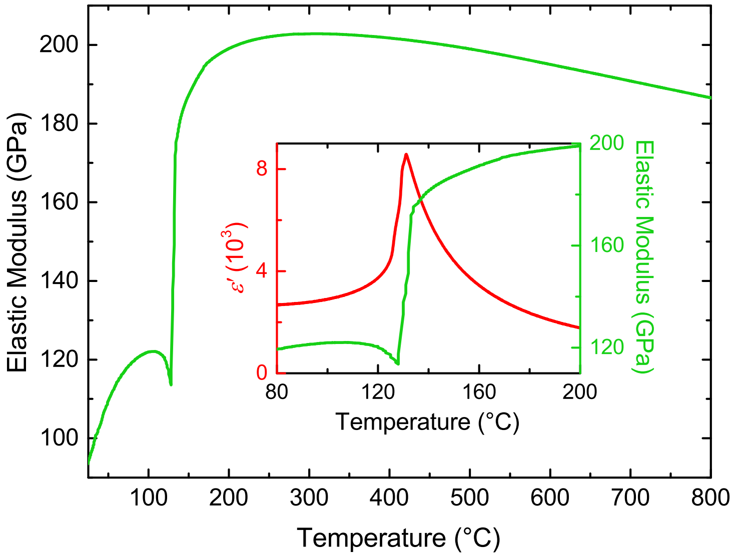

Figure 3.5: Elastic modulus E and permittivity ε' of polycrystalline $BaTiO_3$ as a function of temperature.

The elastic modulus showed an initial increase with increasing temperature in the ferroelectric phase below T_C, which was again most likely due to the vicinity of the orthorhombic-to-tetragonal phase transition [396]. At the Curie point, the material revealed a significant softening followed by a sharp increase in E. Interestingly, $E(T)$ was found to change in slope over a broad temperature region with further heating until reaching a linear decrease with increasing temperature at approximately 520 °C. A reason for that could be that polar (nano)regions existed above T_C, resulting in a gradual change in the elastic properties [397–400].

3.2.2 Influence of Compressive Stress on the Order of the Ferroelectric-to-Paraelectric Transition

It is well known from previous reports that the ferroelectric-to-paraelectric phase transition of $BaTiO_3$ is a first order phase transition [2]. One of the characteristic observations for a first order phase transition is that the Curie point and the Curie-Weiss temperature in Equation 1.13 do not coincide, as in the case of a second order phase transition. Figure 3.6 shows the Curie point and

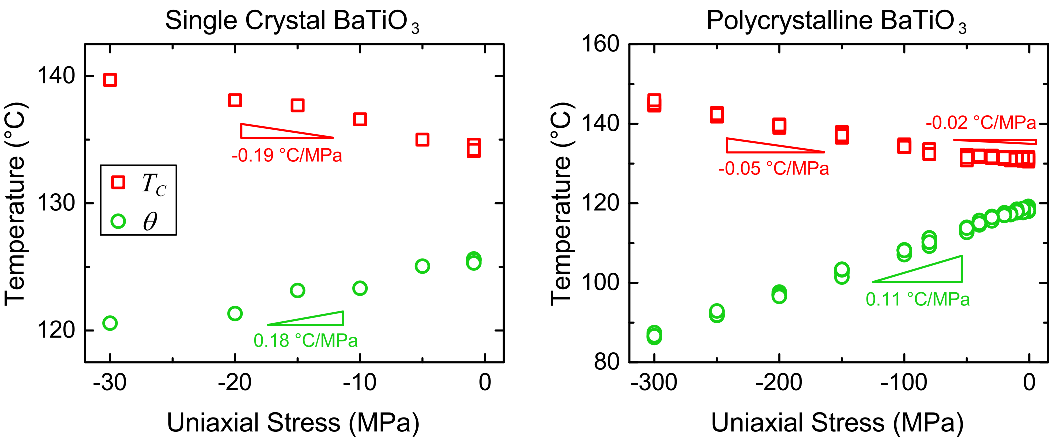

Figure 3.6: Shift of Curie point T_C and Curie-Weiss temperature θ of single crystal and polycrystalline $BaTiO_3$ due to uniaxial mechanical compressive stress. In the case of the polycrystalline samples five measurements were carried out at each load step to ensure repeatability, whereas this was done only for the measurement at –0.9 MPa in the case of single crystal $BaTiO_3$. (after Ref. [387])

the Curie-Weiss temperature of single crystal and polycrystalline $BaTiO_3$ as a function of uniaxial mechanical compression.

As already seen qualitatively in Figure 3.1, the Curie point was shifted to higher temperatures with increasing mechanical compression for both single crystal and polycrystalline $BaTiO_3$. In the case of the $BaTiO_3$ single crystal, a maximum increase in T_C of 5.6 °C was determined between the measurements at –0.9 MPa and –30 MPa mechanical bias stress. The zero-stress value of T_C was 134.2 °C on average, whereas the Curie-Weiss temperature was determined to be 125.6 °C with a maximum shift of –5 °C between the zero-stress condition at –0.9 MPa and the measurement at –30 MPa. Figure 3.6 shows that both T_C and θ have a linear increase and decrease, respectively, with increasing compressive mechanical stress X. This resulted in a in $\mathrm{d}T_C/\mathrm{d}X = -0.19$ °C/MPa and in $\mathrm{d}\theta/\mathrm{d}X = 0.18$ °C/MPa. Please note that the signs for both rates represent not the intuitive but rather the mathematically correct indication, because a uniaxial compressive stress usually has a negative sign and the mathematically correct values of $\mathrm{d}T_C/\mathrm{d}X$ and $\mathrm{d}\theta/\mathrm{d}X$ are required for the phenomenological analysis in Section 3.2.3.

The polycrystalline $BaTiO_3$ showed the same overall trend in the stress dependence of T_C and θ. At –0.8 MPa mechanical preload, the Curie point was found to be 131.1 °C and increased by 13.9 °C at a mechanical bias stress of –300 MPa. In contrast to the observation for the $BaTiO_3$ single crystals, the stress dependence of T_C was not linear and showed a quadric-like behavior with an apparent change in stress dependence at a mechanical bias stress of –50 MPa. In the low- and high-stress regime, $\mathrm{d}T_C/\mathrm{d}X$ could be determined to –0.02 °C/MPa and to –0.05 °C/MPa, respectively, which is four to ten times smaller than the $\mathrm{d}T_C/\mathrm{d}X$ found in the single crystal material. Interestingly, the Curie-Weiss temperature did not show the same two-regime behavior and, within a bias stress range of –0.8 MPa and –300 MPa, the Curie-Weiss temperature (118.6 °C at –0.8 MPa preload) decreased by 31.8 °C, revealing a linear $d\theta/dX$ of 0.11 °C/MPa.

As expected for a first order transition, T_C and θ did not coincide for both single crystal and polycrystalline material. The difference of these two parameters was actually found to increase with applied compressive mechanical bias stress. This resulted also in the observed decrease of the maximum permittivity at T_C according to the Curie-Weiss law in Equation 1.13 [71] and in an increased first order nature of the phase transition with increasing mechanical compression. In contrast, previous publications reported a change from a first order to a second order phase transition in $BaTiO_3$ by applying a sufficiently large hydrostatic pressure [333, 334, 336, 339]. This was experimentally indicated by a by the vanishing of the difference between T_C and θ [336].

The Curie constant C of single crystal and polycrystalline $BaTiO_3$ was determined for all mechanical bias loads by a linear fit of the temperature-dependent inverse permittivity between 170 °C and 200 °C, where $1/\varepsilon'$ was found to be a linear function of temperature for all stresses. No significant stress dependence of C could be found in the case of the $BaTiO_3$ single crystals within the resolution of the measurement, as it is depicted in Figure 3.7. A similar observation was made for the polycrystalline material below –50 MPa mechanical bias stress. However, a decrease by approximately 3 % on average was found with further increasing stress.

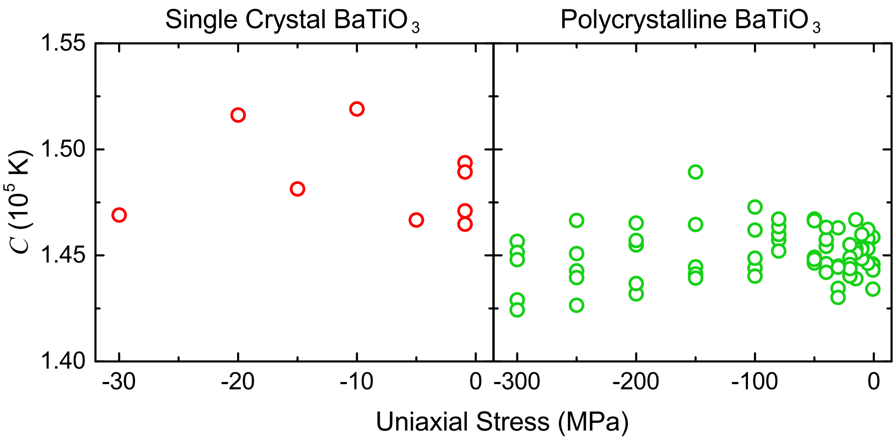

Figure 3.7: The Curie constant C as a function of uniaxial mechanical stress for single crystal and polycrystalline $BaTiO_3$. (after Ref. [387])

3.2.3 Thermodynamic Analysis

In this section, a modification of the LGD theory developed by Prof. Dr. George A. Rossetti, Jr., (University of Connecticut, Storrs, Connecticut, USA) was implemented in order to describe the phase transition behavior of single crystalline and polycrystalline $BaTiO_3$ under the application of compressive uniaxial mechanical stress. Since this theory is strictly only valid for monodomain single crystals, the calculations will firstly focus on single crystalline barium titanate. According to Devonshire [83, 84], the Gibbs free energy $G(T,X,P)$ can be expressed as the sum of the temperature- and polarization-dependent Landau potential $G_L(T,P)$, the stress-dependent elastic energy $G_E(X)$, and the energy $G_C(X,P)$, which accounts for the electrostrictive coupling between stress X and spontaneous polarization P:

$$G(T,X,P) = G_L(T,P) + G_E(X) + G_C(X,P). \tag{3.2}$$

The Landau potential $G_L(T,P)$ is expanded in its components up to the sixth order for this analysis

$$\begin{aligned} G_L(T,P) = {} & \frac{1}{2}\chi(T)\ \left(P_1^2+P_2^2+P_3^2\right) + \frac{1}{4}\xi\left(P_1^4+P_2^4+P_3^4\right) + \frac{1}{2}\xi'\left(P_1^2P_2^2+P_2^2P_3^2+P_3^2P_1^2\right) \\ & + \frac{1}{6}\zeta\left(P_1^6+P_2^6+P_3^6\right) + \frac{1}{2}\zeta'\left[P_1^4\left(P_2^2+P_3^2\right)+P_2^4\left(P_3^2+P_1^2\right)+P_3^4\left(P_1^2+P_2^2\right)\right] \\ & + \zeta''\left(P_1^2P_2^2P_3^2\right), \end{aligned} \tag{3.3}$$

where χ, ξ, and ζ are the dielectric stiffness and the higher-order stiffness coefficients at constant stress. The elastic contributions $G_E(X)$ to the Gibbs free energy are represented by the Hooke's law

$$\begin{aligned} G_E(X) = {} & -\frac{1}{2}s_{11}\left(X_1^2+X_2^2+X_3^2\right) - s_{12}\left(X_1X_2+X_2X_3+X_3X_1\right) \\ & -\frac{1}{2}s_{44}\left(X_4^2+X_5^2+X_6^2\right), \end{aligned} \tag{3.4}$$

where s_{ij} are the elastic compliances at constant polarization. It is important to note again that compressive stresses X_i are defined here are negative values. Finally, the lowest-order expansion of the electrostrictive energy contribution $G_C(X,P)$ is given by

$$\begin{aligned} G_C(X,P) = {} & -Q_{11}\left(X_1P_1^2+X_2P_2^2+X_3P_3^2\right) \\ & -Q_{12}\left[X_1\left(P_2^2+P_3^2\right)+X_2\left(P_3^2+P_1^2\right)+X_3\left(P_1^2+P_2^2\right)\right] \\ & -Q_{44}\left(X_4P_2P_3+X_5P_3P_1+X_6P_1P_2\right), \end{aligned} \tag{3.5}$$

where Q_{ij} are the electrostrictive coefficients in Voigt notation (see Section 1.14).

In general, the usual form of the Gibbs free energy given in Equation 3.2 is not suitable for describing stress-induced changes in the order of the phase transition unless higher-order elastic or electrostrictive terms are included. In this analysis, a different approach is chosen to describe the observed increase in first order nature of the ferroelectric-to-paraelectric phase transition of $BaTiO_3$ due to a uniaxial stress, namely by introducing stress-dependent Landau parameters in Equation 3.3. Doing so, this analysis will reveal additional terms accounting for the stress dependence of the phase transition. Equation 3.2 is therefore changed to the form

$$G(T,X,P) = G_L(T,X,P) + G_E(X). \tag{3.6}$$

The tetragonal symmetry of $BaTiO_3$ together with the uniaxial compressive stress, which will now be denoted simply by X, result in the reduction of the terms in the Equations 3.3 and 3.4. A substitution of these equations into Equation 3.6 gives finally:

$$G(T,X,P) = \frac{1}{2}\chi(X,T)P_3^2 + \frac{1}{4}\xi(X)P_3^4 + \frac{1}{6}\zeta(X)P_3^6 - \frac{1}{2}s_{11}X^2. \tag{3.7}$$

All Landau coefficients in this equation can be obtained by expanding them in a Taylor series around $X = 0$. The quadratic coefficient χ usually possesses a special form to account for the Curie-Weiss law, which should directly follow from the second partial derivative of Equation 3.7 with respect to polarization in the cubic phase. Therefore,

$$\chi(T,X) = \chi_0(X)\ [T - \theta(X)] \tag{3.8}$$

and

$$\chi_0(X) = \frac{1}{\varepsilon_0 C(X)}, \tag{3.9}$$

where this term is also given by

$$\chi_0(X) = \chi_0(0) + X\left(\frac{\partial \chi_0}{\partial X}\right)_{X=0}. \tag{3.10}$$

The Curie constant $C(X)$ in Equation 3.9 is generally stress-dependent. However, it can be seen in Figure 3.7 that the experiments on $BaTiO_3$ single crystals did not show such a dependence, which is why $C(X)$ is assumed to be stress-independent, and hence $\chi_0(X) \approx \chi_0(0) = \chi_0$. In contrast, the Curie-Weiss temperature θ was found to be a function of stress and can be also expressed in a lower-order expansion

$$\theta(X) = \theta(0) + X \left(\frac{\partial \theta}{\partial X} \right)_{X=0} . \tag{3.11}$$

Figure 3.6 shows that the Curie-Weiss temperature of the $BaTiO_3$ single crystal decreased linearly with increasing mechanical compression, *i.e.* $\partial \theta / \partial X > 0$ in Equation 3.11.

In the framework of the LGD theory, the quartic Landau coefficient ξ in Equation 3.7 controls the order of the phase transition. Therefore, this coefficient also requires a stress dependence in order to account for the observed increased first order nature of the ferroelectric-to-paraelectric phase transition in $BaTiO_3$ with increasing uniaxial stress. Similar to the quadratic coefficient, a lowest-order approximation of the quartic coefficient gives

$$\xi(X) = \xi(0) + X \left(\frac{\partial \xi}{\partial X} \right)_{X=0} . \tag{3.12}$$

An increase in the first order nature with increasing stress, experimentally determined by a increase in the difference between T_C and θ, necessitates

$$\xi(0) < 0 \quad \text{and} \quad \left(\frac{\partial \xi}{\partial X} \right)_{X=0} > 0. \tag{3.13}$$

Since this analysis focuses only on the higher-temperature phase transition at the Curie point of $BaTiO_3$, the temperature dependence of ξ can be neglected as it is already expressed in Equation 3.7. The sextic coefficient ζ in Equation 3.7 can also be expanded in a Taylor series, but for simplicity no stress dependence will be assumed

$$\zeta(X) = \zeta(0) + X \left(\frac{\partial \zeta}{\partial X} \right)_{X=0} \quad \text{with} \quad \left(\frac{\partial \zeta}{\partial X} \right)_{X=0} \approx 0. \tag{3.14}$$

The condition $\zeta(0) > 0$ ensures that the free energy in Equation 3.7 will result in finite minima without diverging into negative in the case of a first order phase transition. A substitution of the Equations 3.8, 3.11, 3.12, and 3.14 into Equation 3.7 finally results in

$$G(T,X,P) = \frac{1}{2}\chi_0 [T - \theta_0 - \lambda_1 X] P_3^2 + \frac{1}{4} [\xi_0 + \lambda_2 X] P_3^4 + \frac{1}{6}\zeta_0 P_3^6 - \frac{1}{2} s_{11} X^2, \tag{3.15}$$

where $\lambda_1 = \partial \theta / \partial X$ and $\lambda_2 = \partial \xi / \partial X$. The parameters χ_0, ξ_0, and ζ_0 represent the respective stress-free Landau coefficients. It is apparent from Equation 3.15 that λ_1 plays the role of the classical electrostrictive contributions, whereas λ_2 possesses the form of a higher-order electrostrictive term.

In order to calculate the Curie point as a function of uniaxial stress, the free energy in Equation 3.15 is evaluated at $T = T_C$, such that

$$G(T,X,P) = 0. \tag{3.16}$$

Typically in LGD theory, G is defined as the energy difference between the cubic and the non-cubic state of a crystal. Since no electric field was applied during the experiments, it also follows that

$$\frac{\partial G(T,X,P)}{\partial P} = E = 0. \tag{3.17}$$

Solving Equations 3.16 and 3.17 with respect to polarization and choosing the nontrivial solution $P \neq 0$ at T_C, which exists only in the case of a first order phase transition, results in an expression for the spontaneous polarization P_S right at the Curie point

$$P_s^2 = -\frac{3}{4}\frac{[\xi(X)]^2}{\zeta(X)}. \tag{3.18}$$

Inserting Equation 3.18 into Equation 3.16 finally gives the standard expression for the stress-dependent Curie point

$$T_C(X) = \theta(X) + \frac{3}{16}\frac{[\xi(X)]^2}{\chi_0\zeta_0}. \tag{3.19}$$

It was observed from the experimental data in Figure 3.6 that the Curie-Weiss temperature is a linear function of uniaxial stress. This results then in a quadratic stress dependence of the Curie point according to Equation 3.19, which therefore depends on the parameter $\xi(X)$. In order to calculate the value of λ_2, Equation 3.15 and Equation 3.19 are combined and the resultant equation is differentiated with respect to stress:

$$\frac{\partial T_C(X)}{\partial X} - \frac{\partial \theta(X)}{\partial X} = \frac{3}{8\chi_0\zeta_0}\left[\xi_0\lambda_2 + \lambda_2^2 X\right], \tag{3.20}$$

which reduces in the low-stress limit ($X \to 0$) to

$$\frac{\partial T_C(X)}{\partial X} - \frac{\partial \theta(X)}{\partial X} \cong \frac{3\xi_0}{8\chi_0\zeta_0}\lambda_2. \tag{3.21}$$

λ_1 and λ_2 can be found by using the experimental data. In the low-stress limit, λ_2 is directly given by Equation 3.21, whereas for higher uniaxial stresses the quadratic term $\lambda_2^2 X$ in Equation 3.20 cannot be neglected. For determining λ_2 with Equation 3.21, the stress-free Landau parameters χ_0,

Table 3.1: Material parameters for single crystal $BaTiO_3$.

Material Parameter	Value	Unit
χ_0	7.58×10^5	$V\,m\,C^{-1}\,K^{-1}$
ξ_0	-8.20×10^8	$V\,m^5\,C^{-3}$
ζ_0	1.90×10^{10}	$V\,m^9\,C^{-5}$
$(T_C - \theta_0)$	8.8	K
C	1.49×10^5	K
P_0	0.18 [a]	$C\,m^{-2}$

[a] Ref. [50]

ξ_0, and ζ_0 were needed, which could be directly calculated from the experimental data by using Equation 3.10 and the following standard relations [4]

$$\xi_0 = -4\frac{T_C - \theta_0}{\varepsilon_0 C P_0^2}, \tag{3.22}$$

$$\zeta_0 = 3\frac{T_C - \theta_0}{\varepsilon_0 C P_0^4}. \tag{3.23}$$

All values used for calculating ξ_0 and ζ_0 of single crystal $BaTiO_3$ are given in Table 3.1

The resultant values of the Landau parameters were in good agreement with previously reported calculations [401]. λ_1 is related to $\theta(X)$ via Equation 3.11 and is directly given by the rate of decrease of the Curie-Weiss temperature with respect to stress for both single crystal and polycrystalline $BaTiO_3$. In order to determine λ_2 in the high-stress limit, Equation 3.19 was fitted to the measured stress-dependent values of T_C and θ by using the single crystal material parameters given in Table 3.1. This simplified approach implies that the difference in the phenomenological theory between single crystal and polycrystalline material is represented by the different stress dependences of the Landau coefficients. Table 3.2 finally gives the calculated results for all λ_1 and λ_2.

With the values of Table 3.2 it was possible to calculate the Curie point and the Curie-Weiss temperature for single crystal and polycrystalline $BaTiO_3$. A comparison of the experimental data with the calculated values is depicted in Figure 3.8 and reveals good qualitative agreement. In particular, the linear behavior of θ and the quadratic shift of T_C with respect to uniaxial stress was correctly reproduced by the calculations. In the case of the single crystal $BaTiO_3$, the theoretical results quantitatively matched the experimental data. The discrepancy between the measurement

Table 3.2: The parameters λ_1 and λ_2 for single crystal and polycrystalline $BaTiO_3$.

Material Parameter	Method	Single Crystal	Polycrystalline	Unit
λ_1	Fit	1.82×10^{-7}	1.08×10^{-7}	$K\,m^2\,N^{-1}$
λ_2	Fit (high-stress limit)	14.20	4.65	$m^8\,C^{-4}$
λ_2	Predicted (low-stress limit)	17.42	5.97	$m^8\,C^{-4}$

and the calculated values for T_C in the low-stress limit (dotted line in Figure 3.8) originated from the neglect of the quadratic term in Equation 3.20. However, a good agreement of theory and experiment was gained for the single crystal $BaTiO_3$ in the high-stress limit.

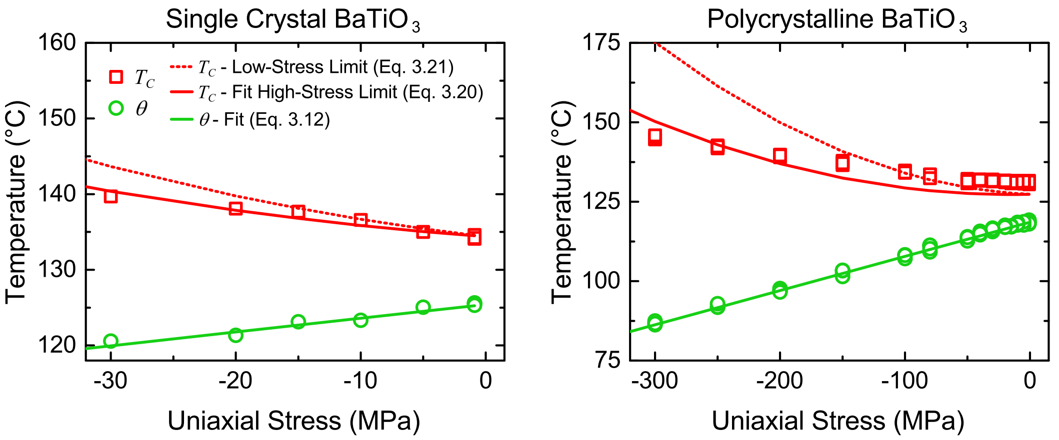

Figure 3.8: Comparison between experimentally determined stress-dependent Curie point T_C (red squares) and Curie-Weiss temperature θ (green circles) of $BaTiO_3$ and model predictions for single crystal and polycrystalline samples. For comparison, predictions from both high- and low-stress relations are shown. (after Ref. [387])

A different situation was observed for the polycrystalline material, which showed a good qualitative match between calculated and measured $T_C(X)$ only at stresses below –50 MPa. At higher mechanical loads, the computed and the measured values differed significantly. Some reasons for that could be that no averaging in the macroscopic behavior of the polycrystalline $BaTiO_3$ samples was taken into account by the calculations, which used the single crystal material parameters in Table 3.1. In addition, radial stresses in the sample due to clamping and friction in the experimental setup might have also played a role for the deviations between experiment and theory.

It could be concluded form the above results, that the parameter λ_1, *i.e.* the electrostrictive coupling, controls the shift of the Curie-Weiss temperature, whereas the parameter λ_2 influences the nature of the phase transition. In the end, the stress dependence of the Curie point is influenced by both λ_1 and λ_2 and especially the latter turned out to be important at higher uniaxial stress above –50 MPa.

3.3 Low-Temperature Phase Transitions and Ferroelastic Behavior of Polycyrstalline $BaTiO_3$

As shown in the previous section, applied compressive stress can influence the ferroelectric-paraelectric phase transition behavior of single crystal and polycrystalline $BaTiO_3$. The aim of this section is to investigate the role of stress on the lower-temperature structural phase transitions between the rhombohedral, orthorhombic, and tetragonal phases. The temperature-dependent permittivity of polycrystalline barium titanate was measured again at various uniaxial mechanical bias stresses between –5 MPa and –500 MPa between –150 °C and 250 °C. A uniaxial load frame equipped with a liquid nitrogen-cooled temperature chamber was used (see Section 2.4), which initially heated up the samples to 250 °C at –5 MPa preload before the actual mechanical bias stress was applied at 250 °C in the cubic phase. After that, the temperature-dependent permittivity was measured at a frequency of 1 kHz during cooling to –50 °C with a rate of 2 °C/min. Figure 3.9 shows the measurement results for polycrystalline $BaTiO_3$.

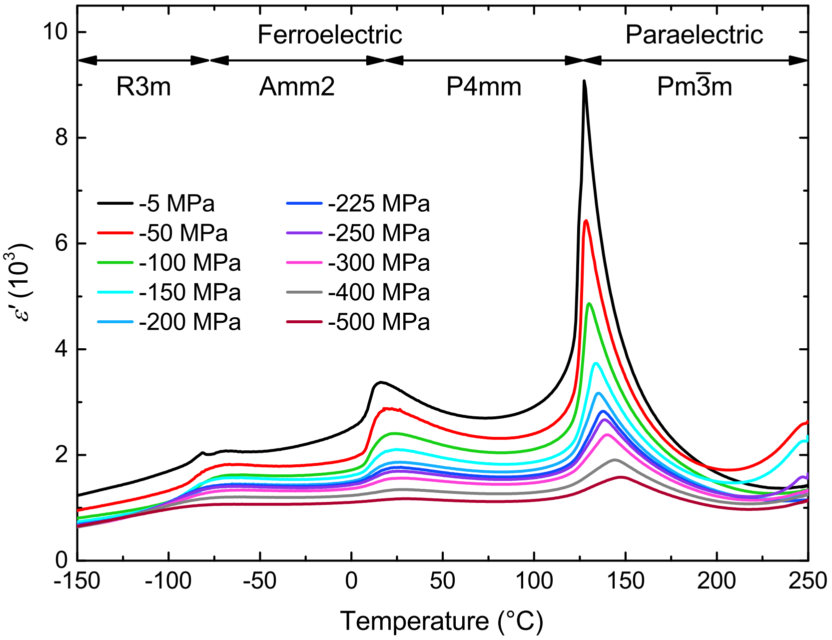

Figure 3.9: Temperature-dependent permittivity of polycrystalline barium titanate measured at 1 kHz during cooling at various constant uniaxial mechanical stresses.

Similar to the tetragonal-to-cubic phase transition at the Curie point, the lower-temperature phase transitions into the orthorhombic and the rhombohedral phase were accompanied by a maxima in the temperature-dependent permittivity as well. However, these maxima were found to be less pronounced, which is in good agreement with previous reports on single crystal $BaTiO_3$ [392]. The application of uniaxial mechanical bias stresses resulted in a decrease of the permittivity at all temperatures primarily due to domain wall clamping. At the same time, the maxima in $\varepsilon'(T)$ at the phase transition temperatures became broader and were shifted with increasing stress toward higher temperatures. In particular, the maxima in $\varepsilon'(T)$ of the lower-temperature phase transitions were not as sharp as the permittivity peak at the Curie point and showed a significant broadening with increasing mechanical compression. The phase transition temperatures of polycrystalline $BaTiO_3$ were determined by the position of the maxima in $\varepsilon'(T)$ during cooling and the results are depicted in Figure 3.10 together with the permittivity-temperature curve measured at –5 MPa.

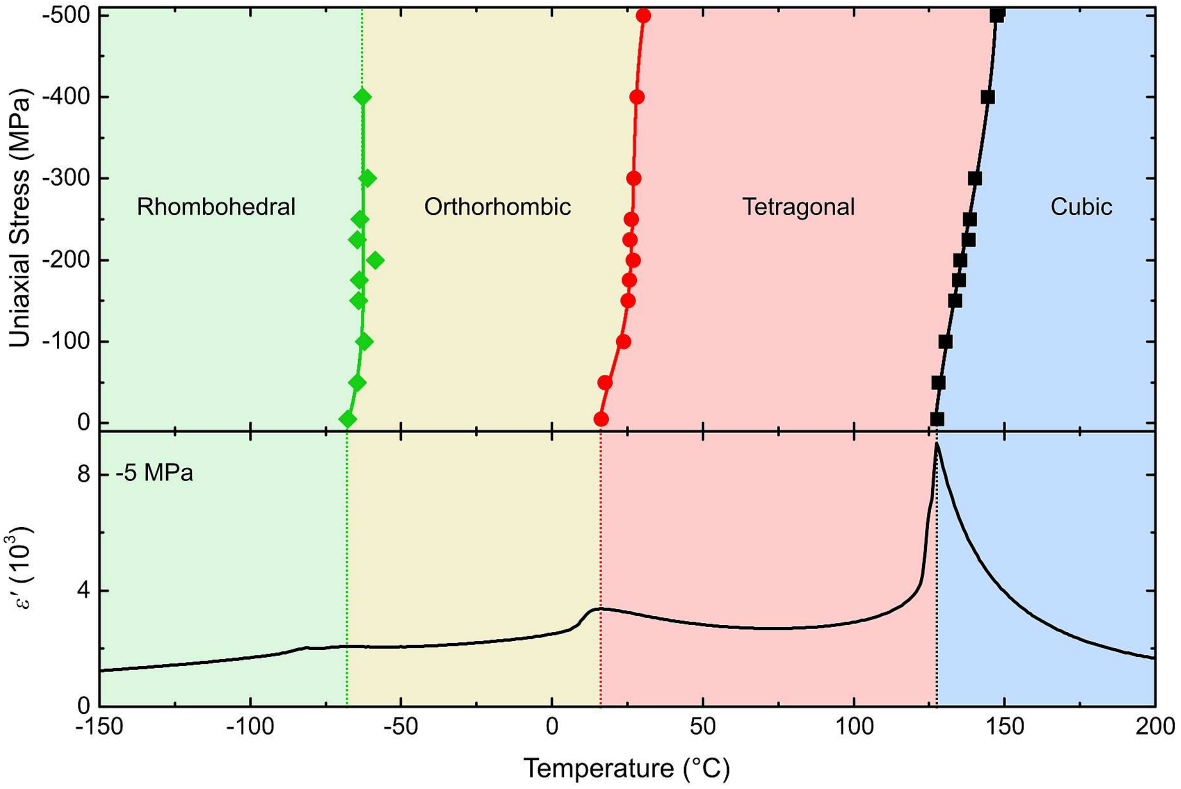

Figure 3.10: Stress-dependent phase diagram of polycrystalline $BaTiO_3$. The phase transition temperatures were determined by the maxima of the $\varepsilon'(T)$ curves shown in Figure 3.9 during cooling. This diagram should be read in temperature direction only. For comparison, the temperature-dependent permittivity of $BaTiO_3$ measured at –5 MPa mechanical bias preload is shown as well.

The experiments revealed that the lower-temperature ferroelectric-to-ferroelectric phase transitions were less stress sensitive than the ferroelectric-to-paraelectric transition. Whereas a maximum increase of the Curie point of 16.7 °C was observed between the measurements at –5 MPa and –400 MPa, the tetragonal-to-orthorhombic and the orthorhombic-to-rhombohedral phase transition temperatures were increased by 11.9 °C and 4.9 °C, respectively, in the same stress interval.

Sinyakov *et al.* found a comparable shift of the tetragonal-to-orthorhombic transition of single crystal $BaTiO_3$ with applied uniaxial stress, although the temperature of the orthorhombic-to-rhombohedral transition decreased with increasing stress in their experiments [51]. Similar to the observations made in Section 3.2 for the stress-dependent Curie point, Figure 3.10 shows that differences in the stress dependence of the lower-temperature phase transitions existed between the stresses below approximately –100 MPa and the high-stress regime. These observations could also be attributed to clamping and frictional effects between the samples and the tungsten carbide pressing tools, resulting in an addition radial stress distribution and therefore in a not purely uniaxial loading condition. This could alter the measured phase transition temperatures.

Additional temperature-dependent stress-strain measurements were performed on polycrystalline $BaTiO_3$ in order to correlate the ferroelastic properties with the phase transition behavior. Picht *et al.* have already done similar investigations for the ferroelectric-to-paraelectric phase transition [349], which will be expanded in this work to the lower-temperature phase transitions. Cylindrically shaped polycrystalline $BaTiO_3$ samples (see Section 2.2) were mechanically characterized at numerous constant temperatures between –150 °C and 25 °C. A uniaxial screw-driven load frame (see Section 2.4) applied a maximum load of –400 MPa with a rate of 4 MPa/s on the samples. The resultant stress-strain curves are depicted in Figure 3.11 for five representative temperatures.

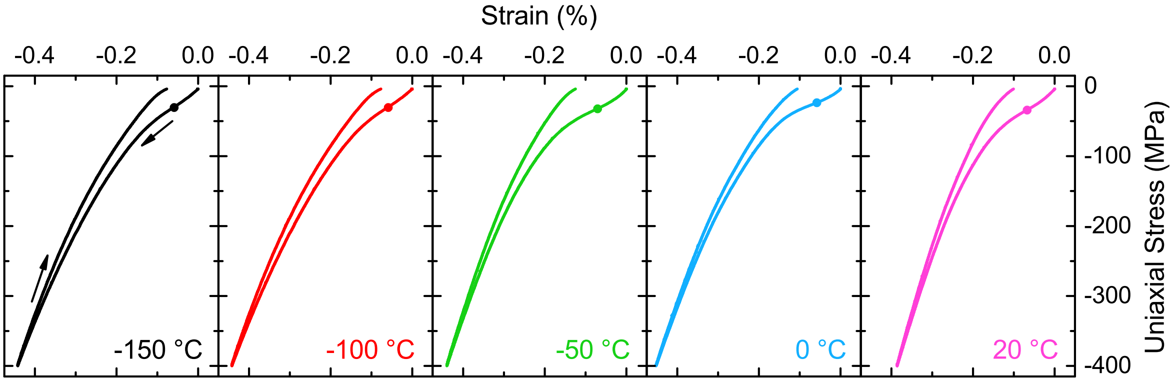

Figure 3.11: Stress-strain measurements performed on polycrystalline $BaTiO_3$ at various constant temperatures. The arrows in the diagram for –150 °C indicate the loading and unloading direction, whereas the circles represent the coercive stress, *i.e.* the inflection point of the curves.

Typical nonlinear ferroelastic behavior was observed for polycrystalline $BaTiO_3$ at all measured temperatures. The coercive stress was determined by the inflection point of the stress-strain curve and represents the stress at which the ferroelastic switching of the domains is at maximum rate. Besides the apparent nonlinear stress-strain behavior, Figure 3.11 also reveals a remanent strain after unloading the samples back to –5 MPa preload, which originated from irreversible domain switching due to the mechanical stress. Backswitching processes were responsible for the nonlinear stress-strain behavior during unloading. All these processes are temperature-dependent and were therefore determined at all temperatures. Figure 3.12 shows the coercive stress X_c and the remanent strain S_r of polycrystalline $BaTiO_3$ as a function of temperature. In addition, the experimental data from Picht *et al.* for temperature above 25 °C is also included [349]. All results are correlated to the temperature-dependent permittivity measured at –5 MPa mechanical preload.

It is apparent from Figure 3.12 that the ferroelastic properties of polycrystalline $BaTiO_3$ showed, similar to the permittivity, anomalies at the phase transition temperatures. No remanent strain was observed at temperatures above the Curie point, as expected in the paraelectric phase. However, a stress-induced paraelectric-to-ferroelectric phase transition was observed by Picht *et al.* at temperatures right above T_C, which was also the origin of the strongly increasing coercive stress above the Curie point [349]. With decreasing temperature below T_C, the remanent strain was found to increase. This is due to decreased backswitching and an increase in the spontaneous strain with decreasing temperature [59, 349]. The coercive stress increased with decreasing temperature below T_C and showed a maximum at approximately 80 °C. Similar behavior, *i.e.* a maximum in the remanent strain and a minimum in the coercive stress, were observed also for at the

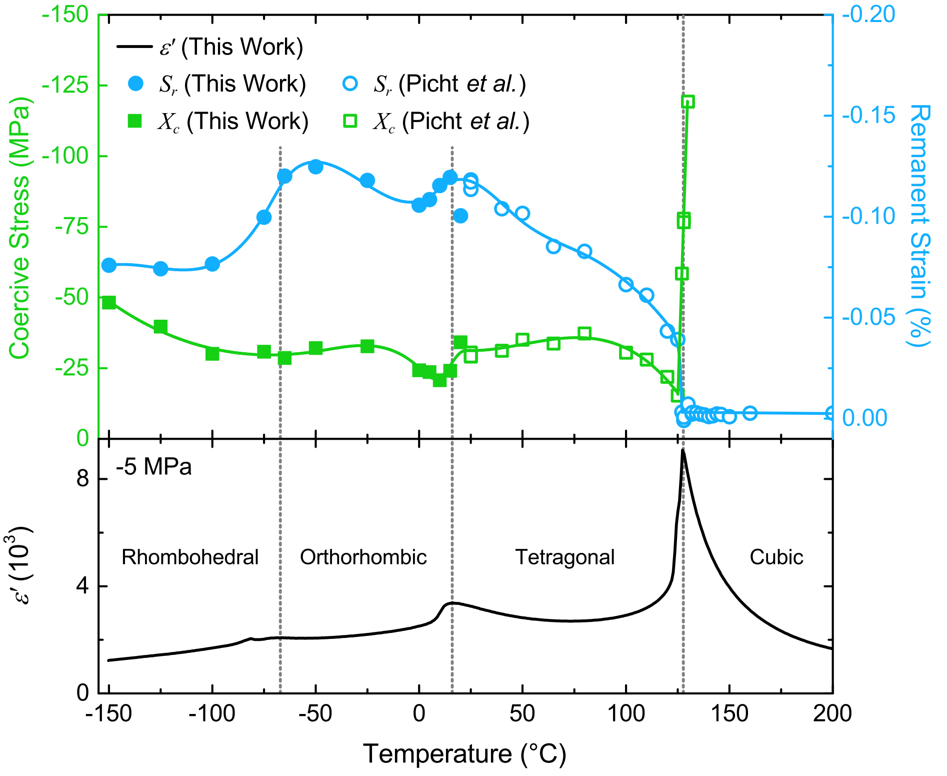

Figure 3.12: Coercive stress X_c and remanent strain S_r of polycrystalline $BaTiO_3$ as a function of temperature. The data collected in this work are represented by filled symbols, whereas open symbols show data taken from Reference [349]. For comparison, the temperature-dependent permittivity measured at –5 MPa prestress is given as well.

lower-temperature phase transitions. Finally, the remanent strain was found to saturate at lower temperatures in the rhombohedral phase, whereas the coercive stress increased with increasing temperature. The former effect is likely due to the temperature-independent spontaneous strain in the rhombohedral phase [59]. The latter effect, however, was due to the increased stability of rhombohedral phase at low temperatures, marked by a deepening of the free energy density wells, leading to an increase in the required mechanical stresses for ferroelastic switching. Figure 3.12 also shows that the maxima in $S_r(T)$ and the minima in $X_c(T)$ did not exactly coincide with the phase transition temperatures determined by the maxima of temperature-dependent permittivity. A possible reason for that could be that the permittivity was measured during constant cooling, whereas the ferroelastic measurements were performed at constant temperature.

3.4 Summary

In this chapter, the influence of a compressive uniaxial mechanical bias stress on the phase transition behavior of single crystal and polycrystalline $BaTiO_3$ was investigated. The observed increase and decrease of the permittivity with increasing bias stress were rationalized by domain wall clamping and ferroelastic switching of the domains, which possess an anisotropic permittivity. With increasing mechanical bias stress, the Curie point was found to shift to higher temperatures, whereas at the same time the Curie-Weiss temperature decreased. This indicated an increase in the first order nature of the tetragonal-to-cubic phase transition due to the application of uniaxial stress. By introducing stress-dependent coefficients in the LGD theory, the observed shift in T_C and the change in the phase transition behavior could be described theoretically. The computed results revealed a qualitatively good agreement with the experimental data and could have possible impact on the simulation of the behavior of domain walls, for which phase field models usually predict high internal stress fields. These fields could then alter the properties of the material and affect the motion of the domain walls [402]. Another possible application could be the modeling of thin films, which may exhibit phase [95, 388] and property changes due to high in-plane strains [100, 344].

In addition to the high-temperature phase transition at the Curie point, the lower-temperature phase transitions of polycrystalline $BaTiO_3$ were investigated and revealed a similar shift of the phase transitions toward higher temperatures with increasing uniaxial mechanical compression. Stress-strain measurements in the same temperature range showed a change in the ferroelastic behavior within the different phases. The remanent strain and the coercive stress possessed anomalies, which correlated with the phase transition temperatures. These finding indicated, that the large field ferroelastic properties of polycrystalline $BaTiO_3$ significantly soften not only at the Curie point, but also at the other ferroelectric-to-ferroelectric phase transitions at lower temperatures.

4 Mechanical Stability of the Piezoelectric Properties and the Phase Transitions in Lead-Containing Perovskite Ferroelectrics

4.1 Introduction

Lead-containing perovskites are the materials of choice for most piezoelectric applications due to their high electromechanical properties and their excellent temperature stability. A variety of Pb-based commercial materials are available on the market, designed for specific applications and their significantly diverse requirements. One of the main material classes used for these applications is the well-known, lead-containing solid solution $Pb(Zr_xTi_{1-x})O_3$ (PZT), which will be investigated in this chapter with regards to its electromechanical properties under uniaxial mechanical compressive stress. This investigation focuses on two representative commercial PZT materials, namely PIC151 and PIC181 from PI Ceramic GmbH, Lederhose, Germany. Both compositions are located at the tetragonal side of the MPB, but are modified by additional elements to fulfill specific product requirements. Although both are co-substituted with donor and acceptor ions, PIC151 shows soft ferroelectric behavior, whereas PIC181 possesses the properties of a hard ferroelectric material. A more detailed description of these modified PZT compositions is given in Section 1.10.3.

Previous studies have shown that externally applied mechanical, electrical, and thermal fields significantly influence the macroscopic constitutive behavior of ferroelectric materials [43, 46], which can result in a shift of the Curie point [330] as well as in electric field- and stress-induced phase transitions [112, 403]. This can affect the design and operation of these materials especially in actuation applications that, for example, apply a mechanical preload to a piezoelectric actuator during electrical activation [208, 320, 325, 327]. Such important problems require a deeper understanding of the underlying physics and, consequently, the stress dependence of the piezoelectric properties of PZT materials has already been investigated in detail [23, 29, 40, 361, 363, 365, 404–408]. However, relatively little data is available on the temperature- and frequency dependence of piezoelectric properties combined with application of external mechanical fields. For example, Rayleigh measurements at room temperature have revealed that a static compressive load significantly changes both the intrinsic and extrinsic contributions to the direct piezoelectric coefficient [24], depending significantly on the dopant content [408].

The dielectric and piezoelectric properties of lead-containing ferroelectric materials will be investigated as a function of temperature and uniaxial mechanical compression at various frequencies in the following sections. A special focus will be placed on the phase transition behavior under mechanical loads, revealing a deeper insight into the underlying mechanisms. Section 4.2 will deal with general dielectric and piezoelectric properties of the above-mentioned commercial ferroelectrics. Especially of interest is the temperature-dependent ferroelasticity due to the external mechanical stress, which will be used to explain and discuss the experimental results. Furthermore, the correlation between the stress-induced domain texture during temperature-dependent ferroelastic measurements and the degradation of the piezoelectric coefficient with stress and temperature of PIC151 will be studied in Section 4.3. As previously noted, significant additional substitutions are utilized in PIC151 and PIC181, changing the properties and the phase transition behavior from that of undoped tetragonal PZT. The PIC181 composition shows hard ferroelectric behavior due to acceptor doping, which eventually results in the formation of oxygen vacancies and polar defects (see Section 1.10.2). Section 4.4 deals with the influence of a mechanical stress on these polar defects and addresses the question if polar defects can also be oriented by a mechanical load rather than just by electrical load. The presented results and the analysis have been published in: Schader *et al.*, Journal of Applied Physics 117, 194101, (2015) [409]. Finally, the phase stability of $<001>_{PC}$-oriented $x\mathrm{Pb(In_{1/2}Nb_{1/2})}$–$(1{-}x{-}y)\mathrm{Pb(Mg_{1/3}Nb_{2/3})}$–$y\mathrm{PbZiO_3}$ (PIN-PMN-PT) single crystals is investigated under the influence of mechanical stress in Section 4.5. Due to their extraordinary high piezoelectric properties, these single crystals are of particular interest for sonar transducer and high power applications where elevated mechanical bias stresses are typically used.

4.2 Phase Transition Behavior of Soft and Hard PZT under Uniaxial Mechanical Bias Stress

Cylindrical samples of polycrystalline PIC151 and PIC181 with a diameter of approximately 5.8 mm were drilled from an as-sintered plate and subsequently ground on both circular faces to a final height of 6 mm, as described in Section 2.2. Following the grinding procedure each sample was annealed at 400 °C for 1 h in the case of PIC151 and at 450 °C for 30 min in the case of PIC181 in order to thermally depole domains that may have been reoriented during the machining procedure. Gold-palladium electrodes were sputtered onto the circular faces of each sample. Finally, the samples were poled at 120 °C with a d.c. electric bias field of 2 kV/mm for 5 min in a silicone oil bath, followed by field cooling to room temperature. Before testing, a minimum waiting time of 24 h after poling was used.

All measurements were performed in a screw-driven uniaxial load frame with an integrated heating chamber, which was described in detail in Section 2.4. The samples were heated from room temperature to 350 °C (PIC151) or 450 °C (PIC181) with a rate of 1 °C/min while measuring the permittivity at frequencies between 100 Hz and 1 MHz with a maximum voltage amplitude of 1 V_{rms} applied to the sample by the LCR meter. Alternating with the permittivity measurement, the small signal piezoelectric coefficient d_{33} was determined in a frequency range of 0.5 Hz to 240 Hz with an amplitude of ±0.5 MPa by using a reference capacitor with a capacitance of 4.514 μF (see Figure 2.5). Due to electrical noise induced into the measurement signal by the power line frequency of 50 Hz, this frequency and all multiples of it were avoided in the d_{33} measurements. The measurements were repeated for different constant uniaxial mechanical compressive stress between –5 MPa and –300 MPa, which was held constant by the load frame during the entire heating process. Due to the special design of the experimental setup, the permittivity and d_{33} values could be directly correlated, since they were performed nearly simultaneously.

Figure 4.1 and Figure 4.2 show the temperature dependence of the permittivity and the piezoelectric coefficient at four representative mechanical compressive stresses of electrically poled PIC151 and PIC181. For all stresses tested, the permittivity of both compositions showed a monotonic, frequency-dispersive increase with temperature up to a maximum. This was followed by a frequency-independent decrease of the permittivity at higher temperatures. At –5 MPa mechanical prestress and 1 kHz measurement frequency, the maximum of the permittivity-temperature curve was observed at T_m = 254 °C in the case of PIC151 and T_m = 341 °C in the case of PIC181. This difference was expected because hard PZT has a more stable polar ferroelectric phase due to the internal electric field of the polar defects present in this material, which stabilize the induced remanent polarization against thermal fluctuations.

At the lowest bias stress value of –5 MPa in Figure 4.1, PIC151 displayed an initial modest increase in the piezoelectric coefficient with temperature up to 50 °C. This was followed by a decrease in d_{33} up to approximately 140 °C during further heating, and a final subsequent increase to the maximum at 233 °C. In contrast, the dielectric response at –5 MPa did not display this temperature dependence. Above the maximum of $d_{33}(T)$ a drop in the piezoelectric coefficient was observed, which could be attributed to the depolarization temperature determined to be 247 °C via the inflection point of the $d_{33}(T)$ curve [410]. This value is in excellent agreement with the inflection

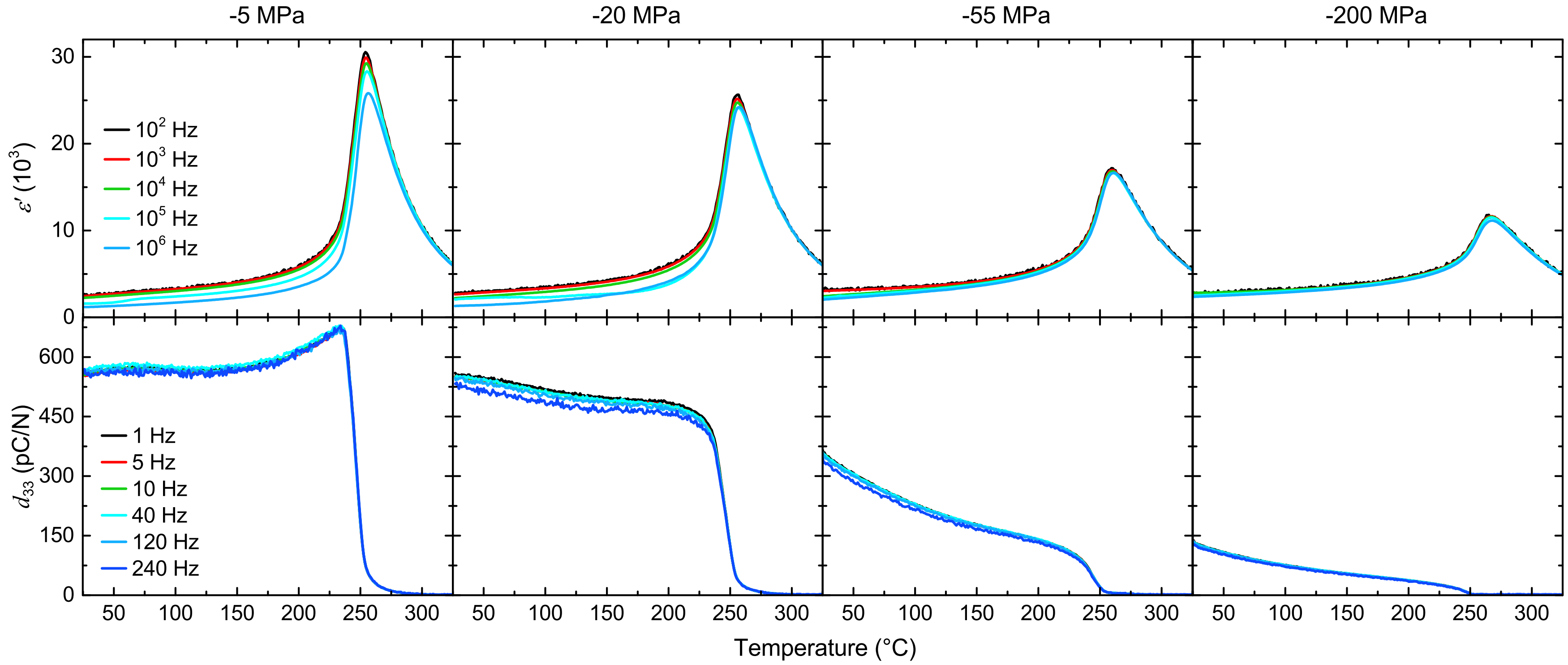

Figure 4.1: Temperature-dependent permittivity ε' and piezoelectric coefficient d_{33} of electrically poled soft PZT (PIC151) at various frequencies and constant uniaxial mechanical bias stresses.

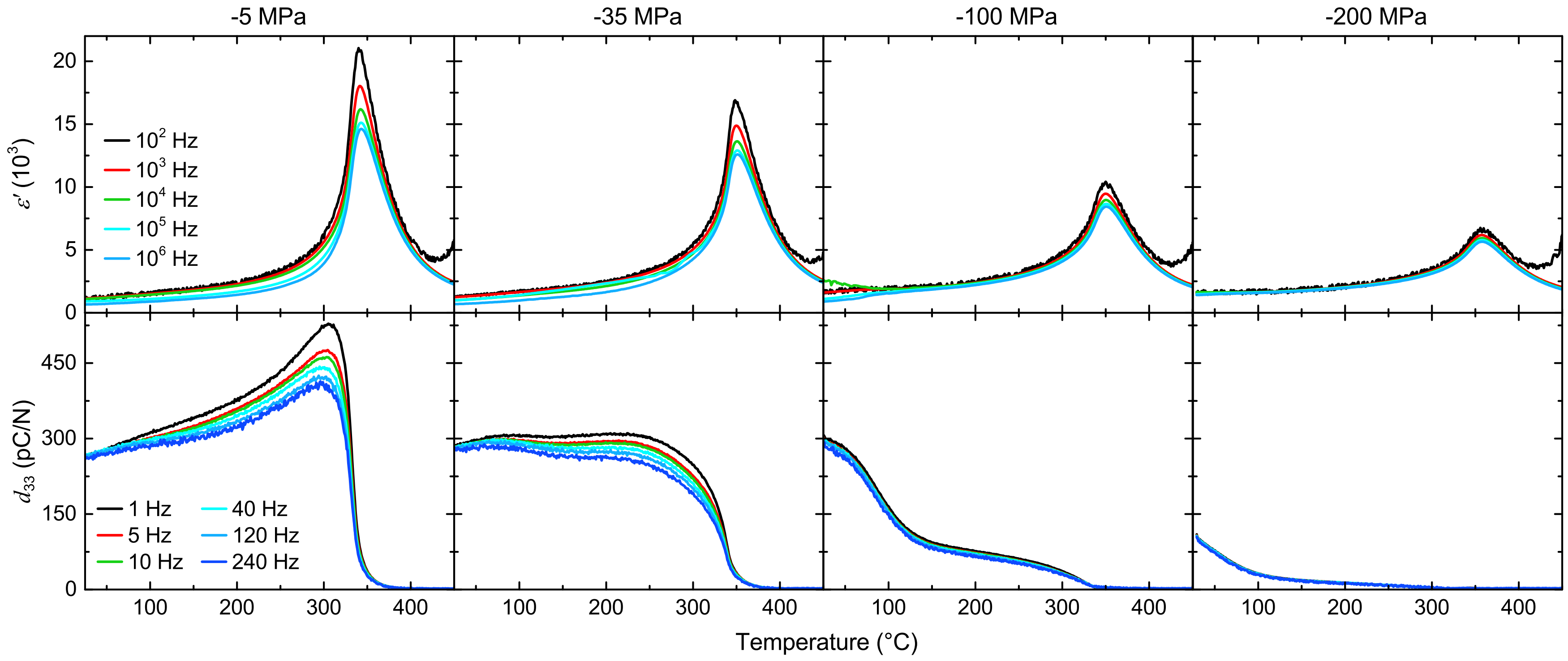

Figure 4.2: Temperature-dependent permittivity ε' and piezoelectric coefficient d_{33} of electrically poled hard PZT (PIC181) at various frequencies and constant uniaxial mechanical bias stresses.

point of the permittivity-temperature curve (246 °C) at –5 MPa constant prestress, which was 8 °C lower than T_m. Interestingly, the d_{33} peak occurred at 233 °C, 13 °C below the actual depolarization temperature. This is because the temperature dependence of d_{33} is coupled to the temperature dependence of the permittivity ε'_{33} and macroscopic polarization P_3 by Equation 4.1 [8]:

$$d_{33} = 2Q_{11}P_3\varepsilon'_{33}\varepsilon_0. \tag{4.1}$$

In the vicinity of T_m the permittivity increases strongly ($\varepsilon'_{33} \approx 25{,}000 - 30{,}000$ at T_m, compared to 1,200 – 2,500 at 25 °C), resulting in higher d_{33} values if a constant electrostrictive coefficient is assumed [12, 372]. In addition, thermally enhanced domain wall motion leads to lower stresses needed for ferroelastic switching, marked by a decreased coercive stress at elevated temperatures [44]. This also results in an enhanced extrinsic contribution, *i.e.* an increased macroscopic piezoelectric coefficient. Parallel to this thermally stimulated increase in d_{33}, the spontaneous polarization decreases with increasing temperature, which lowers d_{33}. Eventually these competing effects lead to the observed maximum in $d_{33}(T)$, when the latter effect outweighs the influence of the permittivity in Equation 4.1 at elevated temperatures just below T_d.

It was shown in Chapter 3 that the structural phase transitions in barium titanate are accompanied by peaks in the permittivity-temperature curve (see Figure 3.9 and also Section 1.8.2). This is also expected for other normal ferroelectrics like PZT. However, previous temperature-dependent ferroelastic measurements and X-ray diffraction experiments performed on PIC151 revealed a tetragonal structure up to 300 °C to 320 °C, far above its reported T_m [43, 321]. A possible reason for that could be the high amount of additional elements in these PZT-based materials, which could change the phase transition behavior significantly. Therefore, T_m will not be referred to as "phase transition temperature" in the following discussion, although it is closely connected to the structural phase transition in PIC151.

In the case of PIC181 in Figure 4.2, an initial increase in d_{33} with increasing temperature was found as well, even though no secondary maximum could be observed for the –5 MPa measurement at lower temperatures like in PIC151. The maximum $d_{33}(T)$ again did not coincide with the maximum $\varepsilon'(T)$. In addition, the temperature of the maximum piezoelectric coefficient was found to be strongly frequency-dependent. However, the respective inflections points of $\varepsilon'(T)$ and $d_{33}(T)$ were found to match, similarly to PIC151, and were determined to be 331 °C (1 kHz) and 332 °C (10 Hz), respectively, for a –5 MPa preload. In contrast to PIC151 results, a significant frequency dispersion in $d_{33}(T)$ developed at elevated temperatures for mechanical bias stresses up to –150 MPa. This is most likely due to the thermally enhanced mobility of the polar defects in this material, which likely have a mobility on the order of the applied frequency that allowed the domain walls to follow the electric field easier at lower frequencies. In general, the pinning of domain walls by defects was found to be the main reason for the comparatively large frequency dispersion of the piezoelectric coefficient in ferroelectrics containing acceptor dopants [22]. The frequency dispersion was highly reduced at elevated mechanical loads (above –100 MPa), indicating that the polar defects were realigned either directly by the load or indirectly by following the ferroelastically switched neighboring domains. Furthermore, a two-step behavior was found in the temperature curve of the piezoelectric coefficient at –100 MPa. An initial drop in d_{33} occurred at about 40 °C, which limits the usage of PIC181 in applications with high mechanical preloads to lower temperature regime applications. At higher temperatures, the domain walls probably overcame the pinning caused by the polar defects due to the combined thermally enhanced mobility and the applied stress, thus resulting in the onset of the thermal depolarization of the sample. Around 150 °C, the slope of $d_{33}(T)$ changed again and the following temperature behavior followed a trend similar to that of PIC151, which revealed a significant decrease of the influence of the polar defects. A more detailed investigation on this topic will be presented in Section 4.4.

In order to more directly compare the measurements at various mechanical preloads of the two investigated PZT compositions, Figure 4.3 depicts the temperature-dependent permittivity, loss tangent, and piezoelectric coefficient at different compressive bias stresses. For the sake of clarity, only the 1 kHz signal is shown for ε' and $\tan(\delta)$, and only the 10 Hz signal for d_{33}. At lower temperatures, the permittivity of PIC151 was found to initially increase up to a compressive stress of –55 MPa, followed by a subsequent decrease with further increasing stress. This is understood to be due to that anisotropic dielectric properties of this modified PZT material, similar to $BaTiO_3$ [54]. In the poled state, the domains are primarily oriented in the direction of the field. During mechanical loading, however, domains can ferroelastically reorient perpendicular to the loading direction, increasing the permittivity due to the higher intrinsic permittivity perpendicular to the polar axis. At stresses above –55 MPa, domain wall clamping became the dominating effect and resulted in a decreasing permittivity. In principle, the same effect is observed in PIC181, but here the initial increase in permittivity at lower temperatures could be observed up to stresses of –100 MPa. This could be most likely explained by the stress-induced release of the domain walls pinned by polar defects, increasing the extrinsic contribution to the permittivity.

Above approximately 200 °C for PIC151 and 300 °C for PIC181, the permittivity decreased monotonically with increasing mechanical compression. The maximum value in the temperature-permittivity curve was found to decrease with increasing mechanical stresses up to –300 MPa by

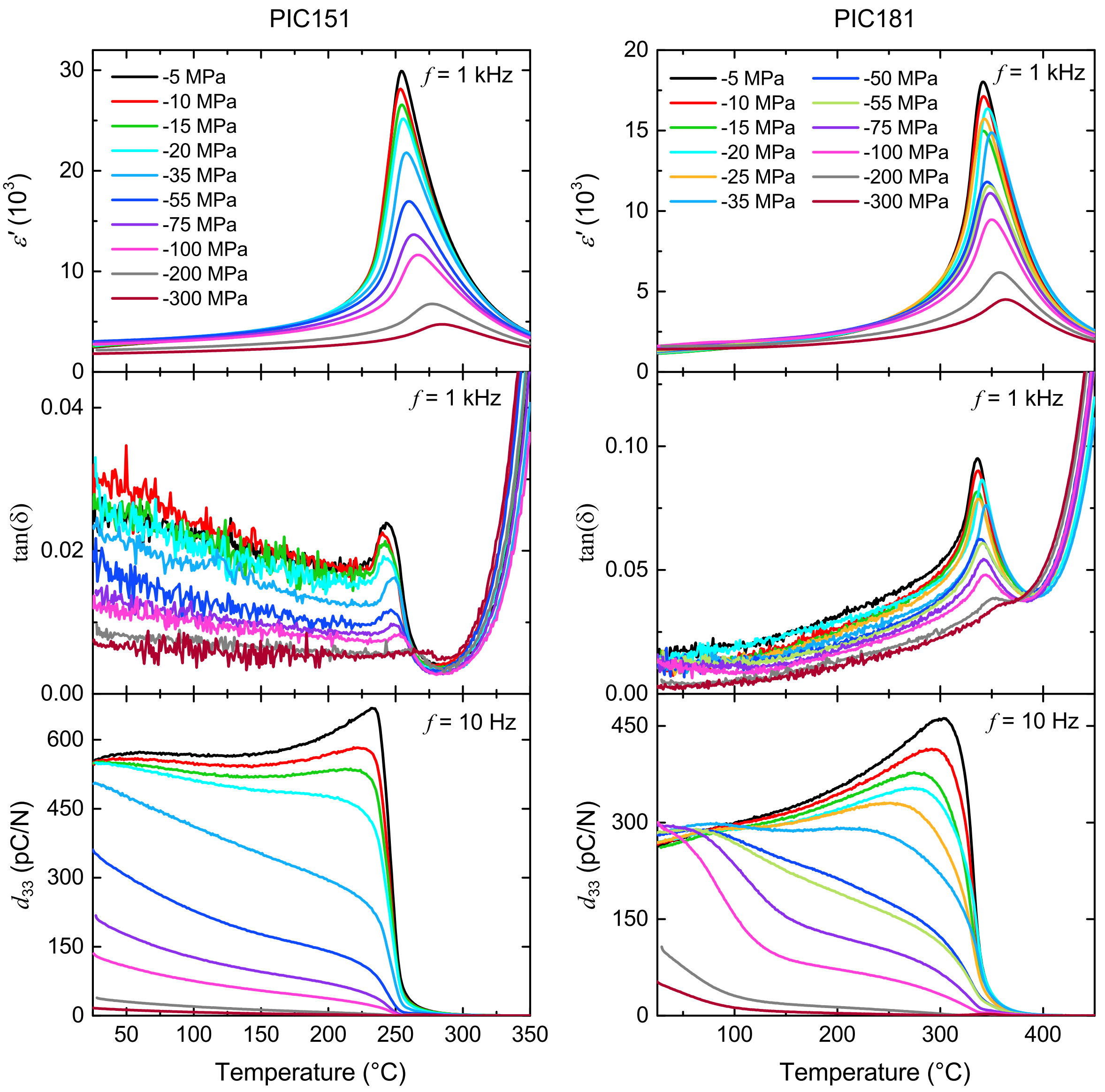

Figure 4.3: Comparison of the temperature-dependent permittivity ε', loss tangent $\tan(\delta)$ and piezoelectric coefficient d_{33} of soft (PIC151) and hard (PIC181) PZT at various constant uniaxial stresses. For the sake of clarity, only the 1 kHz signal of ε' and $\tan(\delta)$ and the 10 Hz signal of d_{33} are shown here.

84 % and 75 % for PIC151 and PIC181, respectively. Above the temperature T_m at maximum permittivity, the observed decrease of the permittivity could be rationalized by the stress-dependent decrease of the intrinsic contribution. In addition, the maximum in ε' broadened and T_m was shifted to higher values with increasing mechanical compression. Thus the stress acted to stabilize the ferroelectric order of both compositions. The broadening of the permittivity maximum was due to the different stress states of the differently oriented grains in the polycrystalline sample relative to the loading direction. This resulted in a broader distribution of depolarization temperatures and therefore in a broader maximum in permittivity with increasing stress. Similar observations were made for $BaTiO_3$ and were presented in Chapter 3. It is important to note that not all measurements (especially at –20 MPa and –35 MPa) on PIC181 followed the general trends in the

temperature behavior of ε' discussed in this part and may be due to general scattering between the different samples used in these measurements.

The dielectric loss tangent of PIC151 shown in Figure 4.3 was found to decrease with increasing temperature, but formed a maximum around the depolarization temperature. A subsequent drop of $\tan(\delta)$ with further heating could be attributed to the vanishing influence of ferroelectric domains, whereas the strong increase of the loss tangent at even higher temperatures was most likely due to the onset of electrical conductivity. It was observed that the loss tangent decreased with increasing compressive mechanical bias stress. The maximum $\tan(\delta)$ at the depolarization temperature was decreased with increasing stress and shifted to higher temperatures, similar to the maximum in the permittivity. In contrast, the loss tangent of PIC181 at room temperature was found to be approximately 40 % smaller than the one measured for PIC151 and generally showed an increase with temperature. These trends are in qualitative agreement with literature about soft and hard PZT [411, 412]. The increase in $\tan(\delta)$ of PIC181 below T_d was due to the presence of polar defects that could increase the energy loss in the material at elevated temperatures, where the motion of the defects was enhanced. This also probably corresponded to the increased frequency dispersion of the piezoelectric coefficient at higher temperatures. Like in PIC151, a maximum in $\tan(\delta)$ was observed at T_d, which decreased and shifted to higher temperatures with increasing mechanical stress.

In the case of PIC151 in Figure 4.3, the piezoelectric coefficient was found to be relatively stable at room temperature for compressive stresses below approximately –20 MPa. Above this stress level, the initial d_{33} value decreased with increasing applied stress due to the stress-induced loss of polarization and due to domain wall clamping. Interestingly, the temperature stability of d_{33} was enhanced for an applied compressive stress of –10 MPa, displaying only a ±2.5 % variation between room temperature and 200 °C. In contrast, a variation of ±2.5 % was limited to between the temperatures of 25 °C and 175 °C for –5 MPa and further limited to between 25 °C and 100 °C for –15 MPa. These results reveal that the choice of a proper preload could significantly increase the temperature stability and therefore the useful temperature range for applications of this material. With further increase of the compressive bias stress, the observed d_{33} decreased sharply with increasing temperature. The local maximum in $d_{33}(T)$ located just prior to T_d was found to decrease with increasing stress and vanished at mechanical bias stresses above –20 MPa. In addition, the sharp drop in d_{33} at the depolarization temperature became more gradual with increasing mechanical load, indicating that the applied stress affected the domains over a broader temperature range depending on the thermal stability of the local fields. The previously mentioned distribution of T_d

observed in the permittivity curve, attributed to the different stress states in differently oriented grains, can also be used to explain this broadening. Whereas the room-temperature piezoelectric coefficient of PIC151 decreased monotonically with stress above –20 MPa, an initial increase in d_{33} was observed for the hard PZT, up to –75 MPa. This can be rationalized by the enhanced piezoelectric activity of the material due to the stress-induced unpinning of the domain walls. A more detailed discussion of this effect will be given in Section 4.4. Like in PIC151, the maximum in d_{33} of PIC181 was lowered with increasing mechanical compression and vanished at a stress level between –35 MPa and –50 MPa. In parallel, the already described two-step process observed for d_{33} occurred above –35 MPa and became more pronounced with increasing mechanical compression. No clear correlation to these d_{33} observations could be found in stress and temperature curves of the dielectric loss tangent of PIC181.

Figure 4.1 and Figure 4.2 have shown that the piezoelectric coefficient of electrically poled PIC151 and PIC181 dropped at the depolarization temperature, but the signal did not vanish completely and a small, gradually decreasing d_{33} value could still be measured at significantly higher temperatures. In order to investigate this phenomenon and its dependence on the uniaxial compressive mechanical bias stress in more detail, Figure 4.4 and Figure 4.5 depict the temperature-dependent piezoelectric coefficient of PIC151 and PIC181, respectively, at various mechanical stresses in the specific temperature intervals of interest, *i.e.* much above the T_d at each

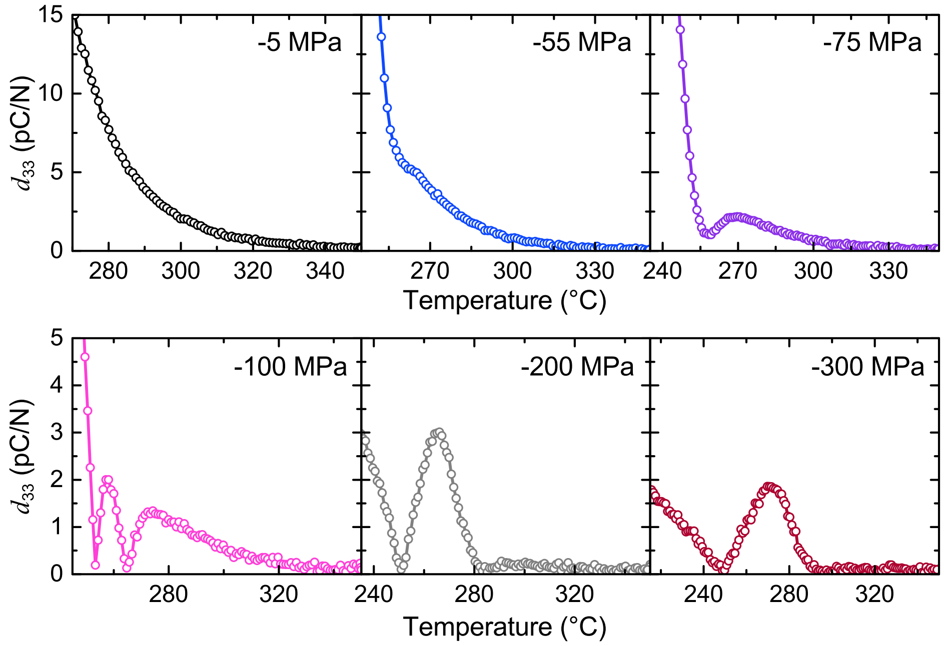

Figure 4.4: Temperature-dependent piezoelectric coefficient d_{33} of soft PZT (PIC151) measured at a frequency of 10 Hz at various mechanical preloads. The special focus lies on the observation that d_{33} was still measureable at temperatures far above T_d and in the development of an anomaly in $d_{33}(T)$ at stresses above –55 MPa.

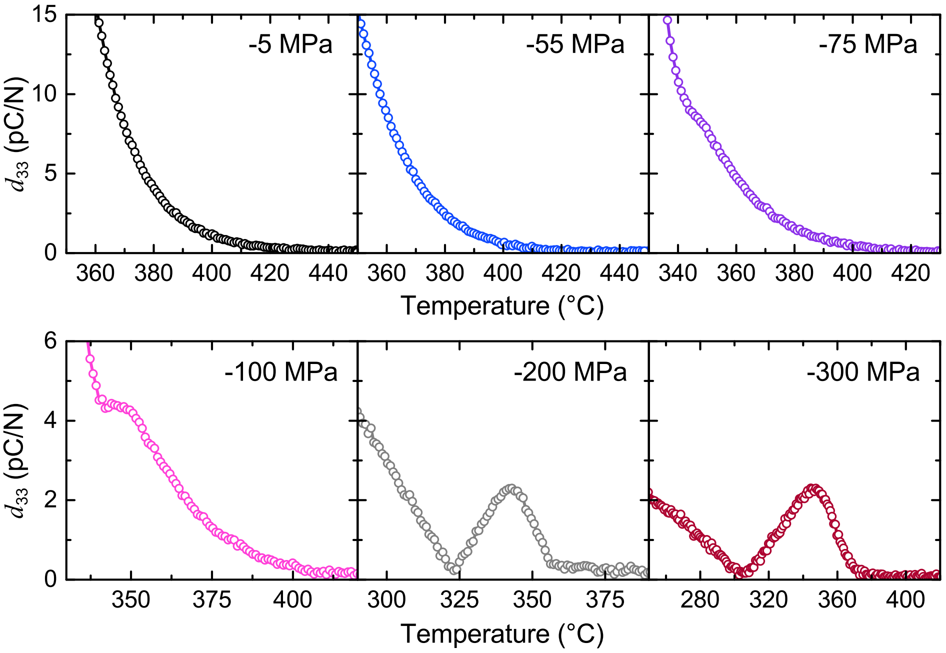

Figure 4.5: Temperature-dependent piezoelectric coefficient d_{33} of hard PZT (PIC181) measured at a frequency of 10 Hz at various mechanical preloads. The special focus lies on the observation that d_{33} was still measureable at temperatures far above T_d and in the development of an anomaly in $d_{33}(T)$ at stresses above –75 MPa.

given mechanical stress. For the sake of clarity, only the 10 Hz d_{33} data was used in this evaluation. At the lowest mechanical preload of –5 MPa, the piezoelectric coefficient of PIC151 decreased gradually with heating above the depolarization temperature and reached the value of zero at approximately 340 °C, about 93 °C above T_d. Please note in this context the relatively low scattering and the high amount of data points. It was possible to achieve a relatively high resolution in d_{33} of approximately 0.1 pC/N during the development and the testing of the experimental setup. This supports the validity of the described observations, which could lead to the conclusion that polar regions with a measureable macroscopic polarization still existed at temperatures far above T_d. Indeed, a similar observation will be presented in Section 5.2 during the discussion of the lead-free material NBT-xBT. Figure 4.2 reveals a similar behavior for PIC181, which showed a nonzero d_{33} signal up to approximately 425 °C in the measurement at –5 MPa prestress, also about 93 °C above the depolarization temperature.

Another interesting and surprising effect was observed at mechanical stresses above –75 MPa and –200 MPa for PIC151 and PIC181, respectively. The measured piezoelectric coefficient was found to rise again after reaching a value of nearly zero and showed an additional maximum (in the case of PIC151 at –100 MPa even two maxima) in $d_{33}(T)$. An apparent anomaly, indicated by a shoulder in the $d_{33}(T)$ curves, developed already at lower stresses, namely at –55 MPa for PIC151 and at –75 MPa for PIC181. Although this effect was in the range of only a few pC/N, it could be clearly resolved in the presented measurements. So far, no satisfying explanation for this obviously stress-induced phenomenon could be found, but the following, more detailed analysis could give at least some evidence about the underlying physical phenomena.

In addition to the load amplitude and polarization signal, the fast Fourier transform used during the data evaluation process (see Section 2.5.2) also gave information about the phase angle of the measured and analyzed periodic signals. Figure 4.6 and Figure 4.7 show the resulting phase shift between the applied sinusoidal mechanical load and the polarization signal as a function of temperature for PIC151 and PIC181, respectively, at various constant mechanical stresses. Interestingly, the phase angle switched at a specific temperature from 0° to approximately –180° or below, indicating that the polarization was inversely phased to the stress in that specific temperature range. This switching was observed to start at the same temperature where the value of d_{33} reached zero for the first time (Figure 4.1 and Figure 4.2) and appeared first at a compressive stress of –100 MPa in the case of PIC151 and at –200 MPa in the case of PIC181. At lower stress, while an additional maximum in $d_{33}(T)$ was already visible, no phase angle change could be determined (see for instance the –75 MPa measurement on PIC151 in Figure 4.6).

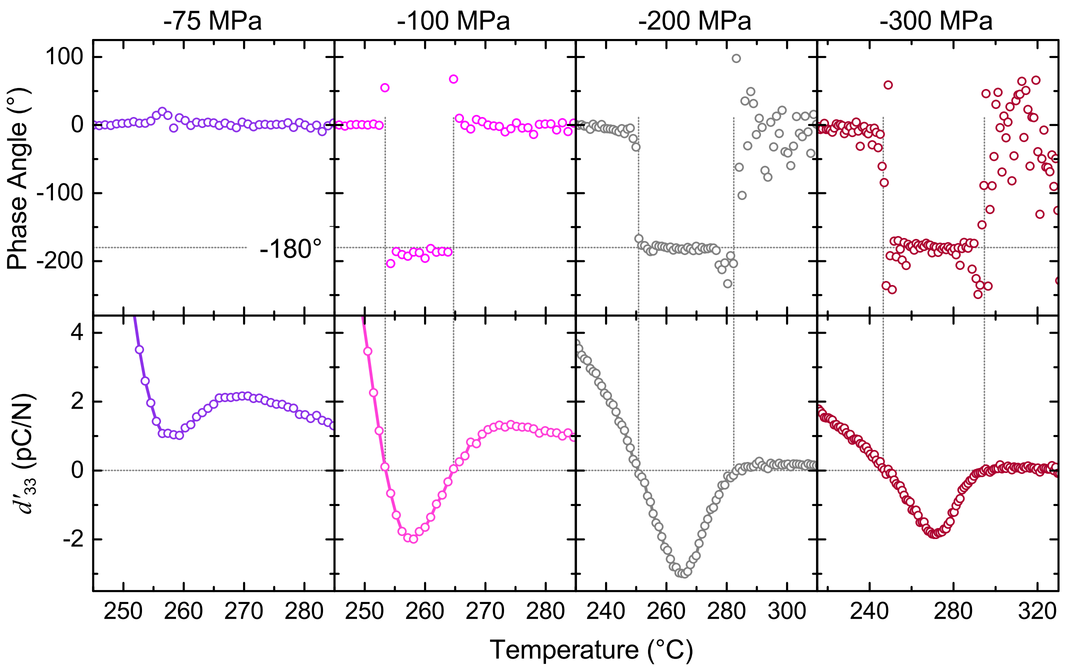

Figure 4.6: Phase angle between the load and the polarization signal and real part d'_{33} of the piezoelectric coefficient of soft PZT (PIC151) as a function of temperature, measured at a frequency of 10 Hz and at various constant uniaxial mechanical stresses.

It has been previously suggested that the piezoelectric coefficient, like the permittivity, should be treated as a complex quantity [413–415]. By doing so, the real part of the piezoelectric coefficient, *i.e.* d'_{33}, would become negative if the phase angle equals –90° or below. The result of this temperature-dependent phase angle evaluation is shown for PIC151 and PIC181 in Figure 4.6

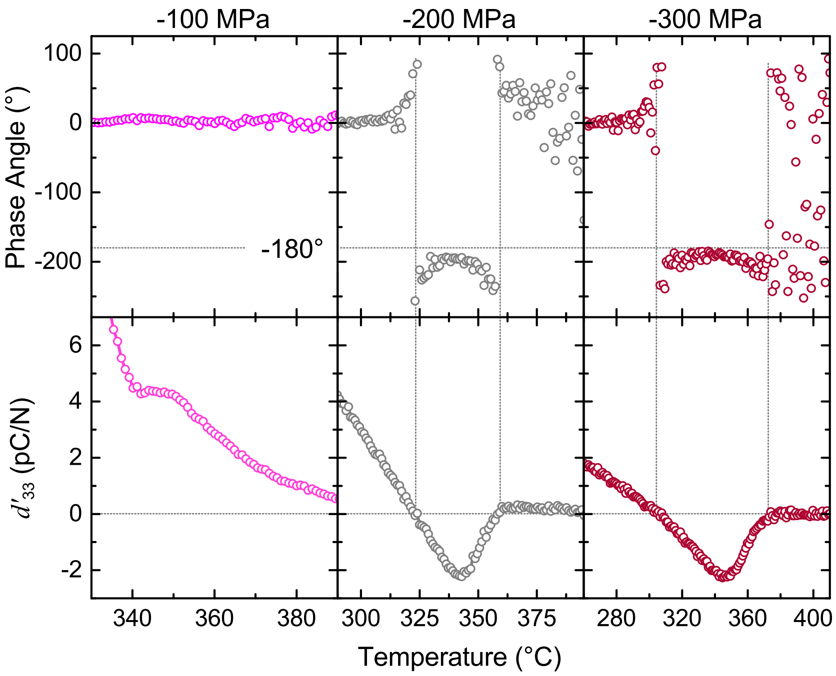

Figure 4.7: Phase angle between the load and the polarization signal and real part d'_{33} of the piezoelectric coefficient of hard PZT (PIC181) as a function of temperature, measured at a frequency of 10 Hz and at various constant uniaxial mechanical stresses.

and Figure 4.7, respectively, and reveals a drop of the phase angle to –180° or even below and the corresponding negative values of the real part of the piezoelectric coefficient d_{33} are therefore displayed in these regions. In this case, the sinusoidal mechanical stress and resulting change in polarization were antiphase with each other in this temperature region. Since the observed value of a physical quantity is always an absolute value, d_{33} was determined during the measurement to be positive even if the phase between load and polarization change dropped to –90° or below. Negative values of the phase angle and of the piezoelectric coefficient have already been previously reported by Damjanovic *et al.* In that case the example of a bilayer of two different piezoelectric materials was used, which showed a Maxwell-Wagner type relaxation of the piezoelectric coefficient [416].

The temperature interval in which the real part of the piezoelectric coefficient of PIC151 was negative increased in width with increasing uniaxial mechanical load from 11 °C to 48 °C between the –100 MPa and –300 MPa measurements, respectively. The same trend was found for PIC181, but the width of the temperature interval was larger and increased from 36 °C to 68 °C between the measurements at bias stresses of –200 MPa and –300 MPa. In addition, the phase angle was determined to switch to values even slightly below –180° for PIC181. The increase in phase angle below –180° is likely due to the larger energy dissipation in this composition compared to PIC151, which was also reflected by the higher loss tangent in this temperature range (Figure 4.3). Unfortunately, a satisfying explanation for all the observed phenomena regarding the phase switching of d_{33} in

PIC151 and PIC181 at higher mechanical compressive stresses remains unresolved. It should be kept in mind that polycrystalline samples consist of areas with different piezoelectric coefficients due to the different internal stress distribution resulting from varying grain and domain orientations relative to the applied load. This could maybe give an explanation similar to the bilayer model described by Damjanovic *et al.* [415, 416].

The stress dependence of the characteristic temperatures of the $\varepsilon'(T)$ and $d_{33}(T)$ curves could be determined by evaluating the inflection points of the corresponding measurement curves from Figure 4.3 for various mechanical compressive stresses. Figure 4.8 depicts the inflection points $T_{\mathrm{inf}}^{\varepsilon'}$ and $T_{\mathrm{inf}}^{d_{33}}$ of $\varepsilon'(T)$ and $d_{33}(T)$, of both PIC151 and PIC181 as a function of uniaxial mechanical compressive stress. In addition, the temperature T_m corresponding to the maximum value of permittivity as a function of stress is also shown. The 1 kHz and the 10 Hz signals were used for evaluating the $\varepsilon'(T)$ and the $d_{33}(T)$ curve, respectively. Since the results for PIC181 presented in Figure 4.2 and Figure 4.3 revealed some problems, particularly for the –20 MPa and the –35 MPa measurements, the data from these two experiments was not used for the evaluation presented in Figure 4.8.

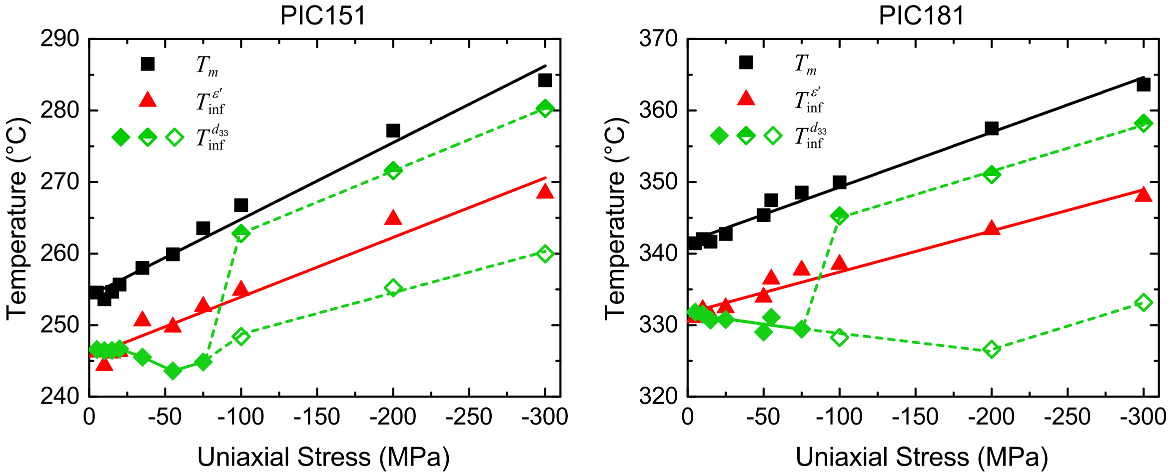

Figure 4.8: Stress-dependent temperature at maximum permittivity T_m and inflection points $T_{\mathrm{inf}}^{\varepsilon'}$ and $T_{\mathrm{inf}}^{d_{33}}$ of $\varepsilon'(T)$ and $d_{33}(T)$, respectively, of soft (PIC151) and hard (PIC181) PZT as a function of uniaxial mechanical compression. For evaluation, the 1 kHz and the 10 Hz signal of $\varepsilon'(T)$ and $d_{33}(T)$ were used, respectively. The solid and dashed lines serve to guide the eye. Above a certain stress level, $d_{33}(T)$ showed two inflection points, which are represented by half-open (high temperature inflection points) and open (low-temperature inflection points) symbols.

The inflection points determined from ε' and $d_{33}(T)$ of both PIC151 and PIC181 revealed an approximately linear increase with increasing mechanical bias stress. Similar shifts in T_m have also been observed in single crystalline and polycrystalline $BaTiO_3$ under hydrostatic [330], radial [342], and uniaxial compressive stress (Ref. [71, 387] and Chapter 3) as well as in single crystalline $PbTiO_3$ [336]. In these cases the linear increase was attributed to a change in the ferroelectric-paraelectric phase transition temperature. It can be seen from Table 4.1 that the rates of increase were in general higher for PIC151, indicating a larger stress sensitivity of the phase transition behavior and of the depolarization of the soft PZT material. This result is expected as the higher amount of polar defects present in the hard PIC181 stabilizes the ferroelectric long-range order. Another observation for both compositions was that the rate of increase of T_m was determined to be higher than the rate of increase of $T_{\text{inf}}^{\varepsilon'}$. The origin of this discrepancy is unclear but could be attributed either to the increased broadening of the permittivity peak with increasing uniaxial stress or to the decoupling of the thermal depoling and the structural phase transition in these materials.

Table 4.1: Rates of increase in °C/MPa of the temperature of maximum permittivity T_m and of the inflection points $T_{\text{inf}}^{\varepsilon'}$ and $T_{\text{inf}}^{d_{33}}$ of $\varepsilon'(T)$ and $d_{33}(T)$, respectively, with respect to applied uniaxial compressive stress of soft (PIC151) and hard (PIC181) PZT. Since $d_{33}(T)$ showed two inflections point at stresses above −100 MPa, rates of increase are given here for both low- and high-temperature inflection points.

Material	$\mathrm{d}T_m/\mathrm{d}X$	$\mathrm{d}T_{\text{inf}}^{\varepsilon'}/\mathrm{d}X$	$\mathrm{d}T_{\text{inf}}^{d_{33}}/\mathrm{d}X$ **low-temp.**	$\mathrm{d}T_{\text{inf}}^{d_{33}}/\mathrm{d}X$ **high-temp.**
PIC151	0.11	0.08	0.06	0.09
PIC181	0.08	0.06	0.06	–

In contrast to the characteristic temperatures determined from the permittivity measurements, the behavior of inflection points of the $d_{33}(T)$ curves was relatively unclear. The inflection points of both $\varepsilon'(T)$ and the $\varepsilon'(T)$ coincided below −25 MPa for both PZT compositions and could be identified as the depolarization temperature T_d, which was closely correlated to the structural phase transition between the tetragonal ferroelectric and the cubic paraelectric phase. At higher loads, $T_{\text{inf}}^{d_{33}}$ deviated from the stress dependence determined for $T_{\text{inf}}^{\varepsilon'}$ and was found to decrease for both PIC151 and PIC181 up to bias stresses of −75 MPa and −100 MPa, respectively. A reason for that could probably be that the thermal depolarization and the structural phase transition decoupled at higher loads. However, this needs to be investigated in more detail.

For the behavior of $T_{\text{inf}}^{d_{33}}$, *i.e.* the depolarization behavior, no clear trend was found at mechanical bias stresses above −100 MPa for both materials. It was shown in Figure 4.4 and Figure 4.5 that an additional maximum in $d_{33}(T)$ appeared at these mechanical stresses for PIC151 and PIC181. It is doubtful if the temperature at which d_{33} first reached zero should be considered as the true depolarization temperature, however, because the absolute value of the piezoelectric coefficient rose again upon further heating (additional maximum in Figure 4.4 and Figure 4.5). An analysis of the complex piezoelectric coefficient revealed a more accurate portrayal of the depolarization behavior, as depicted in Figure 4.6 and Figure 4.7 for PIC151 and PIC181, respectively. The minimum in $d'_{33}(T)$ results in two inflection points; one below and one above the temperature at minimum d'_{33}. These inflection points are also depicted in Figure 4.8, where open and half-open symbols represent the inflection point below and above the minimum, respectively. Table 4.1 gives the calculated rates of increases of these inflection points. In the case of PIC151, the behavior of the inflection points was found to be comparable to the stress dependence of T_m and $T_{\text{inf}}^{\varepsilon'}$ above –100 MPa, even if the rates of increase were slightly lower. The same observation was made for the high-temperature inflection points determined for PIC181 above the minimum in $d'_{33}(T)$, but the behavior of the low-temperature inflection point below the minimum in $d'_{33}(T)$ remains unclear. In this case, additional stress measurements between –100 MPa and –300 MPa or an increased number of samples would perhaps help clarify the trends in these inflection points. Any further interpretation of these results is rather complicated, since the high amount of additional elements in the investigated modified PZT compositions highly affects the phase transition behavior. Furthermore, the uniaxial stress caused an additionally broadening of the depolarization temperatures due to the distribution of stress states in the polycrystalline samples.

Besides the above discussed behavior of the temperature-dependent dielectric and electromechanical properties of PIC151 and PIC181, a purely mechanical material property, *i.e.* the temperature-dependent elastic modulus, was investigated. Figure 4.9 shows a comparison of the temperature-dependent permittivity (1 kHz signal at –5 MPa prestress), the piezoelectric coefficient (10 Hz signal at –5 MPa prestress) and the elastic modulus E (no prestress) of soft and hard PZT. The elastic modulus was measured by using the acoustic emission resonance method presented in Section 2.6, whereas the sample preparation is described in Section 2.2. All elastic data was collected during heating, with a rate of 2 °C/min, which was twice the heating rate used for measuring $\varepsilon'(T)$ and $d_{33}(T)$.

In the case of PIC151, the minimum in the temperature-dependent elastic modulus corresponded well to the inflection points of $\varepsilon'(T)$ and $d_{33}(T)$, already previously identified as the depolarization temperature. Interestingly, $E(T)$ showed a similar trend to that observed for the piezoelectric coefficient between room temperature and T_d. An initial increase of the temperature-dependent elastic modulus to around 70 °C was followed by a broad minimum and a second increase with further heating before dropping at T_d. With increasing temperature above T_d, a strong nonlinear increase in the elastic modulus was found, which was due to the higher elastic modulus of the paraelectric phase [417, 418]. The gradual increase of E above T_d indicated that the phase transition from the tetragonal to the cubic phase was gradual and that a phase mixture probably still existed above T_d [418], which corresponds to the previous discussion the nonzero d_{33} above T_d in this section.

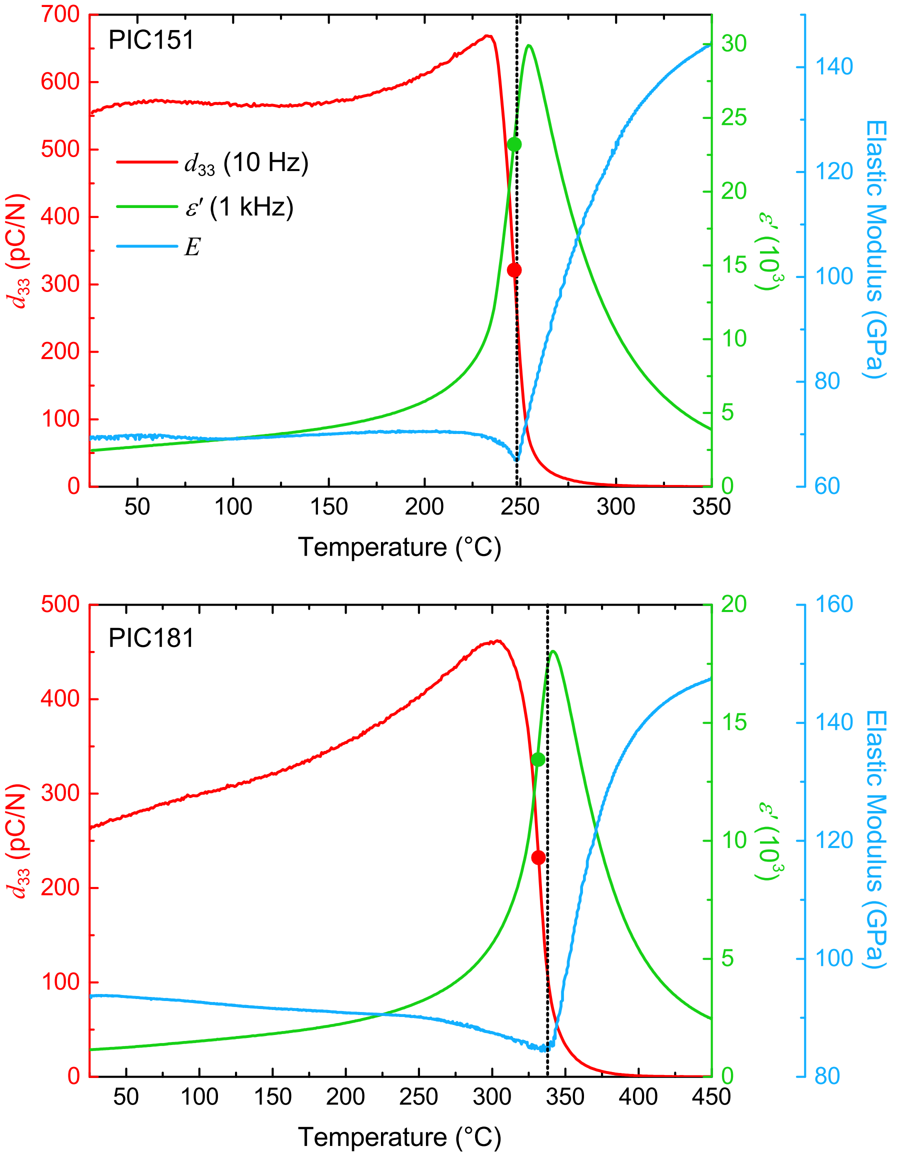

Figure 4.9: Comparison of the temperature-dependent permittivity ε' measured at 1 kHz, the piezoelectric coefficient d_{33} measured at 10 Hz, and the elastic modulus E of soft (PIC151) and hard (PIC181) PZT. The inflection points of $\varepsilon'(T)$ and $d_{33}(T)$ are represented by filled circles. Dielectric and electromechanical measurements were done at a constant mechanical preload of −5 MPa.

Figure 4.9 reveals a temperature-dependent behavior of the elastic modulus of PIC181 quite similar to that of PIC151, although the minimum in $E(T)$ at the depolarization temperature was found to be less pronounced in the hard material. In general, PIC181 possessed a higher elastic modulus than PIC151, e.g. 94 GPa compared to 70 GPa at room temperature for PIC181 and PIC151, respectively. The observed nonlinear, gradual increase of the elastic modulus was very likely originating from the same mechanisms already discussed for PIC151.

4.3 Temperature-Dependent Correlation between a Ferroelastically-Induced Texture and the Corresponding Change of d_{33} in Soft PZT

During the application of an external compressive stress, domains can ferroelastically reorient, resulting in the development of remanent strain. The amount of remanent strain observed in a particular ferroelastic material depends on the temperature, the lattice distortion, the applied load, and the coercive stress, in addition to microstructural considerations, e.g. grain size and porosity [419]. To elucidate the role of temperature-dependent ferroelasticity on the small signal piezoelectric and dielectric properties of electrically poled soft PZT (PIC151), the macroscopic remanent strain and polarization were characterized during full unloading experiments at 30 °C, 100 °C, 170 °C, and 233 °C (Figure 4.10). Similar measurements have been previously used to investigate the stress-dependent elastic properties and backswitching behavior of ferroelastic materials [42, 386].

For the measurements presented here, cylindrical shaped polycrystalline samples with a height of 6 mm and a diameter of 5.8 mm were used, similar to those in Section 4.2. The conditions for the d.c. electrical bias field poling were similar to those described in the previous section as well. During testing the load was increased, reduced back to the initial preload of –5 MPa, and then subsequently increased again to a higher maximum stress level by using a loading rate of 4 MPa/s. This process was continued for numerous maximum stress values, which corresponded to the different constant compressive bias stresses chosen for the measurements on PIC151 in Section 4.2. More details about the experimental setup can be found in Section 2.4.

The chosen temperatures were selected to correspond to temperatures of interest in the temperature-dependent measurements of the piezoelectric coefficient (see Figure 4.10). Note that the maximum in $d_{33}(T)$ was located at approximately 233 °C at –5 MPa bias prestress. To ensure comparability with the d_{33} measurements, the ideal remanent strain S_r and the ideal remanent polarization P_r, which exclude the contribution of backswitching, were determined by extrapolating the linear regime of the stress-strain curves and the stress-polarization curves in Figure 4.10 during unloading to the preload level of –5 MPa. The used linear regime represents a stress range of 10 % of the maximum applied stress. This process is schematically shown in Figure 4.10 for the maximum applied stress in the room-temperature measurement.

It is apparent from Figure 4.10 that the maximum remanent strain as well as the maximum remanent polarization decreased with increasing temperature. This originated from the thermally induced depolarization of the material, which is more effective at higher temperatures. In order to

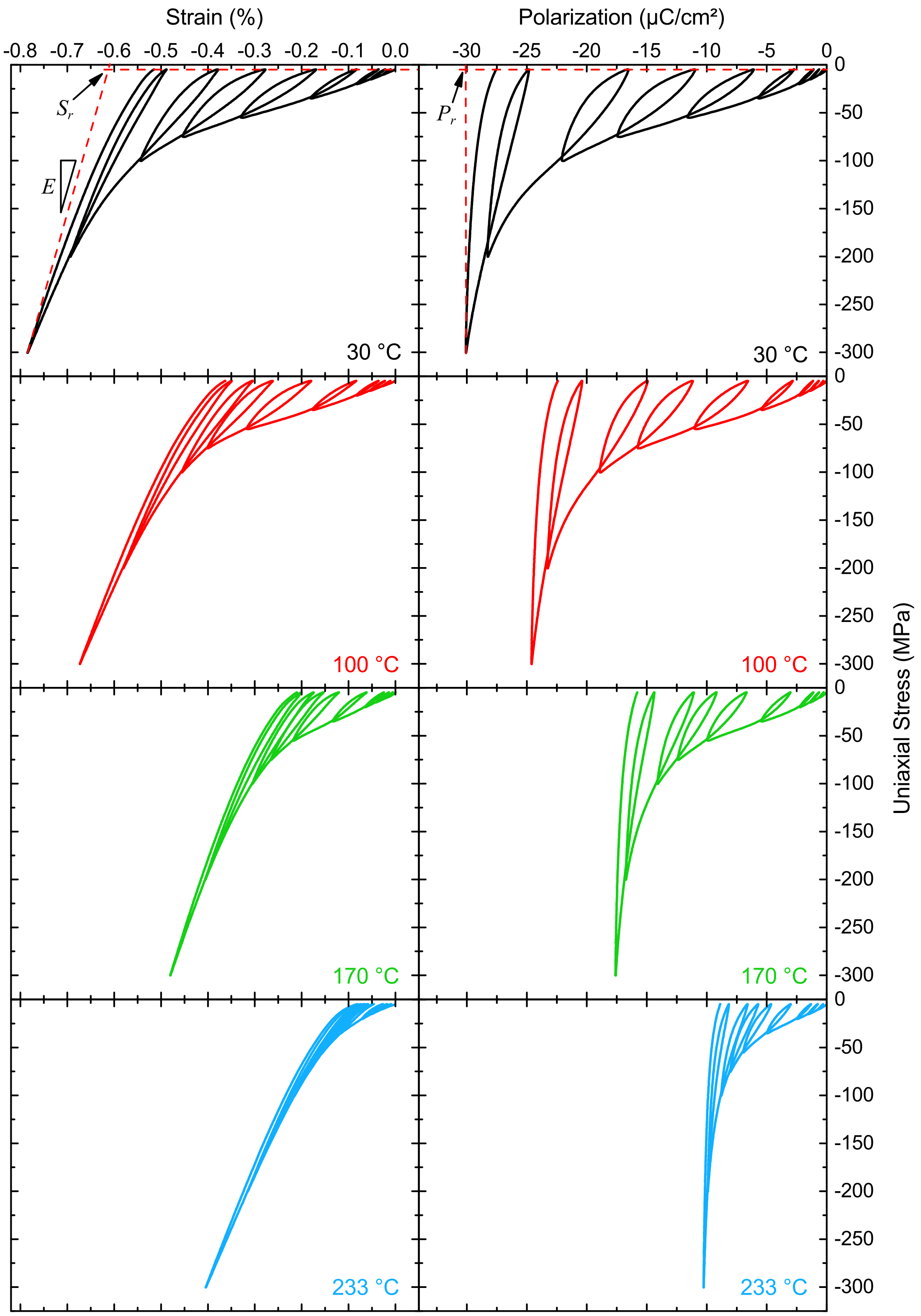

Figure 4.10: Strain and polarization of soft PZT (PIC151) as a function of uniaxial compressive stress during full unloading experiments at different temperatures. In the top left diagram it is shown how the ideal remanent strain S_r with respect to the −5 MPa preload was determined.

further analyze the results of the ferroelastic measurements presented above, a comparison of the ideal remanent strain S_r and the ideal remanent polarization P_r as a function of uniaxial mechanical compressive stress is presented in Figure 4.11 for different representative temperatures.

Figure 4.11 shows that S_r and P_r increased with increasing maximum applied stress, which has been previously observed in various ferroelastic materials [44, 420]. At stress levels above the coercive stress, which was determined to approximately –50 MPa for PIC151 at room temperature [44], the increase of remanent values showed the onset of saturation. However, additional evolution of the remanence was observed with increasing stress, indicating that the maximum applied stress of –300 MPa at room temperature was not enough to ferroelastically switch all available domains. It is expected that a further increase in stress would result in a full saturation of the remanent strain and polarization, even at room temperature.

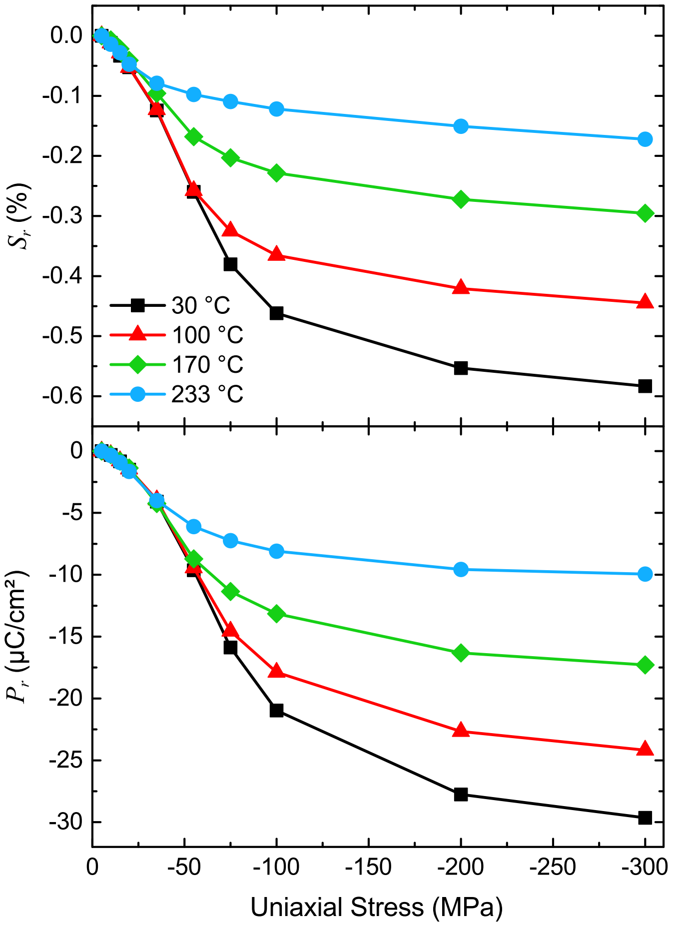

Figure 4.11: Ideal remanent strain S_r and ideal remanent polarization P_r of soft PZT (PIC151) as a function of uniaxial compressive stress at different constant temperatures.

At elevated temperatures, a corresponding decrease in both the remanent strain and the remanent polarization was observed. The ideal remanent strain and polarization at maximum stress were found to be reduced from –0.58 % to –0.17 % and –29.6 C/cm^2 to –10.0 C/cm^2 during heating from room temperature to 233 °C, representing a decrease of approximately 71 % in S_r and 66 % in P_r. A reason for these observations was that the fraction of domains parallel to the loading direction decreased with increasing temperature due to thermal depoling. As a result, less ferroelastic switching processes were possible at elevated temperatures, leading to a reduced remanent strain. Interestingly, the saturation behavior showed an apparent temperature dependence, *i.e.* the remanent strain and polarization revealed a saturation beginning at a lower applied stresses with increasing temperature. These effects also originated from a thermally enhanced ferroelasticity due to the decreasing coercive stress with increasing temperature, leading to a shift of the onset of the saturation to lower stresses at higher temperatures [44].

Finally, the ideal remanent strain and polarization were normalized by their respective maximum values, which is shown in Figure 4.12. The data for d_{33} were taken from Figure 4.3, while the data for S_r and P_r were extracted from Figure 4.11. Up to a compressive stress of –20 MPa the room-temperature d_{33} was found to be stable and not affected by the mechanical load. The onset stress, at which ferroelastic domain switching starts, is approximately –25 MPa for the PIC151 composition [47], which means that no significant ferroelastic response and, therefore, only little change in d_{33} is expected below this stress. At higher mechanical loads, the piezoelectric coefficient decreased due to mechanical depolarization and increased domain wall clamping. A similar stress-dependent decrease was also observed by Ehmke *et al.* in perovskite $(1\text{–}x)\text{Ba}(\text{Zr}_{0.2}\text{Ti}_{0.8})\text{O}_3\text{–}x(\text{Ba}_{0.7}\text{Ca}_{0.3})\text{TiO}_3$, which was attributed to a combination of ferroelastic switching and a reduction in domain wall mobility with applied stress using ex-situ XRD analysis [366]. In addition to stress, temperature also played an important role. The decrease of all three parameters at higher temperatures already appeared at lower stresses, which corresponded to previous temperature-dependent stress-strain data showing a decrease in onset stress at elevated temperatures [43, 44, 421]. Therefore, domain switching occurred at lower stresses and the material mechanically depoled faster with respect to the applied stress.

The change in the piezoelectric coefficient was found to be closely correlated to the stress-dependent decrease in the ideal remanent strain and polarization, as depicted in Figure 4.12. The overall trend remained constant with increasing temperature, while the critical stress at which the piezoelectric coefficient and remanent properties decrease was found to decrease. Although it is anticipated that ferroelasticity and domain wall clamping both contribute to the decreasing piezoelectric response with increasing mechanical loading, it was not possible to clearly separate these contributions with the current measurements. It can also be observed that the d_{33} values saturate more quickly with increasing temperature than the ideal remanent strain and polarization, marked

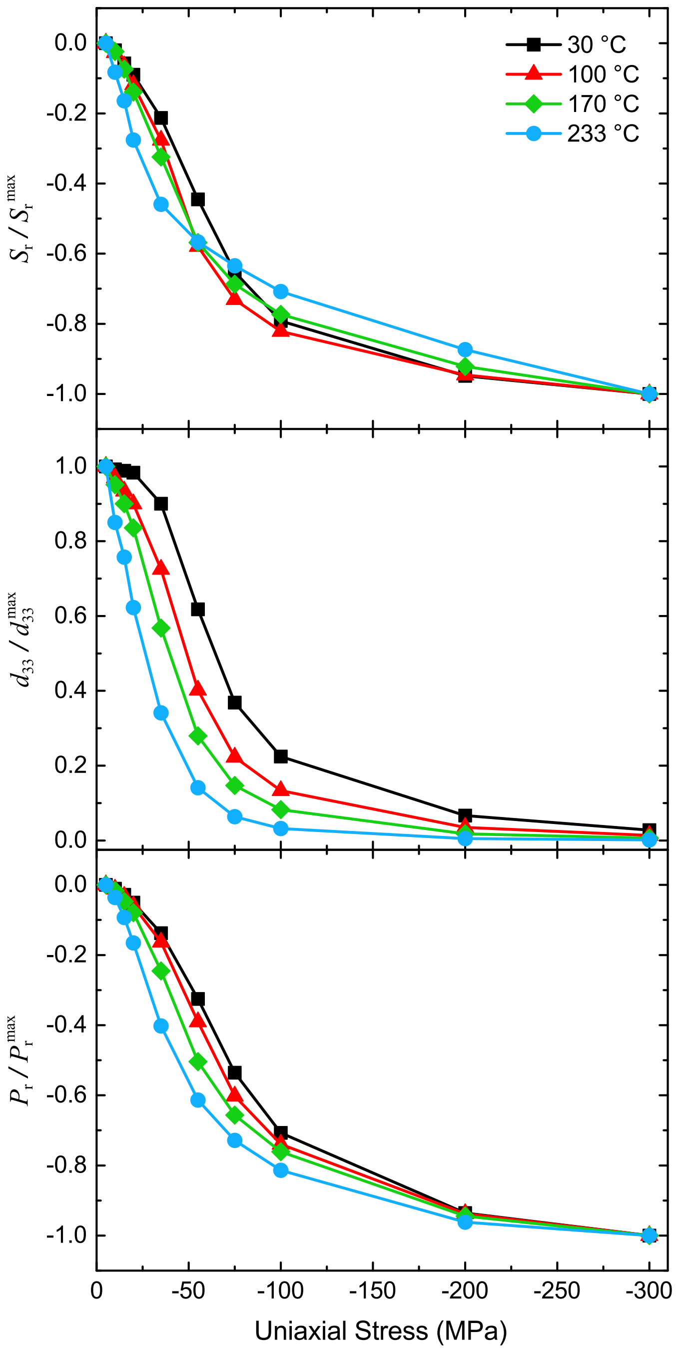

Figure 4.12: Ideal remanent strain S_r, piezoelectric coefficient d_{33}, and ideal remanent polarization P_r of soft PZT (PIC151) as a function of uniaxial compressive stress at different temperatures. The data for d_{33} were taken directly from Figure 4.3, while the data for S_r and P_r were extracted from Figure 4.11. All values are normalized to their maximum values to facilitate a direct comparison.

by a nearly flat d_{33}-stress relationship above approximately −100 MPa at, for example, 233 °C. In order to explain these findings it is also important to note that the remanent strain and polarization are quasi-static values, while the piezoelectric coefficient was measured dynamically. The small-signal d_{33} values included primarily reversible contributions, whereas the only contributions to the remanent values S_r and P_r were irreversible processes like domain switching (see Section 1.6.2). Therefore, different effects of the applied uniaxial mechanical stress on these contributions could be the origin of the observed differences in the behavior of d_{33}, S_r, and P_r. At loads above –55 MPa the curve of the ideal remanent strain at 233 °C differed from the expected behavior based on the results of the d_{33} and polarization measurements. The $S_r/S_r^{\max}$ decreased with a lower rate compared to the other temperatures, which was not observed in the polarization measurements and cannot be clearly explained with the current experimental data.

In conclusion, an apparent temperature-dependent correlation could be made between the ferroelastically-induced domain texture, as determined by P_r and S_r values, and the change of the piezoelectric coefficient for soft PIC151.

4.4 Mechanical Stability of Piezoelectric Properties of Ferroelectrically Soft and Hard PZT

The aim of this section is determine the stress-dependent piezoelectric properties of hard and soft PZT. A particularly strong focus is on the possible influence of the mechanical load on the orientation and the movement of polar defects that are present in the hard PZT material PIC181 due to the additional acceptor dopant elements in this composition (see Section 1.10.3). For all mechanical measurements presented in this section, the cylindrical shaped polycrystalline samples were used. All measurements were done using the experimental setup described in Section 2.5.

Following the machining process, all samples were annealed at 450 °C for 30 min and slowly cooled to room temperature with a maximum cooling rate of 1 °C/min. For the subsequent poling process at 150 °C, a d.c. electric bias field of 3 kV/mm was applied to the samples for 5 min while they were located in a temperature controlled silicone oil bath. For achieving an optimum poling efficiency, the samples were cooled down to room temperature with the electric field still applied. A minimum waiting time of 24 h was used before the experiments were performed. The stress-dependent piezoelectric coefficient of PIC151 and PIC181 at room temperature was characterized at uniaxial compressive stresses between –5 MPa and –400 MPa and at frequencies between 5 mHz and 240 Hz. During the measurement a dwell time of 5 min was used at each stress step to ensure steady-state conditions. The load amplitude and the capacitance of the reference capacitor were chosen to be ±0.5 MPa and 4.514 μF, respectively, where the load amplitude was readjusted at each load step to account for variations in the sample's elastic stiffness. Figure 4.13 depicts the results of the measurements for both PIC151 and PIC181.

As shown in Section 4.2, the soft PIC151 displayed a d_{33} of 550 pC/N to 600 pC/N at a preload of –5 MPa, compared to the hard PIC181, which showed a d_{33} of only 250 pC/N to

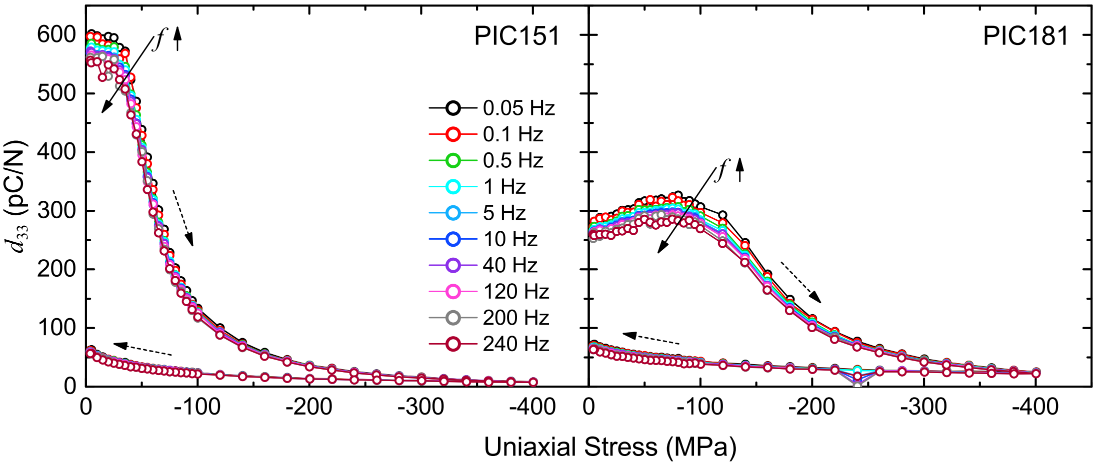

Figure 4.13: Frequency-dependent piezoelectric coefficient d_{33} during uniaxial compressive loading soft (PIC151) and hard (PIC181) PZT. The solid arrows indicate the direction of increasing measurement frequency, which was varied from 50 mHz to 240 Hz. The dashed arrows illustrate the loading direction. (after Ref. [409])

300 pC/N. In both cases, a frequency dispersion was observed, as seen in Figure 4.13, where the solid arrows indicate increasing measurement frequency. The lower piezoelectric response of the hard material originated from the pinning of the domain walls by polar defects, which significantly reduced the intrinsic d_{33} contribution [21]. Above a stress level of approximately –25 MPa, the d_{33} of PIC151 showed a sharp decrease, which coincided with the onset stress of ferroelastic switching in this material, *i.e.*, the stress at which the stress-strain curve of the material deviated from a linear behavior [44]. Above this stress, domains started to ferroelastically switch from an initial alignment parallel to the loading direction into a perpendicular orientation (see also Figure 3.2). This resulted in a loss of the macroscopic polarization and therefore a decrease in the piezoelectric coefficient. In addition, the increasing mechanical stress hindered the domain wall motion due to clamping, which further reduced the piezoelectric response. An apparent saturation of these effects could be observed for PIC151 at stresses above –300 MPa, but a d_{33} of approximately 8 pC/N was still measureable at the highest investigated mechanical load of –400 MPa. This is due to the fact that not all existing domains could be ferroelastically switched at this load. In order to make sure that this low d_{33} value is not a measurement artifact, the same measurement was done with polycrystalline alumina, which revealed a d_{33} value of 0 pC/N as expected. At this juncture, the resolution of the apparatus could be determined to be 0.1 pC/N, as already mentioned in Section 4.2. During unloading, the measurements on PIC151 (Figure 4.13) revealed a partial recovery of the initial d_{33} value to 62 pC/N due to backswitching of domains and the reduced clamping of domain walls with decreasing mechanical compression. The overall behavior of the stress-dependent piezoelectric coefficient of PIC151 is similar to that observed in other perovskite ferroelectrics [366].

In contrast to the observations made for PIC151, the stress-dependent behavior of the hard PZT composition PIC181 was significantly different (Figure 4.13). With increasing mechanical compression an initial increase of d_{33} was found, showing a maximum at approximately –75 MPa. This behavior has already been reported in literature, where a similar increase in d_{33} has been observed in Fe-doped PZT [408]. However, the subsequent decrease of d_{33} with further increasing stress shown in Figure 4.13 was not observed in this study, because the maximum applied mechanical load was –80 MPa. In contrast, Zhang *et al.* found qualitatively comparable experimental results for soft and hard PZT at higher stresses [362]. The occurrence of the maximum in $d_{33}(X)$ was understood to be due to an internal electric field created during the poling process. The polar defects present in PIC181 aligned with the electric poling field applied at a temperature of 150 °C, at which the polar defects were considered to be already mobile, *i.e.* able to reorient [196]. Since the mobility of the polar defects was considerably reduced at lower temperatures, most of the defect dipoles remained in that orientation during cooling the samples to room temperature with the d.c. electric poling field still applied. These properties of polar defects were previously reported by Warren *et al.* in Fe-doped barium titanate, who demonstrated a nearly four orders of magnitude longer reorientation time of the polar defects in an electric field at 24 °C compared to 100 °C [196].

An alignment of the polar defects with the d.c. electric field during poling resulted in an shifting of the polarization-electric field hysteresis loop along the electric field-axis [192], which was due to the formation of an internal net electric field. Similar increases in the electric field-induced unipolar strain with applied mechanical bias stress have been observed for other ferroelectric materials as well [324, 364, 372]. The underlying mechanism of this increase could also explain previous electric field-dependent measurements of the indirect d_{33}, which showed similar results for aged, Fe-doped PZT [422]. In particular, if the applied uniaxial compressive stress was increased, the domains are able to ferroelastically switch to positions away from the direction of the applied electric field, resulting in an increased unipolar strain response, because more domains are available for ferroelectric switching due to the application of the external electric field. At sufficiently higher stresses the mechanical load clamps more of the domains and the applied electric field is not able to switch these domains anymore, which subsequently leads to a reduced unipolar strain response [324, 364, 372].

The observed maximum in $d_{33}(X)$ in Figure 4.13 can be rationalized in a similar manner, namely by replacing the external electric field with the internal electric field created by the aligned polar defects. With increasing mechanical compression, the stress and internal electric field acted antagonistically, resulting in an increased piezoelectric response due to the domain walls over-coming the pinning of the polar defects with the application of stress. With further loading, the domain walls became mechanically clamped and the material was depolarized due to irreversible ferroelastic domain switching process. These effects finally overcame the influence of the internal electric field at mechanical stresses above –75 MPa and led to the observed decrease of the piezoelectric coefficient of PIC181 with increasing mechanical stress, similar to the findings for the soft PZT composition PIC151. It is expected that with the application of a larger stress amplitude and/or an increased degree of orientation of the polar defects parallel with loading direction, *i.e.* an increased internal electric field, the maximum in $d_{33}(X)$ would shift to higher stresses.

A nonlinear increase in d_{33} during unloading could be revealed from Figure 4.13 for both PIC151 and PIC181. This increase originated from reduced domain wall clamping and from domain backswitching. Since the tested materials were of polycrystalline nature, local stresses and electric fields are present due to defects and inhomogeneities. Some domains, which were ferroelastically switched during loading, could be forced back to their initial orientations by these local fields if they were sufficiently large, resulting in an increased piezoelectric coefficient during the unloading of the sample. The soft material PIC151 showed a recovery of the piezoelectric coefficient from approximately 8 pC/N at –400 MPa to 62 pC/N at –5 MPa, which was only about 10 % of the initial value. In comparison to that, the measured value of d_{33} of hard PIC181 increased from 25 pC/N at –400 MPa by 26 % to 70 pC/N at –5 MPa. A significantly larger effect was expected for PIC181 due to the influence of the polar defects and the correspondingly larger internal electric field, which would act to reorient the domains to a larger extent after unloading if the internal field was stable under load. The loss of an apparent internal bias field indicates that the external stress likely resulted in a reorientation of the polar defects. Indeed, previous experiments showed a decrease in the asymmetry of the polarization-electric field hysteresis loop, *i.e.* a reduced internal electric field, of hard PZT after the application of a uniaxial mechanical compressive stress up to 20 h [41]. In addition, the initially large frequency dependence of d_{33} was only weakly recovered after unloading (Figure 4.13).

In order to elucidate the effect of a mechanical stress on the internal electric field in PIC181, $P(E)$ hysteresis loops of differently treated samples were measured at room temperature. The results are depicted in Figure 4.14, which shows $P(E)$ hysteresis loops of an annealed sample, an electrically poled sample, and a sample after the stress-dependent d_{33} measurements in Figure 4.13. The pinched $P(E)$ loop of the annealed, initially unpoled PIC181 sample showed a clear influence of the polar defects, which pinned the domains in their original orientation. A certain electric field level was required to overcome this hindering, which resulted in the observed pinching of the $P(E)$ hysteresis loop. In contrast to that, the sample poled with a d.c. electric field showed a highly asymmetric $P(E)$ loop and an internal bias field of $E_i = -0.68\,\mathrm{kV/mm}$, where $E_i = \frac{1}{2}\left(E_C^{(+)} - \left|E_C^{(-)}\right|\right)$ and $E_C^{(+)}$ and $E_C^{(-)}$ are the positive and negative coercive fields, respectively. The internal bias field was found to be decreased to –0.25 kV/mm for the sample tested after the stress-dependent measurement of the piezoelectric coefficient shown in Figure 4.13, *i.e.* after loading the sample to a maximum mechanical stress of –400 MPa. This result corresponds very well with the previously made conclusion that a uniaxial mechanical compression has a significant influence on the orientation of polar defects.

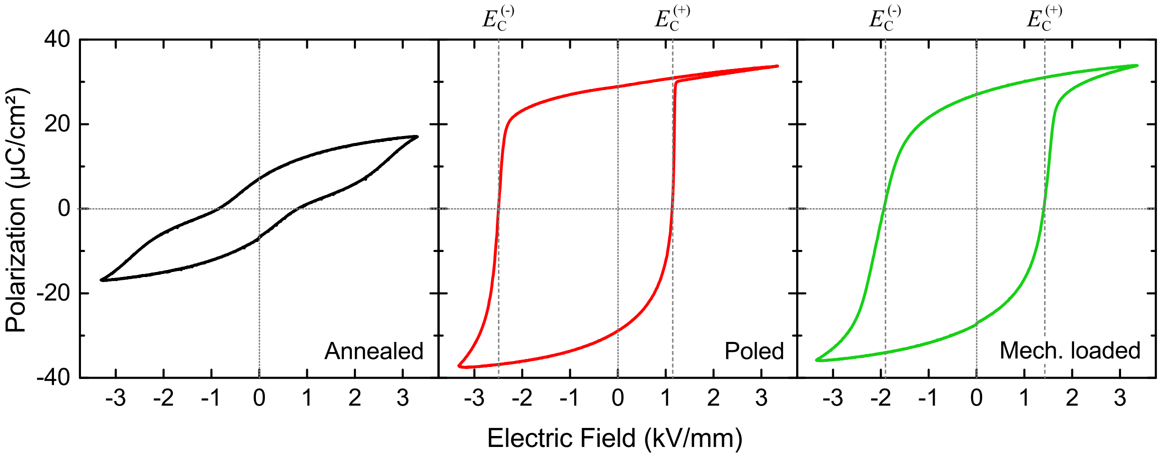

Figure 4.14: Room-temperature polarization-electric field hysteresis loops of hard PZT (PIC181) at 50 mHz after annealing, poling, and mechanical loading. (after Ref. [409])

One of the most apparent effects of the polar defects in PIC181 is the pinning of domain wall motion due. An evaluation and comparison of the frequency dispersion of both investigated soft and hard PZT compositions could help to elucidate the stress dependence of the reversible and irreversible domain wall motion [22, 23]. Therefore, Figure 4.15 shows the frequency dependence of the piezoelectric coefficient of PIC151 and PIC181 at different selected uniaxial mechanical bias stresses between –5 MPa and –400 MPa. The d_{33} data used for the evaluation was taken from the measurements in Figure 4.13.

It can be revealed from an analysis performed by Prof Dr. Kyle G. Webber that both materials showed a linear decrease of the piezoelectric coefficient as a function of the natural logarithm of the frequency (Figure 4.15), similar to previous findings in literature [23]. This Rayleigh-type relation originates from the relaxation characteristics of the domain wall motion in ferroelectrics, especially in connection with pinning centers like polar defects and can be described with the following equation [22]:

$$d_{33}(f) = d_0 - \beta \ln(f). \qquad (4.2)$$

In Equation 4.2, d_0 is the static piezoelectric coefficient and represents the frequency-independent contribution to the piezoelectric response of the material. β is the slope of the $d_{33}(f)$ curve and stands for the frequency sensitivity of the domain wall motion.

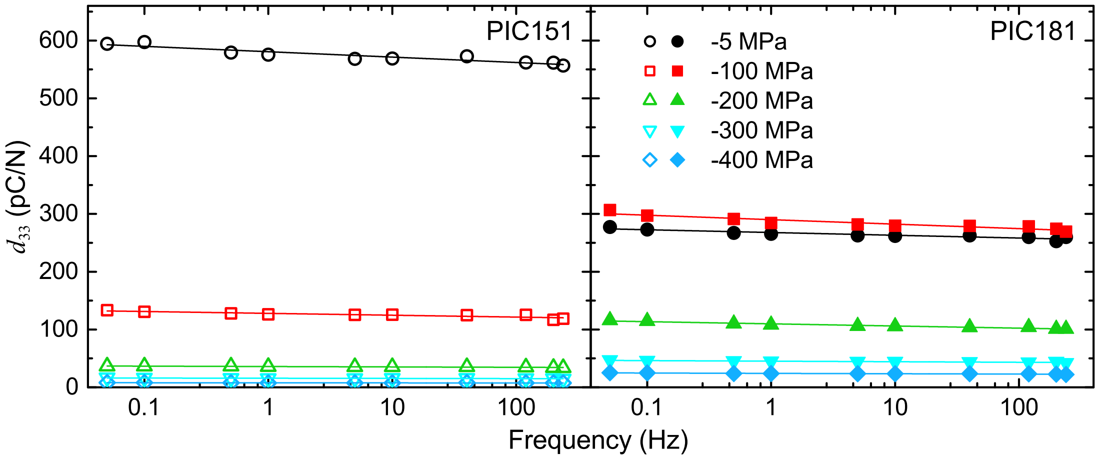

Figure 4.15: The frequency-dependent direct piezoelectric coefficient for soft (PIC151) and hard (PIC181) PZT at selected uniaxial compressive bias stresses. The solid line represents a linear regression based on Equation 4.2. (after Ref. [409])

It is apparent from Figure 4.15 that both parameters were stress-dependent and consequently Figure 4.16 shows d_0 and β of PIC151 and PIC181 as a function of uniaxial mechanical compressive stress, determined by a linear regression of the data in Figure 4.15.

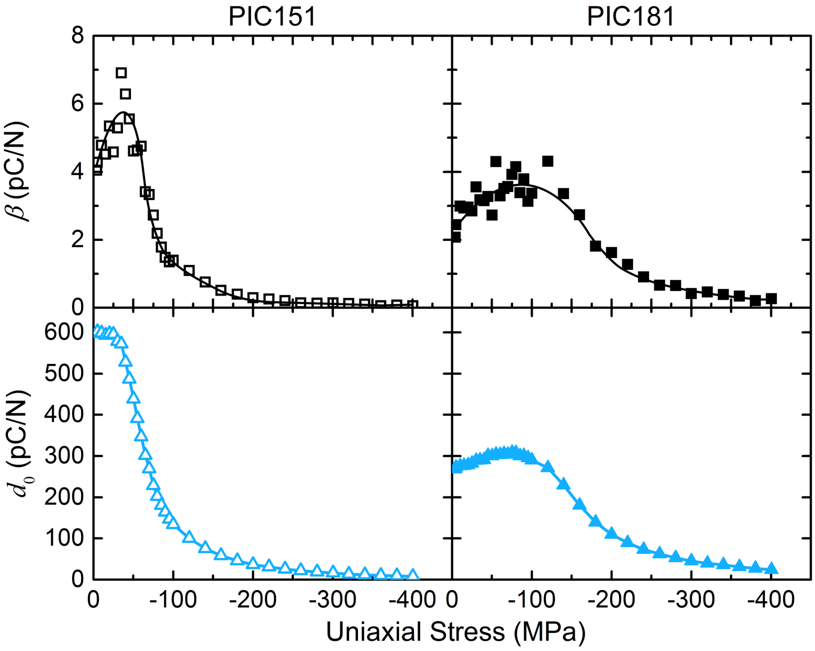

Figure 4.16: The material parameters β and d_0 as a function of uniaxial compressive stress in soft (PIC151) and hard (PIC181) PZT. The lines are only meant to guide the eye. (after Ref. [409])

Both PIC151 and PIC181 revealed an initial increase in β with increasing mechanical stress and showed a maximum in $\beta(X)$ at –34 MPa and –84 MPa, respectively. These critical stresses corresponded well to the observed onset of the piezoelectric coefficient decrease (Figure 4.16). It could be concluded that the irreversible domain wall motion was initially increased for both PIC151 and PIC181 with increasing mechanical compressive stress due to the release of local, internal stresses, and, in the case of hard PIC181, due to the stress-induced unpinning of the domain walls. The subsequent decrease of β with further increasing stress could then be attributed to an increased domain wall clamping. d_0 as a function of stress showed a similar trend to that of the stress-dependent d_{33} as observed in Figure 4.16. Interestingly, the contribution of β was found to be rather small and consequently the stress dependence of the parameter d_0 dominated the overall piezoelectric response of both PIC151 and PIC181.

In order to better understand the effect of the internal electric bias field in hard PZT, quenching experiments were performed on PIC151 and PIC181. All samples were annealed at 450 °C for 5 h and afterwards either slowly cooled to room temperature with a maximum cooling rate of 1 °C/min or quenched in air. Immediately after the cooling-down, the samples were electrically poled at 3 kV/mm for 5 min either at room temperature or at 150 °C. In the latter case, the d.c. electric poling field remained applied to the samples also during cooling. Stress-dependent d_{33} measurements were performed directly after poling without any further waiting time, but in the exact same manner as the measurements presented in Figure 4.13. The results of these experiments are presented in Figure 4.17, which shows only the 10 Hz signal and only the loading branch of the measurement for the sake of clarity.

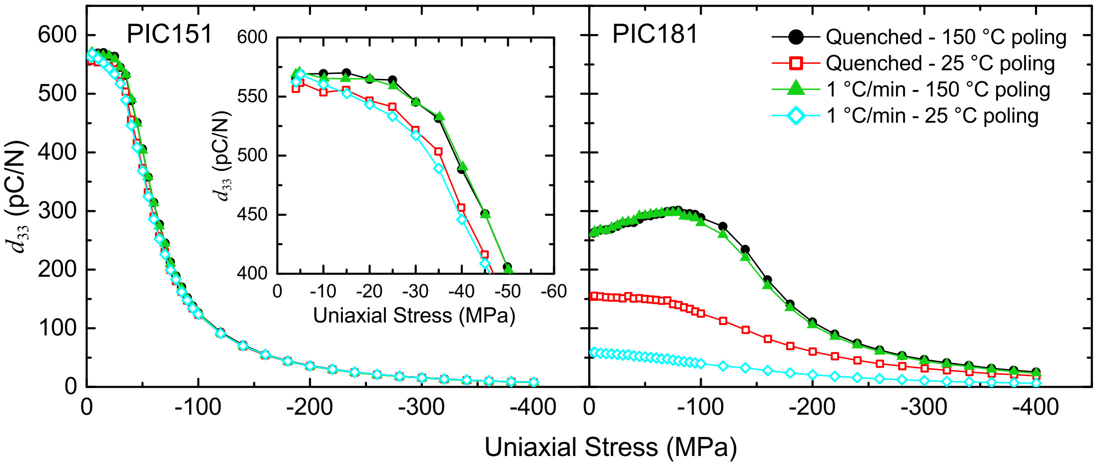

Figure 4.17: The stress-dependent direct piezoelectric coefficient of air quenched and slowly cooled (1 °C/min) soft (PIC151) and hard (PIC181) PZT, both electrically poled at either 25 °C (open symbols) or 150 °C (closed symbols), and measured at a frequency of 10 Hz. (after Ref. [409])

The soft PZT composition showed nearly no difference piezoelectric coefficient as a function of stress for all sample treatments. Only a minor difference appeared at lower stresses between the samples poled at high temperature and the ones poled at room temperature. It is therefore assumed that the concentration of polar defects in PIC151 is relatively small, consistent with all other observations and results discussed in this chapter. In contrast, the results for PIC181 in Figure 4.17 revealed significant changes in the stress dependence of d_{33} for differently cooled and poled samples. The piezoelectric coefficient was found to be lower for samples poled at room temperature than for samples poled at 150 °C, accompanied by the vanishing of the maximum in $d_{33}(X)$. Additionally for the samples poled at 25 °C, the slowly cooled samples showed a nearly two times smaller d_{33} than the quenched samples. When both samples were poled at 150 °C, however, they revealed exactly the same behavior including a maximum in $d_{33}(X)$ regardless of the cooling method after annealing. It can be concluded that a d.c. electric field of 3 kV/mm was large enough to realign the polar defects in PIC181 at a poling temperature of 150 °C. This is supported by observations made for Fe-doped PZT by Zhang and Ren, who found the pinched polarization hysteresis loop of this material to disappear at temperatures above 125 °C, which was attributed to the relaxation of the orientation of the polar defects [423].

All the observations regarding the behavior of PIC181 described above originated from the relative orientation of the polar defects and the ferroelectric domains with respect to the poling/loading direction, in combination with their subsequent modification by uniaxial mechanical stress applied to the electrically poled samples. The orientation of the polar defects and the domains could influence the energy profile of the domain wall and could therefore have a significant influence on the material behavior, as pointed out by Robels and Arlt [202]. In general, the polar defects are mobile at elevated temperatures and their orientation can be changed relatively easily by internal and external electric fields. If the material is cooled below the Curie point, domains are formed that can reorient the polar defects parallel to the local spontaneous polarization of the domain. With further cooling, the polar defects become less mobile and act to hinder the domain wall motion, resulting in a reduced poling efficiency at room temperature and decreased extrinsic contributions to the piezoelectric coefficient. This configuration is schematically shown in Figure 4.18a.

The situation is substantially different in quenched samples poled at room temperature, as the polar defects do not have sufficient time to align with the local spontaneous polarization of the ferroelectric domains as they form during cooling. As a result, some polar defects are oriented in directions other than the domains in which they reside, which is schematically depicted

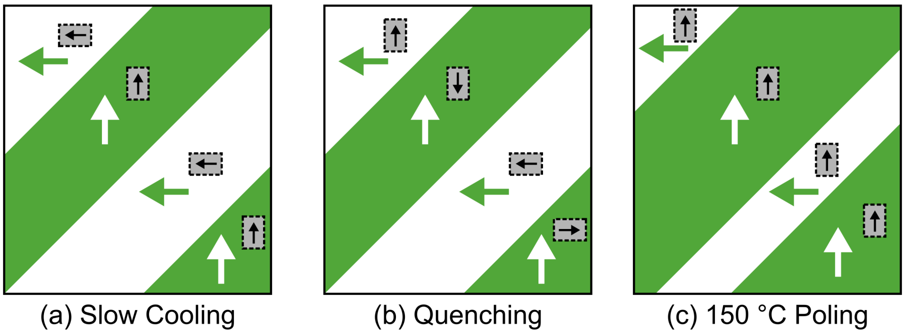
(a) Slow Cooling
(b) Quenching
(c) 150 °C Poling

Figure 4.18: Schematic of the room-temperature domain structure in relation to the orientation of the polar defects for slowly (a) cooled samples, (b) quenched samples, and (c) samples poled at 150 °C. (after Ref. [409])

in Figure 4.18b. The formation of domains occurs by ion displacement in the unit cell, whereas the reorientation of polar dipoles is a diffusion process. This results in two different timescales. While the former process is (on an atomic scale) nearly instantaneous, a significantly longer time is needed for the latter process, which is also highly temperature-dependent [198, 199]. The consequences of the quenched configuration in Figure 4.18b are an increased poling efficiency at room temperature and a larger piezoelectric response, since some polar defects might favor changes in the polarization direction. Both orientation configurations of the polar defects in Figure 4.18a and Figure 4.18b remain mostly stable if the samples are poled at room temperature and no internal bias field can develop. This corresponds to the measurements in Figure 4.17 for PIC181, which did not show a maximum in $d_{33}(X)$ for the samples poled at room temperature, but did show an increase in the value of d_{33} for quenched sample compared to the slow cooled one.

The increased piezoelectric response of the samples poled at high temperatures could be rationalized by the assumption that the polar defects were more thoroughly aligned with the electric poling field at higher temperatures, which created an internal bias field (see Figure 4.18c). This internal field persisted during cooling and therefore partially prevented the backswitching of domains when removing the dc poling field at room temperature. This should then lead to a stabilization of the domain structure formed at higher temperatures and to an enhanced piezoelectric response of the material. Within the framework presented here and with the schematic display in Figure 4.18, the observations for PIC181 described and discussed above could be easily rationalized. However, it is important to note that the experiments could not give a final answer as to whether a mechanical load acts on polar defects directly or indirectly via the ferroelastic switching of domains. In-situ characterization techniques, such as electron paramagnetic resonance, could directly observe the influence of external stress on the reorientation of polar defects in perovskite crystals.

4.5 Phase Transitions in Ferroelectric PIN-PMN-PT Single Crystals under Uniaxial Mechanical Compression

Ferroelectric single crystals are of particular importance for applications like sonar transducers [243, 244] or energy harvesters [248] due to their extraordinary electromechanical properties. These and other devices are often exposed to mechanical stresses during their usage that can highly influence their piezoelectric properties and their phase transition behavior. An overview of such effects has already been given in the previous Sections 4.2 – 4.4. The aim of this section is to show the phase stability and piezoelectric properties of $x\mathrm{Pb(In_{1/2}Nb_{1/2})}$–$(1{-}x{-}y)\mathrm{Pb(Mg_{1/3}Nb_{2/3})}$–$y\mathrm{PbTiO_3}$ (PIN-PMN-PT) single crystals under the influence of uniaxial mechanical compression and temperature. A more detailed overview about properties, advantages and disadvantages of ferroelectric single crystals can be found in Section 1.11.

All ferroelectric $<001>_{PC}$-oriented PIN-PMN-PT single crystals investigated in the present work were provided by TRS Technologies Inc. (State College, PA, USA). Figure 4.19 shows one of the single crystals with dimensions of 4 x 4 x 12 mm^3. An inductively coupled plasma optical emission spectrometry performed on one of the provided crystals at the Friedrich-Alexander-Universität Erlangen-Nürnberg (Erlangen, Germany) revealed a composition of 26.43 mol% PIN, 46.51 mol% PMN, and 27.06 mol% PT. The crystals possessed a rhombohedral symmetry at room temperature [424]. The electrical poling process was done by the manufacturer along the $[001]_{PC}$-direction, corresponding to the 12 mm edge. This resulted in a domain engineered state with four equivalent possible orientations of the polarization in the $<111>_{PC}$-directions [352, 425]. Sputtered gold layers on the 4 x 4 mm^2 ends of the sample served as electrodes.

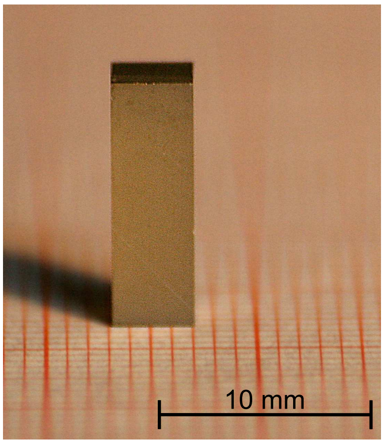

Figure 4.19: $x\mathrm{Pb(In_{1/2}Nb_{1/2})}$–$(1{-}x{-}y)\mathrm{Pb(Mg_{1/3}Nb_{2/3})}$–$y\mathrm{PbTiO_3}$ (PIN-PMN-PT) single crystalline sample manufactured by TRS Technologies Inc. (State College, PA, USA). The composition of the crystals used in this investigation was determined by inductively coupled plasma optical emission spectrometry to be 26.43 mol% PIN, 46.51 mol% PMN, and 27.06 mol% PT.

In order to investigate the influence of a uniaxial mechanical compression on the phase transitions and on the temperature evolution of the piezoelectric coefficient of PIN-PMN-PT single crystals, $d_{33}(T)$ was measured at constant mechanical loads of −5 MPa, −15 MPa, −25 MPa, and −50 MPa. The experimental procedure was previously discussed in detail (Section 2.5). A load amplitude of ±0.5 MPa was used, but due to the change of the mechanical properties of the samples with temperature this amplitude varied between ±0.3 MPa and ±1.1 MPa, depending on frequency and temperature. For the small signal d_{33} measurements frequencies between 0.1 Hz and 240 Hz were used and the uniaxial mechanical stress was applied along the 12 mm length, *i.e.* along $<001>_{PC}$-direction of the crystal. The capacitance of the reference capacitor was chosen to be 4.514 μF. During the measurements, the samples were continuously heated with a rate of 1 °C/min up to 140 °C.

Figure 4.20a shows the temperature-dependent d_{33} measurements at a mechanical preload of −5 MPa at various frequencies. The piezoelectric coefficient measured at 10 Hz increased sig-

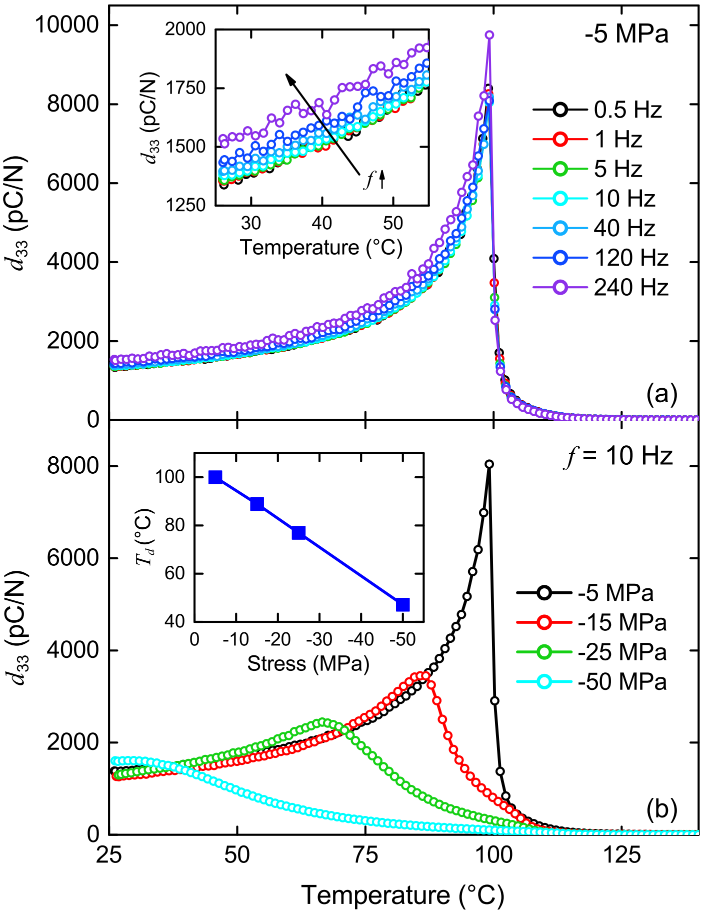

Figure 4.20: Temperature-dependent piezoelectric coefficient d_{33} of $<001>_{PC}$-PIN-PMN-PT single crystals at (a) different frequencies between 0.5 Hz and 240 Hz at a constant uniaxial preload of −5 MPa and (b) different bias stresses between −5 MPa and −50 MPa at a constant measurement frequency of 10 Hz. The inset in (a) shows details of the d_{33}-temperature curves, whereas the inset in (b) depicts the depolarization temperature T_d, *i.e.* the inflection point of $d_{33}(T)$, as a function of uniaxial mechanical compression.

nificantly with increasing temperature from approximately 1383 pC/N at room temperature to about 8045 pC/N at 99 °C, which represents an increase of 582 %. Compared to the observation for the modified PZT compositions discussed in Section 4.2, this value is surprisingly large. Theoretical considerations of Davies *et al.* attributed similar effects in domain engineered crystals to polarization rotation at the transition temperatures [426]. A sharp drop in d_{33} was observed at the depolarization temperature of 99 °C, which could be identified as the temperature at which the phase transition between rhombohedral and tetragonal crystal symmetry occurs in this material [235, 239].

In order to quantify the decrease of the depolarization temperature with increasing stress, the inflection points of the $d_{33}(T)$ curves at various mechanical loads were determined, similar to the approach used in Section 4.2. The results of this evaluation are depicted by the inset in Figure 4.20b, revealing a linear decrease of the inflection point of $d_{33}(T)$, *i.e.* the depolarization temperature T_d with a rate of –1.18 °C/MPa. This indicates that the increasing mechanical compression likely shifted the rhombohedral-to-tetragonal phase transition to lower temperatures, resulting in a stabilization of the tetragonal symmetry under compressive stress.

Similar to the observations for PIC151 and PIC181 in Figure 4.4 and Figure 4.5, respectively, the piezoelectric coefficient measured at –5 MPa preload did not vanish completely at T_d but rather was found to gradually decrease with increasing temperature, finally reaching a value of zero at approximately 135 °C. Figure 4.21 shows this observation in more detail and also shows its occurrence for different constant compressive bias stresses at a measurement frequency of 10 Hz.

It can be concluded that a part of the crystal was still macroscopically polarized above 99 °C in the tetragonal phase, such that the depolarization due to the phase transition was not complete at the T_d. The temperature, at which d_{33} finally vanished seemed to be shifted to higher values with increasing mechanical compression as well. Furthermore, an apparent anomaly in the gradual decrease of d_{33} with increasing temperature above T_d was observed at mechanical bias stresses above –15 MPa. These anomalies are indicated by arrows in Figure 4.21. One reason for this observation might be that a minor amount of a secondary phase was present, which was observed in optimally poled crystals [427–429]. There could also be a connection between the findings in Figure 4.21 and the appearance of the additional maximum in $d_{33}(T)$ of PIC151 and PIC181 above the depolarization temperature at higher stresses, shown in Figure 4.4 and Figure 4.5, respectively. It appears that the anomaly in the $d_{33}(T)$ of the PIN-PMN-PT single crystals would also have become more pronounced with further increases to mechanical compressive stress.

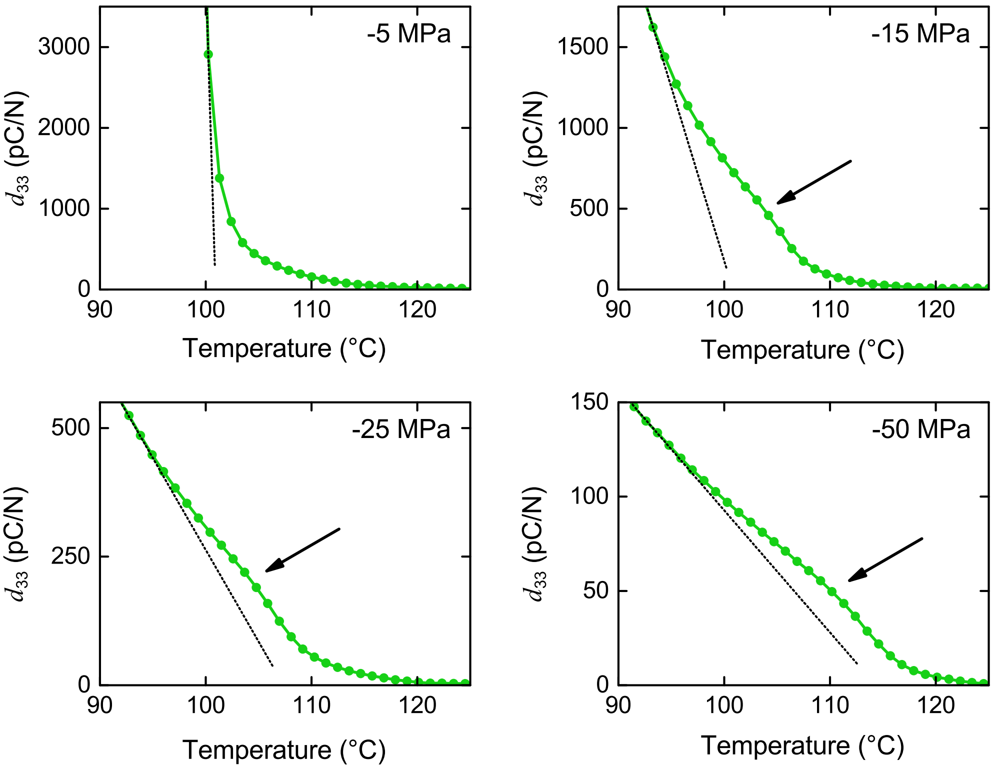

Figure 4.21: Temperature-dependent piezoelectric coefficient d_{33} of <001>$_{PC}$-PIN-PMN-PT single crystals measured at a frequency of 10 Hz at various constant mechanical bias stresses. The arrows indicate an apparent anomaly in $d_{33}(T)$ observed at stresses above −15 MPa. The dotted lines serve only to increase the visibility of the anomaly. Please note that the y-axis scale is different for each figure.

The measurements presented in Figure 4.20b indicate a stress-dependent piezoelectric coefficient of single crystalline PIN-PMN-PT at room temperature, namely there is an apparent increase in the room temperature d_{33} with increasing bias stress. Additional experiments were performed in order to investigate this in more detail. For that purpose, the stress-dependent piezoelectric response of a poled PIN-PMN-PT single crystal was characterized from –2 MPa and –200 MPa, similar to previous measurements presented for PZT (Figure 4.13). The results of these experiments are shown in Figure 4.22, where only the 10 Hz signal of two subsequent loading and unloading cycles is shown for clarity.

During the first loading cycle, d_{33} initially increased with increasing stress and showed a maximum around –50 MPa. This corresponded well to the previous observations in Figure 4.20b and could probably be related to a stress-induced phase transition from rhombohedral to orthorhombic symmetry. Such a phase transition due to the application of a mechanical stress was previously reported also for other ferroelectric single crystals [243, 425, 430]. With further increasing mechanical stress, the piezoelectric coefficient was found to decrease monotonically, which was most likely due to stress-induced domain wall clamping and also due to the switching of the polarization vector because of the still ongoing phase transition to orthorhombic symmetry. A loss in d_{33}

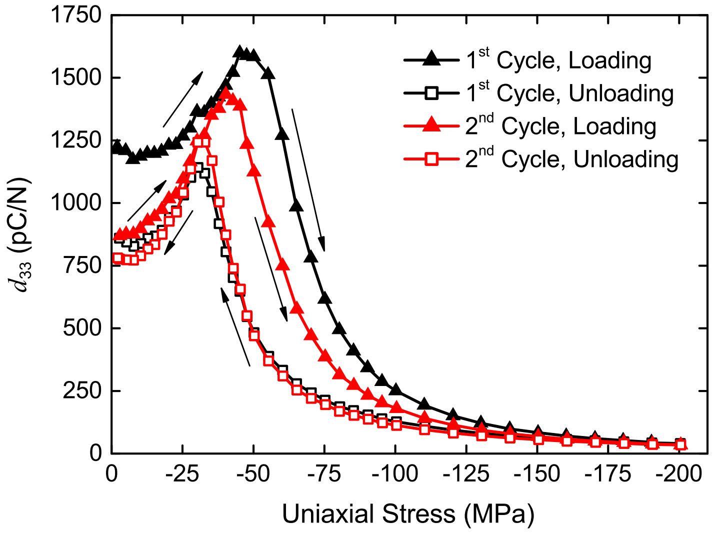

Figure 4.22: Piezoelectric coefficient d_{33} of a <001>$_{PC}$-oriented PIN-PMN-PT single crystal as a function of uniaxial compressive stress. Two subsequent loading and unloading cycles were performed at room temperature with a frequency of 10 Hz. The arrows indicate the loading and unloading directions.

of nearly 97 % was determined between –2 MPa and –200 MPa, but complete saturation to 0 pC/N was not able to be observed.

The piezoelectric coefficient increased again during unloading and also showed a maximum. This behavior was similar to the loading branch, but the maximum occurred at –30 MPa, 20 MPa lower than during loading. It is argued that this maximum in $d_{33}(X)$ could correspond to a reverse phase transition from orthorhombic back to tetragonal symmetry and therefore nearly 70 % (860 pC/N) of the initial d_{33} was recovered after unloading. This was in contrast to the findings for the soft and hard PZT materials in Figure 4.13, which revealed a recovery of the initial d_{33} value of only 10 % and 26 %, respectively. A comparable behavior of a reversible stress-induced phase transition was observed by Janolin *et al.* for $0.955\text{Pb}(\text{Zn}_{1/3}\text{Nb}_{2/3})\text{O}_3$–$0.045\text{PbTiO}_3$ (PZN-PT) single crystals [352] and by Finkel *et al.* for PIN-PMN-PT single crystals [431, 432]. An explanation for the reversibility of the stress-induced rhombohedral-to-orthorhombic phase transition in PZT-PT single crystals was given by Okawara and Armin [430]. The authors claimed that charged domain walls, created by the stress-induced phase transition, induce a driving force that reorients polarization vector switching back from the $<011>_{PC}$ orientation of the induced orthorhombic phase into the $<111>_{PC}$ orientation of the initial rhombohedral symmetry [228].

The second loading cycle in Figure 4.22 showed the same trend as the first cycle but with a lower magnitude of maximum d_{33}. However, the maximum during loading also occurred at a lower stress of –41 MPa, whereas in the unloading branch the stress at maximum d_{33} remained stable. Interestingly, the maximum value of d_{33} during unloading in the second cycle exceeded the one obtained during the first cycle. After the second compression cycle the piezoelectric coefficient was reduced by 10 % from 870 pC/N to 780 pC/N at –2 MPa mechanical preload. This was a significantly lower loss in d_{33} from the cycling process than after the first loading cycle, but still apparent. A reason for this could be that (micro-)cracks were induced into the crystal during the mechanical loading, which reduced the piezoelectric properties.

4.6 Summary

The influence of mechanical compressive stress on the temperature-dependent piezoelectric and dielectric behavior of commercial soft and hard PZT compositions was characterized from room temperature to above the ferroelectric-paraelectric phase transition temperature. It was found that a sufficiently large mechanical load significantly decreases the properties of both materials due to the stress-induced depolarization and domain wall clamping. The hard PZT, PIC181, turned out to be less stress sensitive than the soft PZT, PIC151, but showed lower overall electromechanical properties. This effect is mainly due to the existence of polar defects in the material, which stabilize the ferroelectric phase because of an internal electric bias field developed during the electrical poling process via the alignment of said polar defects. With increasing compressive stress, the ferroelectric-to-paraelectric phase transition was shifted to higher temperatures.

In addition to the temperature-dependent measurements at constant mechanical bias load, the stress-dependent piezoelectric response of hard and soft PZT was investigated as a function of frequency to elucidate the role of mechanical fields on the domain wall pinning capability of charged point defects. The findings indicated that a compressive stress could reduce the intrinsic forces generated by electrostatic ordering of the charged defect population. This resulted in the presence of a two-step depolarization in hard PZT with increasing temperature that was rationalized to be due to the increasing mobility of the charged point defects. These data, however, could not directly determine whether the observed behavior is due to the direct influence of stress on the polar defects or the indirect switching caused by reorientation of ferroelastic domains. Further stress-dependent electron paramagnetic resonance measurements are suggested in order to directly address this concern.

A mechanical compressive stress was also found to influence the piezoelectric properties and the phase transition behavior of the ferroelectric single crystalline PIN-PMN-PT. The experimental results suggested that a mechanical bias stress applied during temperature-dependent measurements stabilizes the high-temperature tetragonal phase resulting in a lower depolarization temperature. This limits the application of this material in combined high-stress and high-temperature environments. However, a significant increase in the piezoelectric response was measured in the low-stress regime at elevated temperatures below 100 °C. This could be either helpful or problematic, since a temperature-stable material response is normally preferred for many applications in real devices.

5 Lead-free Ferroelectrics and Relaxors under Uniaxial Mechanical Compression

5.1 Introduction

After investigating the dielectric, electrical, mechanical, and electromechanical properties of lead-based ferroelectrics, this chapter now deals with a modern class of lead-free piezoelectric materials: $(1\text{–}x)(\mathrm{Na}_{1/2}\mathrm{Bi}_{1/2})\mathrm{TiO}_3\text{–}x\mathrm{BaTiO}_3$. As mentioned in previous chapters, the material will be abbreviated by "NBT-xBT", where in this work x equals 3 mol%, 6 mol%, 9 mol%, and 12 mol%. These compositions where chosen because NBT-3BT and NBT-12BT are located at the rhombohedral (-3BT) and tetragonal (-12BT) side of the phase diagram (see Section 1.12.2), whereas NBT-6BT and NBT-9BT are both in the vicinity of the MPB region. NBT-6BT is on the rhombohedral side, whereas NBT-9BT is on the tetragonal side. Compositions on the rhombohedral side of the MPB, especially NBT-6BT, are considered good candidates for replacing lead-containing materials due to the previously observed large strain properties [151, 259, 262, 265].

In the following sections, the dielectric and piezoelectric properties of NBT-xBT will be investigated as a function of temperature, uniaxial mechanical compression, and frequency. Although the effect of mechanical stress is especially important for applications, it gives a deeper insight into the phase transition behavior of these materials as well. It will be shown that stress-induced phase transitions have a significant influence on the temperature evolution of the dielectric and electromechanical properties of NBT-xBT. These stress-induced results will turn out to be quite similar to the effect of an applied electric field, although a uniaxial mechanical stress induces only a two-dimensional ordering in the material and therefore some differences in the temperature dependence of the material properties will be shown and discussed.

Starting with the electrically poled samples from Section 5.2, the influence of a compressive mechanical bias stress on the depolarization and phase transition behavior of NBT-xBT will be investigated by measuring the piezoelectric coefficient and the permittivity as a function of temperature. In order to better distinguish between electrically or possibly mechanically induced phases in the material, similar measurements with electrically unpoled NBT-6BT samples will be presented, which underwent stress field cooling – stress field heating experiments. These results will be shown in Section 5.3, whereas Section 5.4 indicates that it could be possible to induce a remanent ferroelectric phase in NBT-6BT by applying a uniaxial mechanical load similar to electrical d.c. bias poling. The results and the discussion presented in this section have been published in: Schader *et al.* Physical Review B 93(13), 134111 (2016), ©2016 American Physical Society, [433]. Based on these findings and from the stress-dependent permittivity measurements at different constant temperatures, a stress-temperature phase diagram of NBT-6BT is proposed. Finally, iron-doped NBT-6BT and NBT-15BT will be qualitatively investigated in Section 5.5, with a focus on the influence of acceptor doping on the stress-dependent thermal evolution of the dielectric and piezoelectric properties of these materials.

5.2 Phase Transition Behavior of Poled NBT-*x*BT under Uniaxial Mechanical Compressive Stress

Cylindrical shaped polycrystalline samples of NBT-*x*BT with a diameter of 5.8 mm and a height of 6 mm were heated in a silicone oil bath to 150 °C. After temperature stabilization, an electric field of 2 kV/mm was applied to the samples using a high voltage power source. This was followed by cooling the samples to room temperature with the field still applied (field cooling). The samples were allowed to rest for a minimum of 24 h prior to further measurements.

Temperature-dependent measurements of the piezoelectric coefficient d_{33} and the real part ε' of the permittivity were performed using the experimental setup described in Section 2.5. This setup allowed the measurement of both properties alternately on the same sample during the same measurement and, therefore, the obtained results can be directly compared. A heating rate of 0.5 °C/min was used to ensure a sufficiently small change in temperature during one measurement cycle, especially at low frequencies. Prior to each measurement the load frame applied a constant uniaxial bias stress between –5 MPa and –300 MPa to the sample and maintained this load during the entire heating, cooling, and measurement process. The frequencies for the permittivity measurements ranged between 1 kHz and 1 MHz with a maximum applied voltage of 1 V_{rms}, but the 1 MHz signal should be treated carefully due to non-ideal electrical contacts inside the experimental setup. Furthermore, the recorded dielectric loss could not be used for analysis in this measurement series because the noise of the signal did not allow for proper quantitative evaluation. In the case of the d_{33} measurements, frequencies between 0.1 Hz and 240 Hz were used, but multiples of the 50 Hz power line frequency were specifically avoided because they were significantly disturbed by interference and, therefore, extra noisy. Since the measurements of the piezoelectric coefficient were intended to be small signal measurements where the irreversible contributions to the polarization signal are reduced to a minimum, the samples were sinusoidally unloaded with an amplitude of ±0.5 MPa, resulting in a maximum periodical unloading of 1 MPa (see Section 2.5 and Figure 2.6). A reference capacitor with a capacitance of 4.514 μF was chosen for the d_{33} measurements.

Figure 5.1 and Figure 5.2 show the results of all measured frequencies for NBT-3BT and NBT-12BT, respectively, at four representative bias stresses of –5 MPa, –50 MPa, –100 MPa, and –300 MPa. NBT-3BT and NBT-12BT are located away from the MPB in the NBT-xBT system and possess ferroelectric rhombohedral and tetragonal symmetry, respectively [144]. Similar poling effects were observed in other relaxor ferroelectrics as well [135, 434, 435]. The induced ferroelectric order was also reflected by the comparatively low frequency dispersion of the permittivity below the depolarization temperature. In NBT-3BT, a discontinuity (see arrows in Figure 5.1) in the permittivity curve marks the depolarization temperature T_d. This occurs at approximately 172 °C (inflection point of the $\varepsilon'(T)$ curve) in the case of the measurement at –5 MPa preload. Above this temperature, the material is expected to be in the relaxor state [410] and finally, at temperatures above the Burns temperature should reach the paraelectric phase [436]. This same kind of phase evolution is assumed to happen in all of the NBT-xBT compositions investigate here.

The piezoelectric coefficient increased with increasing temperature nearly by a factor of 2 below T_d at –5 MPa preload. This is attributed to thermally enhanced domain wall oscillations as well as to the similarly increasing permittivity, which is coupled via Equation 4.1 to d_{33}. A maximum in d_{33} occurred at 169 °C, followed by a drop at the depolarization temperature. This decrease in d_{33} was spread over a temperature interval of approximately 19 °C, which likely indicates that different volume fractions of the sample possessed different depolarization temperatures. Around the maximum, the piezoelectric coefficient showed increased frequency dispersion similar to the permittivity.

With increasing mechanical compressive stress, the shoulder in the $\varepsilon'(T)$ curve occurring at T_d was found to become more pronounced and widened, whereas the frequency dispersion nearly vanished at –300 MPa. Simultaneously, the maximum in the piezoelectric coefficient became more and more suppressed with increasing load, finally resulting in a monotonic, less frequency dispersive decrease of d_{33} with increasing temperature at –300 MPa. The decrease in frequency dispersion in both d_{33} and ε' at higher stresses could be mainly attributed to domain wall and PNR clamping at such high loading conditions.

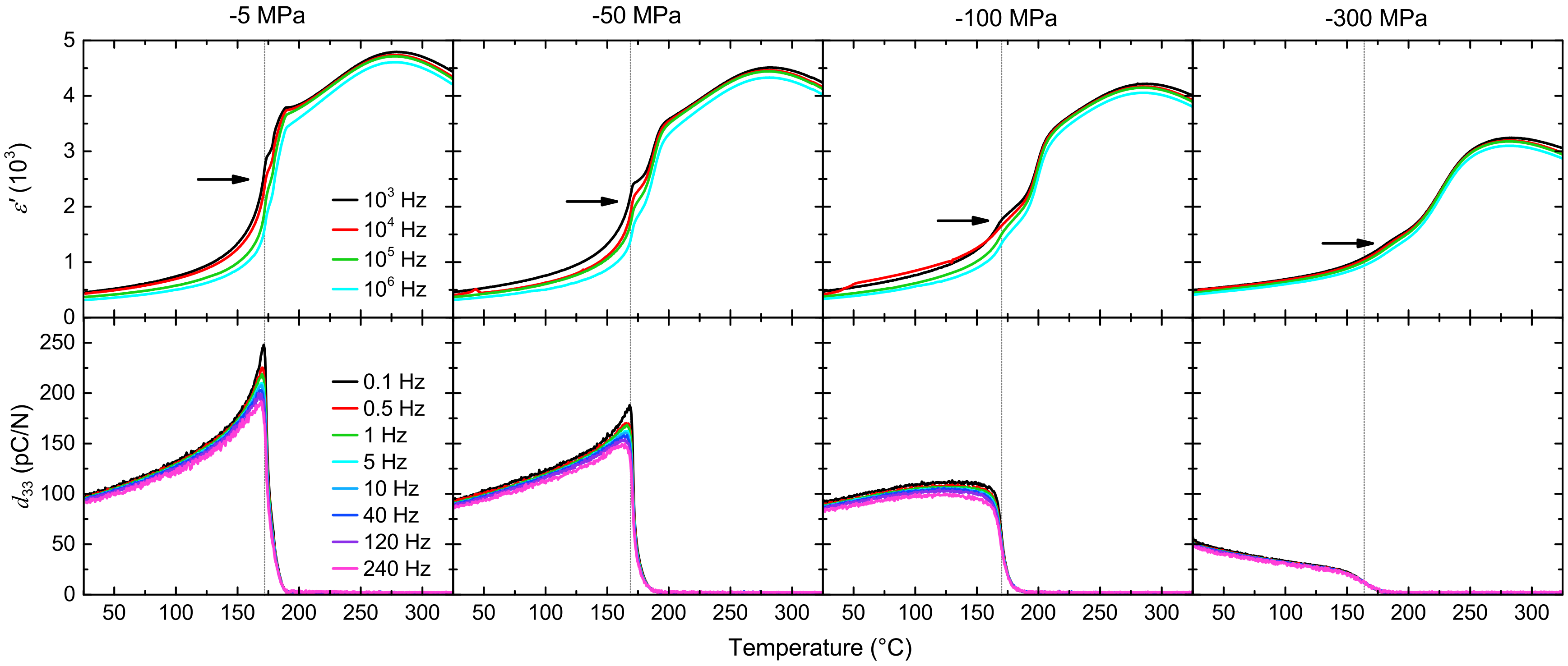

Figure 5.1: Frequency-dependent permittivity ε' and piezoelectric coefficient d_{33} of electrically poled polycrystalline NBT-3BT as a function of temperature at various constant uniaxial mechanical stresses. The dotted lines mark the depolarization temperatures, *i.e.* the inflection point of $d_{33}(T)$.

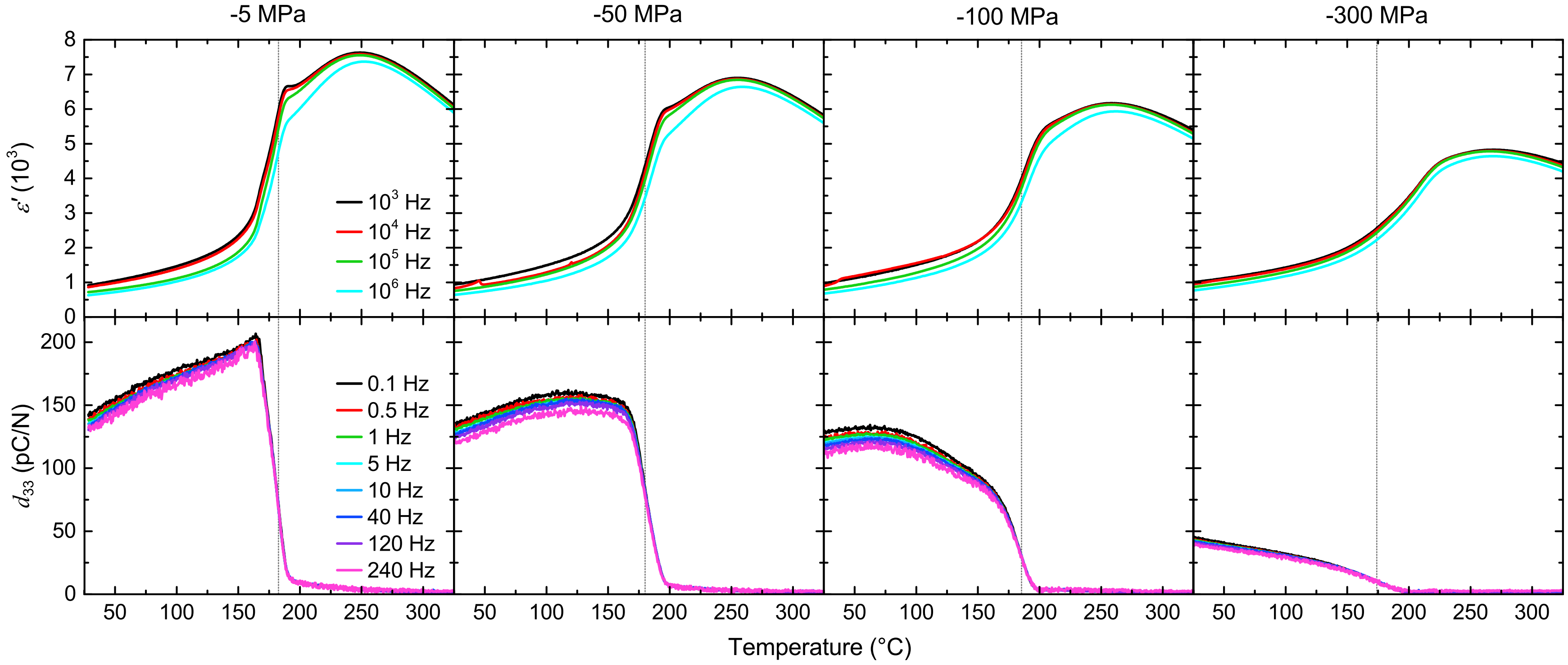

Figure 5.2: Frequency-dependent permittivity ε' and piezoelectric coefficient d_{33} of electrically poled polycrystalline NBT-12BT as a function of temperature at various constant uniaxial mechanical stresses. The dotted lines mark the depolarization temperatures, *i.e.* the inflection point of $d_{33}(T)$.

The temperature evolution of the permittivity of the tetragonal composition NBT-12BT (Figure 5.2) was found to behave similarly. In contrast to NBT-3BT, no clear shoulder in the $\varepsilon'(T)$ curve was observed at T_d. Probably the steeper increase of the permittivity in the measurement at –5 MPa around T_d was overlapping and masking a shoulder directly associated with the depolarization temperature at 162 °C (as more clearly seen in NBT-3BT). The piezoelectric coefficient as a function of temperature at –5 MPa mechanical preload showed an additional inflection point between room temperature and T_d. This was followed by a maximum and a drop, again in a surprisingly wide temperature interval of 27 °C at –5 MPa. The overall influence of stress in the permittivity curves was similar to the findings for NBT-3BT, but the piezoelectric coefficient as a function of temperature behaved differently. With increasing stress the maximum in $d_{33}(T)$ was lowered and two regimes arose, revealing a nearly linear decrease in d_{33} in the second of these regimes with increasing temperature between the broad maximum and the depolarization temperature at –100 MPa. Finally, at –300 MPa the frequency dispersion of $d_{33}(T)$ was found to be highly reduced and no maximum was observable anymore.

A similar set of measurements is presented in Figure 5.3 and Figure 5.4 for NBT-6BT and NBT-9BT. These compositions are believed to be in the MPB region and possess mixed rhombohedral and tetragonal symmetry [144]. In prior reports, NBT-6BT showed a higher amount of rhombohedral phase, whereas NBT-9BT was found to be predominately tetragonal [144]. NBT-6BT is an interesting composition due to its comparatively high unipolar strain [262, 281] and will be also subjected to more detailed investigations and discussions in the following sections. An apparent discontinuity in the permittivity curve at –5 MPa preload was found at the depolarization temperature of approximately 77 °C, accompanied by a sharp drop in d_{33}, which occurred within a temperature interval of less than 1 °C. This is significantly different from the observed behavior of NBT-3BT and NBT-12BT, but similar to that already observed in a previous investigation [316, 317]. The value of T_d also corresponded well to previous publications, which showed that T_d is closely related to the transition temperature from an electrically induced ferroelectric to the relaxor phase [435]. Indeed, it can be inferred from Figure 5.3 that the transition temperature $T_{F\text{-}R}$ from the ferroelectric to the relaxor state marked by the kink in $\varepsilon'(T)$ is exactly at the depolarization temperature determined from the sharp drop in $d_{33}(T)$. In contrast, Jo *et al.* found T_d and $T_{F\text{-}R}$ to be different [146, 151]. A reason for that discrepancy might be that Jo *et al.* used a heating rate of 2 °C/min whereas in this work the sample was heated up with 0.5 °C/min, leading to more quasi-static conditions and, therefore, what had looked like a two-stage process could not be observed here. Furthermore, the use of two different experimental setups for measuring T_d and

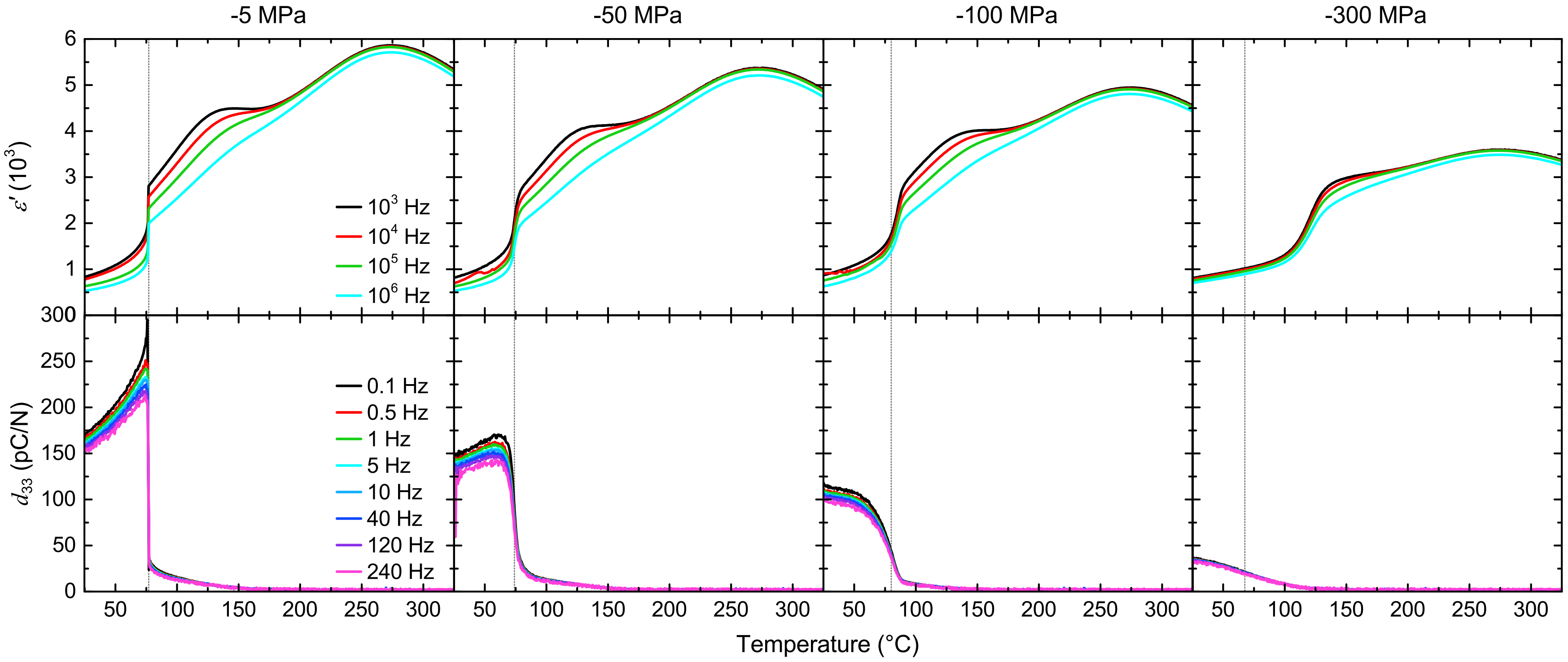

Figure 5.3: Frequency-dependent permittivity ε' and piezoelectric coefficient d_{33} of electrically poled polycrystalline NBT-6BT as a function of temperature at various constant uniaxial mechanical stresses. The dotted lines mark the depolarization temperatures, *i.e.* the inflection point of $d_{33}(T)$.

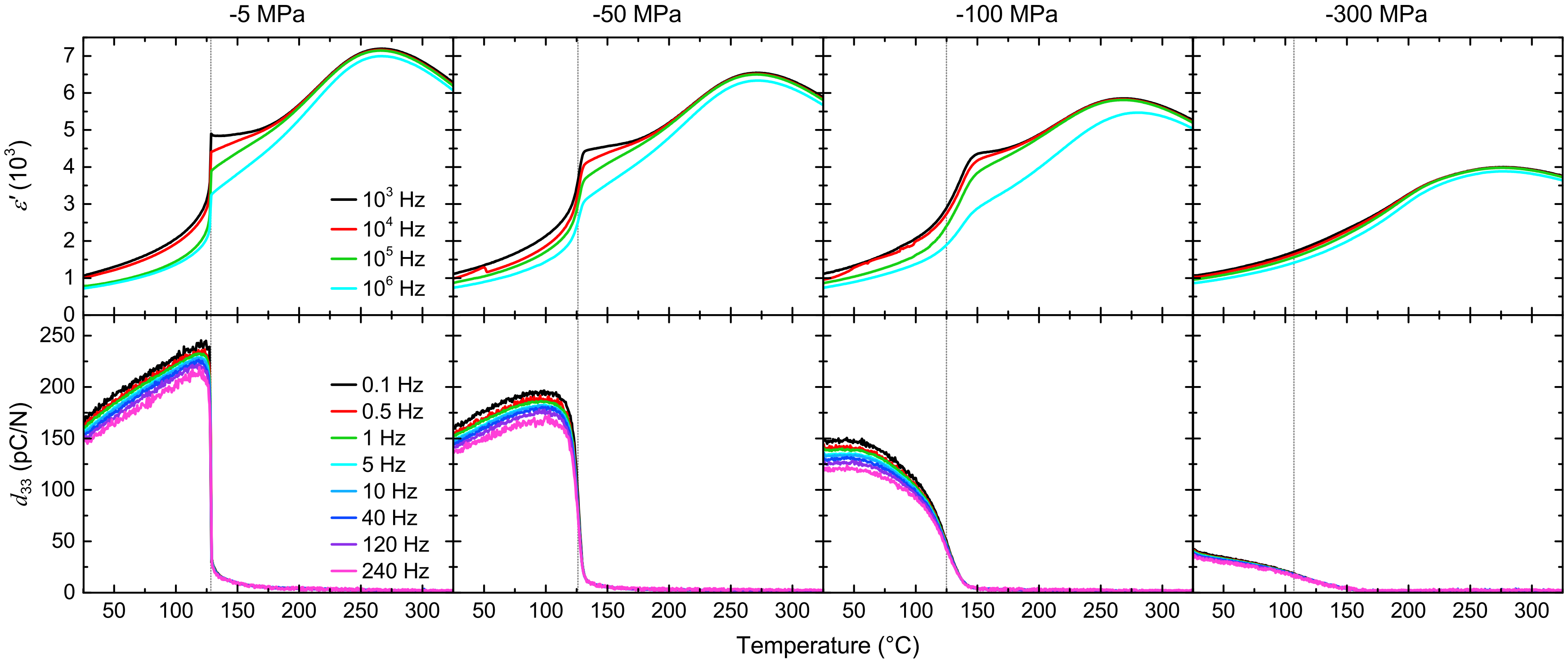

Figure 5.4: Frequency-dependent permittivity ε' and piezoelectric coefficient d_{33} of electrically poled polycrystalline NBT-9BT as a function of temperature at various constant uniaxial mechanical stresses. The dotted lines mark the depolarization temperatures, *i.e.* the inflection point of $d_{33}(T)$.

$T_{F\text{-}R}$ in the previous study could also result in the observed difference or at least in its enhancement. This issue was resolved in the present work by developing a new experimental device (see Chapter 2).

The frequency dispersive part of the permittivity curve in Figure 5.3 above $T_{F\text{-}R}$ clearly indicates a relaxor type of behavior in NBT-6BT, where rhombohedral and tetragonal PNRs are present [435]. A further increase in temperature eventually resulted in the vanishing of the frequency dispersion and the formation of a second permittivity maximum. This behavior was attributed by Jo *et al.* to the transformation of the rhombohedral PNRs into tetragonal PNRs and to additional underlying relaxation processes, which in the end theoretically resulted in the observed $\varepsilon'(T)$ curve [435]. An additional explanation could be possible by taking into account the motion and the number of PNRs as a function of temperature. Above the temperature of the frequency-dispersive shoulder in $\varepsilon'(T)$ far above $T_{F\text{-}R}$, it is proposed that the PNRs present in the material decreased in size due to the reduced correlation length, which corresponds to the observed vanishing of the frequency dispersion with increasing temperature. The remaining isolated PNRs may then result in a higher permittivity with rising temperature due to their increased mobility. At the same time, the total number of PNRs decreased with increasing temperature, resulting in a lower response to the voltage applied by the LCR meter. If these two opposite effects overlapped, this could lead to the frequency-independent maximum as seen in the measured permittivity curve.

The temperature difference ΔT between T_d and the temperature at maximum d_{33} increased with increasing mechanical bias stress, e.g. from a ΔT of approximately 1 °C at –5 MPa to 14.5 °C at –50 MPa stress. This is most likely attributed to a nonuniform depolarization behavior of the sample under the application of mechanical stress. The depolarization nonuniformity is caused by differently oriented grains possessing different stress states, resulting in a distribution of depolarization temperatures over a broader temperature interval. Furthermore, the frequency dispersion of both permittivity and piezoelectric coefficient was found to be significantly reduced at highest stresses of about –300 MPa due to clamping of domain walls and PNRs (for the latter effect, see also Section 5.4).

As there were strong similarities between NBT-3BT and NBT-12BT samples, the behavior of NBT-9BT (Figure 5.4) is highly comparable to the observations made for NBT-6BT, yet still different from the former pair of compositions. For NBT-9BT at –5 MPa preload the depolarization temperature coexists at the ferroelectric-relaxor transition temperature, and is again clearly marked by a step in $\varepsilon'(T)$ and a sharp drop in $d_{33}(T)$, both occurring at the same temperature of approximately 128 °C. The maximum in the $d_{33}(T)$ curve was found to be slightly broader than in NBT-6BT and the difference between the temperature at maximum piezoelectric coefficient and T_d was more prominent. As an example, this difference was determined to be 10.2 °C at –5 MPa prestress for NBT-9BT, which was significantly larger than the 1.0 °C difference found for NBT-6BT. In general, the permittivity curve of NBT-9BT was revealed to be more stress sensitive since the frequency dispersive shoulder vanished nearly completely at –300 MPa. It will be shown later on in Section 5.4 that a uniaxial mechanical compressive stress can induce a ferroelectric long-range order in NBT-6BT, which could also be the case in NBT-9BT. Like in the other tested NBT-xBT compositions, the frequency dispersion of the piezoelectric coefficient was found to be rather independent of stress below –100 MPa, whereas it was highly reduced at –300 MPa.

In general, an apparent frequency dispersion of the piezoelectric coefficient was observed for all investigated NBT-xBT compositions at least under lower compressive mechanical bias stresses. This frequency dispersion can be mainly attributed to the frequency-dependent periodic domain wall motion or vibration. As possible origins for the frequency dependency, damping and frictional effects at the domain walls [32, 437] are discussed as well as the pinning of domain walls at defects [22, 23], which were also undoubtedly present in the investigated NBT-xBT materials. These models and descriptions require the treatment d_{33} as a complex quantity, assigning the different contributions of electromechanical loss to the imaginary part.

After discussing each tested material separately, Figure 5.5 now summarizes the measurements by comparing $\varepsilon'(T)$ measured at 1 kHz and $d_{33}(T)$ measured at 10 Hz for all compositions tested at constant uniaxial bias stresses between –5 MPa and –300 MPa. In general, between room temperature and approximately 40 °C the permittivity was found to be independent from stress up to –300 MPa for all compositions in the poled, field-induced ferroelectric state. This is a rather surprising result, since the piezoelectric coefficient is significantly influenced by the mechanical compression in the same temperature regime. A possible explanation could be that the intrinsic contributions, such as domain wall motion, dominated the dielectric response at room temperature. In addition, domain walls could be pinned by defects in the material at room temperature and a mechanical load of –300 MPa was perhaps not enough to overcome this pinning effect. This would fit to the observation that the stress had increased influence on the permittivity at higher temperatures, where domain wall motion is thermally enhanced. Above T_d, the motion of PNRs is hindered by the mechanical compression, which resulted in a decrease in permittivity with increasing stress. If the breathing model [159] of PNRs is considered, the mechanical stress may also lead to a reduction in motion of the walls of the PNRs, which would then also decrease the value of the

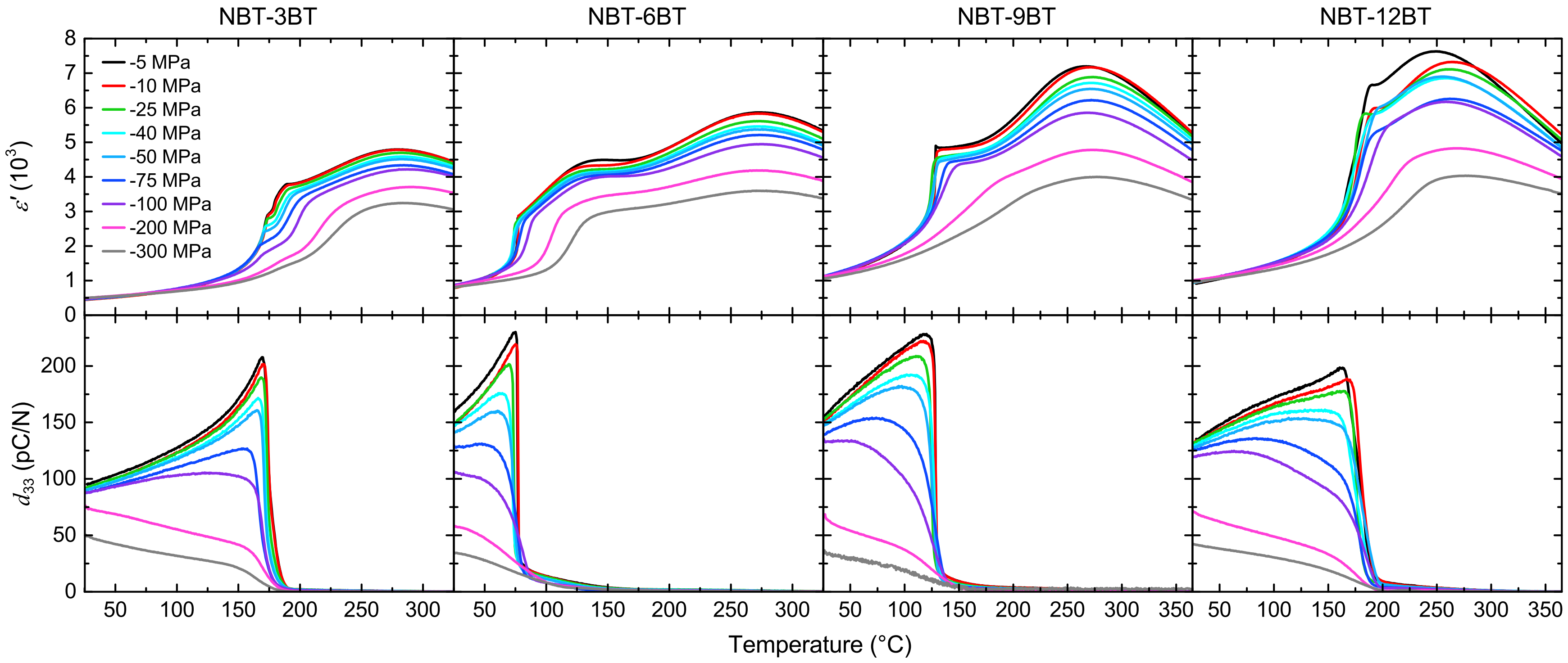

Figure 5.5: Permittivity d_{33} at 1 kHz and piezoelectric coefficient d_{33} at 10 Hz of electrically poled polycrystalline NBT-xBT as a function of temperature at various constant uniaxial mechanical bias stresses. The legend given in the top-left diagram is valid for the whole figure.

permittivity. However, this contribution is likely small compared to the influence of the stress on the overall motion of the PNRs.

For a better comparison, the change in the room temperature values of ε' and of d_{33} are shown for all compositions in Figure 5.6. Both parameters were normalized with respect to the values measured at −5 MPa. The stress sensitivity of ε' was found to increase with increasing $BaTiO_3$ content and showed an increasing difference between the compositions with increasing uniaxial mechanical compression. It could be observed that the permittivity initially increased with increasing stress and shows a maximum at −100 MPa (NBT-6BT) or −200 MPa (NBT-9BT and NBT-12BT). This could be attributed to the onset of the ferroelastic switching of domains at lower stress values and an anisotropic permittivity of the crystal unit cell. In $BaTiO_3$, for example, the permittivity along the a-axis perpendicular to the spontaneous polarization is nearly an order of magnitude larger than along the c-axis [62]. As compressive stress statistically reorients domains perpendicular to the poling direction, such an effect can be the origin of the observed behavior here. Compared to the behavior of d_{33}, the permittivity was found to be less affected by the mechanical compression. Initially, the d_{33} showed little stress-induced decrease. This is because the applied stress was below the onset and coercive stress. At stresses above these critical values, d_{33} was decreased due to the stress-induced depolarization, which is the dominating nonlinear, hysteretic mechanism at room temperature in poled NBT-xBT. It is apparent that permittivity displayed more stress-insensitivity due primarily to the stress-insensitivity of the reversible contributions. The electrical voltage applied by the LCR meter was 1 V_{rms} at maximum, whereas a load amplitude of ±0.5 MPa was used for the d_{33} measurement, leading to a small, but not negligible fraction of irreversible contributions. Since a mechanical bias stress is expected to have a higher influence

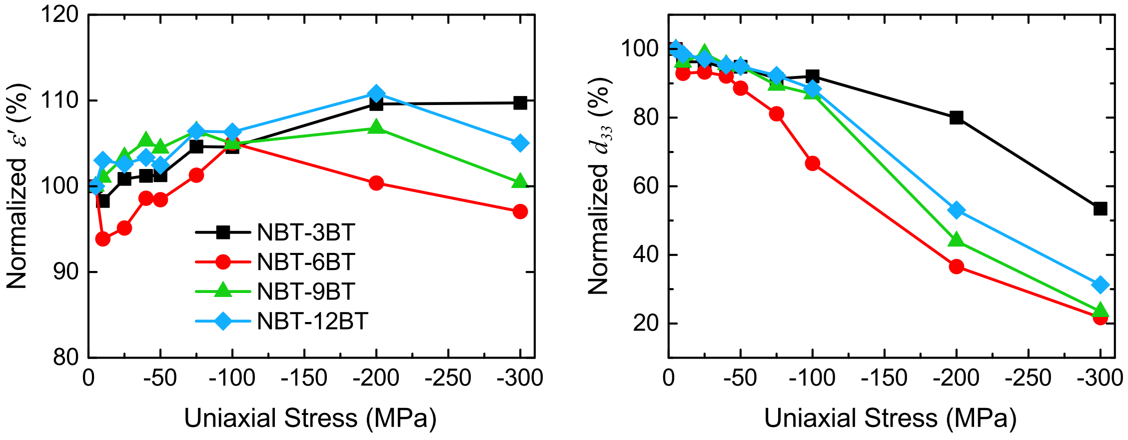

Figure 5.6: Stress-dependency of the permittivity ε' and the piezoelectric coefficient d_{33} at room temperature, measured at 1 kHz and 10 Hz, respectively. The values of both parameters were taken from Figure 5.5 and normalized with respect to their values at −5 MPa.

on the irreversible contributions, d_{33} decreased more significantly with increasing mechanical load than ε'. It can be seen from Figure 5.6 that the piezoelectric coefficients of MPB materials NBT-6BT and NBT-9BT are more stress sensitive at room temperature than the other compositions. Interestingly, the d_{33} of NBT-3BT showed a higher stress stability than the other compositions with higher $BaTiO_3$, but possessed on the other hand also the smallest d_{33} of all investigated NBT-xBT materials after electrical poling (see Figure 5.5).

The permittivity curves of NBT-3BT at different bias stresses (Figure 5.5) exhibited a stress insensitive permittivity-temperature behavior up to –75 MPa from room temperature to T_d, where the shoulder appeared and a significant influence of stress on the permittivity was observed. At –100 MPa and above, $\varepsilon'(T)$ deviated from the curve at –5 MPa preload at lower temperatures. A reason for that could probably be the onset of ferroelastic switching processes, which is also temperature-dependent.

In general, the increase in permittivity at the depolarization temperature became broadened and less steep with increasing stress for all compositions. This probably indicates an increased diffusivity of the transitions due to a distribution of T_d within the sample because of different stress states in differently oriented grains and domains. Similar to that, the drop in the piezoelectric coefficient was found to broaden with increasing stress for all tested materials. This observation is accompanied by a suppression of the maximum in $d_{33}(T)$, indicating a ferroelastic depolarization with increasing stress.

Of particular interest is the shift of the characteristic temperatures, *i.e.*, the phase transition behavior of NBT-xBT with uniaxial mechanical stress. It can be seen from Figure 5.5 and from the previous discussion, that it is rather complicated to define and to determine a specific transition temperature from these measurements. This is especially the case at higher mechanical stresses, at which the transition between the induced ferroelectric state to the relaxor state and the depolarization process noticeably broaden. For that reason, the inflection points of both $\varepsilon'(T)$ at 1 kHz and $d_{33}(T)$ at 10 Hz were used for the evaluation as already suggested by Anton *et al.* previously [410]. The results of this investigation are depicted in Figure 5.7 for all four tested NBT-xBT compositions as a function of uniaxial compressive stress.

At mechanical stresses below –50 MPa, both inflection points showed nearly similar behavior for all compositions. In the case of NBT-3BT and NBT-6BT, an initial decrease and subsequent increase of the characteristic temperatures with increasing stress could be observed. In comparison, the inflection points of NBT-9BT were found to be rather stable, whereas the trend of NBT-12BT was unclear in that load range. With further increasing mechanical compression, the inflection points

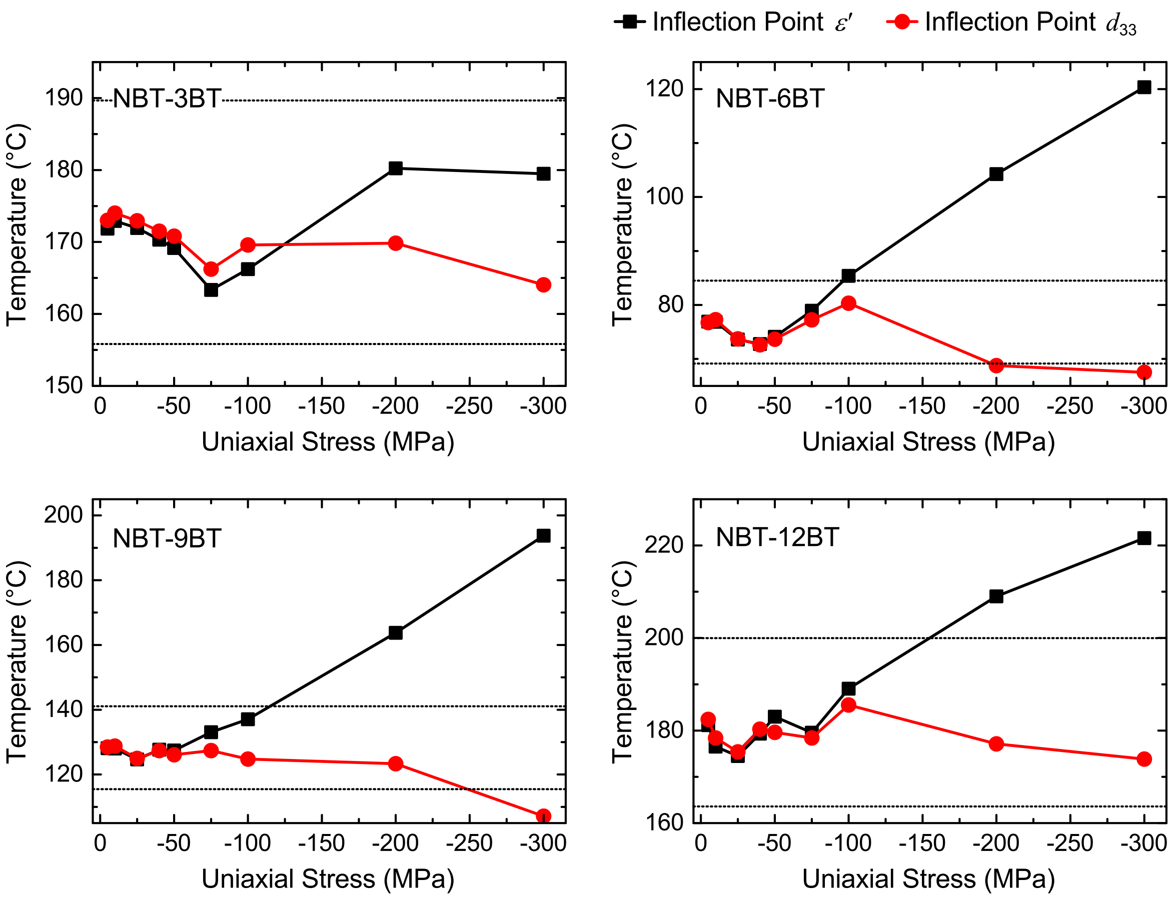

Figure 5.7: Characteristic transition temperatures of various NBT-xBT compositions, represented by the inflection points of $d_{33}(T)$ and $\varepsilon'(T)$. For evaluation, the permittivity measured at 1 kHz and the piezoelectric coefficient measured at 10 Hz were used. The solid lines only serve to guide the eyes, whereas the dotted lines represent a temperature region of ±10 % of the values of the respective inflection points determined at –5 MPa mechanical bias prestress.

for all compositions began to clearly deviate. The deviation occurred in all compositions between approximately –75 MPa and –100 MPa. In general, the depolarization temperature identified with the inflection point of the $d_{33}(T)$ curve displayed an overall gradual decrease with increasing stress, whereas the inflection point of $\varepsilon'(T)$ increased with stress at a significantly higher rate.

A more detailed evaluation of the trends presented in Figure 5.5 is shown in Figure 5.8a, where the difference $T_{\mathrm{inf}}^{\varepsilon'} - T_{\mathrm{inf}}^{d33}$ between both inflections points is plotted as a function of compressive stress. For all compositions, this difference increased with increasing stress. The largest effect was observed for NBT-9BT, which showed a difference of about 87 °C at –300 MPa, almost six times higher than the lowest value of 15 °C as measured for NBT-3BT at –300 MPa.

The temperature shift $\Delta T_m^{\varepsilon'}$ of the maximum permittivity relative to its position at –5 MPa (Figure 5.8b) showed no clear trend over the entire range of applied stress. Although the temperature shift for NBT-12BT might have appeared significant, the comparison of the individual measurement curves for this material in Figure 5.5 raised doubts if this was not instead due to the scattering between the samples and measurements. The temperature of the maximum in

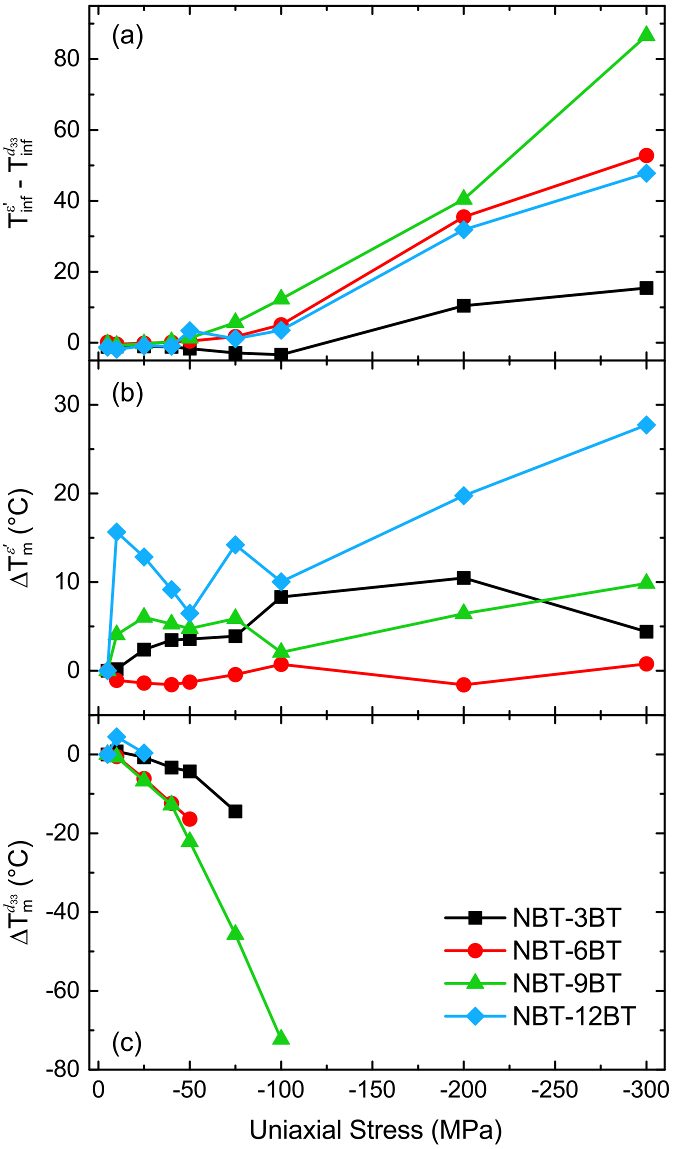

Figure 5.8: Stress dependence of (a) the difference between the inflection points $T_{\text{inf}}^{\varepsilon'}$ and $T_{\text{inf}}^{d_{33}}$ of $\varepsilon'(T)$ and $d_{33}(T)$, (b) the relative shift of the temperature at maximum permittivity $\Delta T_m^{\varepsilon'}$, and (c) the relative shift of the temperature at maximum piezoelectric coefficient $\Delta T_m^{d_{33}}$. The solid lines only serve to guide the eyes.

$d_{33}(T)$ was found to decrease with increasing mechanical stress for all compositions ($\Delta T_m^{d_{33}}$ in Figure 5.8c). However, the appearance of the maximum vanished above certain stress levels, e.g., above −25 MPa for NBT-12BT (lowest value) and above −100 MPa for NBT-9BT (highest value). The weakest stress dependence of the maximum in $d_{33}(T)$ was found for NBT-3BT and the most severe shift of more than −70 °C between the experiments at −5 MPa and −300 MPa was determined in the case of NBT-9BT. An interesting behavior could be observed for NBT-12BT, which revealed two $d_{33}(T)$ peaks even at the lowest mechanical bias stress of −5 MPa (see Figure 5.5). These d_{33} peaks persist up to mechanical bias loads of −100 MPa and are possibly due to the influence of defects, similar to observations in PZT (see Chapter 4 and especially Figure 4.3). If defects were the reason for this observation, the two permittivity peaks could be due to an initial, thermally induced release of the domain walls, which would then be easier to depolarize by the mechanical stress. With further increasing stress, the thermal depolarization occurred, resulting in the second decrease in the permittivity curve.

In the last part of this section some additional features of the measurements presented above will be discussed. It was found that the piezoelectric coefficient indeed dropped at the depolarization temperature but did not vanish completely and a d_{33} signal was still measurable. In order to make this more clear and visible, Figure 5.9 shows again the temperature-dependent piezoelectric coefficient of NBT-xBT at 10 Hz and at –5 MPa preload, but with special focus on this phenomenon.

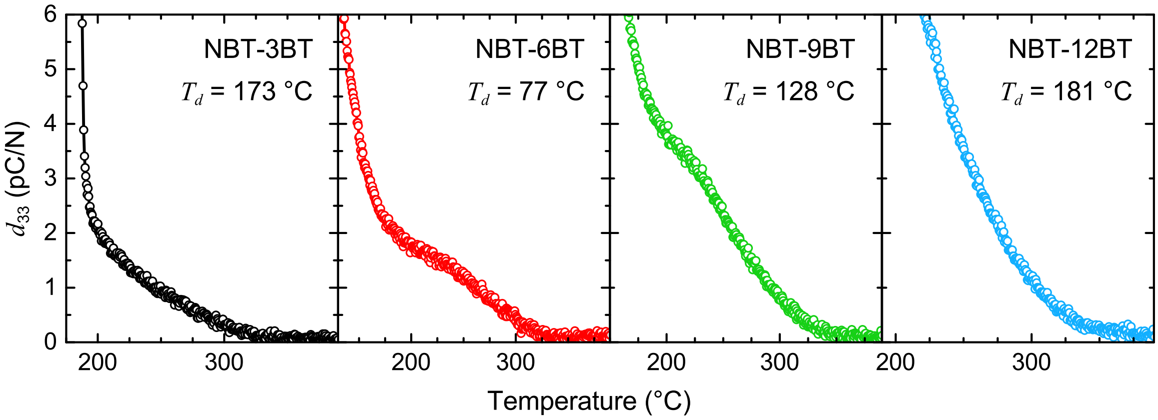

Figure 5.9: Temperature-dependent piezoelectric coefficient d_{33} measured at a frequency of 10 Hz and a preload of –5 MPa for various NBT-xBT compositions. The special focus lies on the observation that d_{33} was still measureable at temperatures far above T_d. Note the high amount of data points collected during these measurements together with the excellent resolution in d_{33}.

The findings indicated, that polarized regions could still persist in the sample even above T_d, similar to previous observations [316]. At sufficiently high temperatures, the piezoelectric coefficient reached zero, but this point is located at a temperature far above the depolarization temperature. The temperature difference ΔT between T_d and the temperature at which d_{33} reaches zero varied between the compositions and was found to be highest in the MPB materials NBT-6BT ($\Delta T \approx 248\,°C$) and NBT-9BT ($\Delta T \approx 212\,°C$), whereas for NBT-3BT and NBT-12BT values of approximately 188 °C and 182 °C were determined for ΔT, respectively. In NBT-6BT, these findings could probably be attributed to the fact that above T_d in the frequency-dispersive temperature region, both rhombohedral and tetragonal PNRs are present in the sample. Jo *et al.* proposed that the rhombohedral PNRs transform with increasing temperature to tetragonal symmetry [435]. In NBT-6BT, the PNRs with rhombohedral symmetry may still yield a remanent macroscopic polarization, leading to a nonzero d_{33} above T_d and a slow decrease of d_{33} at higher temperatures due to an ongoing transformation of rhombohedral PNRs into tetragonal ones. Since a nonzero value for d_{33}

above T_d was also observed for the highly modified tetragonal PZT materials in Chapter 4, other polar defects probably played a role in this phenomenon for both systems. In addition to these findings, the decrease in the piezoelectric coefficient showed in Figure 5.9 was found to be not uniform for NBT-6BT and NBT-9BT. While the $d_{33}(T)$ of the other materials gradually decreased to zero, these MPB compositions showed an interim slowdown of the decrease, marked by a small and broad hump. There is no explanation so far for this feature.

Another interesting and surprising effect was observed only at elevated mechanical stresses. The piezoelectric coefficient was found to increase again after reaching a value of nearly zero and showed one or even two (for NBT-12BT) additional maxima in $d_{33}(T)$. Figure 5.10 depicts this unexpected behavior for all tested compositions at a measurement frequency of 10 Hz. As before, this observation was also made already in the modified PZT materials examined in Chapter 4. So far, no satisfying explanation for this obviously stress-induced phenomenon could be found. It is apparent from Figure 5.10 that the behavior of NBT-12BT seemed to be different from the other compositions, especially regarding the existence of two maxima in $d_{33}(T)$ above T_d and also the comparatively sharp change in slope when reaching zero. Because of this NBT-12BT was chosen for a more detailed evaluation.

Besides the amplitude of load and polarization signal, the built-in LabVIEW function used during the data evaluation process (see Section 2.5.2) also determined information about the phase angle of the measured and analyzed periodic signals. Figure 5.11 shows the phase shift between the applied sinusoidal mechanical load and the resulting polarization signal as a function of temperature. Interestingly, the phase angle switched at a specific temperature from nearly 0° to approximately –180° for mechanical bias stresses above –100 MPa, indicating that the polarization was inversely phased to the stress in a specific temperature range. Like in the case of the PZT materials investigated in Section 4.2, the real part of the piezoelectric coefficient, *i.e.*, d'_{33}, is expected to become negative if the phase angle equals –180°. The result of the evaluation is shown in the lower portion of Figure 5.11, and reveals exactly the presumptions. At the temperatures where d_{33} displayed a sharp change in slope (see Figure 5.10) there was, in fact, a phase angle switch and d'_{33} became negative.

Since the measured value of a physical quantity is always the absolute value, d_{33} was determined to be positive even if the phase between load and resulting polarization became –180°. Negative values of the phase angle of the piezoelectric coefficient has been already previously reported by Damjanovic *et al.* using the example of a bilayer of two different piezoelectric materials which showed a Maxwell-Wagner relaxation of the piezoelectric coefficient [416]. The phenomenon de-

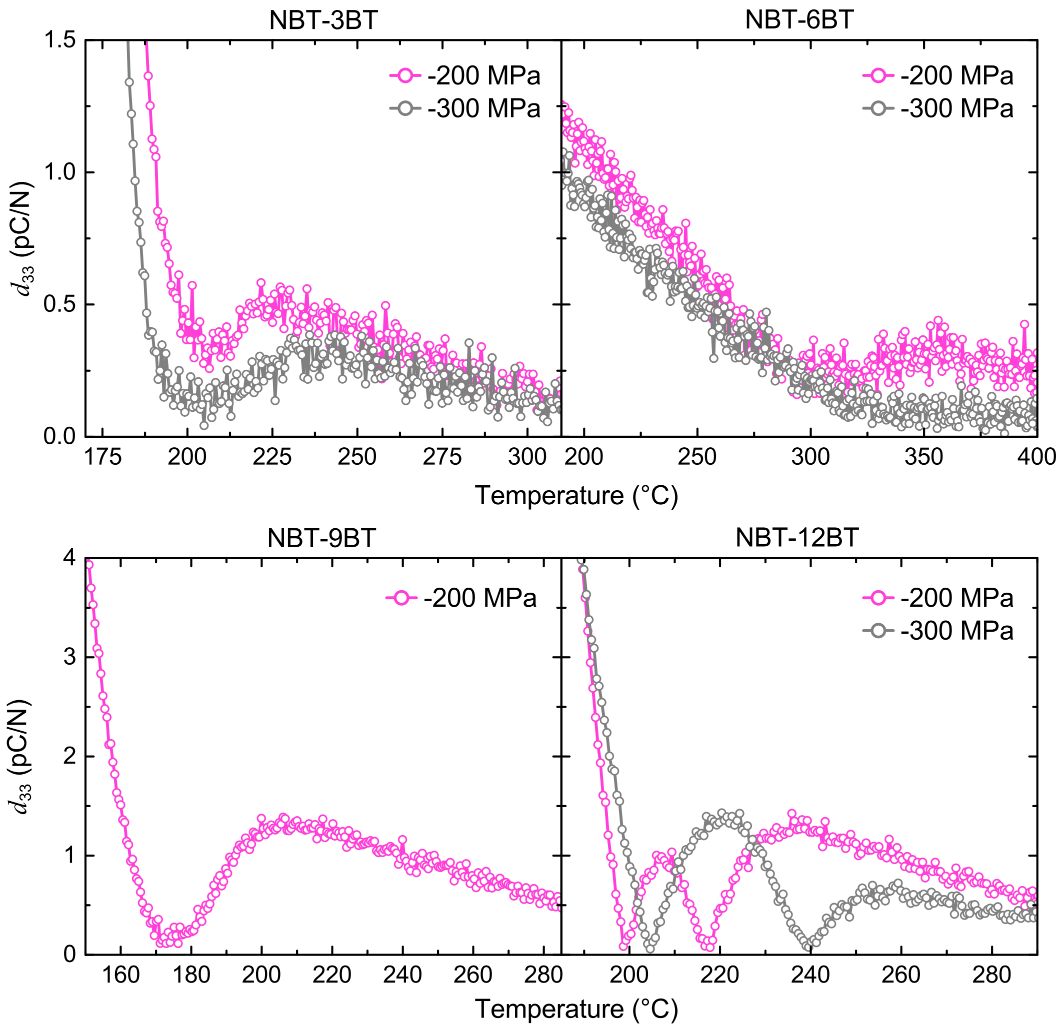

Figure 5.10: Piezoelectric coefficient d_{33} of various NBT-xBT compositions as a function of temperature, measured at a frequency of 10 Hz and at −200 MPa and −300 MPa constant uniaxial mechanical stress. No data at −300 MPa constant bias stress was available for NBT-9BT due to an anomalously high noise in the measurement signal within the temperature interval of interest.

scribed here was not observable for other NBT-xBT compositions, but is believed to be identical with the findings for soft and hard PZT in Section 4.2. Of course, further investigation is required to elucidate the mechanisms behind these observations. This is, however, out of the scope of the current investigations.

It can be concluded from the measurements and the evaluation presented above that without the application of any significant mechanical compressive stress, the depolarization temperature T_d and the transition temperature between induced ferroelectric state and relaxor state $T_{F\text{-}R}$ were equal in NBT-xBT. With increasing stress these temperatures increasingly differed from each other, as shown in Figure 5.8a. A reason for that could be that the uniaxial stress not only influenced the depolarization of the material (marked by the drop in $d_{33}(T)$), but also induced a ferroelectric order at temperatures above T_d. This induced state would not possess a macroscopically oriented polarization, but would remain ferroelectric. With increasing mechanical compression, the transi-

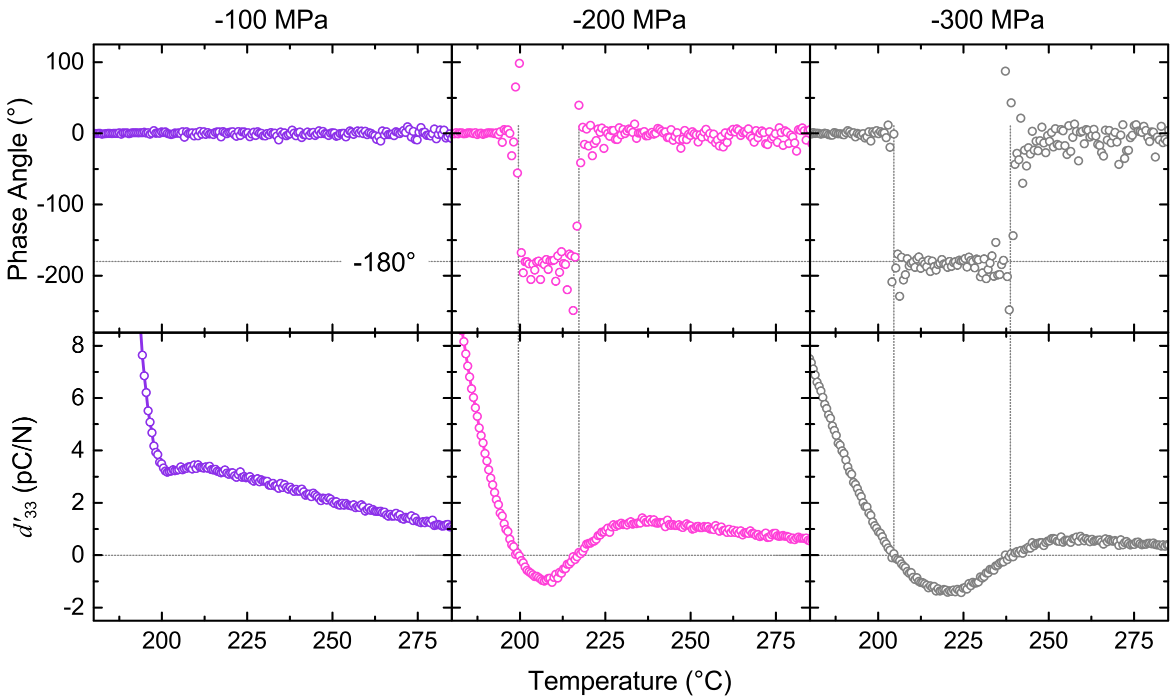

Figure 5.11: Phase angle between load and polarization signal and real part of the piezoelectric coefficient d'_{33} of polycrystalline NBT-12BT as a function of temperature, measured at a frequency of 10 Hz and at −100 MPa, −200 MPa, and −300 MPa constant uniaxial mechanical stress.

tion temperature $T_{F\text{-}R}$ between this non-oriented, stress-induced ferroelectric phase and the relaxor state was shifted to higher temperatures. This had an associated general increase in $\varepsilon'(T)$ around $T_{F\text{-}R}$. In order to further elucidate the influence of a mechanical stress on the relatively complex phase transition behavior of NBT-xBT it was necessary to reduce some of the input parameters in these investigations. For that reason, the next two sections will deal with the temperature-dependent permittivity of electrically unpoled NBT-6BT samples under constant mechanical stress, eliminating the influence of the electrical poling from consideration.

5.3 Temperature-dependent Dielectric Properties of Electrically Unpoled NBT-6BT under Uniaxial Compressive Mechanical Bias Stress

In this section, the investigation of the phase transition behavior of NBT-xBT under uniaxial mechanical stress will focus on the MPB composition NBT-6BT. As already stated, this composition is a promising candidate to replace lead-containing materials in some applications due to its comparatively large electromechanical strain [151, 259, 262]. In order to separate electrically and mechanically induced phase transitions, the samples used here were not electrically poled and all samples were annealed at 400 °C for 30 min prior to each measurement in a separate oven without any preload applied in order to achieve a quasi-virgin state. Sample shapes and dimension were the same then in Section 5.2, *i.e.*, cylindrically shaped with a diameter of 5.8 mm and a height of 6 mm. The permittivity as a function of temperature between –150 °C and 450 °C at various constant mechanical stresses was measured by using a uniaxial screw-driven load frame equipped with a special thermal chamber capable of heating and cooling the sample in a carefully regulated manner (see Section 2.4 for technical details). After applying a mechanical preload of –5 MPa the sample was heated up to 450 °C. At this temperature, NBT-6BT was in the ergodic relaxor state where uncorrelated PNRs exist (see also Section 1.9). In this state, a constant uniaxial mechanical compressive stress between –5 MPa and –500 MPa was applied to the sample and a waiting time of 10 min was used before starting the temperature program for the permittivity measurement. While still under applied stress, the sample was cooled down with a rate of 2 °C/min to –150 °C (afterwards referred to as "stress field cooling"). This was next followed without interruption by a reheating to 450 °C ("stress field heating"). During this stress field cooling – stress field heating process, the permittivity was measured as a function of temperature at frequencies between 100 Hz and 1 MHz. A comparison of the stress field cooling and subsequent stress field heating measurements at constant uniaxial bias stresses of –5 MPa and –500 MPa is depicted by Figure 5.12.

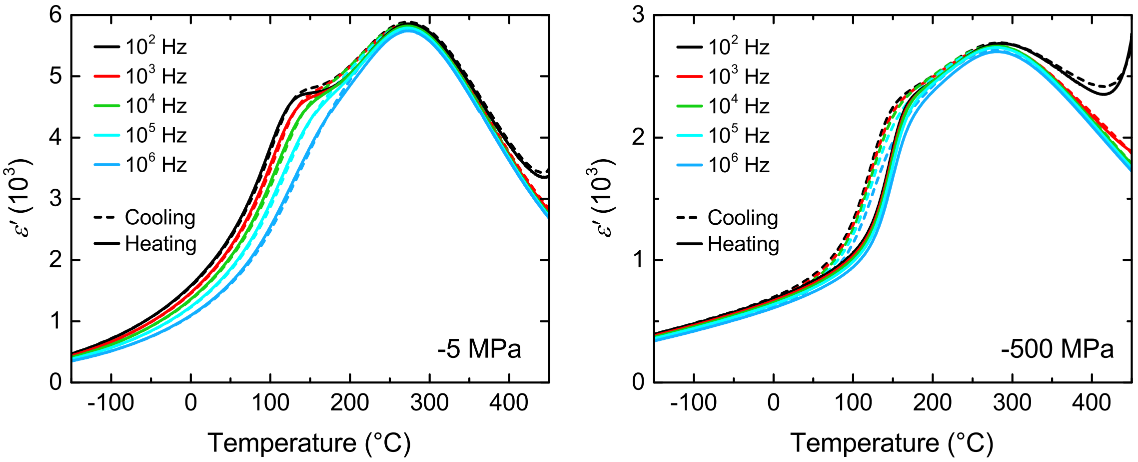

Figure 5.12: Temperature-dependent permittivity ε' of polycrystalline NBT-6BT at –5 MPa and –500 MPa constant bias stress. The mechanical compressive stress was applied after heating up the samples to 450 °C, followed by measuring $\varepsilon'(T)$ during stress field cooling and stress field heating at frequencies between 100 Hz and 1 MHz.

In the case of –5 MPa applied stress, nearly no difference between the stress field cooling and the stress field heating measurement could be observed. Only in the temperature interval between approximately 125 °C and 250 °C a slight deviation between cooling and heating was found. This was probably due to the reduced correlation between the PNRs at these temperatures, which was indicated by the reduction of the frequency dispersion. Since this process is thermally stimulated, a weak hysteresis could be reasonable. However, the measurement done at –500 MPa in Figure 5.12

showed a significantly different behavior. The steeper increase in $\varepsilon'(T)$ is believed to be due to a stress-induced transition between the relaxor and the ferroelectric phase. This would also explain the apparent thermal hysteresis between stress field cooling and stress field heating around the transition temperature $T_{F\text{-}R}$. Significantly reduced frequency dispersion was measured for both stress field heating and cooling at –500 MPa mechanical compression. This lack of frequency dispersion indicates that the applied load effectively clamped the domains at lower temperatures and also impeded the motion of PNRs at higher temperatures, both in response to the small electric field applied by the LCR meter.

Figure 5.13 shows a direct comparison of the measurements done on stress field cooled (dotted lines) and electrically poled (solid lines) samples during stress field heating at four representative uniaxial bias stresses. The data of the electrically poled samples was taken from Section 5.2. Please also note that different experimental setups were used for electrically poled and stress field cooled samples, although this is not expected to have a strong influence on the results.

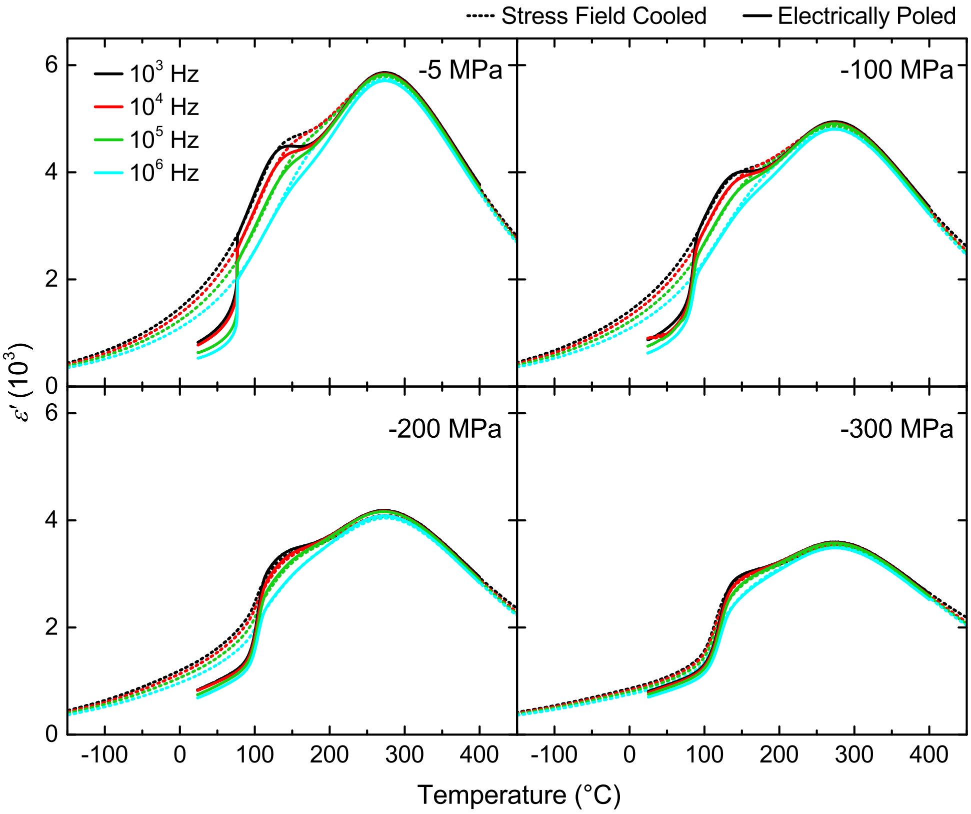

Figure 5.13: Temperature-dependent permittivity ε' of stress field cooled (dotted lines) and electrically poled (solid lines) NBT-6BT at different constant mechanical bias stresses at frequencies between 1 kHz and 1 MHz during heating.

It can be seen from Figure 5.13 that above T_d, both experiments showed the same permittivity response except around the shoulder in $\varepsilon'(T)$, where the frequency dispersion vanished. However, with increasing mechanical bias stress, also these differences decreased and the influence of the electrical poling was nearly entirely removed by the uniaxial mechanical compression. Below –200 MPa, no stepwise increase of $\varepsilon'(T)$ could be observed in the stress field cooled samples, whereas at higher bias stresses such an increase was clearly visible. This coincided with the step in the temperature-dependent permittivity curve of the poled samples. The temperature-dependent permittivity measurement performed on poled samples in Section 5.2 showed that at higher mechanical bias stresses a difference between $T_{F\text{-}R}$ and T_d developed as represented by a stepwise increase of $\varepsilon'(T)$, and marked by a drop in $d_{33}(T)$, respectively. By combining the findings of both experiments, it was determined that the mechanical load induced a ferroelectric order and $T_{F\text{-}R}$ shifted to higher temperatures with increasing mechanical compressive stress, starting at loads between –100 MPa and –200 MPa. The stress-induced ferroelectricity seems be comparable with the effect of an electric poling field on this material, but of course without any macroscopic polarization created for the case of an in situ applied stress. As a result, $T_{F\text{-}R}$ was indeed different from T_d at higher mechanical loads. A similar depolarization and phase transition mechanism was previously suggested by Woodward *et al.* for electrically poled but mechanically unstressed $0.98(0.8Na_{1/2}Bi_{1/2}TiO_3–0.2K_{1/2}Bi_{1/2}TiO_3)–0.02Bi(Zn_{1/2}Ti_{1/2})O_3$ [147].

A summary of all results received from the stress field heating measurements is depicted in Figure 5.14, which shows the permittivity and loss tangent as a function of temperature and uniaxial compressive stress. For a better comparability between the bias stresses only the 1 kHz signal is shown in the figure. Since the measurements presented in Figure 5.14 covered a relatively large temperature and stress range, some conclusions can be drawn regarding the stress sensitivity of the permittivity at different temperatures. Between the measurements at –5 MPa and –500 MPa the permittivity was decreased by 13 % at –150 °C, which was the lowest value found in these experiments. In contrast, the maximum in $\varepsilon'(T)$ decreased by 53 % between –5 MPa and –500 MPa, which is comparable to the decrease in ε' by 59 % found at room temperature within the same stress range. This indicated, that the permittivity is most sensitive to stress in this higher temperature region, where either (induced) ferroelectric domains or PNRs are present. This conclusion is supported by the fact that the difference of the permittivity between the –5 MPa and the –500 MPa measurement in Figure 5.14 at 450 °C was reduced to only 33 %. At this temperature, the number of PNRs has already been significantly decreased. As proposed in Section 5.2, the main contribution to the permittivity was most likely the movement of domain walls and PNRs in the electric field, which was hindered more and more with increasing compressive stress.

A stress-induced step in $\varepsilon'(T)$ for the stress field cooled samples occurring at mechanical loads above of –200 MPa was found to change in slope and to shift to higher temperatures with

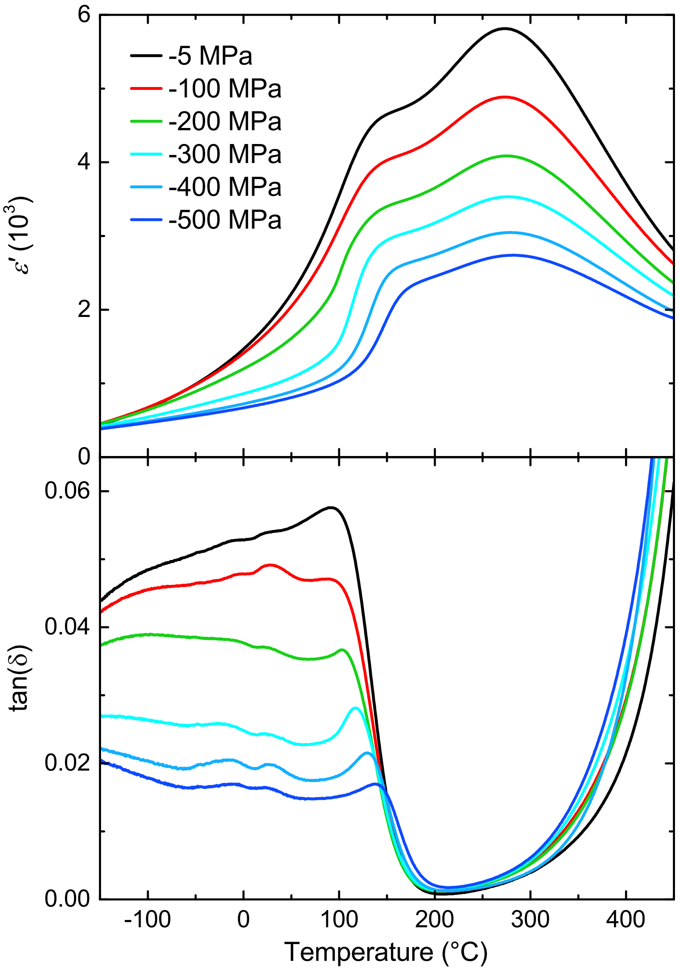

Figure 5.14: Permittivity ε' and loss tangent $\tan(\delta)$ of NBT-6BT as a function of temperature at different constant uniaxial stresses. The measurement data at 1 kHz is characterized during stress field heating after stress field cooling.

increasing stress. The mechanical load stabilized the induced ferroelectric order, which was why the transition temperature $T_{F\text{-}R}$ increased with increasing mechanical load. A broader transition from the induced ferroelectric to the relaxor state, which corresponded to a more gradual transition in the permittivity curve, could be due to different stress states in the grains and domains of the polycrystalline sample and therefore due to a larger distribution of transition temperatures at higher stresses. A similar observation was made for polycrystalline $BaTiO_3$ (Chapter 3). The steepest slope of the anomaly in $\varepsilon'(T)$ at $T_{F\text{-}R}$ was found in the measurement at –300 MPa bias stress, maybe indicating that –200 MPa were not sufficient to induce ferroelectric order in the entire sample.

Due to the use of an experimental setup developed specifically for these measurements, it was also possible to record a nearly noise-free dielectric loss tangent of the NBT-6BT samples as a function of temperature during the experiments presented in Figure 5.14. The experiments revealed a quite low dielectric loss, indicating good sample quality with low conductivities. A general observation was that the apparent maximum in the loss tangent occurred at higher temperatures with increasing mechanical compression. It could not be distinguished from the experiments, however, if this maximum matched to a transition and even if it did, to which transition this maximum would really correspond. At stresses lower than –200 MPa, no ferroelectric phase was induced by the mechanical load and therefore no transition took place. It can be seen in Figure 5.14 that the shape of the maximum qualitatively changed at –200 MPa and above, so that it became more pronounced and sharp. This was probably connected to the underlying transition from the induced ferroelectric state to the relaxor state. For all measurements, a significant drop of $\tan(\delta)$ was observed for temperatures above the maximum in $\tan(\delta)$. Furthermore, the subsequent increase of the loss tangent with increasing temperature was due to the rising conductivity of the material at higher temperatures, which also became noticeable by the increase of the permittivity at 100 Hz above 400 °C in Figure 5.12. In addition to the temperature-dependent effects, the loss tangent of NBT-6BT was found to be highly stress sensitive between –150 °C and 150 °C. For example, a decrease in $\tan(\delta)$ of 54 % at 1 kHz between the –5 MPa and the –500 MPa measurements was observed at –150 °C. This drastic change at low temperatures could be because of the increased clamping of PNRs and further enhanced at stresses above –200 MPa by the clamping of domain walls.

Due to the comparatively strongly diffuse nature of the transition between induced ferroelectric and relaxor state, a qualitative evaluation of the measurement data proved to be difficult. An attempt to gain more information about $T_{F\text{-}R}$ and the possible width of the transition was made in Figure 5.15 by using the tangent method. A linear regression was performed on the 1 kHz $\varepsilon'(T)$ data in the low temperature regime, shown in Figure 5.15a for two representative compressive mechanical bias stresses during the stress field heating permittivity measurement, Two regression lines were used, with the first around the stepwise increase in permittivity at $T_{F\text{-}R}$ and the second in the temperature interval around the second inflection point of $\varepsilon'(T)$ at temperatures above the frequency-dispersive shoulder. The intersection of the resulting linear functions ("tangents") was determined.

It could be concluded from the earlier discussion that the inflection point of $\varepsilon'(T)$ at 1 kHz at –300 MPa bias stress may be seen as the temperature at which the rate of the ferroelectric-relaxor transition is at a maximum. The upper and lower intersections obtained from the tangent method shown in Figure 5.15a could therefore serve as a measure of the transition region. Because no $T_{F\text{-}R}$ existed below –200 MPa uniaxial bias stress, the phase diagram in Figure 5.15b does not show data below –200 MPa and should be only read in temperature direction for any given value of stress. All characteristic temperatures were found to increase with stress, and the average width ΔT of

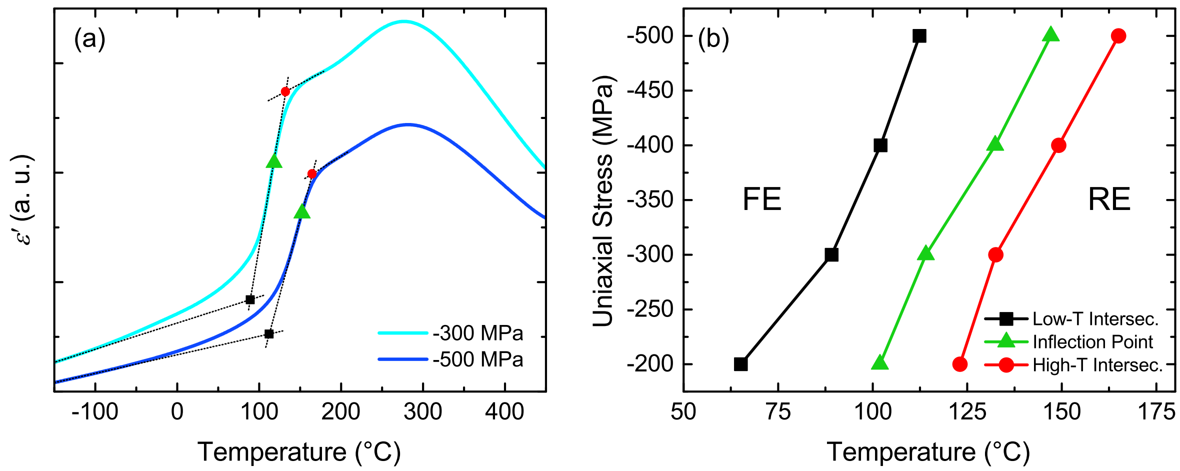

Figure 5.15: (a) Tangent method used for the quantitative evaluation of the temperature-dependent permittivity ε' at 1 kHz at constant mechanical stresses during stress field heating after stress field cooling, exemplarily shown for –300 MPa and –500 MPa bias stresses. For a better readability of the diagram, the permittivity curves of the different loads are shifted along the y-axis and the inflection points are marked. (b) Characteristic temperatures obtained from the data evaluation described in (a), presented here as a phase diagram, which should be only read in temperature direction.

the transition region was revealed to be $\Delta T = (50 \pm 8)$ °C. Therefore, the uniaxial mechanical compression can be said to have stabilized the stress-induced ferroelectric state. At –200 MPa the width of the transition seemed to be broader, probably due to an incomplete induction of the ferroelectric state. In the case of higher stresses, different stress states in differently oriented domains and grains in the sample may have resulted in a distribution of $T_{F\text{-}R}$ over a broader temperature range, consistent with the conclusions from the discussion of Figure 5.15 above. Interestingly, the temperature at maximum permittivity was not significantly affected by the mechanical load and showed only a slight increase of 9 °C between the measurements at –5 MPa and –500 MPa, whereas $T_{F\text{-}R}$ was increased by about 47 °C in the same temperature range. This implies that a bias mechanical stress has only minor influence on the thermodynamics of the PNRs at higher temperatures, *i.e.*, the development of correlations between PNRs.

After discussing the effect of a constant bias stress on the depolarization behavior and the ferroelectric-to-relaxor transition observed in the temperature-dependent permittivity behavior of electrically poled and stress field cooled NBT-xBT the question that naturally arose was, could a mechanical load have the same effect as an electric poling field? Can a mechanical load induce a remanent ferroelectric phase? In order to investigate this in more detail and in order to support the conclusions made above, mechanically textured NBT-6BT samples will be tested for the induced phase transition in the following section. For this purpose, the electrical poling field will be replaced by a mechanical stress "poling" field and the consequences for the temperature-dependent permittivity resulting from this treatment will be investigated.

5.4 Stress Modulated Relaxor-to-Ferroelectric Transition in NBT-6BT Ferroelectrics

The application of an electric field to a ferroelectric material usually results in a macroscopic polarization. Typically this polarization is remanent and the sample remains poled until it is intentionally destabilized, e.g. heated up above the depolarization temperature. It has already been shown Section 5.2 that a phase transition from the ferroelectric to the relaxor phase occurs in electrically poled NBT-6BT during heating, marked by a stepwise increase in ε' and a drop in d_{33}. It is also well-known that the electrical poling conditions have an influence on the phase transition temperatures [135, 438]. Currently, however, the influence of a mechanical field is not understood. The aim of this section is to investigate the role of a compressive stress on the stress-free, temperature-dependent permittivity.

Figure 5.16 shows the permittivity and the loss tangent of NBT-6BT as a function of temperature for three different types of sample treatment prior to testing: virgin, electrically poled, and mechanically textured. The data for the electrically poled sample was taken directly from Figure 5.3 (–5 MPa prestress) in Section 5.2. In the case of the mechanically textured sample, the procedure was exactly the same as the one for the high temperature poling during an application of an electric field of 2 kV/mm. However, instead of the electric field, a constant mechanical stress of –500 MPa was applied by a uniaxial screw-driven load frame (see Section 2.4) at 150 °C for 5 min, followed by cooling the sample to room temperature with the mechanical load still applied ("stress field cooling"). This process will be called "texturing" in the following discussion. As before, a minimum waiting time of 24 h prior to the measurements was used. All permittivity measurements were done at a prestress of –5 MPa, which will be referred to as "zero-field" condition during heating in the following discussion. The application of a mechanical field leads to an apparent dielectric anomaly during zero-field heating, consistent with the electrically poled sample. This clearly indicates a stress-induced long-range order at lower temperatures due to the increased correlation length of the PNRs. In contrast, hydrostatic pressure was found to decrease the correlation length of PNRs during stress field cooling [379].

The loss tangent of the electrically poled sample at $T_{F\text{-}R}$ showed a sharp peak, followed by a broad maximum present in all measurements. The $\tan(\delta)$ peak of the mechanically textured sample was less pronounced and formed a step rather than a peak. In addition, the ferroelectric-to-relaxor transition of the mechanically textured NBT-6BT occurred at a temperature of approximately 63 °C, which is 14 °C lower than $T_{F\text{-}R}$ = 77 °C measured for the electrically poled sample. A possible reason for this could be that the electrically poled state was thermodynamically more stable than

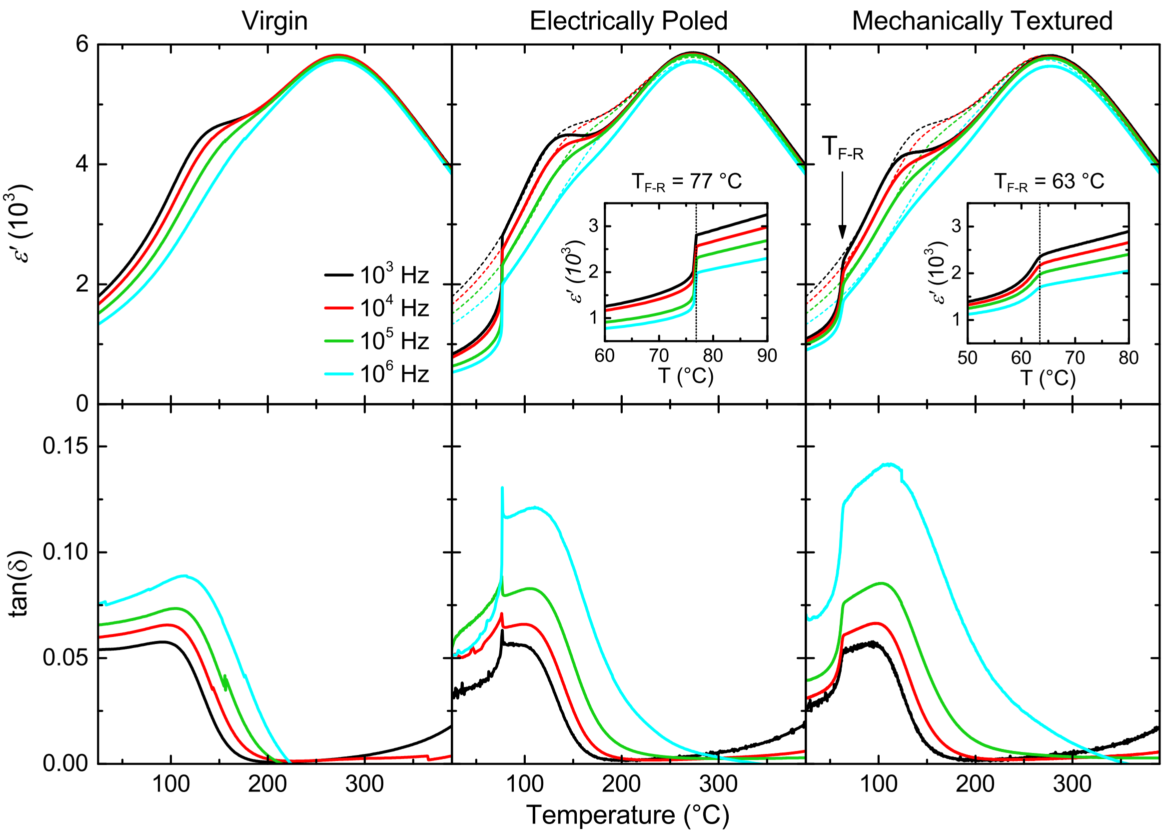

Figure 5.16: Temperature-dependent permittivity ε' and loss tangent $\tan(\delta)$ of virgin, electrically poled, and mechanically textured polycrystalline NBT-6BT samples. The mechanically poled sample was loaded to −500 MPa at 150 °C for 5 min, whereas to the electrically poled sample a 2 kV/mm electric field was applied for 5 min at the same temperature. Both samples were subsequently field cooled to room temperature prior to testing. The dotted lines in are the data for the unpoled, virgin sample and were plotted as comparison. (after Ref. [433])

the textured state, since the degree of ordering was higher and therefore the decomposition of the ferroelectric domains into PNRs required higher temperatures. Please note that the measurement of the electrically poled sample was taken from Section 5.2, where a heating rate of 0.5 °C/min was used instead of a rate of 2 °C/min in this experiment. This could have an influence of the measured $T_{F\text{-}R}$. However, a higher rate would increase the difference between the mechanically textured and the electrically poled sample. It is expected that increasing heating rates result in higher $T_{F\text{-}R}$ values. Therefore, the overall conclusions of the measurements presented here would not be effected. Furthermore, the temperature at which the shoulder in $\varepsilon'(T)$ occurred was lower in the mechanically textured sample compared to the poled one. A reason for that could be that the ratio between rhombohedral and tetragonal PNRs in the mechanically stressed samples could be different to the ratio in the electrically poled samples, leading to a different relaxation behavior at the shoulder in $\varepsilon'(T)$. However, above $T_{F\text{-}R}$ (aside from a certain temperature interval around the shoulder) Figure 5.16 shows that the permittivity curves of both poled and textured samples matched the $\varepsilon'(T)$ behavior of the virgin sample.

Similar to electrical poling, the holding time of the mechanical load during texturing should also have an influence on $T_{F\text{-}R}$. For that reason, the experiment shown in Figure 5.16 was repeated with a holding time of 1 h instead of 5 min at 150 °C and –500 MPa. The resultant transition temperature was found at 68 °C, 5 °C higher than in the case of the 5 min dwelling time, leading to the conclusion that the mechanical texturing of the sample was more complete if a longer holding time was used. Another parameter, which was very likely to have an influence on the phase transition behavior, was the level of the texturing stress. In the previous sections it was already made clear that different constant bias mechanical loads resulted in a significantly different behavior of the material, especially regarding the characteristic transition temperature. In order to investigate the influence of different mechanical texturing stresses in NBT-6BT, additional experiments were performed by using compressive stresses between –100 MPa and –500 MPa at 150 °C for 1 h. The results are shown in Figure 5.17, where only the 1 kHz signal is depicted for better comparability.

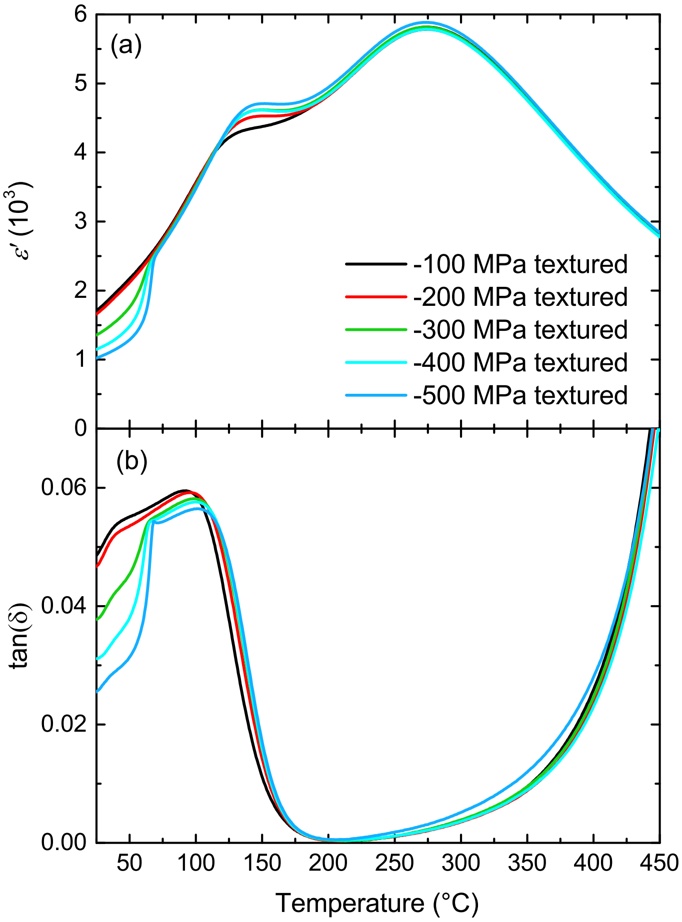

Figure 5.17: Permittivity ε' and loss tangent $\tan(\delta)$ of NBT-6BT as a function of temperature measured at 1 kHz during zero-field heating. The samples were mechanically textured at different mechanical stresses for 1 h at 150 °C prior to testing. (after Ref. [433])

One of the most immediately apparent results of the zero-field measurements presented in Figure 5.17 was that the anomaly in the permittivity-temperature curve occurring at texturing stresses above –200 MPa became sharper and more pronounced with increased mechanical bias during texturing. Previous investigations on polycrystalline $Pb(Mg_{1/3}Nb_{2/3})_{0.87}Ti_{0.13}O_3$ showed a similar increase in the $T_{F\text{-}R}$ anomaly during electric field cooling – zero-field heating experiments with increasing poling electric field [439]. This finding was explained by an incomplete transition from the relaxor to ferroelectric phase, resulting in a phase mixture at lower fields. It could be concluded from the results in Figure 5.17 that this behavior took place in the mechanical textured case in NBT-6BT as well. In addition, the loss tangent as a function of temperature also reflected this observation by showing a stepwise anomaly above –200 MPa texturing stresses, which became sharper with increasing mechanical load. Generally, both permittivity and loss tangent were found to decrease significantly at room temperature with increasing texturing stresses (above –200 MPa), also indicating the development of a long-range ferroelectric order due to the increased correlation length of the PNRs. These results corresponded well to the separately determined coercive stress of NBT-6BT of approximately –275 MPa [351]. Above –200 MPa there was a continual increase in the dielectric anomaly without an apparent saturation up to –500 MPa. Despite this, the stepwise increase in $\varepsilon'(T)$ at $T_{F\text{-}R}$ was still not as sharp as observed for the electrically poled sample in Figure 5.16. A reason for this could be that the mechanical texturing stress was still not high enough to transform the entire sample from the relaxor to the ferroelectric state. Compressive stresses above –500 MPa were not used in this investigation because of the increasing risk of cracking and failure during higher loading conditions.

In addition to the influence of the texturing stress on the transition temperature, the linear region of $\varepsilon'(T)$ in Figure 5.17 above $T_{F\text{-}R}$ was found to be independent from the degree of texturing and followed the measurement of the unstressed sample for all texturing stresses. Above approximately 110 °C, the onset of the shoulder in $\varepsilon'(T)$ was shifted to higher temperatures with increasing mechanical load and the shoulder itself became more prominent. The reasons for these observations are not clear but could be due to the different influence of the mechanical texturing stress on PNRs of different symmetry during the field cooling process. As a result, the transformation process of the PNRs in that temperature region, as proposed by Jo *et al.* [435], could be different at different texturing stresses and this could affect the shape and the onset of the shoulder in $\varepsilon'(T)$. At temperatures above approximately 225 °C, all measurements coincided and displayed nearly the same $\varepsilon'(T)$ behavior as the virgin sample.

The results presented so far were obtained from temperature-dependent measurements at different bias loads or different texturing stresses. In order to obtain a more detailed picture of the stress-induced ferroelectric ordering in NBT-6BT, stress-dependent measurements of the permittivity and the loss tangent were performed at different constant temperatures between –50 °C and 160 °C. Uniaxial mechanical compressive stresses up to –600 MPa were applied with a rate of 0.5 MPa/s by using the screw-driven load frame with an integrated temperature chamber described in Section 2.4. Figure 5.18 depicts the permittivity and the loss tangent of NBT-6BT as a function of stress at five representative temperatures.

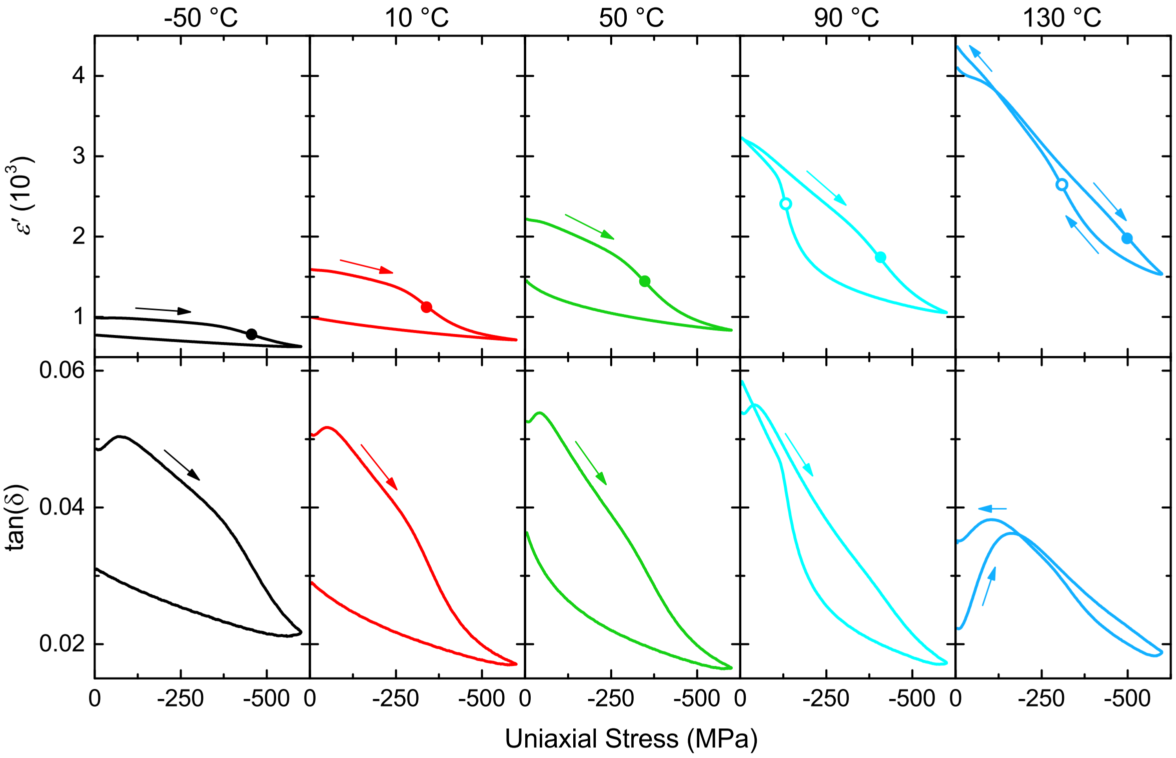

Figure 5.18: Stress-dependent permittivity ε' and loss tangent $\tan(\delta)$ at various constant temperatures for polycrystalline NBT-6BT. To illustrate the critical forward relaxor-to-ferroelectric transition stress, determined by the inflection point in the relative permittivity curve during loading, a solid circle is shown in the permittivity diagrams. The critical converse ferroelectric-to-relaxor transition stress, determined as the inflection point during unloading, is represented by an open circle. For measurements done at temperatures lower than 50 °C, a converse ferroelectric-to-relaxor transition was not observed. (after Ref. [433])

At –50 °C, the permittivity initially decreased only slightly with increasing stress due to clamping of the PNRs and the increased correlation length with increasing mechanical compression, resulting in a lower response to the oscillating voltage of the LCR meter. This behavior changed at a stress of approximately –300 MPa, above which a nonlinear decrease in ε' was observed. In the framework of the earlier discussion in this chapter, a stress-induced relaxor-ferroelectric phase transition could be attributed to this nonlinearity. Like before, the transition stress was determined by the inflection point, in this case of $\varepsilon'(X)$ instead of $\varepsilon'(T)$, and there was again a distribution of transition stresses in the polycrystalline material like in the case of the transition temperatures. For the stress case, the observed distribution of transition stresses resulted in a broader transition interval around the inflection point, which is represented by a solid circle in Figure 5.18. This result is similar to ferroelastic stress-strain curves, where the switching does not normally occur only at the coercive stress, but rather in a stress interval around the inflection point of the stress-strain curve.

The stress-induced phase transition described above was found to be remanent at lower temperatures due to the initial nonergodic relaxor state of unstressed NBT-6BT. This is analogous to the remanent electric-field-induced phase transitions observed in this material as well [141, 282, 440]. While the initial permittivity was increased with increasing temperature, it was on the other hand more sensitive to the compressive stress. As a result, the change in permittivity during loading became larger at elevated temperatures because of the increased thermal fluctuations close to the nonergodic-ergodic transition temperature. At 90 °C a closed permittivity-stress loop was observed, indicating a fully reversible relaxor-ferroelectric transition, which is expected for a material in the ergodic relaxor state. The corresponding inflection point of the transition back to the relaxor state of $\varepsilon'(X)$ is marked by an open circle in Figure 5.18 where applicable. Interestingly, the closed loop behavior at 90 °C and above did not correspond to macroscopic ferroelastic experiments previously done by Webber *et al.* for NBT-6BT, which still revealed a remanent strain typical for ferroelasticity at 100 °C [351]. The difference between the macroscopic and small signal response is curious and presently not clear. It seems to indicate that the stress-strain behavior and the stress-dependent dielectric behavior are decoupled. This could be also illustrated by the coercive stress, which was previously measured to be approximately –200 MPa at 90 °C and did not correspond to any of the features observed in the $\varepsilon'(X)$ curve shown in Figure 5.18. Finally, at high temperatures the permittivity after the loading cycle even exceeded the initial value prior to the experiments. This effect is likely connected with a nonlinearity in $\varepsilon'(X)$ apparent at lower stresses in the loading cycle (see for instance the measurement at 130 °C in Figure 5.18), but no concrete explanation for the physics behind this behavior could be determined.

In addition to the nonlinearity in $\varepsilon'(X)$ at low stresses and higher temperatures, an additional observation was made regarding a maximum in permittivity for stresses below approximately –100 MPa at lower temperatures. Figure 5.19 shows a detailed view of the measurements results presented in Figure 5.18 in this specific load range for four different constant temperatures. At –50 °C, a local maximum in $\varepsilon'(X)$ at –51 MPa was found, which can be also clearly seen in the dielectric loss data in Figure 5.18. However, the maximum in stress-dependent $\tan(\delta)$ at

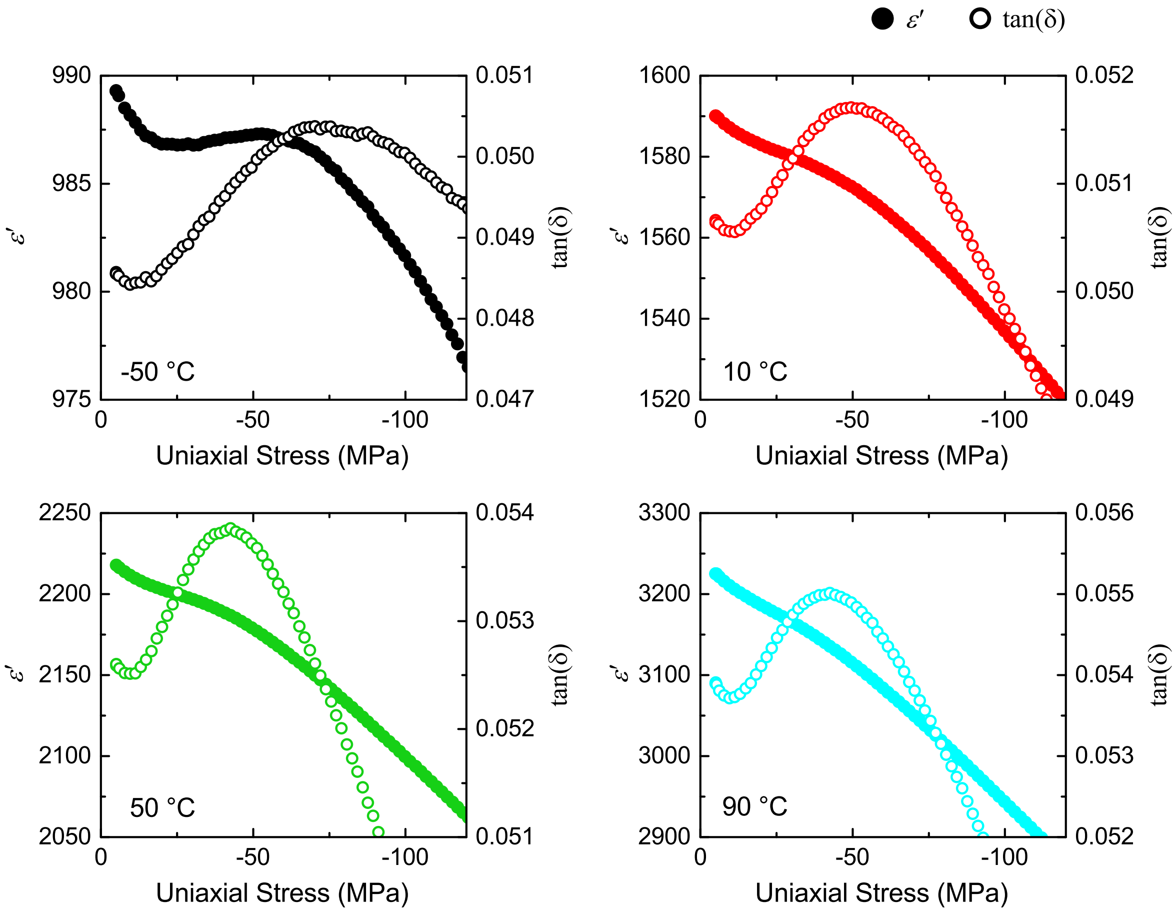

Figure 5.19: Detailed view of the measurement of the stress-dependent permittivity ε' (solid symbols) and the loss tangent $\tan(\delta)$ (open symbols) of NBT-6BT at different constant temperatures. The data was taken from Figure 5.18. (after Ref. [433])

–70 MPa did not coincide with the maximum observed in the permittivity curve and the underlying mechanism remains unclear. Similar observations were also made at the other temperatures depicted in Figure 5.19. A possible origin for the nonlinearity could be the reorientation of PNRs at mechanical loads below the stress-induced relaxor-ferroelectric phase transition. Interestingly, a previous investigation by Bobnar *et al.* also revealed an analogous dielectric nonlinearity in $Pb_{1-x}La_x(Zr_yTi_{1-y})_{1-x/4}O_3$ during electric field loading at constant temperature, although no possible mechanism was suggested [138].

With increasing temperature, the maximum in $\varepsilon'(X)$ became less pronounced, whereas the maximum in the loss tangent was found to be more and more prominent at higher temperatures, as can be seen in Figure 5.18. The mechanical stress where the maximum loss tangent was located decreased initially with increasing temperature down to approximately –42 MPa at 90 °C. Following the transition to a ergodic relaxor, a significant increase at higher temperatures up to –160 MPa at 130 °C was observed. Figure 5.20 displays the mechanical compressive stress X_L at the maximum loss tangent as a function of temperature. Above approximately 77 °C there is a significant increase

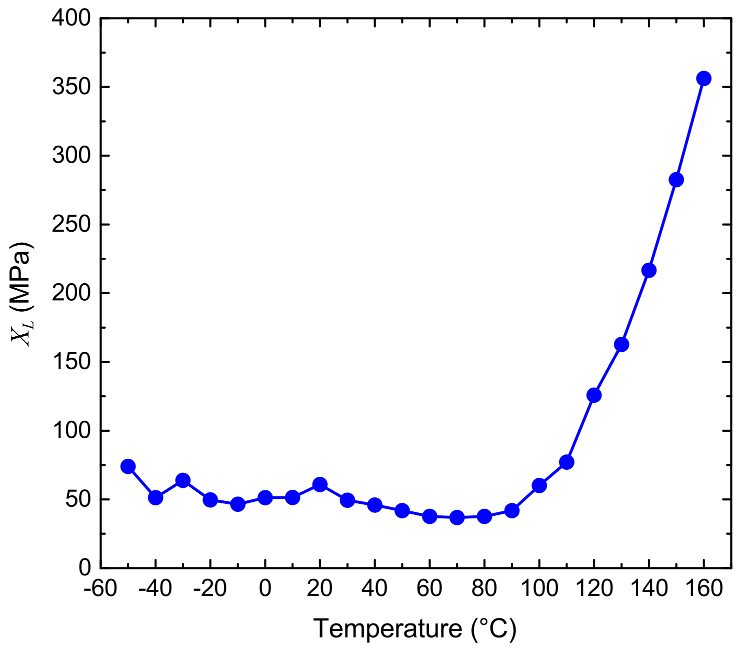

Figure 5.20: Stress at peak loss tangent X_L as a function of temperature during load increase. (after Ref. [433])

in X_L, which is probably closely connected to the increase in the critical stress necessary for inducing a ferroelectric phase in NBT-6BT with temperature (see inflection points in Figure 5.18).

Using the previously discussed data, a stress-dependent phase diagram of NBT-6BT was constructed (Figure 5.21). The inflection points of the permittivity-stress curves during loading and unloading in Figure 5.18 at different constant temperatures were used for determining the critical phase transition stresses between the relaxor and ferroelectric phase and are indicated by arrows pointing up or down, respectively. As already seen in Figure 5.18, the phase transition in the sample was found to be spread over a broad stress interval and therefore the inflection points only represented by the stress at which the rate of the phase transition was at a maximum. Please also note that this is not a phase diagram in the classical physical definition and should be only read in the stress direction, since the data was obtained at constant temperature. In comparison, Figure 5.15b showed a similar phase diagram, but with measurements made in the temperature direction. An extrapolation of the reverse ferroelectric-relaxor transition line to zero stress in Figure 5.21 revealed a transition temperature of 62 °C. This marks the stress-free transition temperature between the nonergodic and the ergodic relaxor state. Consequently, no reverse ferroelectric-relaxor transition was observed below this temperature and the induced ferroelectric state was metastable. In this temperature region, typical ferroelectric polarization hysteresis loops were observed after electrically inducing a ferroelectric phase [151]. In the ergodic state above 62 °C, thermally enhanced fluctuations destroyed the induced long-range order upon mechanical unloading, leading to a reverse ferroelectric-relaxor transition. The stress-temperature phase diagram has the same form as previous electric field-temperature phase diagrams presented for NBT-6BT [13] further indicating the parallels of electrical and mechanical fields on the induced long-range ferroelectric order in relaxor ferroelectrics.

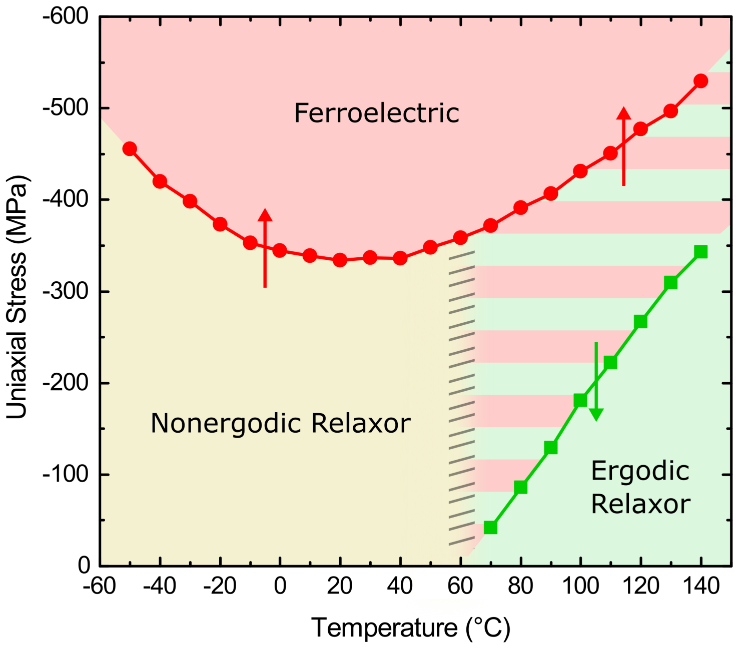

Figure 5.21: Stress-temperature phase diagram for NBT-6BT. The arrows represent the loading direction, whereas the red/green hatched region symbolizes that the phase depends on the loading direction in this region, *i.e.*, ergodic during loading and ferroelectric during unloading. A stress dependence of the transition between nonergodic and ergodic relaxor state was not investigated in this study, which is why the affected area is crossed out in the diagram. (after Ref. [433])

In collaboration with Prof. Dr. John Daniels, Dr. Zhiyang Wang, and Dr. Manuel Hinterstein from the UNSW Australia (Sydney, Australia), room temperature stress-dependent synchrotron diffraction was performed on polycrystalline NBT-6BT at the European Synchrotron Radiation Facility in Grenoble, France. The resultant diffraction patterns were analyzed by using Rietveld refinement by Dr. Z. Wang and Dr. M. Hinterstein; please refer to Ref. [433] for further details. During continuous loading and unloading up to a maximum stress of –593 MPa, the lattice distortion and crystal symmetry (Figure 5.22a) as well as the phase fractions (Figure 5.22b) were determined.

It was found that a phase mixture model of 50 % rhombohedral (*R3c*) and 50 % tetragonal (*P4mm*) symmetry fit the diffraction data best. The data in Figure 5.22a reveals nearly no lattice distortion for either of the proposed two phases present during loading up to –203 MPa, so it was assumed that the material was in a pseudo-cubic phase in this stress region. This was then con-

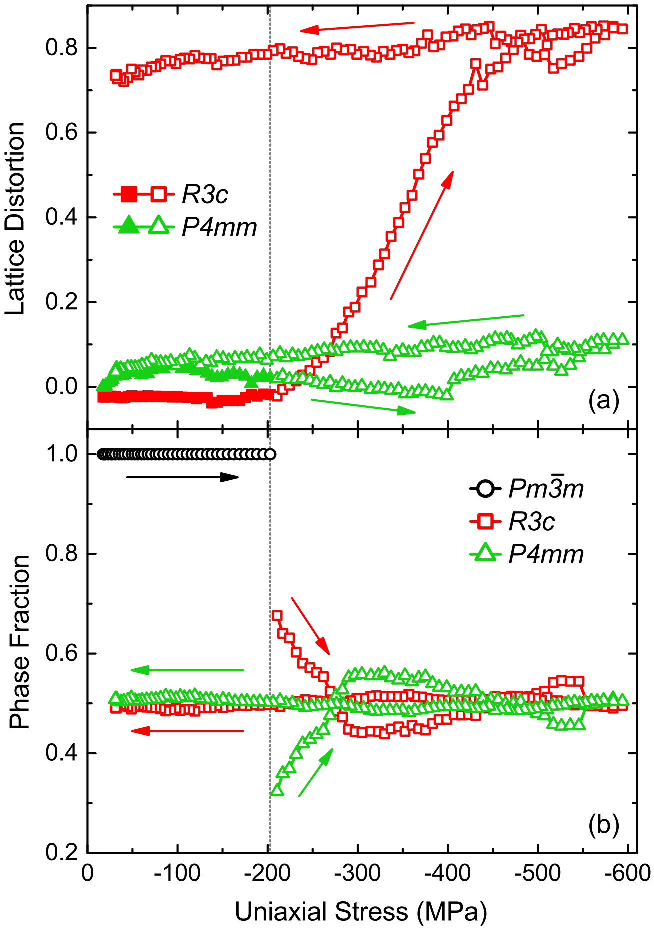

Figure 5.22: (a) The lattice distortion of *R3c* and *P4mm* phases and (b) the phase fractions as a function of compressive stress. For the *R3c* phase, the lattice distortion $\eta_R = c_H/\sqrt{6}a_H - 1$ (a_H and c_H are the unit cell parameters represented in hexagonal axes); for the *P4mm* phase, $\eta_T = c_T/a_T - 1$. The filled symbols in (a) denote the lattice distortions of *R3c* and *P4mm* phases below the critical stress (–203 MPa), depicted with a dotted line. The arrows show the loading direction. (after Ref. [433])

firmed by successfully fitting the diffraction patterns obtained in this region with a pseudo-cubic structure ($Pm\bar{3}m$). Starting at –203 MPa, a significant lattice distortion in the rhombohedral phase fraction clearly indicated a stress-induced phase transition, whereas the tetragonal phase was less affected by the mechanical loading (Figure 5.22a – after the vertical dotted line where solid symbols turn to open symbols). The relative lattice distortions do not clearly indicate the dominance of which phase is present, for this, interpretation of Figure 5.22b is needed. At –203 MPa an immediate change in the phase fraction is seen, such that a mixture of 68 % rhombohedral and 32 % tetragonal phase is found.

With further increases in stress, a nonlinear inter-ferroelectric phase transition from *R3c* to *P4mm* symmetry occurred and was found to be irreversible after removing the mechanical stress (see Figure 5.22b). When returned to zero stress, the lattice distortions remained such that pseudo-cubic fitting was not possible, showing a near 50-50 split in phase fraction between rhombohedral and tetragonal. This is in agreement with the stress-dependent permittivity measurements at room temperature, even if a possible coexistence of all three phases in the transition region suggested by the permittivity measurements could not be revealed directly from the XRD data.

Analogous electric-field-induced phase transitions were also obtained in previous investigations on $(1-x-y)(\mathrm{Na}_{1/2}\mathrm{Bi}_{1/2})\mathrm{TiO}_3-x\mathrm{BaTiO}_3-y(\mathrm{K}_{0.5}\mathrm{Na}_{0.5})\mathrm{NbO}_3$ [313, 441] and were rationalized by the increase in the correlation length of PNRs [293, 379]. By comparing the results of the diffraction experiments and the phase diagram in Figure 5.21, a discrepancy between the transition stress of –203 MPa from the XRD data and –334 MPa from the stress-dependent permittivity measurements at room temperature became apparent. It was argued earlier that the lower stress found in the diffraction experiments corresponded to a kind of onset stress for the stress-induced phase transition, whereas the inflection point in the stress-permittivity curve marked the stress at highest transformation rate. This was also the most likely origin of the observed difference in the phase transition temperature between the XRD and the permittivity measurements.

5.5 Influence of Iron Doping on the Uniaxial Mechanical Compression Effect on the Phase Transition Behavior of NBT-*x*BT

It is well-known that dopants can highly influence the dielectric and electromechanical behavior of perovskite ferroelectric materials [3]. Since the influence of donor and acceptor dopants on PZT materials has already been discussed in detail in Chapter 4, this final section should now give an overview of the influence of dopants on the phase transition behavior of lead-free NBT-*x*BT in connection with uniaxial mechanical compressive stress. For that purpose, NBT-6BT and NBT-15BT powders doped with 1 mol% iron, received from Dr. Eva Sapper and Dr. Robert Dittmer, were processed into cylindrical polycrystalline samples in the same way as described in Section 2.2 for undoped NBT-*x*BT. It is known that the loss of bismuth during calcination and sintering of pure NBT and the addition of the acceptor dopant iron (intentionally or as an impurity in TiO_2 powders) both act to increase the number of oxygen vacancies in the material [442, 443]. This results in the formation of defect complexes consisting of an iron dopant and an oxygen vacancy, which possess a positive net charge and harden the ferroelectric material [436, 443, 444] in a way that is comparable to the observations made for hard doped PZT (see Section 4.4).

The electrical poling process for NBT-*x*BT:Fe required a lower temperature of 100 °C compared to undoped NBT-*x*BT due to the higher conductivity of these samples at elevated temperatures. After poling in silicone oil for 5 min at an electric field of 2 kV/mm and subsequent field cooling down to room temperature, an interesting observation was made. The cylindrical samples showed an apparent color gradient that was visible to the naked eye, shown in Figure 5.23.

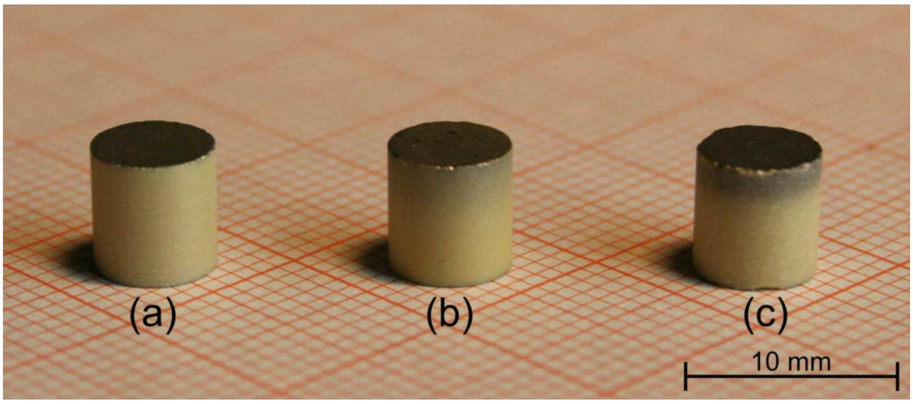

Figure 5.23: Coloring of polycrystalline samples of (a) virgin (b) NBT-6BT and (c) NBT-15BT doped with 1 mol% iron after electrical poling at 100 °C at 2 kV/mm electric field and field cooling to room temperature.

The part of the samples at the cathode side of the poling setup was found to have a darker color after electrical poling. Regarding the composition, some differences could be observed between NBT-6BT:Fe and NBT-15BT:Fe. In the former case (Figure 5.23b), the black color gradually faded in the direction of the anode during poling. In the latter case (Figure 5.23c), the border of the coloring was relatively sharp, nearly forming a second layer in the sample. The origin of these observed color difference are likely due to the migration of oxygen vacancies to the cathode, which was also observed *in-situ* by Ossmer *et al.* in PZT layers during the application of an electric field [445]. As a consequence of this migration, the material appeared dark or black at the cathode side where the oxygen vacancies and/or the resulting defect complexes were accumulating. It is important to note that the defect distribution in the samples was not homogeneous after the poling process.

Similar experiments to those presented and discussed in Section 5.2 were done on poled NBT-6BT:Fe and NBT-15BT:Fe samples. Figure 5.24 shows the permittivity, the loss tangent and the piezoelectric coefficient of NBT-6BT:Fe as a function of temperature and frequency at different mechanical bias stresses between –5 MPa and –300 MPa.

The permittivity curve showed no significant frequency dispersion below the ferroelectric-to-relaxor transition temperature in the induced ferroelectric phase for all bias stresses. The NBT-6BT:Fe samples revealed a $T_{F\text{-}R}$ of approximately 106 °C, which was found to be 29 °C higher than the $T_{F\text{-}R}$ measured for undoped NBT-6BT. This temperature difference was significantly larger than the one determined in previous investigations [436]. The loss tangent showed an maximum at higher temperatures, which did not coincide with any of the observed features in permittivity or

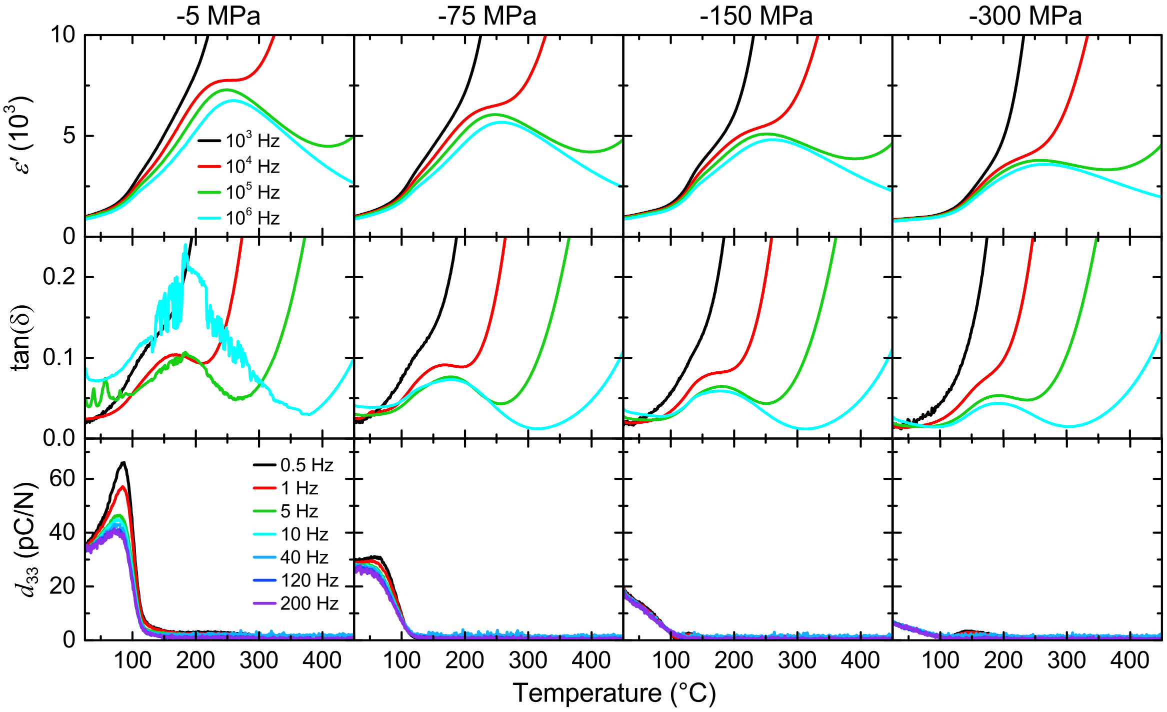

Figure 5.24: Frequency-dependent permittivity ε', loss tangent $\tan(\delta)$, and piezoelectric coefficient d_{33} of electrically poled polycrystalline NBT-6BT doped with 1 mol% iron as a function of temperature and frequency at various constant uniaxial mechanical stresses.

piezoelectric coefficient. At temperatures above $T_{F\text{-}R}$, the material exhibited a relaxor character, visible in the enhanced frequency dispersion and the formation of a maximum in $\varepsilon'(T)$. During the poling process it was observed that NBT-6BT:Fe shows an increased conductivity at elevated temperatures, which is mainly due to the high ionic conductivity of the material originating from a high concentration of mobile oxygen vacancies. This observation could also be confirmed by the unusually strong increase of the low frequency permittivity in Figure 5.24 at high temperatures, accompanied by a high loss tangent typical for samples with rising conductivity.

With increasing compressive stress, the frequency dependent maximum in $\varepsilon'(T)$ was lowered, but $T_{F\text{-}R}$ seemed to increase with higher mechanical loads, probably due to an additional stress-induced long-range order above the electrical T_d, similar to the previous results in pure NBT-6BT (see Section 5.2 and Section 5.3). However, no sharp anomaly in permittivity could be observed in the iron-doped material, rather only a broader increase. This is also reflected in the piezoelectric coefficient as a function of temperature, which at a prestress of –5 MPa exhibited a broader decrease as compared to that of NBT-6BT. In addition, the d_{33} measured at –5 MPa was found to significantly increase (especially at low frequency, nearly doubling in value at 0.5 Hz) with increasing temperature and to form a maximum before dropping at T_d. A reason for this could be that the domain walls pinned at the defect complexes were able to overcome that pinning due to a thermal enhancement, but only at the lowest frequencies. In addition to that, thermally enhanced conductivity could play a role in the strong increase of d_{33} with temperature at lower frequencies.

The depolarization temperature at –5 MPa preload was approximately 100 °C, nearly 23 °C higher than in the undoped material at the same stress. Since the iron doping resulted in a hardening of the material [444], this result is expected. With increasing mechanical bias stress, the maximum in $d_{33}(T)$ as well as the frequency dispersion became more and more suppressed, as was the case in undoped NBT-6BT. In addition, the room temperature value of the piezoelectric coefficient was found to decrease with increasing mechanical stress due to the previously discussed stress-induced depolarization mechanism.

A comparable set of measurements on NBT-15BT:Fe is shown in Figure 5.25. Unlike NBT-6BT:Fe, the permittivity curve of NBT-15BT:Fe revealed a sharp step at $T_{F\text{-}R}$ in the –5 MPa measurement. Again, no frequency dispersion in $\varepsilon'(T)$ could be measured below the transition temperature, indicating a strongly induced ferroelectric nature due to the poling process. Similar to NBT-6BT:Fe, the permittivity at lower frequencies showed a strong increase with increasing temperature, which corresponded to the elevated conductivity due to the Fe doping. The maxima in permittivity and loss tangent were found to be frequency-dependent as well and their dependence decreased with increasing mechanical compression. In comparison to NBT-6BT:Fe, the piezoelec-

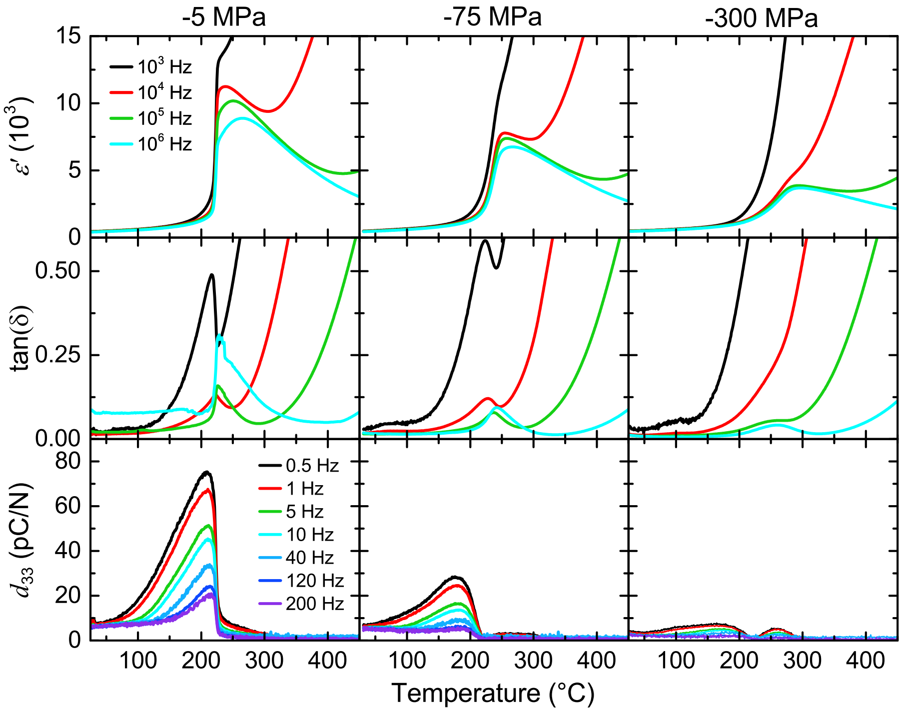

Figure 5.25: Frequency-dependent permittivity ε', loss tangent $\tan(\delta)$ and piezoelectric coefficient d_{33} of electrically poled polycrystalline NBT-15BT doped with 1 mol% iron as a function of temperature and frequency at various constant uniaxial mechanical stresses.

tric coefficient was also found to significantly increase with increasing temperature in iron-doped NBT-15BT. In contrast, the frequency dispersion seemed to be even more pronounced and showed a difference of 72 % between the 0.5 Hz and 200 Hz signal at the maximum of $d_{33}(T)$ measured at –5 MPa prestress. The dispersion was also still more strongly present in the d_{33} values at the mechanical bias stress of –75 MPa as compared to the NBT-6BT:Fe samples. With further increasing mechanical load, the maximum in piezoelectric coefficient decreased, but unlike NBT-6BT:Fe, a stress of –300 MPa was not enough to completely suppress the maximum for all frequencies.

For a better side-by-side comparison of the experiments done at different compressive stresses, Figure 5.26 shows the permittivity, the loss tangent and the piezoelectric coefficient of both NBT-6BT:Fe and NBT-15BT:Fe as a function of temperature and bias stress at 100 kHz (ε' and $\tan(\delta)$) and 10 Hz (d_{33}). The 100 kHz signal of the dielectric measurements was chosen because of the relatively large influence of conductivity on the 1 kHz signal normally used, which was revealed in Figure 5.24 and Figure 5.25. Due to a possibly bad electrical contact, the temperature-dependent loss tangent of NBT-6BT:Fe measured at –5 MPa mechanical prestress showed comparatively high noise.

An anomaly (indicated by an arrow in Figure 5.26) in $\varepsilon'(T)$ at 100 kHz could be observed around $T_{F\text{-}R}$ for NBT-6BT:Fe, which became flatter and broadened with increasing uniaxial compression. This is in agreement with measurements done on undoped NBT-6BT (Figure 5.5). Between the measurement at –5 MPa and the one at –300 MPa bias stress, the maximum in permittivity was shifted by approximately 10 °C towards higher temperatures as the curves broadened, whereas the permittivity value at maximum decreased by 48 % in the same stress interval. In contrast, the magnitude of the permittivity of the ferroelectric phase at room temperature showed only a minor decrease with increasing stress. The temperature-dependent loss tangent of NBT-6BT:Fe on the other hand was found to decrease due to the application of stress. NBT-15BT:Fe revealed a similar behavior, but showed a more pronounced stress sensitivity as depicted in Figure 5.26. Although ε' was stress-independent at temperatures below 175 °C up to –300 MPa mechanical load, the high temperature behavior revealed a significant influence of the mechanical compression. The temperature corresponding to the maximum permittivity value was increased by 43 °C, in connection with a decrease of the permittivity value of 62 %, between the experiments done at –5 MPa and –300 MPa. Like in the case of iron-doped NBT-6BT, a clear broadening of the anomaly at $T_{F\text{-}R}$ with increasing mechanical stress, together with a shift of $T_{F\text{-}R}$ towards higher temperatures was observed. In addition, the maximum in the loss tangent was shifted to higher temperatures with increasing stress for both compositions.

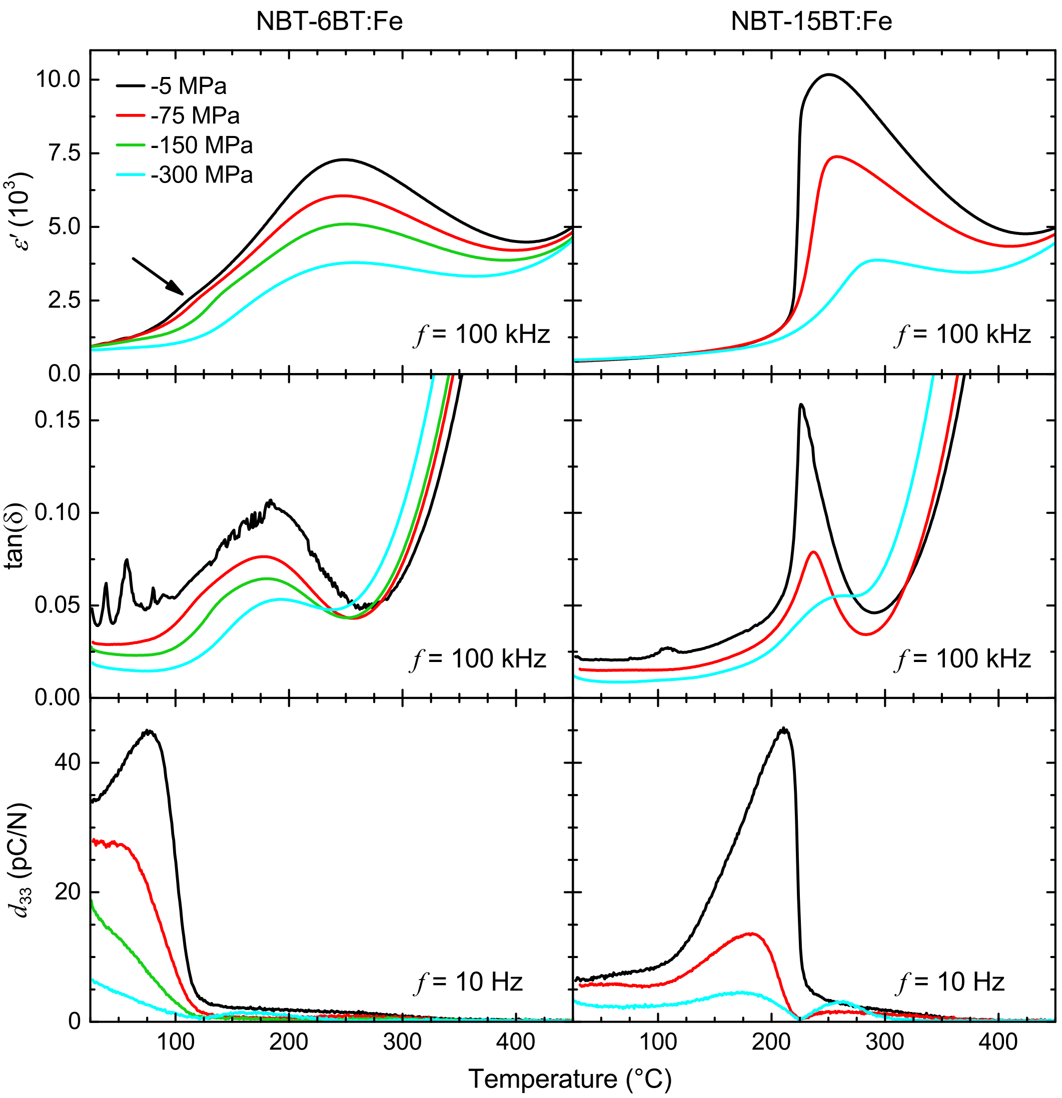

Figure 5.26: Comparison of the temperature-dependent permittivity ε', loss tangent $\tan(\delta)$ and piezoelectric coefficient d_{33} of NBT-6BT and NBT-15BT doped with 1 mol% iron at various constant uniaxial stresses.

It could be revealed from Figure 5.26 that the maximum of $d_{33}(T)$ and therefore the drop in d_{33} at the depolarization temperature broadened and shifted to lower temperatures for both materials. This was in agreement with observations made for the undoped material in Figure 5.5 and originated most likely from the same clamping mechanisms due to the applied stress. A decrease of the piezoelectric coefficient at room temperature of 81 % and 45 % was observed for NBT-6BT:Fe and NBT-15BT:Fe, respectively. Compared to their undoped counterparts, the doped material seemed to be more stress sensitive at room temperature, which is the opposite of that expected for acceptor-doped piezoelectrics that generally have an increased stability of the piezoelectric properties with stress (see for example Section 4.4 and its references). However, it needs to be taken into account that the behavior of the doped materials could be highly influenced by the charge concentration due to doping, the presence of an increased amount of oxygen vacancies, and the formation of dipole complexes. In addition, the defect distributions in the samples were apparently inhomogeneous following the electrical poling treatment (see Figure 5.23), which could also lead to varying stress sensitivity. This was likely the case for NBT-15BT:Fe due to the formation of the sharper interface in the sample coloring visible in Figure 5.23c after d.c. electrical bias poling. Finally, the temperature evolution of the dielectric and the piezoelectric properties of the iron-doped NBT-xBT materials could be significantly influenced by a possible re-homogenization at elevated temperatures. Further investigations are needed here to clarify the interplay of defects, dipole complexes and mechanical stress.

Additional anomalies in the stress-dependent piezoelectric behavior of iron-doped NBT-xBT above the depolarization behavior were also observed. Figure 5.27 shows the piezoelectric coefficient of iron-doped NBT-6BT and NBT-15BT as a function of temperature at various constant uniaxial compressive stresses in enhanced detail. For a better comparison, only the 10 Hz signal is shown. Experimental results in Figure 5.26 and Figure 5.27 reveal that the piezoelectric coefficient did not drop to zero at T_d, but rather showed a continuous decrease with increasing temperature far above the initial thermal depolarization. This behavior is similar to the findings in pure NBT-xBT, as shown in Figure 5.9 and Figure 5.10.

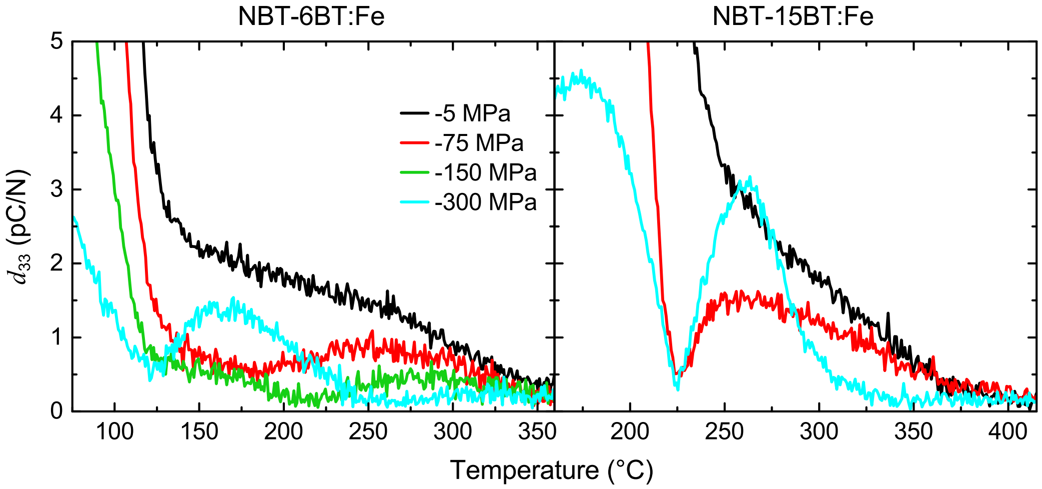

Figure 5.27: Detailed view of the temperature-dependent piezoelectric coefficient d_{33} of NBT-6BT and NBT-15BT doped with 1 mol% iron at various constant uniaxial stresses. For the sake for clarity, only the 10 Hz signal of d_{33} is shown here.

For both doped compositions, a kind of two-regime process could be observed at lower mechanical stresses (–5 MPa) in Figure 5.27, marked by an overall gradual decrease of d_{33} with increasing temperature together with the change in the slope of the $d_{33}(T)$ curve. Similar to findings in other materials like PZT and pure NBT-xBT, the doped NBT-xBT materials in Figure 5.27 showed the rise of a secondary maximum in $d_{33}(T)$. This only occurred at temperatures above T_d and at higher mechanical bias loads above –75 MPa with the maxima becoming sharper for the NBT-15BT:Fe sample. An analysis of a change in phase angle comparable to that done for NBT-

12BT in Figure 5.11 was not possible because the raw phase data of these measurements were too noisy. However, the formation of the secondary maximum in $d_{33}(T)$ was found to be quite severe for NBT-15BT:Fe as the value of d_{33} reached approximately 69 % of the value of the maximum below T_d.

5.6 Summary

It was shown in this chapter that a compressive uniaxial mechanical stress had a significant influence on the phase transitions and thermal evolution of the dielectric and piezoelectric properties of doped and undoped NBT-xBT. Samples poled with an electric d.c. bias field at elevated temperatures showed a general decrease in permittivity and in the piezoelectric coefficient if a sufficiently large mechanical stress was applied. This was due to clamping of PNRs or domain walls and, in the case of the decreased piezoelectric coefficient, also due to stress-induced ferroelastic depolarization. The mixed phase NBT-xBT compositions close to the MPB, *i.e.* NBT-6BT and NBT-9BT, revealed a higher sensitivity to mechanical stress than the rhombohedral NBT-3BT or the tetragonal NBT-12BT. It was found for all NBT-xBT materials that under the application of sufficiently large mechanical bias load during stress field heating, a difference between the depolarization temperature and the ferroelectric-to-relaxor phase transition temperature appeared. This could be attributed to a stress-induced ferroelectric phase, which was more thermally stable than the electric field-induced, macroscopically polarized ferroelectric phase due to the applied constant mechanical compression during heating. Based on temperature-dependent and stress-dependent permittivity measurements performed on electrically unpoled but mechanically textured NBT-6BT samples, the mechanical stress was found to have a similar effect as an electric field on the temperature-dependent permittivity and was shown to induce a remanent ferroelectric phase during stress dependent-measurements. A stress-dependent phase map of NBT-6BT could finally be developed from these experiments.

Fe-doped NBT-6BT and NBT-15BT revealed a significantly different temperature-dependent behavior of the permittivity and the piezoelectric coefficient. The comparatively high conductivity of these materials made dc bias electrical poling at elevated temperatures more complicated and resulted in a lower initial piezoelectric coefficient compared to the undoped materials. However, $T_{F\text{-}R}$ was found to increase in the doped compositions, indicating a stabilization of the ferroelectric phase due to the iron doping. In general, the doped NBT-xBT compositions showed similar behavior on the application of a compressive mechanical bias stress, *i.e.* a reduction in the dielectric and piezoelectric properties and a shift in the depolarization and phase transition temperatures. Defect complexes play an important role in Fe-doped NBT-xBT and are theorized to be the main origin of the different dielectric and piezoelectric properties compared to the undoped compositions. Since it was indicated in Section 4.4 that for ferroelectricly hard PZT, a mechanical stress is probably able to reorient polar defects, a similar mechanism in acceptor-doped NBT-xBT:Fe is conceivable. But this question requires a more detailed investigation, especially with regards to the temperature-dependent mobility of defect complexes in NBT-xBT:Fe.

6 Concluding Remarks and Ideas for Further Investigations

The novel measurement setup described in Chapter 2 was especially developed for this work and allows the realization of various novel experiments. The design as well as the measurement and control software written with LabVIEW is well suitable for further developments and extensions. A first step could be to transfer the d_{33} measurement setup to the second uniaxial load frame (Instron 5967), extending to the low temperature range –150 °C. In addition, it is possible to measure the impedance spectra of materials as a function of temperature and bias mechanical load. An additional experiment, which would be relatively easy to realize, is the measurement of the piezoelectric coefficient during the application of a d.c. electric field. In combination with temperature and uniaxial mechanical stress, such measurements could give deeper insight in the switching behavior and the phase stability of ferroelectric materials. Since it is also possible to characterize complete devices, such as multilayer piezoelectric actuators under conditions close to the real application, this setup might be interesting for cooperation with industry as well. In fact, industrial projects with Bosch, Johnson Matthey, and Merck have already been undertaken on the described equipment.

It would be advantageous for temperature-dependent d_{33} measurements if the load amplitude applied by the stack actuator could be corrected during heating and cooling. This could be achieved by an integrated feed-back loop, which continuously monitors the load signal and corrects the voltage signal used for controlling the stack amplifier accordingly. In addition, different pressing tools, different sample geometries, and electrical contacts on sample faces perpendicular to the loading direction would allow of measuring the coefficient d_{31} as well. Such experiments were already successfully tested. However, further development is required to refine this technique. An additional and particularly challenging future engineering project is the improvement of the strain measurement system, presently done with an LVDT attached to a spring system. Although this system can accurately characterize macroscopic stress-strain behavior, it is not capable of detecting small displacement oscillations, particularly at high frequencies where contact measurement systems are at a disadvantage. Such measurements are required for characterizing the elastic compliance of a sample. A possible solution would be a redesign the strain measurement system, including the replacement of the LVDT by a noncontact displacement system, such as an optical, capacitive displacement, or laser vibrometer sensor.

Barium titanate revealed an increase in the Curie point and a decrease in Curie-Weiss temperature with increasing uniaxial mechanical bias stress. In contrast to the observations made during the application of hydrostatic stress, this resulted in an increase in the first order nature of the ferroelectric-paraelectric phase transition. The changes in the phase transition behavior were successfully describe by introducing stress-dependent coefficients in the LGD theory rather than by increasing the order of the expansion of the free energy function. Since these coefficients are usually used in simulations of ferroelectrics, this could help to improve the theoretical prediction of stress effects on these materials. A similar analysis has been already done by Prof. Dr. George Rossetti, Jr. and Nasser Khakpash (University of Connecticut, Storrs, Connecticut, USA) for the lower temperature phase transitions of barium titante, which were also characterized as a function of uniaxial mechanical bias stress in this work. These results will be the subject of an upcoming publication.

Chapter 4 of this work demonstrated the change in the properties and the phase transition behavior of soft and hard commercial PZT materials due to the application of uniaxial mechanical loads. Especially the stress-induced depolarization revealed significant differences between the two compositions and illustrated the influence of polar defects present in the hard PZT. An important outcome of the experiments was that a mechanical stress is capable of reorienting the polar defects, but further experiments are required to address this problem in more detail. In this context, stress-dependent electron paramagnetic resonance spectroscopy might help to clarify if the influence of the mechanical load on the polar defects is direct or indirect. In addition, the negative phase angle of the piezoelectric coefficient observed in both PZT materials at higher bias stresses above T_d is an interesting topic for further investigation. A negative phase angle is known to potentially cause a clockwise electric field-strain or mechanical stress-polarization hysteresis [415]. This could be experimentally verified by using the current experimental setup at the corresponding combinations of temperature and mechanical stress. In addition, temperature-dependent impedance measurements under the application of a mechanical bias stress could reveal if this effect is also present in the phase angle measured in these experiments. It should be also considered to investigate this effect in a normal ferroelectric material, e.g., barium titanate, in order to elucidate the physical mechanism behind this phenomenon.

One of the most important finding during the investigation of the lead-free material NBT-xBT was that a compressive uniaxial mechanical stress was found to be capable to induce a long-range ferroelectric order into the relaxor state of electrically unpoled NBT-6BT. In order to support this observation, measurements of ferroelectric hysteresis loops at different constant stresses and temperatures might be helpful to improve the determination of the phase boundaries of the stress-temperature phase diagram of NBT-6BT. A prerequisite, however, would certainly be that it would be possible to distinguish in the ferroelectric hysteresis loops between electrical poling and field induced phase transition in the first cycle of the electric field. Furthermore, the stress-dependent XRD measurements could be done at different temperatures to investigate the evolution of the stress-induced ferroelectric order in more detail. The stress-temperature phase diagram of NBT-xBT presented in this work lacks the determination of the stress-dependent boundary between the ergodic and the nonergodic relaxor state. In order to accomplish this, stress- and temperature-dependent impedance spectroscopy could be performed, which will reveal the freezing temperature of the PNRs as a function of uniaxial mechanical compression.

The stress-induced depolarization of electrically poled NBT-xBT could be investigated in more detail by measuring the depolarization current as a function of temperature and mechanical compression. This could also help to elucidate the material's behavior above T_d, where a d_{33} signal, resulting from a remaining macroscopic polarization, was still measureable. In the case of the Fe-doped NBT-xBT, the apparent coloring of the samples after poling could be an interesting starting point for further research. Temperature- and stress-dependent impedance spectroscopy could serve to understand the thermally activated rebalancing processes of the oxygen vacancies in an electrically poled sample during heating, maybe also at different oxygen partial pressures. This additionally raises the question if the application of a mechanical stress could also initiate oxygen vacancy migration. It would be interesting observe the change in the sample coloring during mechanical loading or heating, which could be done by recording an in-situ video during the application of the mechanical stress or during the heating process.

Bibliography

[1] Damjanovic, D. Ferroelectric, dielectric and piezoelectric properties of ferroelectric thin films and ceramics. *Reports on Progress in Physics* **61**(9), 1267 (1998).

[2] Jona, F. & Shirane, G. *Ferroelectric Crystals*. Dover Publications, Inc., (1962).

[3] Jaffe, B., Cook, W. R. & Jaffe, H. *Piezoelectric Ceramics*. Academic Press Ltd., (1971).

[4] Lines, M. E. & Glass, A. M. *Principles and Applications of Ferroelectrics and Related Materials*. Oxford Classic Texts in the Physical Sciences. Calderon Press, Oxford, Oxford, (1977).

[5] Moulson, A. J. & Herbert, J. M. *Electroceramics: Materials, Properties, Applications*. Wiley, Chichester, (2003).

[6] Newnham, R. E. *Properties of Materials: Anisotropy, Symmetry, Structure*. Oxford Univ. Press, Oxford, (2005).

[7] Mohr, P. J., Taylor, B. N. & Newell, D. B. The 2014 CODATA Recommended Values of the Fundamental Physical Constants, (2015).

[8] Sundar, V. & Newnham, R. E. Electrostriction and polarization. *Ferroelectrics* **135**(1), 431–446 (1992).

[9] Curie, J. & Curie, P. Développement, par pression, de l'électricité polaire dans les cristaux hémièdres à faces inclinées. *Comptes rendus hebdomadaires des séances de l'Académie des sciences* **91**, 294–295 (1880).

[10] Schader, F. H. Temperature dependence of the dielectric properties of lead-free ferroelectrics under mechanical loads. Diplomarbeit, Technische Universität Darmstadt, (2011).

[11] von Hippel, A., Breckenridge, R. G., Chesley, F. G. & Tisza, L. High dielectric constant ceramics. *Industrial & Engineering Chemistry* **38**(11), 1097–1109 (1946).

[12] Weaver, P. M., Cain, M. G. & Stewart, M. Temperature dependence of high field electromechanical coupling in ferroelectric ceramics. *Journal of Physics D: Applied Physics* **43**(16), 165404 (2010).

[13] Sapper, E., Novak, N., Jo, W., Granzow, T. & Rödel, J. Electric-field-temperature phase diagram of the ferroelectric relaxor system $(1-x)\mathrm{Bi}_{1/2}\mathrm{Na}_{1/2}\mathrm{TiO}_3-x\mathrm{BaTiO}_3$ doped with manganese. *Journal of Applied Physics* **115**(19), 194104 (2014).

[14] Daniels, J. E., Cozzan, C., Ukritnukun, S., Tutuncu, G., Andrieux, J., Glaum, J., Dosch, C., Jo, W. & Jones, J. L. Two-step polarization reversal in biased ferroelectrics. *Journal of Applied Physics* **115**(22), 224104 (2014).

[15] Arlt, G. Switching and dielectric nonlinearity of ferroelectric ceramics. *Ferroelectrics* **189**(1), 91–101 (1996).

[16] Arlt, G. A model for switching and hysteresis in ferroelectric ceramics. *Integrated Ferroelectrics* **16**(1-4), 229–236 (1997).

[17] Hwang, S. C. & Arlt, G. Switching in ferroelectric polycrystals. *Journal of Applied Physics* **87**(2), 869 (2000).

[18] Hall, D. A. Review nonlinearity in piezoelectric ceramics. *Journal of Materials Science* **36**(19), 4575–4601 (2001).

[19] Jones, J. L., Aksel, E., Tutuncu, G., Usher, T.-M., Chen, J., Xing, X. & Studer, A. J. Domain wall and interphase boundary motion in a two-phase morphotropic phase boundary ferroelectric: Frequency dispersion and contribution to piezoelectric and dielectric properties. *Physical Review B* **86**(2), 024104 (2012).

[20] Arlt, G. The role of domain walls on the dielectric, elastic and piezoelectric properties of ferroelectric ceramics. *Ferroelectrics* **76**(1), 451–458 (1987).

[21] Damjanovic, D. & Demartin, M. The Rayleigh law in piezoelectric ceramics. *Journal of Physics D: Applied Physics* **29**(7), 2057–2060 (1996).

[22] Damjanovic, D. Logarithmic frequency dependence of the piezoelectric effect due to pinning of ferroelectric-ferroelastic domain walls. *Physical Review B* **55**(2), R649–R652 (1997).

[23] Damjanovic, D. Stress and frequency dependence of the direct piezoelectric effect in ferroelectric ceramics. *Journal of Applied Physics* **82**(4), 1788 (1997).

[24] Damjanovic, D. & Demartin, M. Contribution of the irreversible displacement of domain walls to the piezoelectric effect in barium titanate and lead zirconate titanate ceramics. *Journal of Physics: Condensed Matter* **9**(23), 4943–4953 (1997).

[25] Davis, M., Damjanovic, D. & Setter, N. Temperature dependence of the direct piezoelectric effect in relaxor-ferroelectric single crystals: Intrinsic and extrinsic contributions. *Journal of Applied Physics* **100**(8), 084103 (2006).

[26] Rayleigh. XXV. Notes on electricity and magnetism. - III. On the behaviour of iron and steel under the operation of feeble magnetic forces. *Philosophical Magazine Series 5* **23**(142), 225–245 (1887).

[27] Hall, D. A. Rayleigh behaviour and the threshold field in ferroelectric ceramics. *Ferroelectrics* **223**(1), 319–328 (1999).

[28] Pramanick, A., Damjanovic, D., Nino, J. C. & Jones, J. L. Subcoercive Cyclic Electrical Loading of Lead Zirconate Titanate Ceramics I: Nonlinearities and Losses in the Converse Piezoelectric Effect. *Journal of the American Ceramic Society* **92**(10), 2291–2299 (2009).

[29] Fisher, R. S. L., McLaughlin, E. A. & Robinson, H. C. Stress-Dependent Behavior of d_{33} and Y^{E33} in Navy Types III and VI Ceramics. *Journal of Intelligent Materials Systems and Structures* **15**(7), 549–556 (2004).

[30] Damjanovic, D., Demartin, M., Shulman, H. S., Testorf, M. & Setter, N. Instabilities in the piezoelectric properties of ferroelectric ceramics. *Sensors and Actuators A: Physical* **53**(1-3), 353–360 (1996).

[31] Hall, D. A., Steuwer, A., Cherdhirunkorn, B., Withers, P. J. & Mori, T. Micromechanics of residual stress and texture development due to poling in polycrystalline ferroelectric ceramics. *Journal of the Mechanics and Physics of Solids* **53**(2), 249–260 (2005).

[32] Arlt, G. & Dederichs, H. Complex elastic, dielectric and piezoelectric constants by domain wall damping in ferroelectric ceramics. *Ferroelectrics* **29**(1), 47–50 (1980).

[33] Dehlinger, U. & Kröner, E. Der elastische Dipol. *Zeitschrift für Metallkunde* **51**(8), 457–461 (1960).

[34] Salje, E. & Hoppmann, G. Direct observation of ferroelasticity in $Pb_3(PO_4)_2$-$Pb_3(VO_4)_2$. *Materials Research Bulletin* **11**(12), 1545–1549 (1976).

[35] Salje, E. K. H. Ferroelastic Materials. *Annual Review of Materials Research* **42**(1), 265–283 (2012).

[36] Virkar, A. V. & Matsumoto, R. L. K. Ferroelastic Domain Switching as a Toughening Mechanism in Tetragonal Zirconia. *Journal of the American Ceramic Society* **69**(10), C–224–C–226 (1986).

[37] Fett, T., Munz, D. & Thun, G. Polarization measurements on PZT under transverse tensile loading. *Ferroelectrics* **247**(1), 321–332 (2000).

[38] Berlincourt, D. Piezoelectric ceramics: Characteristics and applications. *The Journal of the Acoustical Society of America* **70**(6), 1586–1595 (1981).

[39] Cao, H. & Evans, A. G. Nonlinear Deformation of Ferroelectric Ceramics. *Journal of the American Ceramic Society* **76**(4), 890–896 (1993).

[40] Zhou, D., Kamlah, M. & Munz, D. Effects of Bias Electric Fields on the Non-linear Ferroelastic Behavior of Soft Lead Zirconate Titanate Piezoceramics. *Journal of the American Ceramic Society* **88**(4), 867–874 (2005).

[41] Marsilius, M., Granzow, T. & Jones, J. L. Quantitative comparison between the degree of domain orientation and nonlinear properties of a PZT ceramic during electrical and mechanical loading. *Journal of Materials Research* **26**(09), 1126–1132 (2011).

[42] Fett, T., Munz, D. & Thun, G. Young's modulus of soft PZT from partial unloading tests. *Ferroelectrics* **274**, 67–81 (2002).

[43] Webber, K. G., Aulbach, E., Key, T., Marsilius, M., Granzow, T. & Rödel, J. Temperature-dependent ferroelastic switching of soft lead zirconate titanate. *Acta Materialia* **57**(15), 4614–4623 (2009).

[44] Marsilius, M., Webber, K. G., Aulbach, E. & Granzow, T. Comparison of the Temperature-Dependent Ferroelastic Behavior of Hard and Soft Lead Zirconate Titanate Ceramics. *Journal of the American Ceramic Society* **93**(9), 2850–2856 (2010).

[45] Ji, D. W. & Kim, S.-J. Temperature-dependent ferroelastic switching of ferroelectric ceramics and evolution of linear material properties. *Acta Materialia* **61**(1), 1–11 (2013).

[46] Schäufele, A. B. & Heinz Härdtl, K. Ferroelastic Properties of Lead Zirconate Titanate Ceramics. *Journal of the American Ceramic Society* **79**(10), 2637–2640 (1996).

[47] Zhou, D., Wang, R. & Kamlah, M. Determination of reversible and irreversible contributions to the polarization and strain response of soft PZT using the partial unloading method. *Journal of the European Ceramic Society* **30**(12), 2603–2615 (2010).

[48] Müller, K. A. & Burkard, H. $SrTiO_3$: An intrinsic quantum paraelectric below 4 K. *Physical Review B* **19**(7), 3593–3602 (1979).

[49] Caspari, M. E. & Merz, W. J. The Electromechanical Behavior of $BaTiO_3$ Single-Domain Crystals. *Physical Review* **80**(6), 1082–1089 (1950).

[50] Merz, W. J. Double Hysteresis Loop of $BaTiO_3$ at the Curie Point. *Physical Review* **91**(3), 513–517 (1953).

[51] Sinyakov, E. V., Flerova, S. A. & Kubyshki, O. A. Influence of Unilateral Compression on Phase Transitions in $BaTiO_3$ Single Crystals. *Izvestiya Akademii Nauk SSSR Seriya Fizicheskaya* **31**(11), 1768–1770 (1967).

[52] Wang, Z., Webber, K. G., Hudspeth, J. M., Hinterstein, M. & Daniels, J. E. Electric-field-induced paraelectric to ferroelectric phase transformation in prototypical polycrystalline $BaTiO_3$. *Applied Physics Letters* **105**(16), 161903 (2014).

[53] Franzbach, D. J., Gu, Y. J., Chen, L. Q. & Webber, K. G. Electric field-induced tetragonal to orthorhombic phase transitions in $[110]_c$-oriented $BaTiO_3$ single crystals. *Applied Physics Letters* **101**(23), 232904 (2012).

[54] Meyerhofer, D. Transition to the Ferroelectric State in Barium Titanate. *Physical Review* **112**(2), 413–423 (1958).

[55] Wul, B. Dielectric Constants of Some Titanates. *Nature* **156**(3964), 480 (1945).

[56] Megaw, H. D. Crystal Structure of Bariumtitanate. *Nature* **155**(3938), 484–485 (1945).

[57] Megaw, H. D. Crystal structure of double oxides of the perovskite type. *Proceedings of the Physical Society* **58**(326), 133–152 (1946).

[58] Megaw, H. D. Temperature Changes in the Crystal Structure of Barium Titanium Oxide. *Proceedings of the Royal Society of London. Series A, Mathematical and Physical Sciences* **189**(1017), 261–283 (1947).

[59] Kay, H. F. & Vousden, P. XCV. Symmetry changes in barium titanate at low temperatures and their relation to its ferroelectric properties. *The London, Edinburgh, and Dublin Philosophical Magazine and Journal of Science* **40**(309), 1019–1040 (1949).

[60] Rushman, D. F. & Strivens, M. A. The permittivity of polycrystals of the perovskite type. *Transactions of the Faraday Society* **42**, A231–A238 (1946).

[61] Jonker, G. H. & van Santen, J. H. Properties of Barium Titanate in Connection with Its Crystal Structure. *Science* **109**(2843), 632–635 (1949).

[62] Merz, W. J. The Electric and Optical Behavior of $BaTiO_3$ Single-Domain Crystals. *Physical Review* **76**(8), 1221–1225 (1949).

[63] Wul, B. Barium Titanate: a New Ferro-Electric. *Nature* **157**(3998), 808 (1946).

[64] Kinoshita, K. & Yamaji, A. Grain-size effects on dielectric properties in barium titanate ceramics. *Journal of Applied Physics* **47**(1), 371–373 (1976).

[65] Uchino, K., Sadanaga, E. & Hirose, T. Dependence of the Crystal Structure on Particle Size in Barium Titanate. *Journal of the American Ceramic Society* **72**(8), 1555–1558 (1989).

[66] Frey, M. H. & Payne, D. A. Grain-size effect on structure and phase transformations for barium titanate. *Physical Review B* **54**(5), 3158–3168 (1996).

[67] Arlt, G., Hennings, D. & de With, G. Dielectric properties of fine-grained barium titanate ceramics. *Journal of Applied Physics* **58**(4), 1619–1625 (1985).

[68] Ghosh, D., Sakata, A., Carter, J., Thomas, P. A., Han, H., Nino, J. C. & Jones, J. L. Domain Wall Displacement is the Origin of Superior Permittivity and Piezoelectricity in $BaTiO_3$ at Intermediate Grain Sizes. *Advanced Functional Materials* **24**(7), 885–896 (2014).

[69] Huan, Y., Wang, X., Fang, J. & Li, L. Grain size effect on piezoelectric and ferroelectric properties of $BaTiO_3$ ceramics. *Journal of the European Ceramic Society* **34**(5), 1445–1448 (2014).

[70] van Santen, J. H. & Jonker, G. H. Effect of Temperature on the Permittivity of Barium Titanate. *Nature* **159**(4036), 333–334 (1947).

[71] Samara, G. A. Pressure and Temperature Dependences of the Dielectric Properties of the Perovskites $BaTiO_3$ and $SrTiO_3$. *Physical Review* **151**(2), 378 (1966).

[72] Fesenko, O. E. & Popov, V. S. Phase T,E-diagram of barium titanate. *Ferroelectrics* **37**(1), 729–731 (1981).

[73] Berlincourt, D. & Jaffe, H. Elastic and Piezoelectric Coefficients of Single-Crystal Barium Titanate. *Physical Review* **111**(1), 143–148 (1958).

[74] Physik Instrumente (PI) GmbH & Co. KG. Material Data: Specific Parameters of the Standard Materials, (2014).

[75] Hennings, D. Barium titanate based ceramic materials for dielectric use. *International Journal of High Technology Ceramics* **3**(2), 91–111 (1987).

[76] Landau, L. D. On the theory of phase tranistions - Part I. *Zhurnal Eksperimental'noi i Teoreticheskoi Fiziki* **7**, 19 (1937).

[77] Landau, L. D. On the theory of phase tranistions - Part I. *Physikalische Zeitschrift der Sowjetunion* **11**, 26 (1937).

[78] Landau, L. D. On the theory of phase tranistions - Part II. *Zhurnal Eksperimental'noi i Teoreticheskoi Fiziki* **7**, 627 (1937).

[79] Landau, L. D. On the theory of phase tranistions - Part II. *Physikalische Zeitschrift der Sowjetunion* **11**, 545 (1937).

[80] Landau, L. D. On the theory of phase transitions. In *Collected Papers of L. D. Landau,* ter Haar, D. (Hrsg.), 193–216. Pergamon Press and Gordon and Breach, Oxford (1965).

[81] Ginzburg, V. L. *Zhurnal Eksperimental'noi i Teoreticheskoi Fiziki* **19**(36) (1949).

[82] Ginzburg, V. L. Some remarks on ferroelectricity, soft modes and related problems. *Ferroelectrics* **76**(1), 3–22 (1987).

[83] Devonshire, A. F. Theory of barium titanate - Part I. *Philosophical Magazine Series 7* **40**(309), 1040–1063 (1949).

[84] Devonshire, A. F. Theory of barium titanate - Part II. *Philosophical Magazine Series 7* **42**(333), 1065–1079 (1951).

[85] Devonshire, A. F. Theory of ferroelectrics. *Advances in Physics* **3**(10), 85–130 (1954).

[86] Tagantsev, A. K. Landau Expansion for Ferroelectrics: Which Variable to Use? *Ferroelectrics* **375**(1), 19–27 (2008).

[87] Mueller, H. Properties of Rochelle Salt. *Physical Review* **57**(9), 829–839 (1940).

[88] Mueller, H. Properties of Rochelle Salt. III. *Physical Review* **58**(6), 565–573 (1940).

[89] Strukov, B. A. & Levanyuk, A. P. *Ferroelectric Phenomena in Crystals*. Springer-Verlag, Berlin and Heidelberg, New York, (1998).

[90] Rossetti, G. A. Thermodynamic Theory. In *Piezoelectricity: Evolution and Future of a Technology*, 493–515. Springer Berlin Heidelberg, Berlin and Heidelberg (2008).

[91] Damjanovic, D. Contributions to the Piezoelectric Effect in Ferroelectric Single Crystals and Ceramics. *Journal of the American Ceramic Society* **88**(10), 2663–2676 (2005).

[92] Budimir, M., Damjanovic, D. & Setter, N. Piezoelectric response and free-energy instability in the perovskite crystals $BaTiO_3$, $PbTiO_3$, and $Pb(Zr,Ti)O_3$. *Physical Review B* **73**(17), 174106 (2006).

[93] Zhang, Q. M., Zhao, J., Shrout, T., Kim, N., Cross, L. E., Amin, A. & Kulwicki, B. M. Characteristics of the electromechanical response and polarization of electric field biased ferroelectrics. *Journal of Applied Physics* **77**(6), 2549–2555 (1995).

[94] Rossetti, G. A., Cross, L. E. & Kushida, K. Stress induced shift of the Curie point in epitaxial $PbTiO_3$ thin films. *Applied Physics Letters* **59**(20), 2524–2526 (1991).

[95] Pertsev, N. A., Zembilgotov, A. G. & Tagantsev, A. K. Effect of Mechanical Boundary Conditions on Phase Diagrams of Epitaxial Ferroelectric Thin Films. *Physical Review Letters* **80**(9), 1988–1991 (1998).

[96] Rossetti, G. A., Udayakumar, K. R., Haun, M. J. & Cross, L. E. Thermodynamic Theory of Single-Crystal Lead Titanate with Consideration of Elastic Boundary Conditions. *Journal of the American Ceramic Society* **73**(11), 3334–3338 (1990).

[97] Goswami, A. K. Theory on the Effect of Hydrostatic Pressure on the Permittivity and Curie Point of Single Crystal Barium Titanate. *Journal of the Physical Society of Japan* **21**, 1037 (1966).

[98] Bell, A. J. & Cross, L. E. A phenomenological Gibbs function for $BaTiO_3$ giving correct e field dependence of all ferroelectric phase changes. *Ferroelectrics* **59**(1), 197–203 (1984).

[99] Bell, A. J. Phenomenologically derived electric field-temperature phase diagrams and piezoelectric coefficients for single crystal barium titanate under fields along different axes. *Journal of Applied Physics* **89**(7), 3907–3914 (2001).

[100] Haeni, J. H., Irvin, P., Chang, W., Uecker, R., Reiche, P., Li, Y. L., Choudhury, S., Tian, W., Hawley, M. E., Craigo, B., Tagantsev, A. K., Pan, X. Q., Streiffer, S. K., Chen, L. Q., Kirchoefer, S. W., Levy, J. & Schlom, D. G. Room-temperature ferroelectricity in strained $SrTiO_3$. *Nature* **430**(7001), 758–761 (2004).

[101] Zhu, D. & Ma, W. Effect of mechanical stress on phase stability and polarization states in ferroelectric barium titanate and lead titanate. *Ceramics International* **40**(5), 6647–6654 (2014).

[102] Buessem, W. R., Cross, L. E. & Goswami, A. K. Effect of Two-Dimensional Pressure on the Permittivity of Fine- and Coarse-Grained Barium Titanate. *Journal of the American Ceramic Society* **49**(1), 36–39 (1966).

[103] Buessem, W. R., Cross, L. E. & Goswami, A. K. Phenomenological Theory of High Permittivity in Fine-Grained Barium Titanate. *Journal of the American Ceramic Society* **49**(1), 33–36 (1966).

[104] Bell, A. J., Moulson, A. J. & Cross, L. E. The effect of grain size on the permittivity of $BaTiO_3$. *Ferroelectrics* **54**(1), 147–150 (1984).

[105] Ricinschi, D., Tura, V., Mitoseriu, L. & Okuyama, M. Landau theory-based analysis of grain-size dependence of ferroelectric-to-paraelectric phase transition and its thermal hysteresis in barium titanate ceramics. *Journal of Physics: Condensed Matter* **11**(6), 1601–1613 (1999).

[106] Marton, P., Rychetsky, I. & Hlinka, J. Domain walls of ferroelectric $BaTiO_3$ within the Ginzburg-Landau-Devonshire phenomenological model. *Physical Review B* **81**(14), 144125 (2010).

[107] Zhong, W. L., Wang, Y. G., Zhang, P. L. & Qu, B. D. Phenomenological study of the size effect on phase transitions in ferroelectric particles. *Physical Review B* **50**(2), 698–703 (1994).

[108] Wang, J. J., Eliseev, E. A., Ma, X. Q., Wu, P. P., Morozovska, A. N. & Chen, L.-Q. Strain effect on phase transitions of $BaTiO_3$ nanowires. *Acta Materialia* **59**(19), 7189–7198 (2011).

[109] Franzbach, D. J., Seo, Y.-H., Studer, A. J., Zhang, Y., Glaum, J., Daniels, J. E., Koruza, J., Benčan, A., Malič, B. & Webber, K. G. Electric-field-induced phase transitions in co-doped $Pb(Zr_{1-x}Ti_x)O_3$ at the morphotropic phase boundary. *Science and Technology of Advanced Materials* **15**(1), 015010 (2014).

[110] Haun, M. J., Furman, E., Jang, S. J. & Cross, L. E. Thermodynamic theory of the lead zirconate-titanate solid solution system, Part I: Phenomenology. *Ferroelectrics* **99**(1), 13–25 (1989).

[111] Amin, A., Haun, M. J., Badger, B., McKinstry, H. & Cross, L. E. A phenomenological Gibbs function for the single cell region of the $PbZrO_3$:$PbTiO_3$ solid solution system. *Ferroelectrics* **65**(1), 107–130 (1985).

[112] Seo, Y.-H., Franzbach, D. J., Koruza, J., Benčan, A., Malič, B., Kosec, M., Jones, J. L. & Webber, K. G. Nonlinear stress-strain behavior and stress-induced phase transitions in soft $Pb(Zr_{1-x}Ti_x)O_3$ at the morphotropic phase boundary. *Physical Review B* **87**(9), 094116 (2013).

[113] Li, Y. L., Cross, L. E. & Chen, L. Q. A phenomenological thermodynamic potential for $BaTiO_3$ single crystals. *Journal of Applied Physics* **98**(6), 064101–064104 (2005).

[114] Vanderbilt, D. & Cohen, M. H. Monoclinic and triclinic phases in higher-order Devonshire theory. *Physical Review B* **63**(9), 094108 (2001).

[115] Sergienko, I. A., Gufan, Y. M. & Urazhdin, S. Phenomenological theory of phase transitions in highly piezoelectric perovskites. *Physical Review B* **65**(14), 144104 (2002).

[116] Cross, L. E. Relaxor ferroelectrics. *Ferroelectrics* **76**(1), 241–267 (1987).

[117] Cross, L. E. Relaxorferroelectrics: An overview. *Ferroelectrics* **151**(1), 305–320 (1994).

[118] Ye, Z.-G. Relaxor Ferroelectric Complex Perovskites: Structure, Properties and Phase Transitions. *Key Engineering Materials* **155-156**, 81–122 (1998).

[119] Samara, G. A. Ferroelectricity revisited - Advances in materials and physics. In *Solid State Physics,* Henry, E. & Frans, S. (Hrsg.), Volume 56, 239–458. Academic Press (2001).

[120] Bokov, A. A. & Ye, Z.-G. Recent progress in relaxor ferroelectrics with perovskite structure. *Journal of Materials Science* **41**(1), 31–52 (2006).

[121] Bokov, A. A. & Ye, Z.-G. Dielectric Relaxation in Relaxor Ferroelectrics. *Journal of Advanced Dielectrics* **02**(02), 1241010 (2012).

[122] Shvartsman, V. V., Lupascu, D. C. & Green, D. J. Lead-Free Relaxor Ferroelectrics. *Journal of the American Ceramic Society* **95**(1), 1–26 (2012).

[123] Egami, T., Mamontov, E., Dmowski, W. & Vakhrushev, S. B. Temperature Dependence of the Local Structure in Pb Containing Relaxor Ferroelectrics. Volume 677 of *AIP Conference Proceedings*, 48–54, (2003).

[124] Viehland, D., Jang, S. J., Cross, L. E. & Wuttig, M. Deviation from Curie-Weiss behavior in relaxor ferroelectrics. *Physical Review B* **46**(13), 8003–8006 (1992).

[125] Burns, G. & Dacol, F. H. Glassy polarization behavior in ferroelectric compounds $Pb(Mg_{1/3}Nb_{2/3})O_3$ and $Pb(Zn_{1/3}Nb_{2/3})O_3$. *Solid State Communications* **48**(10), 853–856 (1983).

[126] Burns, G. & Dacol, F. H. Crystalline ferroelectrics with glassy polarization behavior. *Physical Review B* **28**(5), 2527–2530 (1983).

[127] Burns, G. & Dacol, F. H. Ferroelectrics with a glassy polarization phase. *Ferroelectrics* **104**(1), 25–35 (1990).

[128] Bonneau, P., Garnier, P., Calvarin, G., Husson, E., Gavarri, J. R., Hewat, A. W. & Morell, A. X-ray and Neutron-Diffraction Studies of the Diffuse Phase-Transition in $PbMg_{1/3}Nb_{2/3}O_3$Ceramics. *Journal of Solid State Chemistry* **91**(2), 350–361 (1991).

[129] Uwe, H., Lyons, K. B., Carter, H. L. & Fleury, P. A. Ferroelectric microregions and Raman scattering in $KTaO_3$. *Physical Review B* **33**(9), 6436–6440 (1986).

[130] Novak, N., Pirc, R. & Kutnjak, Z. Impact of the Electric Field on the Freezing Dynamics of $Pb(Mg_{1/3}Nb_{2/3})O_3$. *Ferroelectrics* **426**(1), 31–37 (2012).

[131] Noblanc, O., Gaucher, P. & Calvarin, G. Structural and dielectric studies of $Pb(Mg_{1/3}Nb_{2/3})O_3$-$PbTiO_3$ ferroelectric solid solutions around the morphotropic boundary. *Journal of Applied Physics* **79**(8), 4291 (1996).

[132] Algueró, M., Jiménez, B. & Pardo, L. Transition between the relaxor and ferroelectric states for $(1{-}x)Pb(Mg_{1/3}Nb_{2/3})O_3{-}xPbTiO_3$ with $x=0.2$ and 0.3 polycrystalline aggregates. *Applied Physics Letters* **87**(8), 082910 (2005).

[133] Sommer, R., Yushin, N. K. & van der Klink, J. J. Polar Metastability and an Electric-Field-Induced Phase-Transition in the Disordered Perovskite $Pb(Mg_{1/3}Nb_{2/3})O_3$. *Physical Review B* **48**(18), 13230–13237 (1993).

[134] Ye, Z.-G. & Schmid, H. Optical, Dielectric and Polarization Studies of the Electric Field-Induced Phase Transition in $Pb(Mg_{1/3}Nb_{2/3})O_3$ [PMN]. *Ferroelectrics* **145**(1), 83–106 (1993).

[135] Bidault, O., Licheron, M., Husson, E. & Morell, A. The onset of an electric field-induced ferroelectric-like phase in the perovskite $Pb(Mg_{1/3}Nb_{2/3})O_3$. *Journal of Physics: Condensed Matter* **8**(42), 8017–8026 (1996).

[136] Farhi, R., Marssi, M. E., Dellis, J. L., Picot, J. C. & Morell, A. On the nature of the glassy state in 9/65/35 PLZT ceramics. *Ferroelectrics* **176**(1), 99–106 (1996).

[137] Dellis, J. L., Marssi, M. E., Tilloloy, P., Farhi, R. & Viehland, D. A dielectric study of the X/65/35 lanthanum-modified lead zirconate-titanate series. *Ferroelectrics* **201**(1), 167–174 (1997).

[138] Bobnar, V., Kutnjak, Z., Pirc, R. & Levstik, A. Electric-field-temperature phase diagram of the relaxor ferroelectric lanthanum-modified lead zirconate titanate. *Physical Review B* **60**(9), 6420–6427 (1999).

[139] Colla, E. V., Yushin, N. K. & Viehland, D. Dielectric properties of $(\mathrm{PMN})_{(1-x)}(\mathrm{PT})_x$ single crystals for various electrical and thermal histories. *Journal of Applied Physics* **83**(6), 3298–3304 (1998).

[140] Davis, M., Damjanovic, D. & Setter, N. Electric-field-, temperature-, and stress-induced phase transitions in relaxor ferroelectric single crystals. *Physical Review B* **73**(1), 014115 (2006).

[141] Daniels, J. E., Jo, W., Rödel, J. & Jones, J. L. Electric-field-induced phase transformation at a lead-free morphotropic phase boundary: Case study in a 93%$(\mathrm{Bi}_{0.5}\mathrm{Na}_{0.5})\mathrm{TiO}_3$–7%$\mathrm{BaTiO}_3$ piezoelectric ceramic. *Applied Physics Letters* **95**(3), 032904 (2009).

[142] Ehara, Y., Novak, N., Yasui, S., Itoh, M. & Webber, K. G. Electric-field-temperature phase diagram of Mn-doped $\mathrm{Bi}_{0.5}(\mathrm{Na}_{0.9}\mathrm{K}_{0.1})_{0.5}\mathrm{TiO}_3$ ceramics. *Applied Physics Letters* **107**(26), 262903 (2015).

[143] Schaab, S. *Influence of charged defects on the polarization dynamics and phase transitions in the relaxor ferroelectric PLZT*. Édition Scientifique. VVB Laufersweiler Verlag, Giessen, 1. Auflage , (2011).

[144] Jo, W., Daniels, J. E., Jones, J. L., Tan, X., Thomas, P. A., Damjanovic, D. & Rödel, J. Evolving morphotropic phase boundary in lead-free $(\mathrm{Bi}_{0.5}\mathrm{Na}_{0.5})\mathrm{TiO}_3$–$\mathrm{BaTiO}_3$ piezoceramics. *Journal of Applied Physics* **109**(1), 014110 (2011).

[145] Prosandeev, S., Wang, D., Akbarzadeh, A. R., Dkhil, B. & Bellaiche, L. Field-induced percolation of polar nanoregions in relaxor ferroelectrics. *Physical Review Letters* **110**(20), 207601 (2013).

[146] Jo, W., Daniels, J., Damjanovic, D., Kleemann, W. & Rödel, J. Two-stage processes of electrically induced-ferroelectric to relaxor transition in $0.94(\mathrm{Bi}_{1/2}\mathrm{Na}_{1/2})\mathrm{TiO}_3$-$0.06\mathrm{BaTiO}_3$. *Applied Physics Letters* **102**(19), 192903 (2013).

[147] Woodward, D. I., Dittmer, R., Jo, W., Walker, D., Keeble, D. S., Dale, M. W., Rödel, J. & Thomas, P. A. Investigation of the depolarisation transition in Bi-based relaxor ferroelectrics. *Journal of Applied Physics* **115**(11), 114109 (2014).

[148] Zhang, S.-T., Kounga, A. B., Aulbach, E., Ehrenberg, H. & Rödel, J. Giant strain in lead-free piezoceramics $\mathrm{Bi}_{0.5}\mathrm{Na}_{0.5}\mathrm{TiO}_3$–$\mathrm{BaTiO}_3$–$\mathrm{K}_{0.5}\mathrm{Na}_{0.5}\mathrm{NbO}_3$ system. *Applied Physics Letters* **91**(11), 112906 (2007).

[149] Zhang, S.-T., Kounga, A. B., Aulbach, E., Granzow, T., Jo, W., Kleebe, H.-J. & Rödel, J. Lead-free piezoceramics with giant strain in the system $\mathrm{Bi}_{0.5}\mathrm{Na}_{0.5}\mathrm{TiO}_3$–$\mathrm{BaTiO}_3$–$\mathrm{K}_{0.5}\mathrm{Na}_{0.5}\mathrm{NbO}_3$. I. Structure and room temperature properties. *Journal of Applied Physics* **103**(3), 034107 (2008).

[150] Zhang, S.-T., Kounga, A. B., Aulbach, E., Jo, W., Granzow, T., Ehrenberg, H. & Rödel, J. Lead-free piezoceramics with giant strain in the system $\mathrm{Bi}_{0.5}\mathrm{Na}_{0.5}\mathrm{TiO}_3$–$\mathrm{BaTiO}_3$–$\mathrm{K}_{0.5}\mathrm{Na}_{0.5}\mathrm{NbO}_3$. II. Temperature dependent properties. *Journal of Applied Physics* **103**(3), 034108 (2008).

[151] Jo, W., Dittmer, R., Acosta, M., Zang, J., Groh, C., Sapper, E., Wang, K. & Rödel, J. Giant electric-field-induced strains in lead-free ceramics for actuator applications - status and perspective. *Journal of Electroceramics* **29**(1), 71–93 (2012).

[152] Imry, Y. & Ma, S.-k. Random-Field Instability of the Ordered State of Continuous Symmetry. *Physical Review Letters* **35**(21), 1399–1401 (1975).

[153] Westphal, V. V., Kleemann, W. & Glinchuk, M. D. Diffuse phase transitions and random-field-induced domain states of the "relaxor" ferroelectric $PbMg_{1/3}Nb_{2/3}O_3$. *Physical Review Letters* **68**(6), 847–850 (1992).

[154] Kleemann, W. Random Fields in Relaxor Ferroelectrics - A Jubilee Review. *Journal of Advanced Dielectrics* **02**(02), 1241001 (2012).

[155] Viehland, D., Jang, S. J., Cross, L. E. & Wuttig, M. Freezing of the polarization fluctuations in lead magnesium niobate relaxors. *Journal of Applied Physics* **68**(6), 2916 (1990).

[156] Viehland, D., Wuttig, M. & Cross, L. E. The glassy behavior of relaxor ferroelectrics. *Ferroelectrics* **120**(1), 71–77 (1991).

[157] Glazounov, A. E., Tagantsev, A. K. & Bell, A. J. Evidence for domain-type dynamics in the ergodic phase of the $PbMg_{1/3}Nb_{2/3}O_3$ relaxor ferroelectric. *Physical Review B* **53**(17), 11281–11284 (1996).

[158] Tagantsev, A. K. & Glazounov, A. E. Mechanism of polarization response in the ergodic phase of a relaxor ferroelectric. *Physical Review B* **57**(1), 18–21 (1998).

[159] Glazounov, A. E. & Tagantsev, A. K. A "breathing" model for the polarization response of relaxor ferroelectrics. *Ferroelectrics* **221**(1), 57–66 (1999).

[160] Vugmeister, B. E. & Rabitz, H. A phenomenology of relaxor ferroelectrics. *Ferroelectrics* **201**(1-4), 33–42 (1997).

[161] Dec, J., Miga, S., Kleemann, W. & Dkhil, B. Nonlinear Dielectric Properties of PMN Relaxor Crystals within Landau-Ginzburg-Devonshire Approximation. *Ferroelectrics* **363**(1), 141–149 (2008).

[162] Hlinka, J. Do We Need the Ether of Polar Nanoregions? *Journal of Advanced Dielectrics* **02**(02), 1241006 (2012).

[163] Haertling, G. H. Ferroelectric Ceramics: History and Technology. *Journal of the American Ceramic Society* **82**(4), 797–818 (1999).

[164] Shirane, G., Hoshino, S. & Suzuki, K. X-Ray Study of the Phase Transition in Lead Titanate. *Physical Review* **80**(6), 1105–1106 (1950).

[165] Jaffe, H. & Berlincourt, D. A. Piezoelectric transducer materials. *Proceedings of the IEEE* **53**(10), 1372–1386 (1965).

[166] Woodward, D. I., Knudsen, J. & Reaney, I. M. Review of crystal and domain structures in the $PbZr_xTi_{1-x}O_3$ solid solution. *Physical Review B* **72**(10), 104110 (2005).

[167] Michel, C., Moreau, J.-M., Achenbach, G. D., Gerson, R. & James, W. J. Atomic structures of two rhombohedral ferroelectric phases in the $Pb(Zr, Ti)O_3$ solid solution series. *Solid State Communications* **7**(12), 865–868 (1969).

[168] Corker, D. L., Glazer, A. M., Whatmore, R. W., Stallard, A. & Fauth, F. A neutron diffraction investigation into the rhombohedral phases of the perovskite series $PbZr_{1-x}Ti_xO_3$. *Journal of Physics: Condensed Matter* **10**(28), 6251 (1998).

[169] Berlincourt, D. A., Cmolik, C. & Jaffe, H. Piezoelectric Properties of Polycrystalline Lead Titanate Zirconate Compositions. *Proceedings of the Institute of Radio Engineers* **48**(2), 220–229 (1960).

[170] Kamiya, T., Mishima, R., Tsurumi, T., Daimon, M. & Nishimura, T. Mechanism of Temperature Dependence of Piezoelectric Properties for $Pb(Zr,Ti)O_3$. *Japanese Journal of Applied Physics* **32**(9S), 4223 (1993).

[171] Hooker, M. W. Properties of PZT-Based Piezoelectric Ceramics Between -150 and 250 °C. Technical Report NASA/CR-1998-208708, NASA, (1998).

[172] Sabat, R. G., Mukherjee, B. K., Ren, W. & Yang, G. Temperature dependence of the complete material coefficients matrix of soft and hard doped piezoelectric lead zirconate titanate ceramics. *Journal of Applied Physics* **101**(6), 064111 (2007).

[173] Randall, C. A., Kim, N., Kucera, J.-P., Cao, W. & Shrout, T. R. Intrinsic and Extrinsic Size Effects in Fine-Grained Morphotropic-Phase-Boundary Lead Zirconate Titanate Ceramics. *Journal of the American Ceramic Society* **81**(3), 677–688 (1998).

[174] Kamel, T. M. & de With, G. Grain size effect on the poling of soft $Pb(Zr,Ti)O_3$ ferroelectric ceramics. *Journal of the European Ceramic Society* **28**(4), 851–861 (2008).

[175] Noheda, B., Cox, D. E., Shirane, G., Guo, R., Jones, B. & Cross, L. E. Stability of the monoclinic phase in the ferroelectric perovskite $PbZr_{1-x}Ti_xO_3$. *Physical Review B* **63**(1), 014103 (2000).

[176] Cao, W. & Cross, L. E. Theoretical model for the morphotropic phase boundary in lead zirconate–lead titanate solid solution. *Physical Review B* **47**, 4825–4830 (1993).

[177] Guo, R., Cross, L. E., Park, S. E., Noheda, B., Cox, D. E. & Shirane, G. Origin of the High Piezoelectric Response in $PbZr_{1-x}Ti_xO_3$. *Physical Review Letters* **84**(23), 5423–5426 (2000).

[178] Damjanovic, D. Comments on Origins of Enhanced Piezoelectric Properties in Ferroelectrics. *IEEE Transactions on Ultrasonics, Ferroelectrics, and Frequency Control* **56**(8), 1574–1585 (2009).

[179] Damjanovic, D. A morphotropic phase boundary system based on polarization rotation and polarization extension. *Applied Physics Letters* **97**(6), 062906 (2010).

[180] Carl, K. & Härdtl, K. H. On the origin of the maximum in the electromechanical activity in $Pb(Zr_xTi_{1-x})O_3$ ceramies near the morphotropic phase boundary. *physica status solidi (a)* **8**(1), 87–98 (1971).

[181] Schönau, K. A., Schmitt, L. A., Knapp, M., Fuess, H., Eichel, R.-A., Kungl, H. & Hoffmann, M. J. Nanodomain structure of $Pb[Zr_{1-x}Ti_x]O_3$ at its morphotropic phase boundary: Investigations from local to average structure. *Physical Review B* **75**(18), 184117 (2007).

[182] Theissmann, R., Schmitt, L. A., Kling, J., Schierholz, R., Schoönau, K. A., Fuess, H., Knapp, M., Kungl, H. & Hoffmann, M. J. Nanodomains in morphotropic lead zirconate titanate ceramics: On the origin of the strong piezoelectric effect. *Journal of Applied Physics* **102**(2), 024111 (2007).

[183] Berlincourt, D. Piezoelectric ceramic compositional development. *The Journal of the Acoustical Society of America* **91**(5), 3034–3040 (1992).

[184] Jackson, W. High Permittivity Crystalline Aggregates. *Nature* **156**, 717 (1945).

[185] Coursey, P. R. & Brand, K. G. Dielectric Constants of Some Titanates. *Nature* **157**(3984), 297–298 (1946).

[186] Shirane, G. & Suzuki, K. On the Phase Transition in Barium-Lead Titanate (1). *Journal of the Physical Society of Japan* **6**(4), 274–278 (1951).

[187] Goldschmidt, V. M. Die Gesetze der Krystallochemie. *Naturwissenschaften* **14**(21), 477–485 (1926).

[188] Trolier-McKinstry, S. *Piezoelectric and Acoustic Materials for Transducer Applications*, chapter Crystal Chemistry of Piezoelectric Materials, 39–56. Springer US, Boston, MA (2008).

[189] Lambeck, P. V. & Jonker, G. H. The nature of domain stabilization in ferroelectric perovskites. *Journal of Physics and Chemistry of Solids* **47**(5), 453–461 (1986).

[190] Lambeck, P. V. & Jonker, G. H. Ferroelectric Domain Stabilization in $BaTiO_3$ by Bulk Ordering of Defects. *Ferroelectrics* **22**(1-2), 729–731 (1978).

[191] Eichel, R. A., Erhart, P., Traskelin, P., Albe, K., Kungl, H. & Hoffmann, M. J. Defect-dipole formation in copper-doped $PbTiO_3$ ferroelectrics. *Physical Review Letters* **100**(9), 095504 (2008).

[192] Carl, K. & Härdtl, K. H. Electrical after-effects in $Pb(Ti, Zr)O_3$ ceramics. *Ferroelectrics* **17**(1), 473–486 (1978).

[193] Takahashi, S. Effects of impurity doping in lead zirconate-titanate ceramics. *Ferroelectrics* **41**(1), 143–156 (1982).

[194] Chandrasekaran, A., Damjanovic, D., Setter, N. & Marzari, N. Defect ordering and defect-domain-wall interactions in $PbTiO_3$: A first-principles study. *Physical Review B* **88**(21), 214116 (2013).

[195] Morozov, M. I. & Damjanovic, D. Hardening-softening transition in Fe-doped $Pb(Zr,Ti)O_3$ ceramics and evolution of the third harmonic of the polarization response. *Journal of Applied Physics* **104**(3), 034107 (2008).

[196] Warren, W. L., Vanheusden, K., Dimos, D., Pike, G. E. & Tuttle, B. A. Oxygen vacancy motion in perovskite oxides. *Journal of the American Ceramic Society* **79**(2), 536–538 (1996).

[197] Zhang, L., Erdem, E., Ren, X. B. & Eichel, R.-A. Reorientation of $(\mathrm{Mn}_{Ti}''\text{–}V_O^{\bullet\bullet})^\times$ defect dipoles in acceptor-modified $BaTiO_3$ single crystals: An electron paramagnetic resonance study. *Applied Physics Letters* **93**(20), 202901 (2008).

[198] Arlt, G. & Neumann, H. Internal bias in ferroelectric ceramics: Origin and time dependence. *Ferroelectrics* **87**(1), 109–120 (1988).

[199] Erhart, P., Träskelin, P. & Albe, K. Formation and switching of defect dipoles in acceptor-doped lead titanate: A kinetic model based on first-principles calculations. *Physical Review B* **88**(2), 024107 (2013).

[200] Kimmel, A. V., Weaver, P. M., Cain, M. G. & Sushko, P. V. Defect-mediated lattice relaxation and domain stability in ferroelectric oxides. *Physical Review Letters* **109**(11), 117601 (2012).

[201] Jin, L., He, Z. B. & Damjanovic, D. Nanodomains in Fe^{+3}-doped lead zirconate titanate ceramics at the morphotropic phase boundary do not correlate with high properties. *Applied Physics Letters* **95**(1), 012905 (2009).

[202] Robels, U. & Arlt, G. Domain wall clamping in ferroelectrics by orientation of defects. *Journal of Applied Physics* **73**(7), 3454 (1993).

[203] Shannon, R. D. Revised effective ionic radii and systematic studies of interatomic distances in halides and chalcogenides. *Acta Crystallographica, Section A (Crystal Physics, Diffraction, Theoretical and General Crystallography)* **A32**, 751–767 (1976).

[204] Choi, W.-Y., Ahn, J.-H., Lee, W.-J. & Kim, H.-G. Electrical properties of Sb-doped PZT films deposited by dc reactive sputtering using multi-targets. *Materials Letters* **37**(3), 119–127 (1998).

[205] Uchino, K. *Ferroelectric devices*, Volume 16 of *Materials Engineering*. Dekker, New York, (2000).

[206] Benes, E., Gröschl, M., Burger, W. & Schmid, M. Sensors based on piezoelectric resonators. *Sensors and Actuators A: Physical* **48**(1), 1–21 (1995).

[207] Lin, C.-J. & Yang, S.-R. Precise positioning of piezo-actuated stages using hysteresis-observer based control. *Mechatronics* **16**(7), 417–426 (2006).

[208] Randall, C. A., Kelnberger, A., Yang, G. Y., Eitel, R. E. & Shrout, T. R. High strain piezoelectric multilayer actuators - A material science and engineering challenge. *Journal of Electroceramics* **14**(3), 177–191 (2005).

[209] Benajes, J., Molina, S., Novella, R., Amorim, R., Ben Hadj Hamouda, H. & Hardy, J. P. Comparison of two injection systems in an HSDI diesel engine using split injection and different injector nozzles. *International Journal of Automotive Technology* **11**(2), 139–146 (2010).

[210] Chung, S. Y., Kim, S., Lee, J. H., Kim, K., Kim, S. W., Kang, C. Y., Yoon, S. J. & Kim, Y. S. All-solution-processed flexible thin film piezoelectric nanogenerator. *Advanced Materials* **24**(45), 6022–6027 (2012).

[211] Park, K. I., Lee, M., Liu, Y., Moon, S., Hwang, G. T., Zhu, G., Kim, J. E., Kim, S. O., Kim, D. K., Wang, Z. L. & Lee, K. J. Flexible nanocomposite generator made of $BaTiO_3$ nanoparticles and graphitic carbons. *Advanced Materials* **24**(22), 2999–3004 (2012).

[212] Amin Karami, M. & Inman, D. J. Powering pacemakers from heartbeat vibrations using linear and nonlinear energy harvesters. *Applied Physics Letters* **100**(4), 042901 (2012).

[213] Watson, B., Friend, J. & Yeo, L. Piezoelectric ultrasonic micro/milli-scale actuators. *Sensors and Actuators A: Physical* **152**(2), 219–233 (2009).

[214] Muralt, P. Ferroelectric thin films for micro-sensors and actuators: a review. *Journal of Micromechanics and Microengineering* **10**(2), 136–146 (2000).

[215] Zhang, S. & Shrout, T. R. Relaxor-PT Single Crystals: Observations and Developments. *IEEE Transactions on Ultrasonics, Ferroelectrics, and Frequency Control* **57**(10), 2138–2146 (2010).

[216] Zhang, S. & Li, F. High performance ferroelectric relaxor-$PbTiO_3$ single crystals: Status and perspective. *Journal of Applied Physics* **111**(3), 031301 (2012).

[217] Sun, E. & Cao, W. Relaxor-based ferroelectric single crystals: growth, domain engineering, characterization and applications. *Progress in Materials Science* **65**, 124–210 (2014).

[218] Park, S.-E. & Shrout, T. R. Ultrahigh strain and piezoelectric behavior in relaxor based ferroelectric single crystals. *Journal of Applied Physics* **82**(4), 1804 (1997).

[219] Shrout, T. R., Chang, Z. P., Kim, N. & Markgraf, S. Dielectric behavior of single crystals near the (1−x) $Pb(Mg_{1/3}Nb_{2/3})O_3$-(x) $PbTiO_3$ morphotropic phase boundary. *Ferroelectrics Letters Section* **12**(3), 63–69 (1990).

[220] Luo, J., Hackenberger, W., Zhang, S. & Shrout, T. R. The Progress Update of Relaxor Piezoelectric Single Crystals. In *2009 IEEE International Ultrasonics Symposium Proceedings*, 968–971, (2009).

[221] Kuwata, J., Uchino, K. & Nomura, S. Phase transitions in the $Pb(Zn_{1/3}Nb_{2/3})O_3$-$PbTiO_3$ system. *Ferroelectrics* **37**(1), 579–582 (1981).

[222] Zhang, S., Lee, S.-M., Kim, D.-H., Lee, H.-Y. & Shrout, T. R. Electromechanical Properties of PMN-PZT Piezoelectric Single Crystals Near Morphotropic Phase Boundary Compositions. *Journal of the American Ceramic Society* **90**(12), 3895–3862 (2007).

[223] Li, F., Zhang, S., Xu, Z., Wei, X., Luo, J. & Shrout, T. R. Electromechanical properties of tetragonal $Pb(In_{1/2}Nb_{1/2})O_3$–$Pb(Mg_{1/3}Nb_{2/3})O_3$–$PbTiO_3$ ferroelectric crystals. *Journal of Applied Physics* **107**(5), 54107 (2010).

[224] Chen, Y., Lam, K. H., Zhou, D., Cheng, W. F., Dai, J. Y., Luo, H. S. & Chan, H. L. W. High-frequency PIN-PMN-PT single crystal ultrasonic transducer for imaging applications. *Applied Physics A* **108**(4), 987–991 (2012).

[225] Luo, J., Taylor, S., Hackenberger, W. & Shujun, Z. Large field property assessment of Mn: PIN-PMN-PT crystals for high power transducers. In *2013 IEEE International Symposium on the Applications of Ferroelectric and Workshop on the Piezoresponse Force Microscopy (ISAF/PFM)*, 1–4, (2013).

[226] Tang, H., Peng, J., Wang, W., Peng, X., Wang, T. & Chen, S. High-Curie-temperature relaxor piezoelectric single crystals for 1.5D ultrasound phased-array applications. *Materials Letters* **145**, 258–260 (2015).

[227] Fu, H. & Cohen, R. E. Polarization rotation mechanism for ultrahigh electromechanical response in single-crystal piezoelectrics. *Nature* **403**(6767), 281–283 (2000).

[228] Liu, T. & Lynch, C. S. Ferroelectric properties of [110], [001] and [111] poled relaxor single crystals: measurements and modeling. *Acta Materialia* **51**(2), 407–416 (2003).

[229] Liu, T. & Lynch, C. S. Domain Engineered Relaxor Ferroelectric Single Crystals. *Continuum Mechanics and Thermodynamics* **18**(1-2), 119–135 (2006).

[230] Li, F., Zhang, S., Xu, Z., Wei, X., Luo, J. & Shrout, T. R. Composition and phase dependence of the intrinsic and extrinsic piezoelectric activity of domain engineered $(1-x)Pb(Mg_{1/3}Nb_{2/3})O_3$–$xPbTiO_3$ crystals. *Journal of Applied Physics* **108**(3), 034106 (2010).

[231] Wang, Y., Wang, Z., Ge, W., Luo, C., Li, J., Viehland, D., Chen, J. & Luo, H. Temperature-induced and electric-field-induced phase transitions in rhombohedral $Pb(In_{1/2}Nb_{1/2})O_3$−$Pb(Mg_{1/3}Nb_{2/3})O_3$−$PbTiO_3$ ternary single crystals. *Physical Review B* **90**(13), 134107 (2014).

[232] Zhou, D., Wang, F., Luo, L., Chen, J., Ge, W., Zhao, X. & Luo, H. Characterization of complete electromechanical constants of rhombohedral $0.72\text{Pb}(\text{Mg}_{1/3}\text{Nb}_{2/3})$–$0.28\text{PbTiO}_3$ single crystals. *Journal of Physics D: Applied Physics* **41**(18), 185402 (2008).

[233] Tian, J., Han, P., Huang, X., Pan, H., Carroll, J. F. & Payne, D. A. Improved stability for piezoelectric crystals grown in the lead indium niobate-lead magnesium niobate-lead titanate system. *Applied Physics Letters* **91**(22), 222903 (2007).

[234] Xu, G., Chen, K., Yang, D. & Li, J. Growth and electrical properties of large size $\text{Pb}(\text{In}_{1/2}\text{Nb}_{1/2})\text{O}_3$–$\text{Pb}(\text{Mg}_{1/3}\text{Nb}_{2/3})\text{O}_3$–$\text{PbTiO}_3$ crystals prepared by the vertical Bridgman technique. *Applied Physics Letters* **90**(3), 032901 (2007).

[235] Zhang, S., Luo, J., Hackenberger, W., Sherlock, N. P., Meyer, R. J., Jr. & Shrout, T. R. Electromechanical characterization of $\text{Pb}(\text{In}_{0.5}\text{Nb}_{0.5})\text{O}_3$–$\text{Pb}(\text{Mg}_{1/3}\text{Nb}_{2/3})\text{O}_3$–$\text{PbTiO}_3$ crystals as a function of crystallographic orientation and temperature. *Journal of Applied Physics* **105**(10), 104506 (2009).

[236] Li, F., Zhang, S., Lin, D., Luo, J., Xu, Z., Wei, X. & Shrout, T. R. Electromechanical properties of $\text{Pb}(\text{In}_{1/2}\text{Nb}_{1/2})\text{O}_3$–$\text{Pb}(\text{Mg}_{1/3}\text{Nb}_{2/3})\text{O}_3$–$\text{PbTiO}_3$ single crystals. *Journal of Applied Physics* **109**(1), 14108 (2011).

[237] Sun, E., Zhang, R., Wu, F. & Cao, W. Complete matrix properties of [001]c and [011]c poled $0.33\text{Pb}(\text{In}_{1/2}\text{Nb}_{1/2})\text{O}_3$–$0.38\text{Pb}(\text{Mg}_{1/3}\text{Nb}_{2/3})\text{O}_3$–$0.29\text{PbTiO}_3$ single crystals. *Journal of Alloys and Compounds* **553**, 267–269 (2013).

[238] Zhang, Y., Li, X., Liu, D., Zhang, Q., Wang, W., Ren, B., Di Lin, Zhao, X. & Luo, H. The compositional segregation, phase structure and properties of $\text{Pb}(\text{In}_{1/2}\text{Nb}_{1/2})\text{O}_3$–$\text{Pb}(\text{Mg}_{1/3}\text{Nb}_{2/3})\text{O}_3$–$\text{PbTiO}_3$ single crystal. *Journal of Crystal Growth* **318**(1), 890–894 (2011).

[239] Zhang, S., Li, F., Sherlock, N. P., Luo, J., Lee, H. J., Xia, R., Meyer, R. J., Jr., Hackenberger, W. & Shrout, T. R. Recent Developments on High Curie Temperature PIN-PMN-PT Ferroelectric Crystals. *Journal of Crystal Growth* **318**(1), 846–850 (2011).

[240] Huo, X., Zhang, S., Liu, G., Zhang, R., Luo, J., Sahul, R., Cao, W. & Shrout, T. R. Elastic, dielectric and piezoelectric characterization of single domain PIN-PMN-PT: Mn crystals. *Journal of Applied Physics* **112**(12), 124113 (2012).

[241] Huo, X., Zhang, S., Liu, G., Zhang, R., Luo, J., Sahul, R., Cao, W. & Shrout, T. R. Complete set of elastic, dielectric, and piezoelectric constants of $[011]_C$ poled rhombohedral $\text{Pb}(\text{In}_{0.5}\text{Nb}_{0.5})\text{O}_3$–$\text{Pb}(\text{Mg}_{1/3}\text{Nb}_{2/3})\text{O}$–$\text{PbTiO}_3$: Mn single crystals. *Journal of Applied Physics* **113**(7), 74106 (2013).

[242] Wang, Y., Sun, E., Song, W., Li, W., Zhang, R. & Cao, W. Improved thermal stability of [001]c poled $0.24\text{Pb}(\text{In}_{1/2}\text{Nb}_{1/2})\text{O}_3$–$0.47\text{Pb}(\text{Mg}_{1/3}\text{Nb}_{2/3})\text{O}_3$–$0.29\text{PbTiO}_3$ single crystal with manganese doping. *Journal of Alloys and Compounds* **601**, 154–157 (2014).

[243] Amin, A. & Cross, L. E. Elasticity of high coupling relaxor-ferroelectric lead zinc niobate-lead titanate crystals. *Journal of Applied Physics* **98**(9), 094113 (2005).

[244] Amin, A., McLaughlin, E., Robinson, H. & Ewart, L. Mechanical and thermal transitions in morphotropic PZN-PT and PMN-PT single crystals and their implication for sound projectors. *IEEE Transactions on Ultrasonics, Ferroelectrics, and Frequency Control* **54**(6), 1090–1095 (2007).

[245] Li, X., Ma, T., Tian, J., Han, P., Zhou, Q. & Shung, K. K. Micromachined PIN-PMN-PT crystal composite transducer for high-frequency intravascular ultrasound (IVUS) imaging. *IEEE Transactions on Ultrasonics, Ferroelectrics, and Frequency Control* **61**(7), 1171–1178 (2014).

[246] Zhou, Q., Lam, K. H., Zheng, H., Qiu, W. & Shung, K. K. Piezoelectric single crystals for ultrasonic transducers in biomedical applications. *Progress in Materials Science* **66**, 87–111 (2014).

[247] Chen, Z., Li, X., Liu, G. & Dong, S. A two degrees-of-freedom piezoelectric single-crystal micromotor. *Journal of Applied Physics* **116**(22), 224101 (2014).

[248] Dong, W. D., Gallagher, J. A. & Lynch, C. S. Ideal energy harvesting cycle using a phase transformation in ferroelectric crystals. *Smart Materials and Structures* **23**(12), 125026 (2014).

[249] Sadiq, M. R., Kuang, Y., Cochran, S. & Huang, Z. High-performance planar ultrasonic tool based on d_{31}-mode piezocrystal. *IEEE Transactions on Ultrasonics, Ferroelectrics, and Frequency Control* **62**(3), 428–438 (2015).

[250] Kosec, M. Effect of a chemically aggressive environment on the electromechanical behaviour of modified lead titanate ceramics. *Journal of the Korean Physical Society* **32**, S1163 (1998).

[251] Minister of Economy, Trade and Industry, Japan. Law for Promotion of Effective Utilization of Resources, JIS C 0950, (2001).

[252] Department of Toxic Substances Control, California, USA. Electronic Waste Recycling Act of 2003, SB 20/SB 50, (2003).

[253] Environment and Labor Committee of the National Assembly of Korea. Act for Resource Recycling of Electrical and Electronic Equipment and Vehicles, Bill Nr. 6319, (2007).

[254] Ministry of Information Industry, China. Measures for the Administration on Pollution Control of Electronic Information Products, Order of the Ministry of Information Industry No 39, (2007).

[255] Directive 2011/65/EU of the European Parliament and of the Council of 8 June 2011 on the restriction of the use of certain hazardous substances in electrical and electronic equipment. *Official Journal of the European Union* **54**(L 174), 88–110 (2011).

[256] Directive 2012/19/EU of the European Parliament and of the Council of 4 July 2012 on waste electrical and electronic equipment (WEEE). *Official Journal of the European Union* **55**(L197), 34 (2012).

[257] Directive 2000/53/EC of the European Parliament and of the Council of 18 September 2000 on the end-of life vehicles. *Official Journal of the European Union* **43**(L 269), 34–42 (2000).

[258] Commission Directive 2013/28/EU of 17 May 2013 amending Annex II to Directive 2000/53/EC of the European Parliament and of the Council on end-of-life vehicles. *Official Journal of the European Union* **56**(L 135), 14 (2000).

[259] Shrout, T. R. & Zhang, S. J. Lead-free piezoelectric ceramics: Alternatives for PZT? *Journal of Electroceramics* **19**(1), 113–126 (2007).

[260] Takenaka, T., Nagata, H. & Hiruma, Y. Current Developments and Prospective of Lead-Free Piezoelectric Ceramics. *Japanese Journal of Applied Physics* **47**(5S), 3787 (2008).

[261] Panda, P. K. Review: environmental friendly lead-free piezoelectric materials. *Journal of Materials Science* **44**(19), 5049–5062 (2009).

[262] Rödel, J., Jo, W., Seifert, K. T. P., Anton, E.-M., Granzow, T. & Damjanovic, D. Perspective on the Development of Lead-free Piezoceramics. *Journal of the American Ceramic Society* **92**(6), 1153–1177 (2009).

[263] Leontsev, S. O. & Eitel, R. E. Progress in engineering high strain lead-free piezoelectric ceramics. *Science and Technology of Advanced Materials* **11**(4), 044302 (2010).

[264] Coondoo, I., Panwar, N. & Kholkin, A. Lead-free piezoelectrics: Current status and perspectives. *Journal of Advanced Dielectrics* **03**(02), 1330002 (2013).

[265] Rödel, J., Webber, K. G., Dittmer, R., Jo, W., Kimura, M. & Damjanovic, D. Transferring lead-free piezoelectric ceramics into application. *Journal of the European Ceramic Society* **35**(6), 1659–1681 (2015).

[266] Taghaddos, E., Hejazi, M. & Safari, A. Lead-free piezoelectric materials and ultrasonic transducers for medical imaging. *Journal of Advanced Dielectrics* **05**(02), 1530002 (2015).

[267] Hong, C.-H., Kim, H.-P., Choi, B.-Y., Han, H.-S., Son, J. S., Ahn, C. W. & Jo, W. Lead-free piezoceramics - Where to move on? *Journal of Materiomics* **2**(1), 1–24 (2016).

[268] Saito, Y., Takao, H., Tani, T., Nonoyama, T., Takatori, K., Homma, T., Nagaya, T. & Nakamura, M. Lead-free piezoceramics. *Nature* **432**(7013), 84–87 (2004).

[269] Jalalian, A. & Grishin, A. M. Biocompatible ferroelectric (Na,K)NbO_3 nanofibers. *Applied Physics Letters* **100**(1), 012904 (2012).

[270] Li, J.-F., Wang, K., Zhu, F.-Y., Cheng, L.-Q., Yao, F.-Z. & Green, D. J. (K,Na)NbO_3-Based Lead-Free Piezoceramics: Fundamental Aspects, Processing Technologies, and Remaining Challenges. *Journal of the American Ceramic Society* **96**(12), 3677–3696 (2013).

[271] Wang, X., Wu, J., Xiao, D., Zhu, J., Cheng, X., Zheng, T., Zhang, B. & Lou, X. Giant piezoelectricity in potassium-sodium niobate lead-free ceramics. *Journal of the American Ceramic Society* **136**(7), 2905–2910 (2014).

[272] Liu, W. & Ren, X. Large Piezoelectric Effect in Pb-Free Ceramics. *Physical Review Letters* **103**(25), 257602 (2009).

[273] Keeble, D. S., Benabdallah, F., Thomas, P. A., Maglione, M. & Kreisel, J. Revised structural phase diagram of $(Ba_{0.7}Ca_{0.3}TiO_3)$–$(BaZr_{0.2}Ti_{0.8}O_3)$. *Applied Physics Letters* **102**(9), 092903 (2013).

[274] Acosta, M., Novak, N., Jo, W. & Rödel, J. Relationship between electromechanical properties and phase diagram in the $Ba(Zr_{0.2}Ti_{0.8})O_3$–$x(Ba_{0.7}Ca_{0.3})TiO_3$ lead-free piezoceramic. *Acta Materialia* **80**, 48–55 (2014).

[275] Vögler, M., Acosta, M., Brandt, D. R. J., Molina-Luna, L. & Webber, K. G. Temperature-dependent R-curve behavior of the lead-free ferroelectric $0.615Ba(Zr_{0.2}Ti_{0.8})O_3$–$0.385(Ba_{0.7}Ca_{0.3})TiO_3$ ceramic. *Engineering Fracture Mechanics* **144**, 68–77 (2015).

[276] Sasaki, A., Chiba, T., Mamiya, Y. & Otsuki, E. Dielectric and Piezoelectric Properties of $(Bi_{0.5}Na_{0.5})TiO_3$–$(Bi_{0.5}K_{0.5})TiO_3$ Systems. *Japanese Journal of Applied Physics* **38**(9S), 5564 (1999).

[277] Otoničar, M., Škapin, S. D., Spreitzer, M. & Suvorov, D. Compositional range and electrical properties of the morphotropic phase boundary in the $Na_{0.5}Bi_{0.5}TiO_3$–$K_{0.5}Bi_{0.5}TiO_3$ system. *Journal of the European Ceramic Society* **30**(4), 971–979 (2010).

[278] Dittmer, R., Jo, W., Damjanovic, D. & Rödel, J. Lead-free high-temperature dielectrics with wide operational range. *Journal of Applied Physics* **109**(3), 034107 (2011).

[279] Wang, K., Yao, F.-Z., Jo, W., Gobeljic, D., Shvartsman, V. V., Lupascu, D. C., Li, J.-F. & Rödel, J. Temperature-Insensitive (K,Na)NbO_3-Based Lead-Free Piezoactuator Ceramics. *Advanced Functional Materials* **23**(33), 4079–4086 (2013).

[280] Yao, F.-Z., Wang, K., Jo, W., Webber, K. G., Comyn, T. P., Ding, J.-X., Xu, B., Cheng, L.-Q., Zheng, M.-P., Hou, Y.-D. & Li, J.-F. Diffused Phase Transition Boosts Thermal Stability of High-Performance Lead-Free Piezoelectrics. *Advanced Functional Materials* **26**(8), 1217–1224 (2016).

[281] Takenaka, T., Maruyama, K.-i. & Sakata, K. $(Bi_{1/2}Na_{1/2})TiO_3$–$BaTiO_3$ System for Lead-Free Piezoelectric Ceramics. *Japanese Journal of Applied Physics* **30**(9B), 2236–2239 (1991).

[282] Simons, H., Daniels, J., Jo, W., Dittmer, R., Studer, A., Avdeev, M., Rödel, J. & Hoffman, M. Electric-field-induced strain mechanisms in lead-free 94%$(Bi_{1/2}Na_{1/2})TiO_3$–6%$BaTiO_3$. *Applied Physics Letters* **98**(8), 082901 (2011).

[283] McQuade, R. R. & Dolgos, M. R. A review of the structure-property relationships in lead-free piezoelectric $(1-x)Na_{0.5}Bi_{0.5}TiO_3$–$(x)BaTiO_3$. *Journal of Solid State Chemistry* , Article in Press (2016).

[284] Lee, H. J., Ural, S. O., Chen, L., Uchino, K., Zhang, S. & Jones, J. L. High Power Characteristics of Lead-Free Piezoelectric Ceramics. *Journal of the American Ceramic Society* **95**(11), 3383–3386 (2012).

[285] Chiang, Y.-M., Farrey, G. W. & Soukhojak, A. N. Lead-free high-strain single-crystal piezoelectrics in the alkaline-bismuth-titanate perovskite family. *Applied Physics Letters* **73**(25), 3683 (1998).

[286] Chen, C., Jiang, X., Li, Y., Wang, F., Zhang, Q. & Luo, H. Growth and electrical properties of $Na_{1/2}Bi_{1/2}TiO_3$–$BaTiO_3$ lead-free single crystal with morphotropic phase boundary composition. *Journal of Applied Physics* **108**(12), 124106 (2010).

[287] Schneider, D., Jo, W., Rödel, J., Rytz, D. & Granzow, T. Anisotropy of ferroelectric behavior of $(1-x)Bi_{1/2}Na_{1/2}TiO_3$–$xBaTiO_3$ single crystals across the morphotropic phase boundary. *Journal of Applied Physics* **116**(4), 044111 (2014).

[288] Smolenskii, G. A., Isupov, V. A., Agranovskaya, A. I. & Krainik, N. N. New Ferroelectrics of Complex Composition. *Soviet Physics - Solid State* **2**(11), 2651–2654 (1961).

[289] Smolenskii, G. A., Isupov, V. A. & Agranovskaya, A. I. Ferroelectrics of the Oxygen-Octahedral Type with Layered Structure. *Soviet Physics - Solid State* **3**(3), 651–655 (1961).

[290] Smolenskii, G. A., Isupov, V. A., Agranovskaya, A. I. & Popov, S. N. Ferroelectrics with Diffuse Phase Transitions. *Soviet Physics-Solid State* **2**(11), 2584–2594 (1961).

[291] Jones, G. O. & Thomas, P. A. Investigation of the structure and phase transitions in the novel A-site substituted distorted perovskite compound $Na_{0.5}Bi_{0.5}TiO_3$. *Acta Crystallographica Section B: Structural Science* **58**, 168–178 (2002).

[292] Ma, C., Tan, X. & Kleebe, H. J. *In situ* Transmission Electron Microscopy Study on the Phase Transitions in Lead-Free $(1–x)(Bi_{1/2}Na_{1/2})TiO_3–xBaTiO_3$ Ceramics. *Journal of the American Ceramic Society* **94**(11), 4040–4044 (2011).

[293] Ma, C., Guo, H., Beckman, S. P. & Tan, X. Creation and Destruction of Morphotropic Phase Boundaries through Electrical Poling: A Case Study of Lead-Free $(Bi_{1/2}Na_{1/2})TiO_3–BaTiO_3$ Piezoelectrics. *Physical Review Letters* **109**(10), 107602 (2012).

[294] Wylie-van Eerd, B., Damjanovic, D., Klein, N., Setter, N. & Trodahl, J. Structural complexity of$(Na_{0.5}Bi_{0.5})TiO_3–BaTiO_3$ as revealed by Raman spectroscopy. *Physical Review B* **82**(10), 104112 (2010).

[295] Picht, G., Töpfer, J. & Hennig, E. Structural properties of $(Bi_{0.5}Na_{0.5})_{1-x}Ba_xTiO_3$ lead-free piezoelectric ceramics. *Journal of the European Ceramic Society* **30**(16), 3445–3453 (2010).

[296] Hiruma, Y., Watanabe, Y., Nagata, H. & Takenaka, T. Phase Transition Temperatures of Divalent and Trivalent Ions Substituted $(Bi_{1/2}Na_{1/2})TiO_3$ Ceramics. *Key Engineering Materials* **350**, 93–96 (2007).

[297] Hiruma, Y., Yoshii, K., Nagata, H. & Takenaka, T. Investigation of Phase Transition Temperatures on $(Bi_{1/2}Na_{1/2})TiO_3–(Bi_{1/2}K_{1/2})TiO_3$ and $(Bi_{1/2}Na_{1/2})TiO_3–BaTiO_3$ Lead-free Piezoelectric Ceramics by Electrical Measurements. *Ferroelectrics* **346**(1), 114–119 (2007).

[298] Cordero, F., Craciun, F., Trequattrini, F., Mercadelli, E. & Galassi, C. Phase transitions and phase diagram of the ferroelectric perovskite $(Na_{0.5}Bi_{0.5})_{1-x}Ba_xTiO_3$ by anelastic and dielectric measurements. *Physical Review B* **81**(14), 144124 (2010).

[299] Ma, C., Guo, H. & Tan, X. A New Phase Boundary in $(Bi_{1/2}Na_{1/2})TiO_3–BaTiO_3$ Revealed via a Novel Method of Electron Diffraction Analysis. *Advanced Functional Materials* **23**(42), 5261–5266 (2013).

[300] Datta, K., Roleder, K. & Thomas, P. A. Enhanced tetragonality in lead-free piezoelectric $(1–x)BaTiO_3–xNa_{1/2}Bi_{1/2}TiO_3$ solid solutions where x=0.05-0.40. *Journal of Applied Physics* **106**(12), 123512 (2009).

[301] Datta, K., Thomas, P. A. & Roleder, K. Anomalous phase transitions of lead-free piezoelectric $xNa_{0.5}Bi_{0.5}TiO_3–(1\text{-}x)BaTiO_3$ solid solutions with enhanced phase transition temperatures. *Physical Review B* **82**(22), 224105 (2010).

[302] Deluca, M., Picht, G., Hoffmann, M. J., Rechtenbach, A., Töpfer, J., Schader, F. H. & Webber, K. G. Chemical and structural effects on the high-temperature mechanical behavior of $(1–x)(Na_{1/2}Bi_{1/2})TiO_3–xBaTiO_3$ ceramics. *Journal of Applied Physics* **117**(13), 134110 (2015).

[303] Ma, C. & Tan, X. Phase diagram of unpoled lead-free $(1–x)Bi_{1/2}Na_{1/2}TiO_3–xBaTiO_3$ ceramics. *Solid State Communications* **150**(33-34), 1497–1500 (2010).

[304] Tan, X., Ma, C., Frederick, J., Beckman, S., Webber, K. G. & Green, D. J. The Antiferroelectric ⟷ Ferroelectric Phase Transition in Lead-Containing and Lead-Free Perovskite Ceramics. *Journal of the American Ceramic Society* **94**(12), 4091–4107 (2011).

[305] Ranjan, R. & Dviwedi, A. Structure and dielectric properties of $(Na_{0.50}Bi_{0.50})_{1-x}Ba_xTiO_3$: $0 \leq x \leq 0.10$. *Solid State Communications* **135**(6), 394–399 (2005).

[306] Schmitt, L. A., Kling, J., Hinterstein, M., Hoelzel, M., Jo, W., Kleebe, H. J. & Fuess, H. Structural investigations on lead-free $Bi_{1/2}Na_{1/2}TiO_3$-based piezoceramics. *Journal of Materials Science* **46**(12), 4368–4376 (2011).

[307] Garg, R., Rao, B. N., Senyshyn, A., Krishna, P. S. R. & Ranjan, R. Lead-free piezoelectric system $(Na_{0.5}Bi_{0.5})TiO_3$-$BaTiO_3$: Equilibrium structures and irreversible structural transformations driven by electric field and mechanical impact. *Physical Review B* **88**(1), 014103 (2013).

[308] Daniels, J. E., Jo, W., Rödel, J., Rytz, D. & Donner, W. Structural origins of relaxor behavior in a $0.96(Bi_{1/2}Na_{1/2})TiO_3$–$0.04BaTiO_3$ single crystal under electric field. *Applied Physics Letters* **98**(25), 252904 (2011).

[309] Usher, T. M., Forrester, J. S., dela Cruz, C. R. & Jones, J. L. Crystal structure of $0.96(Na_{0.5}Bi_{0.5}TiO_3)$–$0.04(BaTiO_3)$ from combined refinement of x-ray and neutron diffraction patterns. *Applied Physics Letters* **101**(15), 152906 (2012).

[310] Groszewicz, P. B., Breitzke, H., Dittmer, R., Sapper, E., Jo, W., Buntkowsky, G. & Rödel, J. Nanoscale phase quantification in lead-free $(Bi_{1/2}Na_{1/2})TiO_3$–$BaTiO_3$ relaxor ferroelectrics by means of ^{23}Na NMR. *Physical Review B* **90**(22), 220104(R) (2014).

[311] Jo, W. & Rödel, J. Electric-field-induced volume change and room temperature phase stability of $(Bi_{1/2}Na_{1/2})TiO_3$-x mol.% $BaTiO_3$ piezoceramics. *Applied Physics Letters* **99**(4), 042901 (2011).

[312] Yao, Y., Sun, Z., Ji, Y., Yang, Y., Tan, X. & Ren, X. Evolution of the tetragonal to rhombohedral transition in $(1–x)(Bi_{1/2}Na_{1/2})TiO_3$–$xBaTiO_3$ ($x \leq 7\%$). *Science and Technology of Advanced Materials* **14**(3), 035008 (2013).

[313] Daniels, J. E., Jo, W., Rödel, J., Honkimäki, V. & Jones, J. L. Electric-field-induced phase-change behavior in $(Bi_{0.5}Na_{0.5})TiO_3$–$BaTiO_3$–$(K_{0.5}Na_{0.5})NbO_3$: A combinatorial investigation. *Acta Materialia* **58**(6), 2103–2111 (2010).

[314] Kling, J., Tan, X., Jo, W., Kleebe, H. J., Fuess, H. & Rödel, J. In Situ Transmission Electron Microscopy of Electric Field-Triggered Reversible Domain Formation in Bi-Based Lead-Free Piezoceramics. *Journal of the American Ceramic Society* **93**(9), 2452–2455 (2010).

[315] Simons, H., Daniels, J. E., Glaum, J., Studer, A. J., Jones, J. L. & Hoffman, M. Origin of large recoverable strain in $0.94(Bi_{0.5}Na_{0.5})TiO_3$–$0.06BaTiO_3$ near the ferroelectric-relaxor transition. *Applied Physics Letters* **102**(6), 062902 (2013).

[316] Xu, C., Lin, D. & Kwok, K. W. Structure, electrical properties and depolarization temperature of $(Bi_{0.5}Na_{0.5})TiO_3$–$BaTiO_3$ lead-free piezoelectric ceramics. *Solid State Sciences* **10**(7), 934–940 (2008).

[317] Foronda, H., Deluca, M., Aksel, E., Forrester, J. S. & Jones, J. L. Thermally-induced loss of piezoelectricity in ferroelectric $Na_{0.5}Bi_{0.5}TiO_3$–$BaTiO_3$. *Materials Letters* **115**, 132–135 (2014).

[318] Zhang, S.-T., Kounga, A. B., Aulbach, E. & Deng, Y. Temperature-Dependent Electrical Properties of $0.94Bi_{0.5}Na_{0.5}TiO_3$–$0.06BaTiO_3$ Ceramics. *Journal of the American Ceramic Society* **91**(12), 3950–3954 (2008).

[319] Chen, M., Xu, Q., Kim, B. H., Ahn, B. K., Ko, J. H., Kang, W. J. & Nam, O. J. Structure and electrical properties of $(Na_{0.5}Bi_{0.5})_{1-x}Ba_xTiO_3$ piezoelectric ceramics. *Journal of the European Ceramic Society* **28**(4), 843–849 (2008).

[320] Koruza, J., Franzbach, D. J., Schader, F., Rojas, V. & Webber, K. G. Enhancing the operational range of piezoelectric actuators by uniaxial compressive preloading. *Journal of Physics D: Applied Physics* **48**(21), 215302 (2015).

[321] Webber, K. G., Aulbach, E. & Rödel, J. High temperature blocking force measurements of soft lead zirconate titanate. *Journal of Physics D: Applied Physics* **43**(36), 365401 (2010).

[322] Tan, X., Aulbach, E., Jo, W., Granzow, T., Kling, J., Marsilius, M., Kleebe, H. J. & Rödel, J. Effect of uniaxial stress on ferroelectric behavior of $(Bi_{1/2}Na_{1/2})TiO_3$-based lead-free piezoelectric ceramics. *Journal of Applied Physics* **106**(4), 044107 (2009).

[323] Brandt, D. R. J., Acosta, M., Koruza, J. & Webber, K. G. Mechanical constitutive behavior and exceptional blocking force of lead-free BZT-xBCT piezoceramics. *Journal of Applied Physics* **115**(20), 204107 (2014).

[324] Chaplya, P. M. & Carman, G. P. Dielectric and piezoelectric response of lead zirconate-lead titanate at high electric and mechanical loads in terms of non-180 degrees domain wall motion. *Journal of Applied Physics* **90**(10), 5278–5286 (2001).

[325] Kerkamm, I., Hiller, P., Granzow, T. & Rödel, J. Correlation of small- and large-signal properties of lead zirconate titanate multilayer actuators. *Acta Materialia* **57**(1), 77–86 (2009).

[326] Dittmer, R., Webber, K. G., Aulbach, E., Jo, W., Tan, X. & Rödel, J. Optimal working regime of lead-zirconate-titanate for actuation applications. *Sensors and Actuators A: Physical* **189**, 187–194 (2013).

[327] Webber, K. G., Franzbach, D. J., Koruza, J. & Green, D. J. Determination of the True Operational Range of a Piezoelectric Actuator. *Journal of the American Ceramic Society* **97**(9), 2842–2849 (2014).

[328] Bancroft, D. The Effect of Hydrostatic Pressure on the Susceptibility of Rochelle Salt. *Physical Review* **53**(7), 587–590 (1938).

[329] Samara, G. A. Pressure dependence of the ferroelectric properties of rochelle salt. *Journal of Physics and Chemistry of Solids* **26**(1), 121–131 (1965).

[330] Merz, W. J. The Effect of Hydrostatic Pressure on the Curie Point of Barium Titanate Single Crystals. *Physical Review* **78**(1), 52–54 (1950).

[331] Klimowski, J. & Pietrzak, J. Effect of Hydrostatic Pressure on the Dielectric Properties of $BaTiO_3$. *Proceedings of the Physical Society* **75**(3), 456–459 (1960).

[332] Klimowski, J. Effect of high hydrostatic pressure on the dielectric properties of $BaTiO_3$ single crystals. *physica status solidi (b)* **2**(4), 456–459 (1962).

[333] Leonidova, G. G. & Volk, T. R. Phase transition in barium titanate at high hydrostatic pressure. *Soviet Physics - Solid State* **7**(11), 2694–2696 (1966).

[334] Polandov, I. N., Strukov, B. A. & Mylov, V. P. Change in nature of phase transition in barium titanate single crystals under hydrostatic pressure. *Soviet Physics - Solid State* **9**(5), 1153–1156 (1967).

[335] Shirane, G. & Sato, K. Effects of Mechanical Pressures on the Dielectric Properties of Polycrystalline Barium-Strontium Titanate. *Journal of the Physical Society of Japan* **6**(1), 20–26 (1951).

[336] Samara, G. A. Pressure and temperature dependence of the dielectric properties and phase transitions of the ferroelectric perovskites: $PbTiO_3$ and $BaTiO_3$. *Ferroelectrics* **2**(1), 277–289 (1971).

[337] Benguigui, L. Change of the Order of a Phase Transition by the Influence of an External Parameter. *physica status solidi (b)* **60**(2), 835–841 (1973).

[338] Samara, G. A. The Effect of Hydrostatic Pressure on Ferroelectric Properties. *Advances in High Pressure Research* **3**, 155–239 (1969).

[339] Clarke, R. & Benguigui, L. Tricritical point in $BaTiO_3$. *Journal of Physics C: Solid State Physics* **10**(11), 1963–1973 (1977).

[340] Decker, D. L. & Zhao, Y. X. Dielectric and polarization measurements on $BaTiO_3$ at high pressures to the tricritical point. *Physical Review B* **39**(4), 2432–2438 (1989).

[341] Ishidate, T., Abe, S., Takahashi, H. & Môri, N. Phase Diagram of $BaTiO_3$. *Physical Review Letters* **78**(12), 2397–2400 (1997).

[342] Forsbergh, P. W. Effect of a Two-Dimensional Pressure on the Curie Point of Barium Titanate. *Physical Review* **93**(4), 686 (1954).

[343] Jaffe, H., Berlincourt, D. & McKee, J. M. Effect of Pressure on the Curie Temperature of Polycrystalline Ceramic Barium Titanate. *Physical Review* **105**(1), 57–58 (1957).

[344] Choi, K. J., Biegalski, M., Li, Y. L., Sharan, A., Schubert, J., Uecker, R., Reiche, P., Chen, Y. B., Pan, X. Q., Gopalan, V., Chen, L.-Q., Schlom, D. G. & Eom, C. B. Enhancement of Ferroelectricity in Strained $BaTiO_3$ Thin Films. *Science* **306**(5698), 1005–1009 (2004).

[345] Takagi, Y., Sawaguchi, E. & Akioka, T. On the Effect of Mechanical Stress upon the Permittivity of Barium Titanate. *Journal of the Physical Society of Japan* **3**(4), 270–271 (1948).

[346] Sinyakov, E. V., Dudnik, E. F. & Flerova, S. A. Influence of Mechanical Pressure on Polarization Processes in $BaTiO_3$ Single Crystals and in Solid Solutions of $BaTiO_3$–ZnO. *Soviet Physics - Solid State* **8**(10), 2278–2281 (1967).

[347] Suchanicz, J., Stopa, G., Konieczny, K., Wcislo, D., Dziubaniuk, M. & Rymarczyk, J. Uniaxial Pressure Effect on the Dielectric Properties of the $BaTiO_3$ Single Crystals. *Ferroelectrics* **366**(1), 3–10 (2008).

[348] Suchanicz, J. Axial pressure effect on a phase transition nature and ferroelectric properties of single crystal $Na_{0.5}Bi_{0.5}TiO_3$. *Journal of Physics and Chemistry of Solids* **62**(7), 1271–1276 (2001).

[349] Picht, G., Webber, K. G., Zhang, Y., Kungl, H., Damjanovic, D. & Hoffmann, M. J. Critical mechanical and electrical transition behavior of $BaTiO_3$: The observation of mechanical double loop behavior. *Journal of Applied Physics* **112**(12), 124101 (2012).

[350] Daniels, J. E., Picht, G., Kimber, S. & Webber, K. G. Mechanical double loop behavior in $BaTiO_3$: Stress induced paraelastic to ferroelastic phase transformation. *Applied Physics Letters* **103**(12), 122902 (2013).

[351] Webber, K. G., Zhang, Y., Jo, W., Daniels, J. E. & Rödel, J. High temperature stress-induced "double loop-like" phase transitions in Bi-based perovskites. *Journal of Applied Physics* **108**(1), 014101–014106 (2010).

[352] Janolin, P.-E., Dkhil, B., Davis, M., Damjanovic, D. & Setter, N. Uniaxial-stress induced phase transitions in $[001]_C$-poled $0.955Pb(Zn_{1/3}Nb_{2/3})O_3$–$0.045PbTiO_3$. *Applied Physics Letters* **90**(15), 152907 (2007).

[353] Avdeev, M., Jorgensen, J. D., Short, S., Samara, G. A., Venturini, E. L., Yang, P. & Morosin, B. Pressure-induced ferroelectric to antiferroelectric phase transition in $Pb_{0.99}(Zr_{0.95}Ti_{0.05})_{0.98}Nb_{0.02}O_3$. *Physical Review B* **73**(6), 064105 (2006).

[354] Ahart, M., Somayazulu, M., Cohen, R. E., Ganesh, P., Dera, P., Mao, H. K., Hemley, R. J., Ren, Y., Liermann, P. & Wu, Z. Origin of morphotropic phase boundaries in ferroelectrics. *Nature* **451**(7178), 545–548 (2008).

[355] Gröting, M., Kornev, I., Dkhil, B. & Albe, K. Pressure-induced phase transitions and structure of chemically ordered nanoregions in the lead-free relaxor ferroelectric $Na_{1/2}Bi_{1/2}TiO_3$. *Physical Review B* **86**(13), 134118 (2012).

[356] Koch, W. Ferroelektrische Nachwirkungserscheinungen an polykristallinem Bariumtitanat. *Zeitschrift für Naturforschung A* **13**(4), 303–310 (1958).

[357] Ksendzov, Y. M. & Rotenberg, B. A. The Effect of Pressure on the Electric Properties of Barium Titanate in Weak Fields. *Soviet Physics-Solid State* **1**(4), 579–584 (1959).

[358] Brown, R. F. Effect of two-dimensional Mechanical Stress on Dielectric Properties of Poled Ceramic Barium Titanate and Lead Zirconate Titanate. *Canadian Journal of Physics* **39**(5), 741–753 (1961).

[359] Steiner, O., Tagantsev, A. K., Colla, E. L. & Setter, N. Uniaxial stress dependence of the permittivity of electroceramics. *Journal of the European Ceramic Society* **19**(6-7), 1243–1246 (1999).

[360] Klimkowski, G., Suchanicz, J., Karpierz, M., Lewczuk, U., Faszczowy, I., Konieczny, K., Sitko, D., Antonova, M. & Sternberg, A. Uniaxial Pressure Effect on Dielectric Properties of $0.7Na_{0.5}Bi_{0.5}TiO_3$–$0.3SrTiO_3$Ceramics. *Ferroelectrics* **464**(1), 94–100 (2014).

[361] Zhang, Q. M., Zhao, J., Uchino, K. & Zheng, J. Change of the weak-field properties of $Pb(ZrTi)O_3$ piezoceramics with compressive uniaxial stresses and its links to the effect of dopants on the stability of the polarizations in the materials. *Journal of Materials Research* **12**(01), 226–234 (1997).

[362] Zhang, Q. M. M. & Zhao, J. Z. Electromechanical properties of lead zirconate titanate piezoceramics under the influence of mechanical stresses. *IEEE Transactions on Ultrasonics, Ferroelectrics, and Frequency Control* **46**(6), 1518–1526 (1999).

[363] Yang, G., Liu, S. F., Ren, W. & Mukherjee, B. K. Effects of uniaxial stress on the piezoelectric, dielectric, and mechanical properties of lead zirconate titanate piezoceramics. *Ferroelectrics* **262**(1-4), 1181–1186 (2001).

[364] Zhou, D., Kamlah, M. & Munz, D. Uniaxial Compressive Stress Dependence of the High-Field Dielectric and Piezoelectric Performance of Soft PZT Piezoceramics. *Journal of Materials Research* **19**(3), 834–842 (2004).

[365] Algueró, M., Cheng, B. L., Guiu, F., Reece, M. J., Poole, M. & Alford, N. Degradation of the d_{33} piezoelectric coefficient for PZT ceramics under static and cyclic compressive loading. *Journal of the European Ceramic Society* **21**(10-11), 1437–1440 (2001).

[366] Ehmke, M. C., Daniels, J., Glaum, J., Hoffman, M., Blendell, J. E. & Bowman, K. J. Reduction of the piezoelectric performance in lead-free $(1–x)Ba(Zr_{0.2}Ti_{0.8})O_3–x(Ba_{0.7}Ca_{0.3})TiO_3$ piezoceramics under uniaxial compressive stress. *Journal of Applied Physics* **112**(11), 114108 (2012).

[367] Gao, J., Xu, Z., Li, F., Zhang, C., Liu, Y., Liu, G. & He, H. The effect of the hydrostatic pressure on the electromechanical properties of ferroelectric rhombohedral single crystals $Pb(Mg_{1/3}Nb_{2/3})$–$Pb(In_{1/2}Nb_{1/2})$–$PbTiO_3$. *Applied Physics Letters* **99**(6), 062903 (2011).

[368] Gao, J. J., Xu, Z., Li, F., Zhang, C. H., Liu, Y., Liu, G. M. & He, H. L. The hydrostatic pressure dependence of the piezoelectric properties for the barium titanate and lead titanate crystals: Thermodynamic analysis. *Journal of Applied Physics* **109**(11), 114111 (2011).

[369] Zhou, D. Y., Kamlah, M. & Munz, D. Effects of uniaxial prestress on the ferroelectric hysteretic response of soft PZT. *Journal of the European Ceramic Society* **25**(4), 425–432 (2005).

[370] Lynch, C. S. The effect of uniaxial stress on the electro-mechanical response of 8/65/35 PLZT. *Acta Materialia* **44**(10), 4137–4148 (1996).

[371] Chaisan, W., Yimnirun, R. & Ananta, S. Changes in ferroelectric properties of barium titanate ceramic with compressive stress. *Physica Scripta* **2007**(T129), 205–208 (2007).

[372] Dittmer, R., Webber, K. G., Aulbach, E., Jo, W., Tan, X. L. & Rödel, J. Electric-field-induced polarization and strain in $0.94(Bi_{1/2}Na_{1/2})TiO_3$–$0.06BaTiO_3$ under uniaxial stress. *Acta Materialia* **61**(4), 1350–1358 (2013).

[373] Ehmke, M. C., Schader, F. H., Webber, K. G., Rödel, J., Blendell, J. E. & Bowman, K. J. Stress, temperature and electric field effects in the lead-free $(Ba,Ca)(Ti,Zr)O_3$ piezoelectric system. *Acta Materialia* **78**, 37–45 (2014).

[374] Granzow, T., Leist, T., Kounga, A. B., Aulbach, E. & Rödel, J. Ferroelectric properties of lead zirconate titanate under radial load. *Applied Physics Letters* **91**(14), 142904 (2007).

[375] Tanaka, Y., Harigai, T., Adachi, H., Sakamoto, N., Wakiya, N., Suzuki, H. & Fujii, E. Strain-driven control of piezoelectricity in $(Na,Bi)TiO_3$–$BaTiO_3$ epitaxial thin films. *Applied Physics Letters* **102**(19), 192901 (2013).

[376] Grubbs, R. K., Venturini, E. L., Samara, G. A., Wang, Y. & Setter, N. Dielectric properties of Zr-modified $Pb(Mg_{1/3}Ta_{2/3})O_3$ ceramic: Influence of pressure, biasing electric field, and B-site cationic order. *Journal of Applied Physics* **100**(11), 114505–114508 (2006).

[377] Samara, G. A. Pressure as a probe of the glassy properties of disordered ferroelectrics, antiferroelectrics and dielectrics. *Ferroelectrics* **117**(1), 347–372 (1991).

[378] Samara, G. A. & Boatner, L. A. Ferroelectric-to-relaxor crossover and oxygen vacancy hopping in the compositionally disordered perovskites $KTa_{1-x}Nb_xO_3$:C. *Physical Review B* **61**(6), 3889–3896 (2000).

[379] Samara, G. A. The relaxational properties of compositionally disordered ABO_3 perovskites. *Journal of Physics: Condensed Matter* **15**(9), R367–R411 (2003).

[380] Samara, G. A. Glasslike Behavior and Novel Pressure Effects in $KTa_{1-x}Nb_xO_3$. *Physical Review Letters* **53**(3), 298–301 (1984).

[381] Samara, G. A. Pressure-Induced Crossover from Long- to Short-Range Order in Compositionally Disordered Soft Mode Ferroelectrics. *Physical Review Letters* **77**(2), 314–317 (1996).

[382] Samara, G. A. Pressure Induced Crossover and Mechanism for the Ferroelectric-to-Relaxor (Glass-Like) Transition in Compositionally-Disordered Soft Mode Systems. *Ferroelectrics* **274**(1), 183–202 (2002).

[383] Blinc, R., Bobnar, V. & Pirc, R. Coupled spherical pseudospin-phonon model and the pressure-temperature phase diagram of relaxor ferroelectrics. *Physical Review B* **64**(13), 132103 (2001).

[384] Sawyer, C. B. & Tower, C. H. Rochelle Salt as a Dielectric. *Physical Review* **35**(3), 269–273 (1930).

[385] Czichos, H., Skrotzki, B. & Simon, F.-G. *Das Ingenieurwissen: Werkstoffe*. Springer-Verlag Berlin Heidelberg, Berlin and Heidelberg, (2014).

[386] Seo, Y.-H., Vögler, M., Isaia, D., Aulbach, E., Rödel, J. & Webber, K. G. Temperature-dependent R-curve behavior of $Pb(Zr_{1-x}Ti_x)O_3$. *Acta Materialia* **61**(17), 6418–6427 (2013).

[387] Schader, F. H., Aulbach, E., Webber, K. G. & Rossetti, G. A. Influence of uniaxial stress on the ferroelectric-to-paraelectric phase change in barium titanate. *Journal of Applied Physics* **113**(17), 174103 (2013).

[388] Zeches, R. J., Rossell, M. D., Zhang, J. X., Hatt, A. J., He, Q., Yang, C. H., Kumar, A., Wang, C. H., Melville, A., Adamo, C., Sheng, G., Chu, Y. H., Ihlefeld, J. F., Erni, R., Ederer, C., Gopalan, V., Chen, L. Q., Schlom, D. G., Spaldin, N. A., Martin, L. W. & Ramesh, R. A Strain-Driven Morphotropic Phase Boundary in $BiFeO_3$. *Science* **326**(5955), 977–980 (2009).

[389] Frey, M. H., Xu, Z., Han, P. & Payne, D. A. The role of interfaces on an apparent grain size effect on the dielectric properties for ferroelectric barium titanate ceramics. *Ferroelectrics* **206**(1), 337–353 (1998).

[390] Drougard, M. E. & Young, D. R. Dielectric Constant Behavior of Single-Domain, Single Crystals of Barium Titanate in the Vicinity of the Curie Point. *Physical Review* **95**(5), 1152–1153 (1954).

[391] Johnson, C. J. Some Dielectric and Electro-optic Properties of $BaTiO_3$ Single Crystals. *Applied Physics Letters* **7**(8), 221–223 (1965).

[392] Merz, W. J. The Dielectric Behavior of $BaTiO_3$ Single-Domain Crystals. *Physical Review* **75**(4), 687 (1949).

[393] Newnham, R. E., Sundar, V., Yimnirun, R., Su, J. & Zhang, Q. M. Electrostriction: Nonlinear Electromechanical Coupling in Solid Dielectrics. *The Journal of Physical Chemistry B* **101**(48), 10141–10150 (1997).

[394] Pramanick, A., Damjanovic, D., Daniels, J. E., Nino, J. C. & Jones, J. L. Origins of Electro-Mechanical Coupling in Polycrystalline Ferroelectrics During Subcoercive Electrical Loading. *Journal of the American Ceramic Society* **94**(2), 293–309 (2011).

[395] Uchino, K. & Nomura, S. Critical exponents of the dielectric constants in diffused-phase-transition crystals. *Ferroelectrics* **44**(1), 55–61 (1982).

[396] Cheng, B. L., Gabbay, M., Duffy, W. & Fantozzi, G. Mechanical loss and Young's modulus associated with phase transitions in barium titanate based ceramics. *Journal of Materials Science* **31**(18), 4951–4955 (1996).

[397] Dul'kin, E., Petzelt, J., Kamba, S., Mojaev, E. & Roth, M. Relaxor-like behavior of $BaTiO_3$ crystals from acoustic emission study. *Applied Physics Letters* **97**(3), 032903 (2010).

[398] Ko, J.-H., Kim, T. H., Roleder, K., Rytz, D. & Kojima, S. Precursor dynamics in the ferroelectric phase transition of barium titanate single crystals studied by Brillouin light scattering. *Physical Review B* **84**(9), 094123 (2011).

[399] Dul'kin, E. & Roth, M. Nontrivial behavior of T_c at the small electric field in $BaTiO_3$ crystals, detected by means of acoustic emission. *Journal of Physics: Condensed Matter* **25**(15), 155901 (2013).

[400] Salje, E. K. H., Carpenter, M. A., Nataf, G. F., Picht, G., Webber, K., Weerasinghe, J., Lisenkov, S. & Bellaiche, L. Elastic excitations in $BaTiO_3$ single crystals and ceramics: Mobile domain boundaries and polar nanoregions observed by resonant ultrasonic spectroscopy. *Physical Review B* **87**(1), 014106 (2013).

[401] Lee, S., Rossetti, G. A., Liu, Z.-K. & Randall, C. A. Intrinsic ferroelectric properties of the nonstoichiometric perovskite oxide $Ba_{1-x}Ti_{1-y}O_{3-x-y}$. *Journal of Applied Physics* **105**(9), 093519 (2009).

[402] Schrade, D., Mueller, R., Xu, B. X. & Gross, D. Domain evolution in ferroelectric materials: A continuum phase field model and finite element implementation. *Computer Methods in Applied Mechanics and Engineering* **196**(41-44), 4365–4374 (2007).

[403] Tan, X., Frederick, J., Ma, C., Aulbach, E., Marsilius, M., Hong, W., Granzow, T., Jo, W. & Rödel, J. Electric-field-induced antiferroelectric to ferroelectric phase transition in mechanically confined $Pb_{0.99}Nb_{0.02}[(Zr_{0.57}Sn_{0.43})_{0.94}Ti_{0.06}]_{0.98}O_3$. *Physical Review B* **81**(1), 014103 (2010).

[404] Krueger, H. H. A. & Berlincourt, D. Effects of High Static Stress on Piezoelectric Properties of Transducer Materials. *Journal of the Acoustical Society of America* **33**(10), 1339–1344 (1961).

[405] Krueger, H. H. A. Stress sensitivity of Piezoelectric Ceramics Part 1 - Sensitivity to Compressive Stress Parallel to the Polar Axis. *Journal of the Acoustical Society of America* **42**(3), 636–645 (1967).

[406] Krueger, H. H. A. Stress sensitivity of Piezoelectric Ceramics Part 3 - Sensitivity to Compressive Stress Perpendicular to the Polar Axis. *Journal of the Acoustical Society of America* **43**(3), 583–591 (1968).

[407] Liu, Q. D. & Huber, J. E. State dependent linear moduli in ferroelectrics. *International Journal of Solids and Structures* **44**(17), 5635–5650 (2007).

[408] Ochoa, D. A., García, J. E., Tamayo, I., Gomis, V., Damjanovic, D. & Perez, R. Effect of Uniaxial Compressive Stress on Dielectric and Piezoelectric Responses in Lead Zirconate Titanate Based Ceramics. *Journal of the American Ceramic Society* **95**(5), 1656–1660 (2012).

[409] Schader, F. H., Morozov, M., Wefring, E. T., Grande, T. & Webber, K. G. Mechanical stability of piezoelectric properties in ferroelectric perovskites. *Journal of Applied Physics* **117**(19), 194101 (2015).

[410] Anton, E.-M., Jo, W., Damjanovic, D. & Rödel, J. Determination of depolarization temperature of $(Bi_{1/2}Na_{1/2})TiO_3$-based lead-free piezoceramics. *Journal of Applied Physics* **110**(9), 094108 (2011).

[411] Morozov, M. I. & Damjanovic, D. Charge migration in $Pb(Zr,Ti)O_3$ ceramics and its relation to ageing, hardening, and softening. *Journal of Applied Physics* **107**(3), 034106 (2010).

[412] Garcia, J. E., Ochoa, D. A., Gomis, V., Eiras, J. A. & Pérez, R. Evidence of temperature dependent domain wall dynamics in hard lead zirconate titanate piezoceramics. *Journal of Applied Physics* **112**(1), 014113 (2012).

[413] Arlt, G. Piezoelectric relaxation. *Ferroelectrics* **40**(1), 149–157 (1982).

[414] Damjanovic, D., Gururaja, T. R., Jang, S. J. & Cross, L. E. Temperature behavior of the complex piezoelectric d_{31} coefficient in modified lead titanate ceramics. *Materials Letters* **4**(10), 414–419 (1986).

[415] Damjanovic, D. Hysteresis in Piezoelectric and Ferroelectric Materials. In *The Science of Hysteresis,* Mayergoyz, G. B. D. (Hrsg.), 337–465. Academic Press, Oxford (2006).

[416] Damjanovic, D., Demartin Maeder, M., Duran Martin, P., Voisard, C. & Setter, N. Maxwell-Wagner piezoelectric relaxation in ferroelectric heterostructures. *Journal of Applied Physics* **90**(11), 5708 (2001).

[417] Bourim, E. M., Tanaka, H., Gabbay, M., Fantozzi, G. & Cheng, B. L. Domain wall motion effect on the anelastic behavior in lead zirconate titanate piezoelectric ceramics. *Journal of Applied Physics* **91**(10), 6662 (2002).

[418] Cordero, F. Elastic Properties and Enhanced Piezoelectric Response at Morphotropic Phase Boundaries. *Materials* **8**(12), 8195–8245 (2015).

[419] Hoffmann, M. J., Hammer, M., Endriss, A. & Lupascu, D. C. Correlation between microstructure, strain behavior, and acoustic emission of soft PZT ceramics. *Acta Materialia* **49**(7), 1301–1310 (2001).

[420] Leist, T., Webber, K. G., Jo, W., Granzow, T., Aulbach, E., Suffner, J. & Rödel, J. Domain switching energies: Mechanical versus electrical loading in La-doped bismuth ferrite-lead titanate. *Journal of Applied Physics* **109**(5), 054109 (2011).

[421] Li, Y. W., Zhou, X. L. & Li, F. X. Temperature-dependent mechanical depolarization of ferroelectric ceramics. *Journal of Physics D: Applied Physics* **43**(17), 175501 (2010).

[422] Glaum, J., Genenko, Y. A., Kungl, H., Schmitt, L. A. & Granzow, T. De-aging of Fe-doped lead-zirconate-titanate ceramics by electric field cycling: 180 degrees- vs. non-180 degrees domain wall processes. *Journal of Applied Physics* **112**(3), 034103 (2012).

[423] Zhang, L. X. & Ren, X. In situobservation of reversible domain switching in aged Mn-doped $BaTiO_3$ single crystals. *Physical Review B* **71**(17), 174108 (2005).

[424] Zhang, S., Luo, J., Hackenberger, W. & Shrout, T. R. Characterization of $Pb(In_{1/2}Nb_{1/2})O_3$–$Pb(Mg_{1/3}Nb_{2/3})O_3$–$PbTiO_3$ ferroelectric crystal with enhanced phase transition temperatures. *Journal of Applied Physics* **104**(6), 064106 (2008).

[425] Gallagher, J., Lynch, C. & Tian, J. Effects of composition and temperature on the large-field behavior of $[001]_C$ relaxor single crystals. *IEEE Transactions on Ultrasonics, Ferroelectrics, and Frequency Control* **61**(12), 2153–2157 (2014).

[426] Davis, M., Budimir, M., Damjanovic, D. & Setter, N. Rotator and extender ferroelectrics: Importance of the shear coefficient to the piezoelectric properties of domain-engineered crystals and ceramics. *Journal of Applied Physics* **101**(5), 054112 (2007).

[427] Shanthi, M., Hoe, K. H., Lim, C. Y. H. & Lim, L. C. Overpoling-induced property degradation in $Pb(Mg_{1/3}Nb_{2/3})O_3$–$PbTiO_3$ single crystals of near-morphotropic phase boundary compositions. *Applied Physics Letters* **86**(26), 262908 (2005).

[428] Rajan, K. K., Jin, J., Chang, W. S. & Lim, L.-C. Transverse-Mode Properties of [011]-Poled $Pb(Zn_{1/3}Nb_{2/3})O_3$–$PbTiO_3$ Single Crystals: Effects of Composition, Length Orientation, and Poling Conditions. *Japanese Journal of Applied Physics* **46**(2), 681–685 (2007).

[429] Bokov, A. A. & Ye, Z. G. Field-induced shift of morphotropic phase boundary and effect of overpoling in (1–x)Pb($Mg_{1/3}Nb_{2/3}$)O_3–xPbTiO_3 piezocrystals. *Applied Physics Letters* **92**(8), 082901 (2008).

[430] Okawara, C. & Amin, A. dc field effect on stability of piezoelectric PZN-0.06PT single crystals under compressive stress. *Applied Physics Letters* **95**(7), 072902 (2009).

[431] Finkel, P., Robinson, H., Stace, J. & Amin, A. Study of phase transitions in ternary lead indium niobate-lead magnesium niobate-lead titanate relaxor ferroelectric morphotropic single crystals. *Applied Physics Letters* **97**(12), 122903 (2010).

[432] Finkel, P., Benjamin, K. & Amin, A. Large strain transduction utilizing phase transition in relaxor-ferroelectric Pb($In_{1/2}Nb_{1/2}$)O_3–Pb($Mg_{1/3}Nb_{2/3}$)O_3–PbTiO_3 single crystals. *Applied Physics Letters* **98**(19), 192902 (2011).

[433] Schader, F. H., Wang, Z., Hinterstein, M., Daniels, J. E. & Webber, K. G. Stress-modulated relaxor-to-ferroelectric transition in lead-free ($Na_{1/2}Bi_{1/2}$)TiO_3–BaTiO_3 ferroelectrics. *Physical Review B* **93**(13), 134111 (2016).

[434] Raevski, I. P., Prosandeev, S. A., Emelyanov, A. S., Raevskaya, S. I., Colla, E. V., Viehland, D., Kleemann, W., Vakhrushev, S. B., Dellis, J.-L., El Marssi, M. & Jastrabik, L. Bias-field effect on the temperature anomalies of dielectric permittivity in Pb$Mg_{1/3}Nb_{2/3}O_3$–PbTiO_3 single crystals. *Physical Review B* **72**(18), 184104 (2005).

[435] Jo, W., Schaab, S., Sapper, E., Schmitt, L. A., Kleebe, H. J., Bell, A. J. & Rödel, J. On the phase identity and its thermal evolution of lead free ($Bi_{1/2}Na_{1/2}$)TiO_3-6 mol% BaTiO_3. *Journal of Applied Physics* **110**(7), 074106 (2011).

[436] Sapper, E. *Lead-free (1-x)($Bi_{1/2}Na_{1/2}$)TiO_3-xBaTiO_3: The impact of relaxor characteristics and induced long range order on piezoelectric properties*. PhD thesis, TU Darmstadt, (2014).

[437] Arlt, G., Dederichs, H. & Herbiet, R. 90°-domain wall relaxation in tetragonally distorted ferroelectric ceramics. *Ferroelectrics* **74**(1), 37–53 (1987).

[438] Kutnjak, Z., Vodopivec, B. & Blinc, R. Anisotropy of electric field frezing of the relaxor ferroelectric Pb($Mg_{1/3}Nb_{2/3}$)O_3. *Physical Review B* **77**(5), 054102 (2008).

[439] Peräntie, J., Hagberg, J., Uusimäki, A. & Jantunen, H. Temperature characteristics and development of field-induced phase transition in relaxor ferroelectric Pb($Mg_{1/3}Nb_{2/3}$)$_{0.87}Ti_{0.13}O_3$ ceramics. *Applied Physics Letters* **93**(13), 132905 (2008).

[440] Sapper, E., Schaab, S., Jo, W., Granzow, T. & Rödel, J. Influence of electric fields on the depolarization temperature of Mn-doped (1–x)$Bi_{1/2}Na_{1/2}TiO_3$–xBaTiO_3. *Journal of Applied Physics* **111**(1), 014105 (2012).

[441] Hinterstein, M., Knapp, M., Hölzel, M., Jo, W., Cervellino, A., Ehrenberg, H. & Fuess, H. Field-induced phase transition in $Bi_{1/2}Na_{1/2}TiO_3$-based lead-free piezoelectric ceramics. *Journal of Applied Crystallography* **43**(6), 1314–1321 (2010).

[442] Aksel, E., Foronda, H., Calhoun, K. A., Jones, J. L., Schaab, S. & Granzow, T. Processing and properties of $Na_{0.5}Bi_{0.5}TiO_3$ piezoelectric ceramics modified with La, Mn and Fe. *Functional Materials Letters* **3**(1), 45–48 (2010).

[443] Sapper, E., Dittmer, R., Damjanovic, D., Erdem, E., Keeble, D. J., Jo, W., Granzow, T. & Rödel, J. Aging in the relaxor and ferroelectric state of Fe-doped (1–x)($Bi_{1/2}Na_{1/2}$)TiO_3–xBaTiO_3 piezoelectric ceramics. *Journal of Applied Physics* **116**(10), 104102 (2014).

[444] Aksel, E., Erdem, E., Jakes, P., Jones, J. L. & Eichel, R.-A. Defect structure and materials "hardening" in Fe_2O_3-doped $[Bi_{0.5}Na_{0.5}]TiO_3$ ferroelectrics. *Applied Physics Letters* **97**(1), 012903 (2010).

[445] Ossmer, H., Slouka, C., Andrejs, L., Blaha, P., Friedbacher, G. & Fleig, J. Electrocoloration of donor-doped lead zirconate titanate under DC field stress. *Solid State Ionics* **281**, 49–59 (2015).

[446] Wefring, E. T., Schader, F. H., Webber, K. G., Einarsrud, M.-A. & Grande, T. Electrical conductivity and ferroelastic properties of Ti-substituted solid solutions $(1-x)BiFeO_3-xBi_{0.5}K_{0.5}TiO_3$. *Journal of the European Ceramic Society* **36**(3), 497–506 (2016).

[447] Wang, R., Wang, K., Yao, F., Li, J.-F., Schader, F. H., Webber, K. G., Jo, W., Rödel, J. & Zhang, S. Temperature Stability of Lead-Free Niobate Piezoceramics with Engineered Morphotropic Phase Boundary. *Journal of the American Ceramic Society* **98**(7), 2177–2182 (2015).

[448] Christmann, J., Müller, R., Webber, K. G., Isaia, D., Schader, F. H., Kipfstuhl, S., Freitag, J. & Humbert, A. Measurement of the fracture toughness of polycrystalline bubbly ice from an Antarctic ice core. *Earth System Science Data* **7**(1), 87–92 (2015).

Curiculum Vitae

Education

06/2011 – 07/2016	TU Darmstadt: PhD student in materials science
10/2007 – 02/2011	TU Darmstadt: Materials science studies (Dipl.-Ing.)
10/2005 – 09/2007	Ruprecht-Karls-Universität Heidelberg: Physics studies
2005	Lessing-Gymnasium Lampertheim: Abitur

Work Experience

06/2011 – 12/2015	TU Darmstadt: Research Assistant in materials science (NAW, EO)
09/2009 – 12/2009	3M Technical Ceramics, Kempten (Allgäu): Internship in R&D devision
07/2008 – 06/2009	TU Darmstadt: Student Assistant in the Surface Science department

Conference Contributions

Schader, F. H., Isaia, D., Weber, M., Aulbach, E. & Webber, K. G. High Temperature Stress-Dependent Piezoelec-tricity of Pb(Zr,Ti)O_3. (oral presentation) *International Symposium on the Applications of Ferroelectrics (ISAF)*, Penn State University, State College, USA (2014)

Schader, F. H., Aulbach, E., Webber, K. G. & Rossetti, G. A. The Influence of Stress on Phase Transitions in $BaTiO_3$. (oral presentation), *International Symposium on the Applications of Ferroelectrics (ISAF)*, Prag, Czech Republic (2013)

Schader, F. H., Aulbach, E. & Webber, K. G. Stress induced changes in the phase transition behavior of barium titanate. (poster presentation), *European Meeting on Ferroelectricity*, Bordeaux, France (2011)

Publications

Schader, F. H., Wang, Z., Hinterstein, M., Daniels, J. E. & Webber, K. G. Stress-modulated relaxor-to-ferroelectric transition in lead-free $(Na_{1/2}Bi_{1/2})TiO_3$–$BaTiO_3$ ferroelectrics. *Physical Review B* **93**(13), 134111 (2016)

Wefring, E. T., Schader, F. H., Webber, K. G., Einarsrud, M.-A. & Grande, T. Electrical conductivity and ferroelastic properties of Ti-substituted solid solutions $(1–x)BiFeO_3$–$xBi_{0.5}K_{0.5}TiO_3$. *Journal of the European Ceramic Society* **36**(3), 497–506 (2016)

Schader, F. H., Morozov, M., Wefring, E. T., Grande, T. & Webber, K. G. Mechanical stability of piezoelectric properties in ferroelectric perovskites. *Journal of Applied Physics* **117**(19), 194101 (2015)

Wang, R., Wang, K., Yao, F., Li, J.-F., Schader, F. H., Webber, K. G., Jo, W., Rödel, J. & Zhang, S. Temperature Stability of Lead-Free Niobate Piezoceramics with Engineered Morphotropic Phase Boundary. *Journal of the American Ceramic Society* **98**(7), 2177–2182 (2015)

Deluca, M., Picht, G., Hoffmann, M. J., Rechtenbach, A., Töpfer, J., Schader, F. H. & Webber, K. G. Chemical and structural effects on the high-temperature mechanical behavior of $(1–x)(Na_{1/2}Bi_{1/2})TiO_3$–$xBaTiO_3$ ceramics. *Journal of Applied Physics* **117**(13), 134110 (2015)

Koruza, J., Franzbach, D. J., Schader, F., Rojas, V. & Webber, K. G. Enhancing the operational range of piezoelectric actuators by uniaxial compressive preloading. *Journal of Physics D: Applied Physics* **48**(21), 215302 (2015)

Christmann, J., Müller, R., Webber, K. G., Isaia, D., Schader, F. H., Kipfstuhl, S., Freitag, J. & Humbert, A. Measurement of the fracture toughness of polycrystalline bubbly ice from an Antarctic ice core. *Earth System Science Data* **7**(1), 87–92 (2015)

Ehmke, M. C., Schader, F. H., Webber, K. G., Rödel, J., Blendell, J. E. & Bowman, K. J. Stress, temperature and electric field effects in the lead-free $(Ba,Ca)(Ti,Zr)O_3$ piezoelectric system. *Acta Materialia* **78**, 37–45 (2014)

Schader, F. H., Aulbach, E., Webber, K. G. & Rossetti, G. A. Influence of uniaxial stress on the ferroelectric-to-paraelectric phase change in barium titanate. *Journal of Applied Physics* **113**(17), 174103 (2013)

Erklärung zur Dissertation

Hiermit versichere ich, die vorliegende Dissertation ohne Hilfe Dritter nur mit den angegebenen Quellen und Hilfsmitteln angefertigt zu haben. Alle Stellen, die aus Quellen entnommen wurden, sind als solche kenntlich gemacht. Diese Arbeit hat in gleicher oder ähnlicher Form noch keiner Prüfungsbehörde vorgelegen.

Darmstadt, den

(Florian Herbert Schader)